

**Robotic Systems for Environmental Monitoring and Terrain
Characterization**

by

Nicolas Alejandro Olmedo

A thesis submitted in partial fulfillment of the requirements for the degree of

Doctor of Philosophy

Department of Mechanical Engineering

University of Alberta

© Nicolas Alejandro Olmedo, 2020

Abstract

Unmanned ground vehicles (UGVs) can be integrated as part of environmental characterization campaigns in difficult terrains, such as oil sands tailings ponds. The feasibility of using such systems and designing sampling tool payloads which can deliver sufficient performance and reliability to perform field operations in the oil sands has not been previously achieved. A wheeled robotic system for collecting samples and characterizing mine waste deposit soil properties based on terramechanics models was designed and tested under field conditions. An automated vane shear test tool, designed for deployment and field operations onboard the UGV, was built and experimentally validated. A novel measurement apparatus was developed to estimate the inertia tensor of the robot for future simulation and model-based control design purposes. A modular robotic arm, used to deploy and wield the automated vane shear as well as a scoop-type sampler and an instrumented terramechanics wheel, was designed, built and tested in field trials. An improved terramechanics model for the scoop-type sampler was proposed, validated in simulation and experiment and shown to provide superior performance relative to the existing state-of-the-art model. The overall work and its contributions are summarized, limitations are analyzed, and recommendations for future work and commercialization of the developed technology are given.

Preface

Some of the research reported in this thesis was conducted in collaboration with others.

Chapter 2 of this thesis has been published as N. A. Olmedo, M. G. Lipsett, “Design and field experimentation of a robotic system for tailings characterization”, *Journal of Unmanned Vehicle Systems* 4(3):169–192 (2016). The author was responsible for concept formation, system design and construction, field data collection, data analysis, and manuscript preparation. Dr. Lipsett was the supervisory author and was involved in concept formation, assisted with the field data collection, and contributed to manuscript edits.

Chapter 3 of this thesis has been submitted for publication as N. A. Olmedo, B. Fisseha, W. Wilson, M. Barczyk, H. Zhang, M. G. Lipsett, “An automated vane shear test tool for environmental monitoring with unmanned ground vehicles” to the *Journal of Terramechanics*. The author was responsible for concept formation, system design and construction, data collection, data analysis, and manuscript preparation. Dr. Fisseha was involved in concept formation and assisted with data collection. Dr. Wilson was involved in concept formation. Dr. Zhang supported field data collection. Dr. Barczyk assisted with manuscript preparation. Dr. Lipsett was the supervisory author and was involved in concept formation, system design, and contributed to manuscript edits.

Chapter 4 of this thesis has been published as N. A. Olmedo, M. Barczyk, and M. Lipsett, “Experimental determination of the inertial properties of small robotic systems using a torsion platform”, *Mechanical Systems and Signal Processing*, 131:71-96 (2019). The author was responsible for concept formation, system design and construction, data collection, data analysis, and manuscript preparation. Dr. Barczyk was involved in concept formation and contributed to manuscripts edits. Dr. Lipsett was the supervisory author and contributed to manuscript edits.

Chapter 5 of this thesis has been submitted for publication as N. A. Olmedo, M. Barczyk, H. Zhang, W. Wilson, M. G. Lipsett, “A UGV-based modular robotic manipulator for soil sampling and terramechanics investigations on mine waste”, to the *Journal of Unmanned Vehicle Systems*. The author was responsible for concept formation, equipment design and construction, data collection,

data analysis, and manuscript preparation. Dr. Zhang supported field data collection. Dr. Wilson supported equipment construction. Dr. Barczyk was involved in manuscript preparation. Dr. Lipsett was the supervisory author and was involved in concept formation, system design, and contributed to manuscript edits.

Chapter 6 of this thesis has been submitted for publication as N. A. Olmedo, M. Barczyk, M. G. Lipsett, “An improved terramechanics model for a robotic soil surface sampler”, to the Journal of Terramechanics. The author was responsible for concept and model formation, system design and construction, data collection, data analysis, and manuscript preparation. Dr. Barczyk was involved in manuscript preparation. Dr. Lipsett was the supervisory author and was involved in concept formation and model formulation, and contributed to manuscript edits.

Acknowledgements

I would like to gratefully acknowledge the Natural Sciences and Engineering Research Council of Canada (NSERC), the University of Alberta and Alberta Innovates - Energy and Environment Solutions through the NSERC Industrial Research Chair Program for their financial support.

I am profoundly grateful to my supervisory committee: my co-supervisors Dr. Michael Lipsett and Dr. Martin Barczyk have been my advocates for all these years, and have supported all this and other work outside the university. I would like to thank Dr. Lipsett for his supervision, guidance, and trust throughout my undergraduate and graduate studies. I would like to thank Dr. Barczyk for supervising my work, rigorously reviewing my papers, and supporting my other ventures. I would like to thank Dr. Wilson for his support on my ideas and projects. I would like to thank Dr. Zhang for his robotics class and the support of field trials discussed in this thesis.

I wish to thank my friends and colleagues Stephen Dwyer, Jamie Yuen, and Rijesh Augustine, with whom I have studied, learned, worked, and suffered, while building robots.

I am also grateful to the Mechanical Engineering Shop: Rick Conrad, Rick Bubenko, Andrew Campbell, Bernie Faulkner, Daniel Mooney, Dave Waege, and Roger Marchand, who helped me to materialize my ideas, and put in extra effort into my projects.

I would like to thank my parents Rodrigo and Ivonne, sister Alegria, family, and friends for their support, counsel, and heart-felt motivation.

Lastly, I would like to thank my wife, Irina, for her loving support that makes all projects possible.

Contents

Preface	iii
Acknowledgements	v
List of Figures	x
List of Tables	xvi
1 Introduction	1
1.1 Background and Motivation	1
1.2 Objectives of the Present Work	3
1.3 Overview of Content	4
1.4 References	5
2 Design and field experimentation of a robotic system for tailings characterization	8
2.1 Introduction	9
2.2 Related work	12
2.2.1 Recent research on environmental characterization using UGVs	12
2.2.2 Developments of mobile platforms and tooling for studies of tailings deposits	13
2.3 Functional specifications for characterizing oil sands tailings	15
2.3.1 Subsurface sampling	16
2.3.2 Surface characterization	16
2.4 Development of a mobile robot for geotechnical ground surveys of oil sands tailings .	19
2.4.1 Mobile platform	20
2.4.2 Drill	23
2.4.3 Sampler	24
2.4.4 Human-robot interaction and control systems	24
2.5 Field-Testing Experiments	26

2.5.1	Safety and risk management and fail-safe demonstration	27
2.5.2	Surface characterization of dry tailings sand	28
2.5.3	Subsurface sampling of partially dried tailings from tailings treatment cells	28
2.6	Surface & Subsurface Characterization Results	35
2.6.1	Sample analysis	35
2.6.2	Terrain parameters estimation	36
2.7	Lessons Learned and Future Work	37
2.8	Conclusions	39
2.9	References	39
3	An Automated Vane Shear Test Tool for Environmental Monitoring with Unmanned Ground Vehicles	42
3.1	Introduction	42
3.2	Background	45
3.2.1	Robots for Environmental Monitoring of Difficult Environments	45
3.2.2	Vane Shear Testing and Tools	46
3.3	Design of an Automated Vane Shear Tool	49
3.3.1	Design Criteria and Considerations	49
3.3.2	Description of Apparatus	50
3.3.3	Equipment Calibration	51
3.3.4	Equipment Error Analysis	53
3.3.5	Friction Compensation	55
3.4	Laboratory Equipment Validation	57
3.5	Example Laboratory Applications	59
3.6	Integration of AVST onto Unmanned Ground Vehicles	61
3.7	Conclusion	63
3.8	References	64
4	Experimental Determination of the Inertial Properties Of Small Robotic Systems Using a Torsion Platform	68
4.1	Introduction	68
4.2	Background	70
4.3	Estimating the Inertia Tensor Components and the Position of the Centre of Mass of an Object	76
4.3.1	General Method Description and Formulation	78
4.3.2	Experimental Determination of the Position of the Centre of Mass and Diagonal Components of the Inertia Tensor	80
4.3.3	Experimental Determination of Off-Diagonal Components of the Inertia Tensor	82

4.3.4	Method Verification	83
4.4	Design of an Instrumented Torsional Platform	85
4.4.1	Apparatus: Main System Components	86
4.4.2	Equations of Motion of the Torsion Pendulum and Inertia Estimation Method	88
4.4.3	Effects of Friction on the Inertia Estimates	89
4.4.4	Torsion Platform Calibration Procedure and Results	92
4.4.5	Uncertainty of Inertia Estimation with a Torsion Platform	94
4.4.6	Experimental Procedure	94
4.4.7	Apparatus Validation	95
4.4.8	Equipment Validation Results	99
4.5	Validation Experiments: Estimating the Inertia Properties of a Calibration Object	100
4.5.1	Estimating Inertial Properties With the Minimum Number of Configurations	101
4.5.2	Estimating Inertial Properties With Nonlinear Least Squares	103
4.6	Case Study: Estimating the Inertia Tensor of a UAV	105
4.7	Conclusions and Future Work	107
4.8	Acknowledgment	108
4.9	References	108
5	A UGV-based modular robotic manipulator for soil sampling and terramechanics investigations on mine waste	112
5.1	Introduction	112
5.2	Background and Literature Review	115
5.2.1	UGVs for Environmental Monitoring	116
5.2.2	Robotic Surface and Subsurface Sampling	116
5.2.3	Estimating Soil Parameters Using Terramechanics Wheels	118
5.3	Development of a Robotic Manipulator and End-Effectors	119
5.3.1	Design Requirements	119
5.3.2	Robotic Manipulator	120
5.3.3	Surface Sampler And Excavation Tool	127
5.3.4	Terramechanics Wheel End-Effector	130
5.4	Equipment Testing Experiments	132
5.4.1	Terrain Sampling Equipment Test Field Experiments	132
5.4.2	Terramechanics Wheel Field Test Experiments	133
5.5	Conclusion and Future Work	136
5.6	Acknowledgments	137
5.7	References	137
6	An improved terramechanics model for a robotic soil surface sampler	142

6.1	Introduction	142
6.2	Background and Literature Review	144
6.2.1	Tool-Soil Interaction Model for Scoop Samplers	145
6.2.2	Estimating Soil Parameters Using Robotic Excavation Tools	149
6.3	Robotic Sampler Model	150
6.3.1	Forces Acting on the Idealized Failure Wedge	152
6.3.2	Forces and Moments Acting on Sampler	155
6.4	Analysis and Comparison of Models	158
6.4.1	Comparison of Total Forces and Moments Acting on the Sampler	160
6.4.2	Sensitivity analysis of model components	160
6.4.3	Effect of surcharge	162
6.5	Laboratory Experiments	166
6.5.1	Materials	166
6.5.2	Equipment	168
6.5.3	Experiments on Dry Sand	168
6.5.4	Experiments on Centrifuged Tailings	171
6.5.5	Model Assumptions	173
6.6	Conclusion and Future Work	174
6.7	References	175
7	Conclusions	180
7.1	Contributions	180
7.2	Recommendations for Future Work	181
	References	183

List of Figures

2.1	Soft Tailings Drying Production Cell, Athabasca Oil Sands, Alberta.	9
2.2	Floating dock on a tailings treatment test cell with two workers collecting samples. .	11
2.3	Robotic system for tailings characterization.	12
2.4	Gas powered mobile robot.	14
2.5	(a) Soft soil sampler concept. (b) Electric platform with cone penetrometer and soil sampler.	15
2.6	High strength crust on top of a tailings deposit.	16
2.7	Wheel-soil interaction.	18
2.8	Tailings sample return mission: (a) RTC-I driving to the sampling location. (b) Rover drilling through the crust. (c) Rover collecting a sample at depth after repositioning. (d) Rover driving back to shore with sample.	20
2.9	RTC-I with a soft soil sampler mounted on the front (a) and a drill on the back (b).	21
2.10	(a) RTC-I mobile platform. (b) RTC-I with tracks and drill in view.	23
2.11	Outdoors testing of RTC-I: (a) Operator controlling the rover from a distance in a simulated sample return mission. (b) Teleoperating the drilling mechanism. (c) Repositioning the rover using visual feedback from the on-board cameras.	25
2.12	Field testing of RTC-I: Tailings sand surface characterization.	28
2.13	(a) Wheel speeds and slip ratio during sand surface characterization experiment, with measurements show two steady-state regions in this trial. (b) Wheel torque recorded during a surface characterization experiment. (c) Sinkage and calculated front contact angle recorded at steady-state motion.	29
2.14	(a) RTC-I roving into an experimental cell. (b) Auger and drill subsystem test. (c) Sampler subsystem test. (d) On-board camera's view of the partially dried tailings surface.	30
2.15	(a) RTC-I teleoperated into an experimental cell. (b) Drilling through the crust. (c) Sampling tool lowered through the crust. (d) RTC-I with sample collected from 1.7 m depth.	32

2.16	(a) RTC-I teleoperated into a production cell. (b) Drilling through the crust.	33
2.17	RTC-I lowering the sample container into the deposit to collect a sample. The sample container is pictured on the left side of each image. (a) RTC-I repositioned over the hole drilled through the deposit's crust. (b) RTC-I lowering sampling tool. (c) Sampling depth reached. (d) Sampling tool retracted with sample.	33
2.18	(a) Sampling tool repositioned over the drilled hole. (b) Sampling tool lowered through the crust to retrieve a sample. (c) Sampling tool retracted with sample. . .	34
2.19	Particle size distributions of the samples collected.	35
2.20	(a) Recursive estimation results for \hat{c} (a) and $\hat{\beta}$ (b). Error bars show standard error of the estimates.	37
3.1	Centrifuged MFT dedicated disposal area, Athabasca Oil Sands, Alberta	43
3.2	(a) Robotic system for tailings characterization. (b) RTC-I drilling through a soft crust. (c) RTC-I with sample collected from 1.7 m depth. Images from [33]	46
3.3	Vane diagram.	47
3.4	(a) Manually operated field VST device. (b) Manually operated laboratory VST device. (c) Motorized laboratory VST device. (d) Laboratory rheometer.	48
3.5	Main components of proposed AVST design.	50
3.6	AVST system diagram	52
3.7	AVST calibration setup.	53
3.8	Torsion spring calibration. Only one of every seventy-five points used for the calibration are shown.	53
3.9	Observed friction torque under different test conditions.	54
3.10	Parameter error C_{ue} versus vane constant K_v under a friction torque $T_f = 0.003$ Nm	55
3.11	Example of a friction compensation dataset and fitted cyclic function.	56
3.12	Example of distribution of residuals.	57
3.13	Comparison between measured and corrected shear stresses during a test.	57
3.14	Peak stress comparison between AVST and Brookfield DV3THB rheometer. The bars represent the 95% confidence intervals of the tests.	58
3.15	Example of shear stress determination for centrifuged tailings using our AVST and a Brookfield DV3THB rheometer. The Brookfield rheometer automatically stops the test once it determines the peak shear stress has been reached.	59
3.16	AVST laboratory experiments on treated oil sands tailings. The equipment was manually lowered into a container filled with tailings. A linear guide was used to support and lock the equipment in place.	60
3.17	Comparison of shear stress measured at varying vane speeds.	61
3.18	(a) AVST mounted on a Husky A200. (b) Instrumented UGV on outdoor trials. . .	62

3.19	Field measurements example. The data was obtained in clayey soil at three different locations.	63
4.1	Arbitrary rigid body rotating about axis passing through O	71
4.2	(a) A torsional pendulum oscillates an arbitrary object using a spring element with spring constant k_s . The spring can be connected to a light platform to support the object. (b) A multifilar pendulum oscillates an arbitrary object using four wires of length L , spaced at a distance r from the rotation axis. Alternatively, the wires can be connected to a light platform to support the object.	73
4.3	(a) A compound pendulum oscillates an arbitrary object hung by wires rotating on overhead pins. (b) An arbitrary object spins at a constant angular speed ω_C about an axis through its centre of mass.	74
4.4	Arbitrary object with a center of mass located at C	77
4.5	Rotation with $\beta = -\pi/6$	78
4.6	Rotation by $\beta = -\pi/6$, followed by a rotation by $\alpha = \pi/6$	79
4.7	General dimensions of validation block. The cutout section has a fillet with 0.8mm radius.	84
4.8	Instrumented torsion platform.	85
4.9	Torsion pendulum apparatus.	86
4.10	Dimensions of the rotation plate. All dimensions in mm.	87
4.11	Plate and other rotating components	87
4.12	Calibration setup.	93
4.13	Torsion spring calibration. Only one of every twenty-five points used for the calibration are shown.	93
4.14	Example measurements of the oscillation period for ten datasets for configuration 1. The bounded region shows the subset of data used for further analysis.	96
4.15	Example measurements of the oscillation amplitude for ten datasets for configuration 1. The bounded region shows the subset of data used for further analysis.	97
4.16	Mean oscillation period measurements for all datasets for configurations 1–4. The error bars represent the 95% confidence intervals of the average oscillation periods.	97
4.17	Amplitude differences $\Delta\theta$ for successive cycles of an apparatus friction experiment. The bounded region shows the range of data used for the analysis.	99
4.18	Amplitude ratios A_R for successive cycles of an apparatus friction experiment. The bounded region shows the range of data used for the analysis.	99
4.19	Friction torque τ_c for successive cycles of an apparatus friction experiment. The bounded region shows the range of data used for the analysis.	99

4.20	Damping ratio ζ for successive cycles of an apparatus friction experiment. The bounded region shows the range of data used for the analysis.	100
4.21	The aluminum block supported by attachment blocks on the torsion platform. Two configurations (a) and (b) are shown.	101
4.22	The UAV supported by a lightweight metal structure and gimbal mounted on torsional platform. Two configurations (a) and (b) are shown.	106
4.23	Location of UAV centre reference point. Frame O origin is located under and forward.	107
5.1	Example of tailings processing and storage.	114
5.2	Oil sands tailings dedicated disposal area, Athabasca, Alberta.	114
5.3	RTC-I collecting subsurface samples from an oil sands tailings DDA.	117
5.4	RTC-I conducting terramechanics experiments on dry tailings sand.	118
5.5	Robot manipulator mounted on a UGV.	120
5.6	Robotic manipulator components.	121
5.7	Robotic manipulator prototype for laboratory testing.	122
5.8	Robot manipulator angle and link geometry definitions.	123
5.9	Robot manipulator reachable workspace. The boundaries delineate areas in which the robot manipulator can position the end effector for a given angle.	125
5.10	System diagram for the overall design.	127
5.11	User interface screenshot. Two cameras are used to supervise the payload from different angles, and plots present the loads and relevant state variables.	127
5.12	Surface sampler main components. The side plates are shown as transparent to make the internal components visible.	128
5.13	Surface sampler dimensions. The widths of the sampler and vertical blade are w_s and w_b , respectively, and the thickness of the scoop curved blade, side plates, and vertical blade are t_s , t_{sp} , and t_b , respectively.	129
5.14	Terramechanics wheel design. The radius and width of the wheel are r_w and w_w , respectively, and the lug height and thickness are l_h and l_t , respectively.	130
5.15	(a) RTC-II traversing dry uncompacted sand. (b) RTC-II deploying the surface sampler on wet sand.	132
5.16	Sampler payload collecting a sample on dry sand.	133
5.17	RTC-II collecting a sample on saturated sand. (a) The manipulator arm positions the sampler on the terrain and the scoop is closed slowly to collect material. (b) The manipulator lifts the instrument carrying a sample of saturated sand. The soil had sufficient cohesion to maintain the shape of the material collected after the sampler was removed from the ground.	133

5.18	Measurements collected while sampling on dry sand. (a) The distance to the ground from the end-effector connection plate. Two approaches were conducted, resulting in large and small soil deformations. (b) The forces along two axes. There is a large normal force shown during the first approach to collect a sample resulting in large deformations. The second approach, after time 60 s, is smoother and results in smaller reaction forces. (c) The moment measured at the connection plate. It is the combination of the reaction moments with the ground and the interaction forces of the sampler while closing. (d) The torque and angular position of the sampler scoop. The sampler is closed at 0 degrees, as it contacts the vertical blade and pushes against it. The plot shows the sampler closing to collect a sample and opening to drop it. The torque measured is the combination of the tool-terrain interactions and the moment generated by the weight of the rotating scoop.	134
5.19	RTC-II deploying the instrumented terramechanics wheel on (a) dry sand, (b) transition between dry and wet sand.	135
5.20	Measurements collected while sampling on dry sand. (a) The reaction forces on the wheel. The wheel was contacted against the dry sand several times and the normal load and draw bar pull recorded. (b) The reaction moment at the end-effector plate. It is a combination of reaction forces on the wheel, including the traction forces and vertical reactions. (c) The angular speed of the wheel. This was controlled in open loop and is seen to slow down as higher rolling resistance is applied when it contacts the ground. Oscillations are observed due to unbalanced masses of the components mounted inside the wheel, such as the wireless torque transducer battery. (d) The torque measured at the wheel. Increased torque was observed when the wheel was pushed into the ground. Oscillations due to unbalanced masses are observed. Limits on the strain gauge signal amplifiers resulted in the measurements being truncated at approximately 5.6 Nm.	136
6.1	(a) RTC-I, a UGV for tailings characterization was deployed on an oil sands mine waste dedicated disposal area to collect subsurface samples by drilling through a crust and deploying a soft tailings sampler [33]. (b) A custom vane shear test tool was developed for mine waste monitoring and integrated onboard a UGV for remote site investigations [32]. (c) RTC-II, a UGV outfitted with a custom robotic manipulator to deploy soil sampling and terrain characterization tools, such as an instrumented wheel for terramechanics experiments and a surface soil sampler [31].	143
6.2	RTC-II with scoop sampler attached to the robotic manipulator. The robot is used to collect surface samples for environmental monitoring in mine waste.	146
6.3	Hemispherical tool for soil sampling.	146

6.4	Angles and forces between the soil and sampler.	147
6.5	Side surface shear stress and edge pressure.	148
6.6	Simplified shovel assembly interaction forces based on Mohr-Coulomb model.	150
6.7	Scoop sampler geometry.	151
6.8	Forces acting on the idealized failure wedge.	152
6.9	Comparisons of F_x , F_y , and M between MSM and RSM on three materials. (a) forces on dry sand, (b) moments on dry sand, (c) forces on sandy loam, (d) moments on sandy loam, (e) forces on clayey soil, and (f) moments on clayey soil.	163
6.10	(a) Adhesion and cohesion forces estimated with MSM and RSM on three materials. (b) P_p and P estimated with MSM and RSM on three materials.	164
6.11	(a) Components of F_x predicted by MSM on clayey soil. (b) Components of F_x predicted by RSM on clayey soil.	164
6.12	(a) F_5 and F_e on dry sand with c_t equal to 15%. (b) F_5 and F_e on clayey soil with c_t equal to 45%.	165
6.13	(a) Effect of a surcharge q on F_x and F_y on dry sand. (b) Effect of a surcharge q on F_x and F_y on clayey soil.	165
6.14	Surface samples are collected using a robotic manipulator on (a) sandy terrain and, (b) centrifuged tailings.	166
6.15	(a) Picture of sand. (b) Shear response obtained from direct-shear testing of dry sand at three different normal loads (σ_{t1} , σ_{t2} , σ_{t3}). The curves of the shear stress response were produced by fitting the measured responses to Equation (6.6).	167
6.16	Schematics of (a) the robotic system, (b) the robotic sampler.	169
6.17	Sequence (a)-(d) of sampler with removed curved section indenting into dry sand.	170
6.18	Experimentally measured and predicted forces F_{sx} (a), F_{sy} (b) and moment M_s (c) during side wall experiment on dry sand. The error bars are shown every 15 points and represent two times the standard deviation of the measurement errors.	170
6.19	Sequence (a)-(d) of complete sampler indenting into dry sand.	171
6.20	Experimentally measured and predicted forces F_{sx} (a), F_{sy} (b) and moment M_s (c) during complete sampler experiment on dry sand. The error bars are shown every 15 points and represent two times the standard deviation of the measurement errors.	171
6.21	(a) Sampler side walls driven into CT. Measured, RSM- and MSM-predicted forces F_x (b) and F_y (c) during a sampling operation. The error bars are shown every 15 points and represent two times the standard deviation of the measurement errors.	172
6.22	(a) Complete sampler collecting a sample of CT. Measured, RSM- and MSM-predicted forces F_x (b) and F_y (c) during the sampling operation. The error bars are shown every 15 points and represent two times the standard deviation of the measurements.	173

List of Tables

2.1	RTC-I Specifications	22
2.2	Dean Stark Analysis and Methylene Blue Index (MBI) Report	35
2.3	Laser Diffraction Particle Size Analysis	35
2.4	Regression Results	37
2.5	Regression Results For Cohesionless Soil	37
3.1	Torsion spring calibration results	52
3.2	Instrument evaluations: Comparison of AVST and Brookfield DV3THB rheometer on five treated tailings.	58
3.3	Comparison of peak shear stress obtained with varying vane speeds.	60
4.1	Commercial Systems Presently Available, with Moment of Inertia Uncertainty (MOIu), Product of Inertia Accuracy (POIa), Centre of Mass Uncertainty (CoMu) and Ap- proximate Cost. Unreported values are noted as N/A.	76
4.2	Experiments 1-3	80
4.3	Experiments 4-5	81
4.4	Experiment 6	82
4.5	Experiments 7 - 9	83
4.6	Method Verification Experiments	84
4.7	Torsion spring calibration results	94
4.8	Position of the center of the rotating plate	96
4.9	Mean oscillation period, \bar{T} , for all datasets. Units in s.	98
4.10	Uncertainty u_T for each dataset for 95% confidence. Units in s.	98
4.11	Equipment validation results	100
4.12	Validation Block Experiments	102
4.13	Validation Experiments For 9 Configurations	102
4.14	22 Configurations For Validation Block Experiments	104
4.15	Validation Experiments For 22 Configurations	105

4.16	Configurations For UAV Experiments	106
5.1	Chosen ServoCity Linear Actuators	123
6.1	Sampler-soil interaction forces.	151
6.2	Properties of simulated materials	159
6.3	Geometric parameters of simulated sampler	159
6.4	Components of F_x , F_x , and M on Dry Sand	161
6.5	Components of F_x , F_x , and M on Clayey Soil	162
6.6	Particle Size Analysis	167

Chapter 1

Introduction

Industrial operations which generate waste require continuous environmental stewardship and monitoring. Generally, land must be returned to an equivalent original state once industrial activities are finished [1]. Until closure certificates are granted, the aquatic, terrestrial, and atmospheric conditions must be monitored.

The long-term goal of this research is to develop autonomous robotic systems that will lead the field of environmental monitoring of industrial sites. It is conceivable that within the next decade, the functionality of robots deployed for this task will rival those of multi-million dollar robots used for space exploration, e.g. the Curiosity rover [5], both in terms of reliability and complexity of operations.

This thesis compiles advances made towards environmental monitoring in the difficult terrain of oil sands tailings ponds using unmanned ground vehicle systems. To achieve this aim, new sampling tools and manipulators had to be designed, built and tested under field conditions, and improved terramechanics models for tool-soil interaction had to be developed and validated through experiments.

1.1 Background and Motivation

All treated tailings deposits require continuous monitoring for (i) legislative compliance [24], (ii) improving performance of mining processes [15], (iii) environmental monitoring [23], and (iv) timely feedback to refine remediation efforts [12]. Regular soil sampling and measurement of terrain properties are required to identify hazards, understand sedimentation processes, and facilitate reclamation

[14, 2]. Currently the characterization of tailings deposits is done using manual geotechnical sampling and measurement campaigns [6]. Manual campaigns are labour intensive, costly, and may pose risks to workers.

The Alberta Energy Regulator (AER), through Directive 085 (Fluid Tailings Management for Oil Sands Mining Projects) and the Tailings Management Framework (TMF), regulates the allowable volume of fluid tailings, as well as requirements for land reclamation, continuous monitoring, and reporting [3]. This agency has reported that the fluid tailings volumes in oil sands sites in Northern Alberta have increased from 1075 million cubic meters in 2014 to 1253 million cubic meters in 2018 [4]. This translates to an ever-increasing workload for oilsands mining companies to actively monitor their tailings deposits.

There is an unrealized potential to integrate Unmanned Ground Vehicles (UGVs) into ground surveys of tailings deposits. Robotic systems can overcome many of the limitations of manual surveys and provide additional benefits: (i) minimize risk to workers, (ii) characterize locations which are not accessible for manual campaigns, (iii) estimate soil properties in a timely manner, (iv) collect samples from deep deposits, (v) assess trafficability of the terrain, (vi) identify hazards and their location, (vii) minimize risks and costs of surveying, and (viii) generate reports of soil shear strength and fines capture rates for regulatory compliance [14].

Robotic systems have been used to investigate Amazon rainforest rivers [9]; surface vessels were used to study bodies of water [11]; and teams of unmanned aerial vehicles (UAVs) and unmanned ground vehicles (UGVs) have been used to conduct tasks too risky and costly for humans, such as mine waste pond sampling [8, 13]. Specialized UGVs have been used for mapping underground mines that human workers cannot access [7, 10, 17], and for other mining applications such as explosives handling, haulage, surveying, dozing, excavation, and drilling [16].

The benefits of performing geotechnical surveys with robotic systems is a driver for the development of novel technologies to characterize terrain properties and collect soil samples. Soil sampling would allow oil sands tailings operators and researchers to understand and predict consolidation processes by analyzing solids concentration, bitumen content, and mineral content. Continuous monitoring enables mining companies to precisely determine when a holding pond is ready to proceed to the next stage of reclamation, where the tailings are covered with sand and topsoil. Subsurface samples are necessary to monitor changes in the deposit over time, which are affected by factors such as multiple lifting and the presence of a surface charge, or the development of a hard crust which impedes surface evaporation and slows dewatering and consolidation processes.

For recently poured materials and deposits with soft crusts, on-the-fly surface characterization would allow estimation of key soil parameters, as well as associated terrain properties such as shear strength which are important for trafficability assessment. Characterizing surface properties of

soft tailings in real time would enable improved path planning for robotic systems as well as the identification of hazards such as soft spots where a rover might sink.

The research group in the University of Alberta's Integrated Reliable Oil Sands Systems Laboratory has been developing UGVs for tailings characterization in collaboration with companies operating oil sands tailings facilities. The long-term goal of this program is to produce field robotic systems for navigation, sampling, soil parameter estimation, and geotechnical measurements of such environments, and to evaluate their capabilities through laboratory trials and field experiments.

1.2 Objectives of the Present Work

The original objectives of this research project were to consider the potential advantages and technology development requirements for field robotics systems which would contribute to the long-term objective of performing unmanned environmental monitoring in difficult terrains. Specific objectives include:

1. Build a field UGV and validate the idea of using unmanned systems for investigating mine waste through field experiments;
2. Demonstrate improved performance of new robotic geotechnical tools over traditional equipment for characterizing soil properties, with laboratory and field experiments;
3. Propose a methodology and instrumentation to measure the inertia tensor of complex bodies, such as robots and robotic payloads, which can be used for high fidelity simulation and improved model-based control;
4. Develop novel UGV-deployed robotic tools to collect surface samples and conduct terramechanics model parameter identification; and
5. Propose and validate an improved terramechanics model for robotic sampler-soil interactions.

These objectives were formulated to address the hypothesis that environmental monitoring can be improved through the use of robotic systems and payloads. Advancing the understanding of the robotic vehicle, instruments, and terrain-tool interactions is required to maximize the benefits that can be obtained from the proposed solution, to improve on current designs, control strategies, and dynamic models, and to identify further gaps in knowledge that still need to be addressed.

This process has now led to the development of original designs and new technologies, whose details are presented in individual chapters of this thesis. In addition, consideration is given for paths to commercialize some of the technologies created during this research.

1.3 Overview of Content

The work carried out on demonstrating the feasibility of robotic systems for geotechnical and environmental monitoring has been compiled into journal articles, which are presented as individual chapters in this thesis as detailed below. Some of the work has also been presented at international conferences and archived in proceedings.

- Chapter 2 describes an unmanned ground vehicle (UGV) that has been developed and deployed for characterizing reclaimed soil regions. Experiments on tailings treatment cells demonstrated the feasibility of remotely operated sampling technologies as well as parameter estimation methods for some types of soil surfaces based on terramechanics models and on-board measurements of vehicle-soil interactions [22].
- Chapter 3 gives a description and details of the design, development, and characterization of a novel robotic vane shear test tool for measuring undrained shear strength of soils. The proposed system is capable of performing high-resolution torque measurements under controlled rotational speeds. These measurements are then used to estimate the shear strength of soil under both laboratory conditions and in the field from onboard a UGV [21].
- Chapter 4 presents a new methodology and instrumentation for estimating inertia tensors of complicated mechanical assemblies such as UGVs. This work was conducted in support of creating more accurate vehicle dynamical models for improved simulation and control design. The proposed method is shown to produce accurate results, first through simulation to validate the proposed method and choices of design, sensing and parameter estimation, then validated by experiment on samples with precisely known inertial properties. As a case study, the mass moments and products of inertia and the centre of mass location of a small UAV were estimated [18].
- Chapter 5 presents the design of a robotic manipulator and two novel instrument payloads used for evaluating soil properties near the surface. A scoop-type sampler was designed and developed to collect undisturbed soil samples; and an instrumented wheel was developed for terramechanics-based soil parameter estimation. Both instruments were successfully operated in field conditions [20].
- Chapter 6 proposes a new terramechanics model for the robotic scoop surface sampler described in Chapter 5, which captures the behaviour of this sampler more accurately than existing state-of-the-art models for scoop-type tools interacting with soil which is adhesive and cohesive [19].
- Chapter 7 offers conclusions and recommendations for future work to improve the capability

of robotic tools for remote monitoring of terrestrial and aquatic environments, and suggests additional applications.

1.4 References

- [1] Alberta-Energy. Oilsands 101: Reclamation. <http://www.energy.alberta.ca/OilSands/1722.asp>, 2014.
- [2] Alberta-Energy-Regulator. Directive 074: Tailings performance criteria and requirements for oil sands mining schemes. <http://www.aer.ca/rules-and-regulations/directives/directive-074>, 2009.
- [3] Alberta-Energy-Regulator. Backgrounder, directive 085: Fluid tailings management for oil sands mining projects. <https://www.aer.ca/documents/news-releases/NR2016-04-Backgrounder.pdf>, 2016.
- [4] Alberta-Energy-Regulator. State of fluid tailings management for mineable oil sands, 2018. <https://www.aer.ca/documents/oilsands/2018-State-Fluid-Tailings-Management-Mineable-OilSands.pdf>, 2019.
- [5] R.C. Anderson, L. Jandura, A.B. Okon, D. Sunshine, C. Roumeliotis, L.W. Beegle, J. Hurowitz, B. Kennedy, D. Limonadi, S. McCloskey, M. Robinson, C. Seybold, and K. Brown. Collecting samples in gale crater, mars; an overview of the mars science laboratory sample acquisition, sample processing and handling system. *Space Science Reviews*, 170(1-4):57–75, 2012.
- [6] Nicholas Beier, Ward Wilson, Adedeji Dunmola, and David Segó. Impact of flocculation-based dewatering on the shear strength of oil sands fine tailings. *Canadian Geotechnical Journal*, 50(9):1001–1007, 2013.
- [7] S Coetzee, H Swart, P Bosscha, and D Oosthuizen. *Design of an industrial all-terrain robot platform lessons learned in the design of a robotic mine safety platform for South African gold mines*. IEEE, 2012.
- [8] Pedro Deusdado, Eduardo Pinto, Magno Guedes, Francisco Marques, Paulo Rodrigues, André Lourenço, Ricardo Mendonça, André Silva, Pedro Santana, José Corisco, Marta Almeida, Luís Portugal, Raquel Caldeira, José Barata, and Luis Flores. An Aerial-Ground Robotic Team for Systematic Soil and Biota Sampling in Estuarine Mudflats. In *Robot 2015: Second Iberian Robotics Conference*, pages 15–26. Springer International Publishing, Cham, November 2015.
- [9] Gustavo Freitas, Fernando Lizarralde, Liu Hsu, Vitor Paranhos, Ney R. Salvi dos Reis, and Marcel Bergerman. Design, modeling, and control of a wheel-legged locomotion system for the

- environmental hybrid robot. In *Proceedings of the IASTED International Conference*, number CMU-RI-TR-, November 2011.
- [10] Jeremy Green. Underground mining robot: A CSIR project. *SSRR*, pages 1–6, 2012.
- [11] Gregory Hitz, Francois Pomerleau, Marie-Eve Garneau, Cedric Pradalier, Thomas Posch, Jakob Pernthaler, and Ronald Siegwart. Autonomous Inland Water Monitoring: Design and Application of a Surface Vessel. *IEEE Robotics & Automation Magazine*, 19(1):62–72, March 2012.
- [12] Larry A Holm. Strategies for remediation. In *Geotechnical Practice for Waste Disposal*, pages 289–310. Springer US, Boston, MA, 1993.
- [13] M G Lipsett, J D Yuen, N A Olmedo, and S C Dwyer. Condition Monitoring of Remote Industrial Installations Using Robotic Systems. In *Engineering Asset Management 2011*, pages 231–241. Springer London, London, July 2013.
- [14] M.G. Lipsett and S.C. Dwyer. A robotic system to characterize soft tailings deposits. In *Proceedings of Mine and Tailings Waste Conference 2009, Banff Alberta*, November 2009.
- [15] Michael G Lipsett, Nicolas Olmedo, Benoit Rivard, and Ward Wilson. Robotic Systems for Measuring Properties of Tailings Deposits and Collecting Samples. In *Proceedings of the Fourth International Oil Sands Tailings Conference*, Lake Louise, AB, December 2014.
- [16] Joshua A Marshall, Adrian Bonchis, Eduardo Nebot, and Steven Scheduling. Robotics in Mining. In Bruno Siciliano and Oussama Khatib, editors, *Springer Handbook of Robotics*, pages 1549–1576. Springer International Publishing, Cham, 2016.
- [17] A Nuchter, H Surmann, and K Lingemann. 6D SLAM with an application in autonomous mine mapping. . . . *ICRA '04 2004 IEEE . . .*, pages 1998–2003 Vol.2, 2004.
- [18] Nicolas A. Olmedo, Martin Barczyk, and Michael Lipsett. Experimental determination of the inertial properties of small robotic systems using a torsion platform. *Mechanical Systems and Signal Processing*, 131:71 – 96, 2019.
- [19] Nicolas A. Olmedo, Martin Barczyk, and Michael G. Lipsett. An improved terramechanics model for a robotic soil surface sampler. Submitted, 2020.
- [20] Nicolas A. Olmedo, Martin Barczyk, Hong Zhang, Ward Wilson, and Michael G. Lipsett. A ugv-based modular robotic manipulator for soil sampling and terramechanics investigations on mine waste. Submitted, 2020.

- [21] Nicolas A. Olmedo, Bereket Fisseha, Ward Wilson, Martin Barczyk, Hong Zhang, and Michael G. Lipsett. An automated vane shear test tool for environmental monitoring with unmanned ground vehicles. Submitted, 2020.
- [22] Nicolas A Olmedo and Michael G Lipsett. Design and field experimentation of a robotic system for tailings characterization. *Journal of Unmanned Vehicle Systems*, pages juvs–2015–0034, March 2016.
- [23] Geoffrey S Plumlee, Kathleen S Smith, and Walter H Ficklin. *Geoenvironmental Models of Mineral Deposits, and Geology-based Mineral-environmental Assessments of Public Lands*. Number Open-File Report 94-203. U.S. Geological Survey, 1994.
- [24] Barry A Wills and James A Finch. Tailings Disposal. In *Wills' Mineral Processing Technology*, pages 439–448. Elsevier, 2016.

Chapter 2

Design and field experimentation of a robotic system for tailings characterization

Abstract

There is an ongoing requirement to conduct ground surveys of engineered mine tailings deposits to monitor dewatering performance and consolidation prior to completing reclamation work. The deposit variability can make such surveys hazardous for humans. A rover is described that has been developed and deployed for characterizing reclaimed soil regions. This paper presents the functional requirements for unmanned ground vehicles used in this application, including the need for low-risk and timely subsurface sampling and terrain parameter estimations on highly uncertain terrains. Developments of the field-ready prototype wheeled rover are summarized, including tooling; and field tests are described in an industrial site at an Athabasca oil sands facility. Experiments on tailings treatment cells showed the feasibility of the sampling technologies and parameter estimation methods based on classical terramechanics models. The rover capabilities were further demonstrated by collecting samples from production treatment cells and estimating the cohesion and internal friction angle of tailings sand used in fluid containment dykes. The limitations of the current system helped identify future work for the design and development of new mobile robot systems for tailings characterization.

2.1 Introduction

Robotic systems are playing increasingly important roles in the field of environmental monitoring of industrial sites. Industrial operations that affect soil properties require continuous and rigorous monitoring of soil characteristics. One example of this is oil sands bitumen production processes in northern Alberta, Canada. It is currently estimated that there are 170 billion barrels of recoverable oil in Canadian oil sands deposits [3]. The oil sands industry produced 1.9 million barrels of oil per day in 2012 and is expected to double that production rate in the next decade [1]. In surface mining methods, the water-based bitumen extraction process generates fluid tailings, comprising sand, silts, clays, process-affected water, and residual bitumen. Tailings from these plants are deposited into impoundments where the sand forms an earth dam that holds the fine solids suspended in water. The fines slowly settle and form water-saturated layers [11]. These partially consolidated fine solids are called Mature Fine Tailings (MFT). With approximately 30-35 wt% solids [6], MFT has a consistency similar to yogurt and is not trafficable. For this reason, MFT cannot be reclaimed without further treatment. To further densify and consolidate the material, MFT is mixed with reagents (and sometimes tailings sand to provide a weight-bearing charge) [18]. The resulting material called composite or consolidated tailings (CT) is moved into permanent tailings areas. An alternative method is to add anionic flocculants to MFT and partially dry the resulting paste (Fig. 2.1).



Figure 2.1: Soft Tailings Drying Production Cell, Athabasca Oil Sands, Alberta.

In most jurisdictions, land used for industrial operations such as mining must be returned to its equivalent natural state once industrial activities are completed [2]. The challenge is that often the time scale for reclamation and closure of a site is long; and, until the regional regulatory

authority grants a closure certificate, the terrestrial, aquatic, and atmospheric condition must be monitored.

An important example in Canada is reclamation of tailings impoundments. Reclamation work can only be done once fluid tailings (a mixture of water and fine solids) have drained enough water and gained enough bearing strength to support equipment and workers.

Currently, there are over 840 million cubic meters of fluid tailings stored in approximately 170 square kilometers of impoundments on oil sands sites in Northern Alberta [5]. These impoundments are water saturated, and MFT sludge in the bottom of these water-capped ponds consolidates very slowly, reaching only the consistency of thick mud. To deal with the increasing volume of tailings and the extensive land area required to support the operations, companies have developed new tailings treatment processes to produce consolidated tailings that release water and gain shear strength over time. Two main processes have been implemented: coagulant addition, and flocculant addition. Coagulant addition entails mixing gypsum with MFT, and a large volume of sand is added to create a gravity load to press water out of the mixture. Flocculant addition involves adding a polymer to MFT and placing the mixture into a cell to allow dewatering to occur followed by drying. Both processes require ongoing monitoring. The Alberta Energy Regulator has published legislation to regulate tailings management [4]. Measurements of soil properties and sampling are required to identify hazards, understand sedimentation processes, minimize long term storage of tailings, and facilitate progressive reclamation [16, 4].

Currently the characterization of tailings deposits is done using manual geotechnical sampling and measurement campaigns [9]. These campaigns are costly and are limited to very few locations that have been made accessible to workers by installing floating docks on tailings treatment cells, or by employing large amphibious barges (Fig. 2.2). Equipment sinking and injuries to workers are possible risks due to variability in the consistency of the deposits and the nature of the sampling procedures. Due to these limitations and risks, manual surveys do not provide an adequate and timely characterization and mapping of the deposits.

Unmanned Ground Vehicles (UGVs) can be integrated as part of ground surveys of oil sands tailings deposits. Robotic systems can overcome many of the limitations of manual surveys and provide additional benefits: (i) minimize risk to workers, (ii) characterize locations that are not accessible to manual campaigns, (iii) estimate soil properties in a timely manner, (iv) collect samples from deep deposits, (v) assess trafficability of the terrain, (vi) identify hazards and their location, (vii) minimize risk & cost of a survey, and (viii) generate reports of soil shear strength and fines capture rates for regulatory compliance [16]. The potential value of geotechnical surveys with robotic systems is a strong motivation for the development of new technologies that can characterize key soil properties and can collect soil samples.



Figure 2.2: Floating dock on a tailings treatment test cell with two workers collecting samples.

A team at the University of Alberta’s Integrated Reliable Oil Sands Systems Laboratory is developing UGVs for tailings characterization in collaboration with companies that operate oil sands tailings facilities. The goal of this program is to produce a robust field robotic system for navigation, sampling, and geotechnical measurement, and to evaluate its capability through controlled laboratory trials and field experiments. In accordance with this goal, specific objectives are as follows: (i) detail the robotic system’s functionality requirements for characterizing the oil sands tailings, (ii) develop a mobile robot prototype, (iii) conduct field trials on an industrial site, (iv) analyze the results and discuss the feasibility of the proposed system , and (v) provide recommendations based on the results and analysis of the field trials.

The present work discusses the development and field trials of the first field-ready Rover for Tailings Characterization (RTC-I) (Fig. 2.3), in five sections: a discussion of related work and a summary of developments of previous prototypes; functional specifications for characterizing tailings; description of the development of RTC-I; description & discussion of a set of field trials performed in an industrial setting; and recommendations are provided & future work is identified.



Figure 2.3: Robotic system for tailings characterization.

2.2 Related work

This section presents related work focused on the techniques, methods and technologies used to characterize environments using mobile robots, summarizes the group’s previous developments of mobile platforms and geotechnical tooling for monitoring soft tailings deposits, and discusses the limitations of current solutions.

2.2.1 Recent research on environmental characterization using UGVs

Remote sensing with UGVs has been applied to rugged environments. Freitas et al. developed an Environmental Hybrid Robot that has been used to monitor the Amazon rain forest [12]. The robot was designed to operate in various field conditions such as sand, water, marshes, and swamps. Its main objectives were to obtain water samples and insect larvae samples, measure water parameters, and detect combustible gases [12]. The success of this platform demonstrated the value of introducing robotic systems to perform work in areas inaccessible to workers.

Lipsett et al. discussed mission concepts utilizing mobile platforms, both aerial and ground-based, for condition monitoring of industrial installations [17]. The study suggested that a combination of platforms can be commissioned as a remote monitoring solution that can achieve higher timeliness, accuracy and number of collected features of interest than current methods of information gathering.

It was also noted that the robotic systems used for inspection and fault detection must have higher reliability than the overall system and that risk assessment methods, such as Fault Modes and Effects Analysis (FMEA), are well suited to mobile field robotics [17].

Rock and regolith sampling technologies have been advanced for applications in space exploration using mobile robots. Wettergreen et al. developed and field tested a Lunar rover with a regolith core drill system for the surveying of resources in polar craters [21]. The Sample Acquisition/Sample Processing and Handling subsystem of Mars Science Laboratory was designed to study the geological history of Mars [7]. It has been successful in conducting the first extraterrestrial drilling of rocks [13]. Sampling of soft subsurface watered soils still remains a challenge.

Unmanned systems have been proposed to estimate soil properties of unknown environments [15]. Terramechanics models have been utilized to relate loads on a wheel of a vehicle to its motion and key soil properties such as the cohesion stress, c , and the internal friction angle, ϕ [10]. The shear strength of the soil can be computed from these soil properties and can be used to assess the trafficability of an environment. Iagnemma et al., and Yoshida et al. have used Bekker's terramechanics models to estimate the cohesion stress and the internal friction angle of soils using instrumented mobile platforms for space exploration applications [14, 22]. Other studies have focused on the simulation and empirical work on test beds to develop least-square methods for online soil parameter estimation [22]. Terrestrial rovers can be developed and instrumented to use similar techniques to aid in the geotechnical surveys of industrial sites.

2.2.2 Developments of mobile platforms and tooling for studies of tailings deposits

Our group has conducted preliminary work to design and instrument mobile platforms and specialized geotechnical tooling. A lightweight gas powered mobile robot was retrofitted to conduct wheel-soil interaction studies in a laboratory setting [19] (Fig. 2.4). The objective of these studies was to estimate the cohesion stress and internal friction angle of dry sand using an instrumented mobile platform analogous to the mobile equipment used in an industrial environment. Measurements of linear velocity, angular velocity, sinkage, and torque of the front wheels were obtained as the robot moved through sand. A linearized slip-based terramechanics model was used to estimate the soil parameters, with favourable results. There were challenges with the controllability of the hydraulic motors, the vibration of the internal combustion engine, and the high maintenance requirements of the hydraulic system.

A tooling package was then developed for subsurface soil sampling (Fig. 2.5a). The soil sampler was designed to be mounted on the gas-powered rover and capture material from tailings deposits with

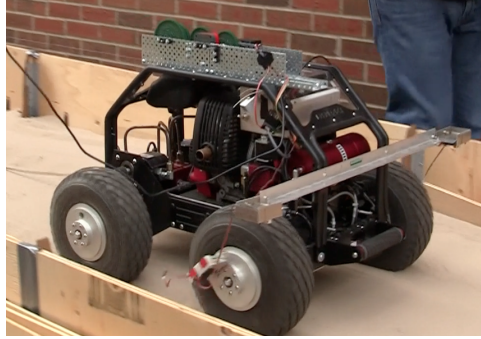


Figure 2.4: Gas powered mobile robot.

shear strengths up to 10 kPa. The system used a vertical hydraulic actuator to push a container through the soil and capture material up to 50 cm deep. Several container configurations were required to manage the uncertainty of the shear strength and cohesive stress of the deposit. The tool was designed to be automated to capture multiple samples using a rotary magazine to switch between containers. A key limitation of this system is that a layer of high strength material on the surface of a tailings deposit, such as a crust, would reduce its functionality.

An electric mobile robot was prototyped to overcome the challenges of the gas powered rover prototype discussed previously (Fig. 2.5b). Electric actuators improved the controllability of the system, produced less vibration and required less maintenance. The electric rover was instrumented to conduct terramechanics studies, similarly to the gas powered rover. The robot was also equipped with a cone penetrometer and a soft soil sampler mounted on linear electric-motor actuators. The geotechnical tools were powered by on-board electronics and teleoperated using a wireless controller (although capability was included for autonomous tool operation). The system was tested in laboratory settings and outdoor environments. Soft soil samples were collected up to 35 cm deep. The mobile platform is limited to traverse deposits with a bearing strength greater than 35 kPa, due to the mass of the platform and payload, and the size of the tires. This is adequate for some tailings structures, noting that other types of structure would require much lower ground-pressures, or even a floating platform for cases where there is no effective shear strength.

The gas powered rover and the electric platform were successful proofs-of-concept of UGVs instrumented for characterizing the surface of a deposit through wheel-soil interaction experiments and geotechnical tooling. The success and limitations of these systems has spurred the development of improved technologies and their evaluation in real industrial settings.

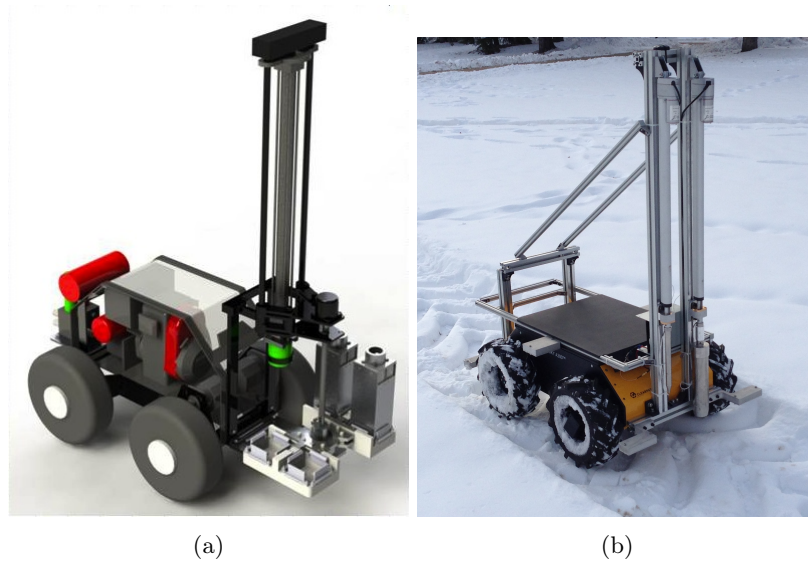


Figure 2.5: (a) Soft soil sampler concept. (b) Electric platform with cone penetrometer and soil sampler.

2.3 Functional specifications for characterizing oil sands tailings

Geotechnical surveys are conducted on tailings treatment cells to monitor the dewatering process. Recently poured, flocculated MFT is water-saturated and has no bearing strength. As water drains, consolidation occurs, and percolation and evaporation result in a crust forming on the surface (Fig. 2.6). This crust can be up to 45 cm deep and have a bearing strength higher than 30 kPa, enough to support a person or low-ground-pressure equipment. The material under the crust does not readily consolidate and its bearing strength can remain very low. Without large and expensive amphibious equipment, robotic systems are the only option to conduct soil sampling and surface soil characterization on these tailings treatment cells.

Soil sampling would allow oil sands tailings operators and researchers to understand and predict consolidation processes by analyzing solids concentration, water chemistry, bitumen content, and mineral content. Mineral content is especially valuable for understanding the relationship between mineral characteristics and reagent addition. Fines abundance, cation exchange activity, and particle size distribution are all important. Decreasing particle size means increasing surface area, in a squared relationship. Knowing that there is a large amount of fines is important for tailings treatment, with the reasonable assumption that with increasing surface area more reagent will be

needed for effective flocculation to promote dewatering and strengthening of the resulting soil. Surface soil characterization would allow estimation of key soil parameters, as well as establishment of relationships with terrain properties such as shear strength for trafficability assessment, which is needed to know when the soil is suitable for the next stage of reclamation where equipment cover the soft tailings with sand and topsoil. As well, understanding the tailings properties can allow better mobility control of the robotic system as well as the identification of hazards such as soft spots where a rover might sink. The requirements for soil sampling and surface soil characterization are summarized based on discussions with oil sands tailings operators and researchers.

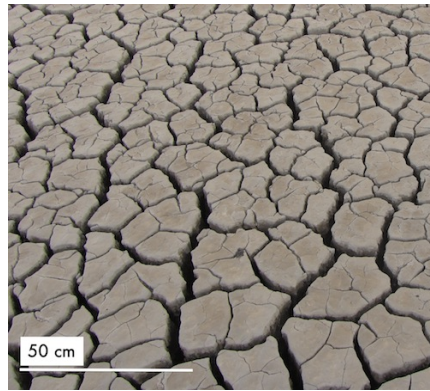


Figure 2.6: High strength crust on top of a tailings deposit.

2.3.1 Subsurface sampling

A teleoperated mobile robot is required to collect tailings samples far from the edge of a treatment cell. For proof-of-concept trials, a distance of 10 metres was deemed to be representative. The robot must be able to maneuver on crusts with bearing strengths as low as 20 kPa and must have a cable tether that can be used to retrieve it in case of excessive sinkage. Subsurface samples must be collected from a minimum of 1.5 m below the surface and have a volume larger than 400 cubic cm. The operator must receive sensory feedback of the sampling process. Undisturbed surface samples can also be collected but these samples are not a priority.

2.3.2 Surface characterization

A teleoperated mobile robot is required to traverse soft ground and estimate properties of the deposit surface. The instrumentation required to accomplish this task will depend on the method

chosen to estimate soil properties. A set of samples can be collected, but the spacing of samples will make the resulting map quite uncertain.

Undisturbed surface samples can be used to validate material properties estimates from other instruments such as a Fourier Transform Infrared Radiometer (FTIR) or hyper-spectral cameras, which can take a set of measurements over the entire surface of interest with reasonable resolution, related to estimating water content, hydrocarbon abundance, and mineral abundance and properties. These remote sensing approaches, however, provide no direct geotechnical shear strength measurements.

Soil properties can be estimated directly by exploring the vehicle-ground interactions. Primary sensors include encoders and torque transducers on the wheel shafts to measure speed and loads. Cohesive stress and internal friction angle are the required parameters to estimate. These parameters can be used to compute the maximum shear stress before failure using Coulomb's equation:

$$\tau_{max} = c + \sigma \tan \phi \quad (2.1)$$

where c is the cohesion stress, σ is the normal stress, and ϕ is the internal friction angle. Terrain trafficability assessment and hazard identification can be conducted with accurate estimates of the shear strength of the deposit. Online soil parameter estimation and hazard detection can also be implemented. The next section reviews the existing soil parameter estimation method based on wheel-soil interactions.

Terramechanics modeling

The wheel-soil interaction is modeled using Bekker's classical slip-based terramechanics models [10]. This formulation has been used extensively, and is currently being used on simulation environments for planetary rovers [23].

The states and loading of a rigid wheel traversing deformable terrain are shown in Figure 2.7, where W , DP , and T are the normal load, draw-bar pull, and torque applied to the wheel respectively. The states of the wheel are the wheel's angular speed ω , ground speed v , and sinkage z . The contact area is defined by the front and rear contact angles θ_1 and θ_2 . The normal and shear stresses are shown by σ and τ and the angle of maximum stress is given by θ_m . In this formulation, the shear and normal stresses are related to the terrain properties using Equations 2.2 and 2.3 where θ is the angular displacement around the wheel, k is the shear displacement under the wheel, and k_c , k_ϕ and n are soil parameters. The terrain is assumed to be homogeneous and isotropic within the

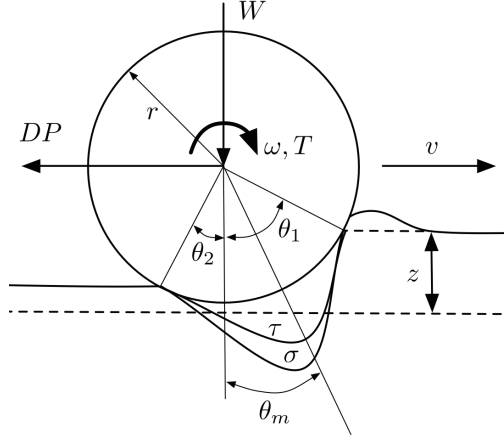


Figure 2.7: Wheel-soil interaction.

volume of interest.

$$\tau(\theta) = (c + \sigma(\theta) \tan \phi) (1 - e^{(-r/k(\theta_1 - \theta - (1-s)(\sin \theta_1 - \sin \theta)))}) \quad (2.2)$$

$$\sigma(\theta) = \left(\frac{kc}{b} + k_\phi \right) z(\theta)^n \quad (2.3)$$

The slip ratio s can be calculated from ω , v , and the wheel radius r , using

$$s = \begin{cases} (r\omega - v)/r\omega & r\omega > v \text{ accelerating} \\ (r\omega - v)/v & r\omega < v \text{ decelerating} \end{cases} \quad (2.4)$$

Linearized stress distributions have been proposed to estimate the loading expected on the wheel during quasi-static motion [14]. The maximum normal and shear stresses, σ_m and τ_m , are assumed to occur at θ_m , midway between the front and rear contact angles. The rear contact angle is assumed to be zero, for in practice it is very small. Previous work has used this assumption for a range of soil parameters [15]. By assuming linear stress distributions, the normal force and torque on the wheel can be related to the wheel's motion, loading, and soil properties using Equations 2.5 and 2.6, where b is the wheel width, and τ_m can be calculated from Equation 2.7.

$$W = \frac{rb(\sigma_m(-\theta_m \cos(\theta_1) + \theta_1 \cos(\theta_m) - \theta_1) - \tau_m(\theta_m \sin(\theta_1) - \theta_1 \sin(\theta_m)))}{\theta_m(\theta_1 - \theta_m)} + \frac{rb(-c(\theta_1 \sin(\theta_m) - \theta_m \sin(\theta_m) - \theta_m \theta_1 + \theta_m^2))}{\theta_m(\theta_1 - \theta_m)} \quad (2.5)$$

$$T = 1/2 r^2 b (\tau_m \theta_1 + c \theta_m) \quad (2.6)$$

$$\tau_m = (c + \sigma_m \tan(\phi)) \left(1 - e^{-(r/k)(\theta_1 - \theta_m - (1-s)(\sin(\theta_1) - \sin(\theta_m)))} \right) \quad (2.7)$$

By manipulating Equations 2.5, 2.6, and 2.7 and ignoring terms of with low relative contribution, as detailed in [15], the parameters of interest are found in the expression shown in Equation 2.8, where terms $C1$, $C2$, and $C4$ are calculated from the motion and loads on the wheel as presented in Equations 2.9, 2.10, and 2.11, where A is calculated using Equation 2.12.

$$C2/C4 = c - \tan(\phi) C1/C4 \quad (2.8)$$

$$C1 = A (\theta_1^2 W r + 4 T \sin(\theta_1) - 8 T \sin(1/2 \theta_1)) \quad (2.9)$$

$$C2 = 4 T (\cos(\theta_1) - 2 \cos(1/2 \theta_1) + 1) \quad (2.10)$$

$$C4 = \theta_1 r^2 b (\cos(\theta_1) - 2 \cos(\theta_1/2) + 2 A \cos(\theta_1) - 4 A \cos(\theta_1/2) + 2 A + 1) \quad (2.11)$$

$$A = 1 - e^{-(r/k)(1/2 \theta_1 + (1-s)(-\sin(\theta_1) + \sin(\theta_1/2)))} \quad (2.12)$$

A linear least-squares regression can be conducted with Equation 2.8 to determine the maximum likelihood estimates of the coefficients c and $\tan(\phi)$, with the assumption that the errors are normally distributed. The calculations of $C1$, $C2$, and $C4$ rely on observations of θ_1 , T , W , k , and s . T is measured with a torque transducer on the wheel axle, s is calculated using the measurements of ω and v , θ_1 is calculated from the sinkage z , and W is calculated from the weight distribution of the robot. k has been shown to have low variations and is taken as a constant [15].

2.4 Development of a mobile robot for geotechnical ground surveys of oil sands tailings

At the outset of the design process the functional specifications discussed in the previous section formed the design basis for the prototype rover RTC-I. The system was designed to take part in two trials: 1) Conduct a sample return mission: drive into deposit, drive to the sampling location, drill through the crust, reposition rover to take a sample, collect sample at depth, and drive back to shore (Fig. 2.8); and 2) Conduct a wheel-soil interaction study by traversing a patch of terrain (tailings sand around the deposit) and take measurements of the loads and state of a wheel to estimate soil parameters.

The following factors are taken into account in the general design of RTC-I: bearing strength of the treatment cell surface, thickness of crust, and depth of sample. In addition, the system needs

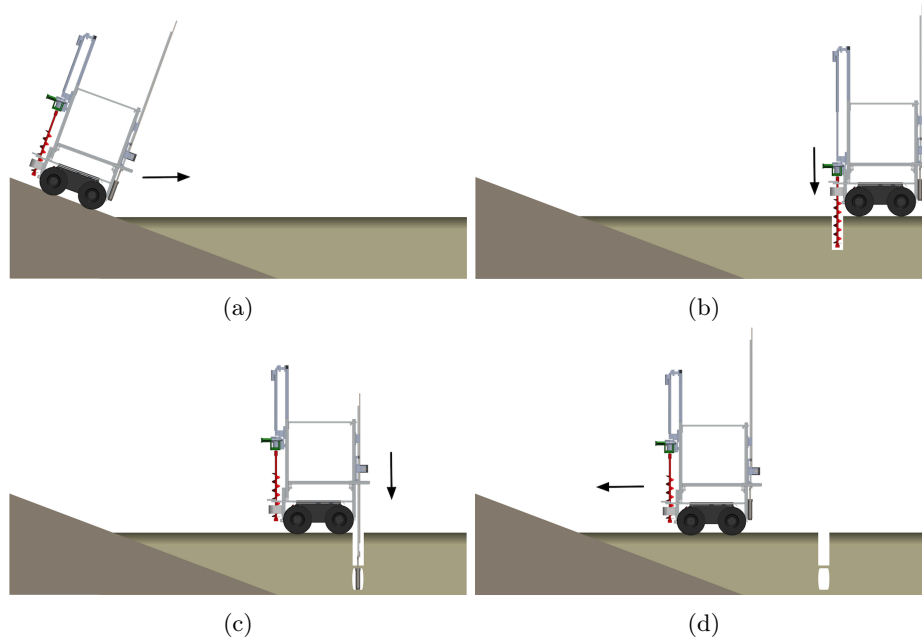


Figure 2.8: Tailings sample return mission: (a) RTC-I driving to the sampling location. (b) Rover drilling through the crust. (c) Rover collecting a sample at depth after repositioning. (d) Rover driving back to shore with sample.

to be ruggedized sufficiently to work in an open industrial environment, and to comply with safety, health, and environment (SHE) requirements of an industrial site.

The prototype comprises three main subsystems: a mobile platform, an auger drill, and a soft soil sampler (Fig. 2.9). The design of RTC-I allows it to traverse deposits with bearings strengths as low as 15 kPa, drill through crusts up to 45 cm thick, and sample up to 3 m deep. The characteristics of the field-ready platform vehicle are summarized in Table 2.1. The following subsections present the design of the subsystems, focusing on solutions specific to meeting the functional specifications.

2.4.1 Mobile platform

Experience acquired while working with previous prototypes drove the selection of an electric platform for this study. A Clearpath Robotics Husky A200 UGV was modified to carry the payloads and instrumentation required for field experiments (Fig. 2.10a). A frame made of standard T-slotted aluminum framing was fixed to the chassis of the robot. This frame forms a high-stiffness

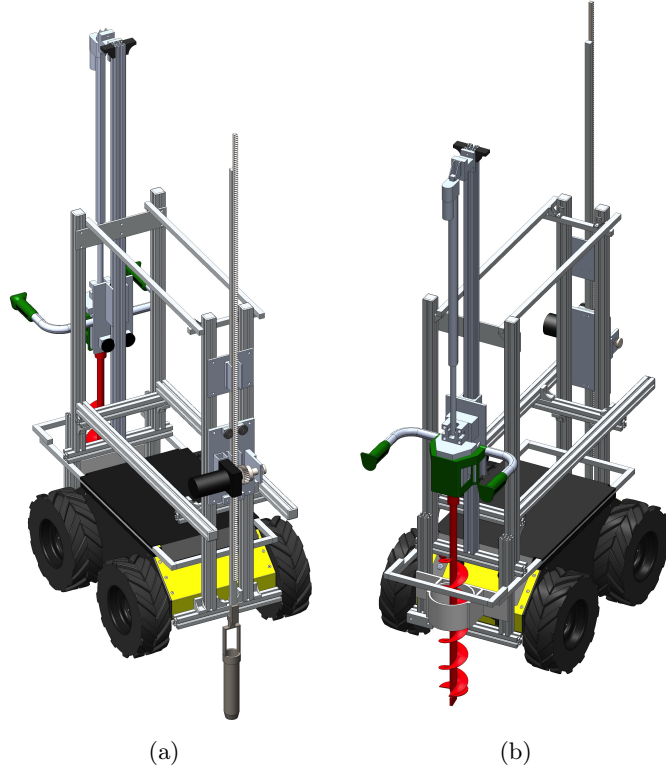


Figure 2.9: RTC-I with a soft soil sampler mounted on the front (a) and a drill on the back (b).

and high-strength structure, into which reaction loads and vibrations can be transmitted during operation of the drill and sampler. The drill and sampler mechanisms are mounted on the front and back of the frame to keep the centre of mass close to the centre of the vehicle. As built, the rover has mass of 123 kg. A key design assumption is that the vehicle operates at slow speeds over a relatively flat terrain, except for the ramp to drive onto the deposit from the perimeter berm of the treatment cell. The rover is capable of a maximum climb grade of 28° and has a roll-over angle of 35° . The position of the centre of gravity (CG) and the static pitch-over and roll-over angles were found empirically.

The robot has two geared brushed DC Motors with rated continuous torques of 19.4 Nm. Each motor drives the wheels of one side of the rover using a belt and pulley transmission. The platform has a skid steering (differential drive) configuration, which was preferred over explicit steering due to its simplicity and because this configuration allows for quick changes in locomotion components, such as adding tracks. The platform does not have a suspension mechanism. The compliance of the pneumatic tires is sufficient to keep ground contact on the four wheels in the terrain of

Table 2.1: RTC-I Specifications

Mass (with payloads)	123 kg
Locomotion speed	1 m s ⁻¹
Wheel diameter	330 mm
Ground clearance	130 mm
Vehicle track	556 mm
Vehicle wheel base	513 mm
CG location from vehicle track centre	7 mm
CG location from wheel base centre	36 mm
CG height from wheel shaft	400 mm
Static pitch-over angle	28°
Static roll-over angle	35°
Drill tower (upright)	2060 mm
Sampler tower (upright)	2570 mm
Runtime (heavy usage)	2 hours

interest at target vehicle speeds. Previous studies have suggested that traditional spring-damper suspensions can lead to instabilities while conducting high vibrations operations such as drilling [8]. Outriggers were considered to secure the mobile platform during drilling, but this was found to be an unnecessary addition.

Tracks were used to reduce the ground pressure of the robot (Fig. 2.10b). The rover requires low ground pressure to be able to traverse tailings with low bearing strengths. A ground pressure of 15 kPa was achieved with the tracks. The tracks were designed to be easily removable in the field without having to remove wheel. In this way, wheel-soil interaction studies could be conducted with this platform without substantial modifications. The tracks were mounted by deflating the pneumatic tires and wrapping the tracks around them. They were secured by inflating the tires back to 20 psi. Initial laboratory testing demonstrated that several point turns on pavement were required for the tracks to show any misalignment with the tires. Additionally, the tracks were found to have sufficient flexibility to maintain ground contact over uneven terrain. No traction failures occurred, even when gravel was forced between the track and tires.

The main compartment in the chassis is used as an electronics bay to enclose the on-board computer, motor controllers, wireless connectivity modules, data acquisition units and batteries. These components are powered with a 24 V 20 Ah sealed lead acid battery. A 12 V 10 Ah lead acid battery is used to power other payloads. The power consumption levels and temperatures are monitored constantly during operation.

The front right wheel was instrumented for wheel-soil interaction studies. The torque on the axle of

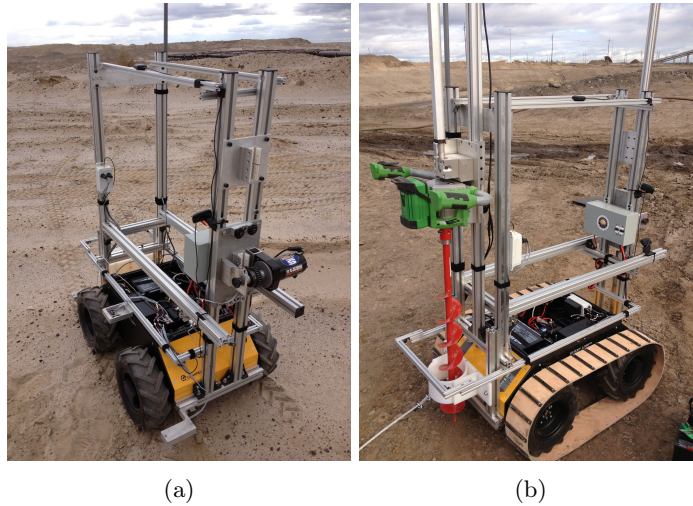


Figure 2.10: (a) RTC-I mobile platform. (b) RTC-I with tracks and drill in view.

the wheel is measured with a wireless torque transducer composed of strain gauges in a Wheatstone bridge configuration mounted on an aluminum shaft, a signal amplifier and a wireless transceiver mounted in the wheel hub. The torque transducer was developed specifically for this application. An aluminum shaft was selected to provide sufficient strength and deformation over the operating range of the wheel. The signal amplifier was built to multiply the analog output signal of the Wheatstone bridge with a variable gain, which was fixed after initial operating range testing of the sensor. The amplified signal is sampled by a 2.4GHz module and transmitted to the robot. The wireless module, signal amplifier and bridge are powered by a rechargeable battery mounted on the hub of the wheel. The transducer was calibrated using a load cell and a lever arm. The digital output of the wireless module was recorded for different torques applied to the shaft over the operating range of the wheel.

In addition the torque on the axle, the contact angles of the wheel are estimated by measuring the sinkage of the wheel with infrared (IR) distance sensors. The wheel's angular and ground (linear) velocities are measured with off the shelf quadrature encoders and optical flow sensors. These measurements are used to estimate the cohesion stress and internal friction angle of the terrain.

2.4.2 Drill

A drilling mechanism was required to make a hole in the crust of the deposit so that the sampler can be lowered to the unconsolidated material. A brushless DC motor drives a 100 mm diameter

auger as shown in Figure 2.10b. This modified commercial auger is powered by a 40 V lithium ion battery and has maximum speed of 180 rpm. The electric drill is mounted on a vertical linear actuator that can produce a maximum weight on bit (WOB) of 650 N and has a maximum extension of 60 cm. Tests of this subsystem in a controlled setting by drilling into compacted turf soil were successful.

2.4.3 Sampler

A custom rack-and-pinion mechanism lowers a sample container through the unconsolidated material to collect samples (Fig. 2.3), driven by a high-power geared DC motor that moves a steel rack vertically on an aluminum extrusion supported by guide rails and linear bearings for T-slotted framing. The mechanism has a pull-push force of approximately 8800 N. The rack has a usable length of approximately 1.9 m, although extensions were built to extend the maximum depth of sampling to 3 m.

A sample container with dimensions of 64 mm diameter and 127 mm length was fixed to one end of the rack with a custom bracket that allowed soft tailings to flow through the sampling container while it was open on both ends. One-way valves inside the bottom of the sample container allow soft material to move through the container as the rack is lowered. When the rack is lifted, the valves close and contain the material.

A GPS module is used to record the location where a sample is collected.

2.4.4 Human-robot interaction and control systems

The RTC-I is primarily controlled by teleoperation. Autonomous system monitoring, fault detection, and recovery routines have been incorporated to address issues when communication links fail or there are human-induced errors. At this point, the operator acts as the high level controller, task planner, and mission manager of the system. In the future, these subsystems can be automated. Automated discrete-event control has been demonstrated for most navigation functionality, and for payload operation, with human supervisor override of autonomous control.

Reliable communication is critical for a robot working in environments that are not accessible to workers. Fault tolerance of the system is improved by implementing two separate communication links between the Operator Control Unit (OCU) and RTC-I. Wireless communication is suitable for this application because RTC-I operates in an open space and remains in line of sight of the operator. The primary communication link (PCL) is composed of a wireless local area network (WLAN) created by the on-board computer's 802.11g wireless access point. The OCU computer

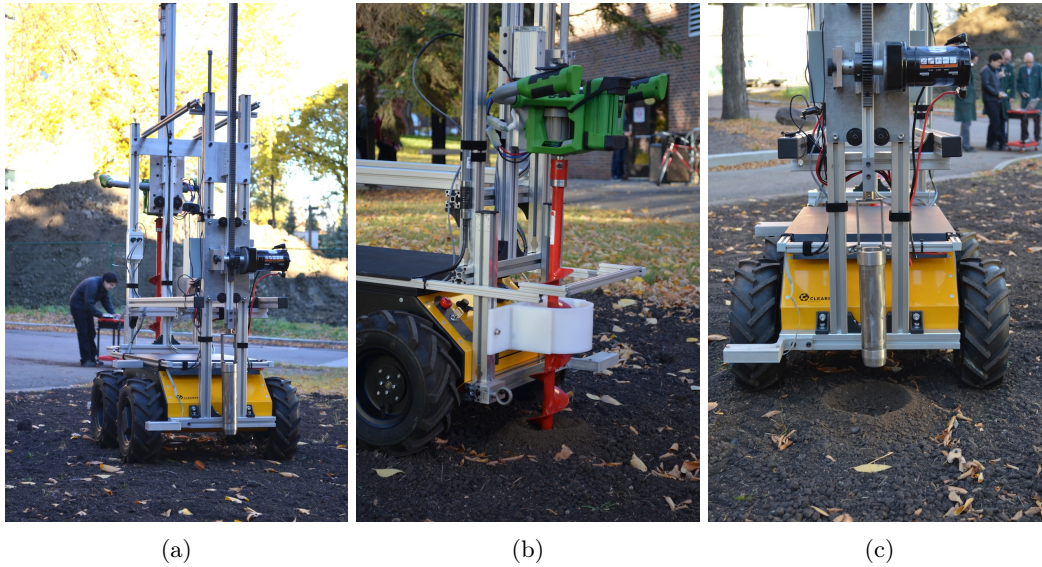


Figure 2.11: Outdoors testing of RTC-I: (a) Operator controlling the rover from a distance in a simulated sample return mission. (b) Teleoperating the drilling mechanism. (c) Repositioning the rover using visual feedback from the on-board cameras.

connects to the network through a long range wireless client bridge. A high gain antenna was used to increase the communication range to over 150 m.

The PCL transmits control commands and receives sensory feedback. The operator's control commands are gathered through a joystick and keyboard. These inputs are mapped to emergency-stop triggers, as well as speed, position, and on-off commands that are used by the mobile platform, drill, and sampler mechanisms. A system diagnostics module was integrated to monitor the status of the communication links and take action if a fault is discovered. If the PCL fails, a secondary communications link (SCL) relays basic motion commands. With this configuration, the user can maintain control of the robot unless there is a system-wide power failure.

The SCL consists of a remote control (RC) transmitter on the OCU and an RC receiver on the robot that has a range of over 1 km. The RC transmitter inputs are used as velocity commands and emergency-stop triggers. Failsafe routines are required to ensure that the payloads are retracted from the ground if the PCL fails. Once the robot's payloads are secured, the operator can use the SCL to drive the robot back.

A steel cable was attached to the rover's chassis to be able to retrieve the robot in case that both communication links fail or if the robot's locomotion system malfunctions. The design did not allow for remote disconnection of the sampler or auger if they had already been deployed. This mission

risk was accepted for proof-of-concept trials; but a commercial system would need to be able to jettison a stuck payload.

The software for the OCU and RTC-I was developed under the Robot Operating System (ROS) standard, which allows for a modular design methodology [20]. ROS software modules running on board the rover interact with data acquisition units and low-level control units. These modules receive control commands from the OCU through the ROS communication layers. Additionally, they transmit sensory feedback to assist the operator on the safe and effective control of the mobile platform and its payloads. Two video cameras monitor the sample collection procedure. One camera points forward, to aid in navigation, while another camera points to the sampling mechanism so that the operator can reposition the mobile platform to align the sampler with the hole drilled through the crust. Other sensory feedback transmitted to the OCU includes the vertical position of the drill, WOB on the auger, battery voltage levels, and mobile platform status. Measurements gathered by the instrumented wheel are also transmitted. The ROS built-in recording tools log all sensory information.

Outdoor trials verified the performance and reliability of the human-robot interaction and control systems (Fig. 2.11). The experimental trials consisted of a simulated sample return mission: (1) an operator controls the robot from a distance to a predetermined sampling location, (2) the operator deploys the drill to make a hole, (3) repositions the rover to align the sampler to the hole using the visual feedback of the two on-board cameras only, and, (4) lowers the sampler to simulate sample collection. The operator was effective in controlling the robot throughout the simulated mission. It was noted that it is necessary to detect possible human-induced errors. We designed an ROS module to monitor the system state to detect command conflicts during operation. For example, the module prevents the operator from moving the robot while the drill or sampler are deployed. System state monitoring was implemented and verified before field testing.

2.5 Field-Testing Experiments

Field trials have been critical in determining the feasibility of introducing unmanned systems to industrial operations for environmental monitoring. This section presents several field-testing experiments that were conducted in October, 2013, at an oil sands operating plant near Fort McMurray, Alberta, Canada. This site contains several tailings treatment cells, both for experimental studies and for commercial production. The experimental cells are small deposits, holding approximately 2000 m², dedicated to test consolidation processes. Production cells are on the order of 100 times larger and are part of tailings operations. The deposits are surrounded by berms made of tailings sand.

2.5.1 Safety and risk management and fail-safe demonstration

Safety and risk management is an essential for introducing new technologies to industrial sites, such as UGVs to oil sands tailings sites. Throughout RTC-I's design process, FMEAs were used to address critical failure modes and improve the overall reliability of the robot. Redundant communication systems and a tether retrieval cable were identified as necessary to manage the effects of possible component failures; both improvements were implemented on the final design. Tether cables are impractical and may pose risks to the robot's stability when it's operating very far away from the shore. A tether cable was used in these field trials because the rover was not expected to travel further than 25 meters away from the shore of partially dried tailings deposits. Tether cables should not be used for long distance operations, instead rescue robots should be deployed to drag the rover back to shore if there is a failure. Rescue vehicles are typically used by tailings operators to retrieve trapped manned vehicles.

Safety training sessions were required for the robot operators before working on the field. A test plan was discussed with the mine operators and a Job Safety Analysis (JSA) was developed by the researchers and operations staff. Before starting any new experiment, a Field Level Risk Assessment (FLRA) was completed and the risks were controlled to acceptable levels.

On site, the rover was first tested to demonstrate the fail-safe systems to the mine operators. The rover was deployed on the sand dyke around the research cells. Mine operators identified the communication links as the components with highest risk of failure. The fault tolerance of the communication system was demonstrated by teleoperating the robot on the sand dyke and forcing the PCL to fail by disconnecting the wireless client bridge from the OCU computer. The broken link was detected by the robot's state monitoring system, triggering recovery routines. First, all actuators including payload and robot motors were stopped; then, any deployed tools were automatically retracted; and finally, the robot's control systems switched to the SCL and control of the mobile platform was maintained through the RC controller. A failure of the SCL was forced by switching the RC transmitter off. Once this failure was detected, all robot actuators were disconnected automatically to facilitate its retrieval using the tether cable. These tests demonstrated the redundancy of the rover's control channels and its fail-safe routines. The demonstrations were sufficient for the mine operators to consider the level of risk acceptable and to allow experiments to be conducted with RTC-I, provided that personnel were not in the area where the RTC-I was operating.

For this initial technology demonstration the mine operators preferred the robot to be teleoperated rather than to be navigated autonomously. Autonomous navigation to the platform is achievable using existing open-source ROS packages and will be demonstrated in future work.

2.5.2 Surface characterization of dry tailings sand

Surface characterization instrumentation and methods were tested on the tailings sand dyke surrounding the fluid tailings (Fig. 2.12). The robot was teleoperated over flat soft soil while collecting wheel loading and state measurements. The tether cable was not attached to the robot during these tests because the tailings sand had sufficient bearing strength to support the rover and workers without excessive sinkage.



Figure 2.12: Field testing of RTC-I: Tailings sand surface characterization.

Measurements were recorded for the wheel's angular speed ω , ground speed v , sinkage z , and torque T . The front contact angle θ_1 was estimated from the sinkage, and the slip ratio s was calculated from ω , v , and the wheel radius r , using Equation 2.4.

An example of the recorded measurements of the angular and ground speeds of the wheel is shown in Fig. 2.13a, with the corresponding slip ratios. The steady-state regions can be used for the parameter estimation algorithms that assume quasi-static motion. In this example, two regions of interest can be identified between the time ranges of 104 s to 106 s and 108 to 110 s. The torques recorded during the test are shown in Figure 2.13b and the sinkage and calculated contact angle on a region of interest are shown in Figure 2.13c. The results of the soil parameter estimations are discussed in Section 2.6.2.

2.5.3 Subsurface sampling of partially dried tailings from tailings treatment cells

Subsurface sampling experiments were carried out on three treatment cells. The first two trials were conducted on experimental cells, and the third trial was conducted on a large scale production cell.

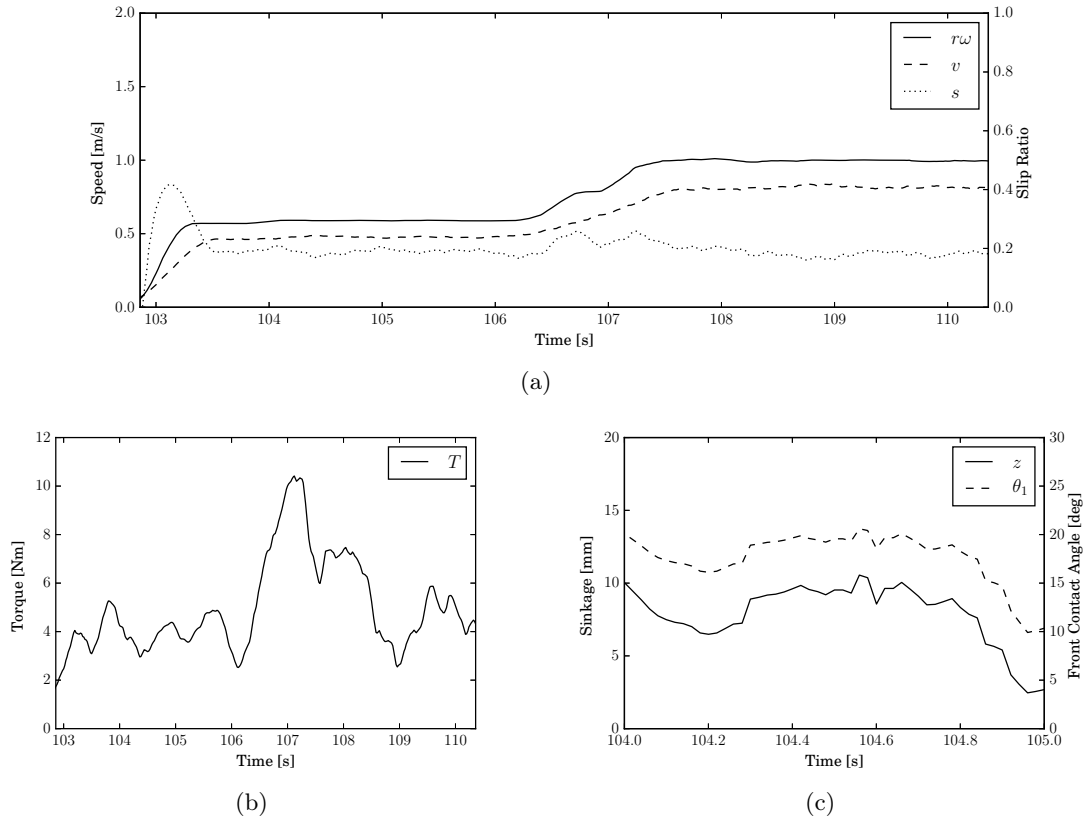


Figure 2.13: (a) Wheel speeds and slip ratio during sand surface characterization experiment, with measurements show two steady-state regions in this trial. (b) Wheel torque recorded during a surface characterization experiment. (c) Sinkage and calculated front contact angle recorded at steady-state motion.

Teleoperation on experimental tailings treatment cell with partially dried crust

The rover was teleoperated into the deposit and positioned approximately 2 meters from the shore of the cell (Fig. 2.14a). Initially, the robot was teleoperated farther away from the shore, but the partially dried crust did not have sufficient bearing strength to support its weight. The auger was tested on the surface of the deposit up to a depth of 30 cm (Fig. 2.14b). Then, the robot was repositioned over the auger hole, and the sampling tool was lowered (Fig. 2.14c). It was found that the material under the crust at 2 meters from the shore was not sufficiently fluid to move through the sampling tool, and therefore no sample was collected. This motivated the subsequent sampling trial to be conducted on an cell with a high-strength dry crust that would support the weight of the robot further away from the shore.

The partially dried crust was pictured from the robot's camera view, as shown in Figure 2.14d. The dried mushroom-shaped structures can have high bearing strengths but the water-saturated cracks can cause the crust to fail easily and induce excessive sinkage of the platform. These instabilities may result in equipment getting stuck and limit manual sampling to floating docks.



Figure 2.14: (a) RTC-I roving into an experimental cell. (b) Auger and drill subsystem test. (c) Sampler subsystem test. (d) On-board camera's view of the partially dried tailings surface.

Experimental cell with dry crust

The robot was deployed on a deposit with high surface strength (Fig. 2.15a). The deposit had an estimated bearing strength of 60 kPa, which permitted the robot to drive a distance of 15 meters from the shore without any noticeable sinkage. The robot was positioned approximately 10 m from the shore of the deposit and the auger was lowered to make a hole 60 cm deep through the crust (Figure 2.15b). The robot was repositioned, the sampling tool was lowered, and a sample was collected at 1.7 meters depth (Fig. 2.15c). The rover was teleoperated back to the shore of the deposit and the sample was contained and stored (Fig. 2.15d).

Production cell

A final sample retrieval trial was conducted on a production cell. The experiment was performed similarly to the previous trials. The rover was teleoperated down a soil ramp onto the surface of the cell, to approximately 15 meters from the shore (Fig. 2.16a). The deposit's crust was partially dried and supported the robot with minimal sinkage, although there was some general deflection of the surface. The rover successfully drilled through the crust (Figure 2.16b), repositioned, deployed the sampling tool to a depth of 1.5 meters and retrieved a sample (Figure 2.17). The sampling process was monitored through the robot's on-board cameras as pictured in Figure 2.18.

The sample qualitatively showed very little shear strength, indicating that rather than the cell acting as an elastic foundation, the crust was acting as a membrane to support the weight of the rover with shear strength at the surface crust only.

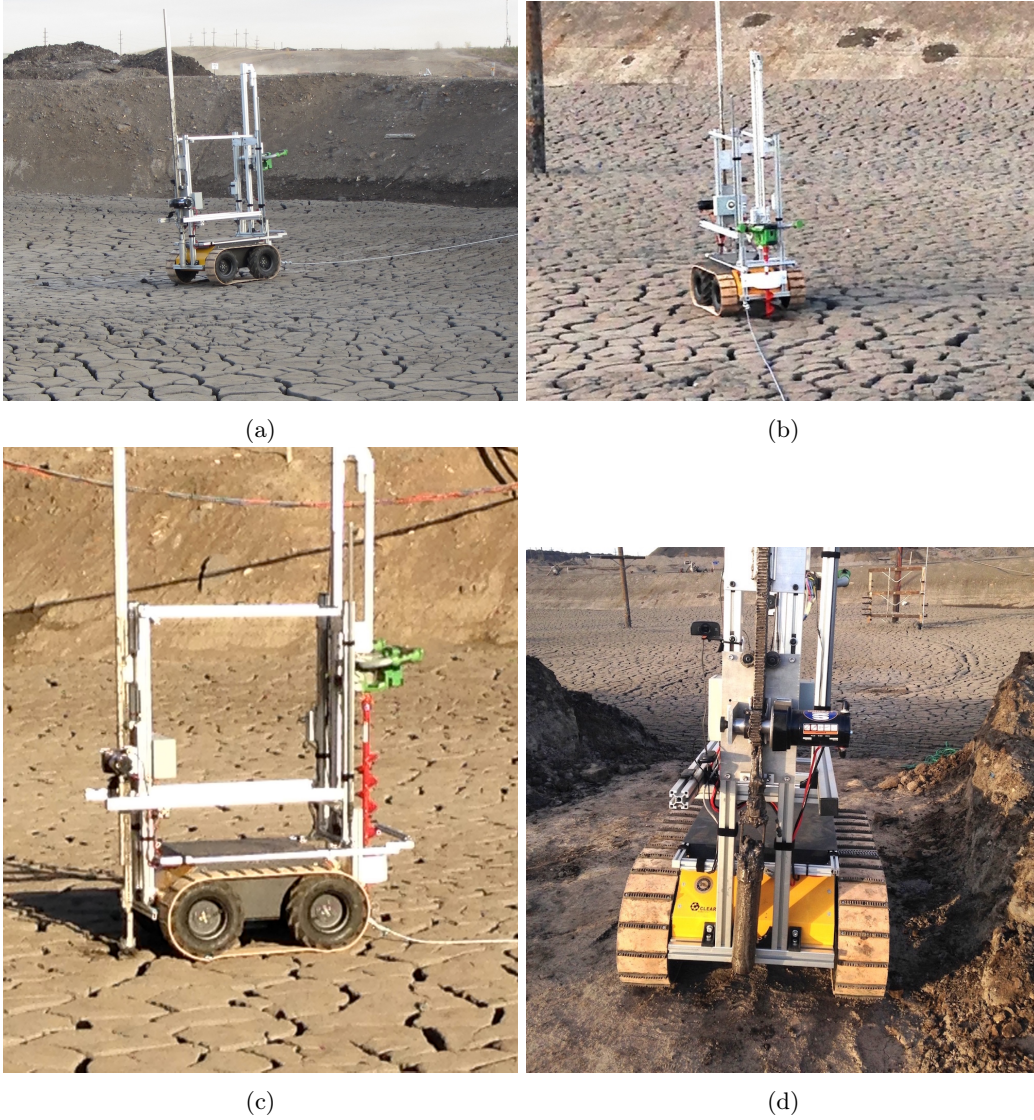


Figure 2.15: (a) RTC-I teleoperated into an experimental cell. (b) Drilling through the crust. (c) Sampling tool lowered through the crust. (d) RTC-I with sample collected from 1.7 m depth.

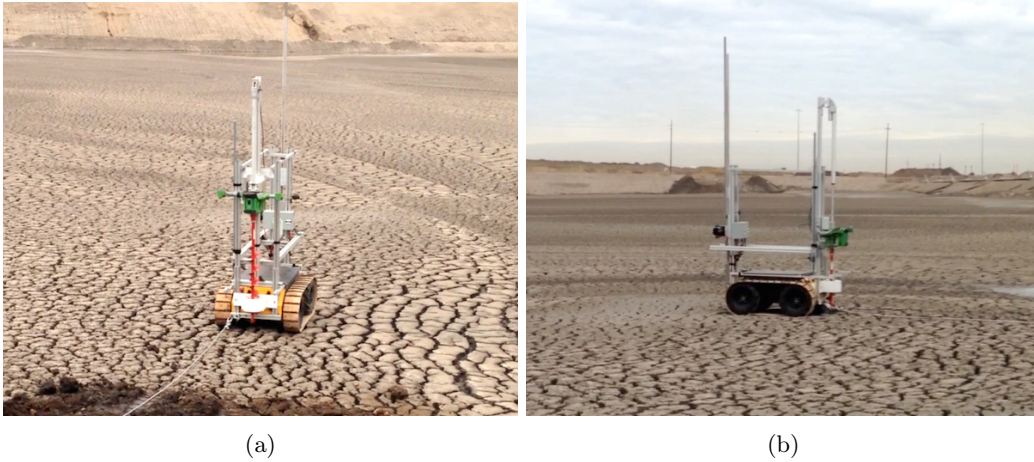


Figure 2.16: (a) RTC-I teleoperated into a production cell. (b) Drilling through the crust.

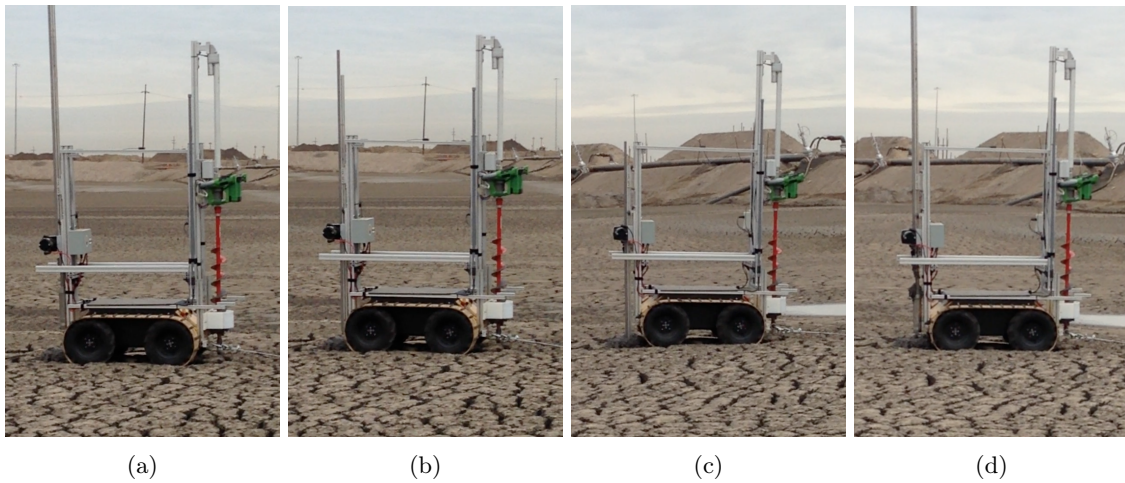


Figure 2.17: RTC-I lowering the sample container into the deposit to collect a sample. The sample container is pictured on the left side of each image. (a) RTC-I repositioned over the hole drilled through the deposit's crust. (b) RTC-I lowering sampling tool. (c) Sampling depth reached. (d) Sampling tool retracted with sample.

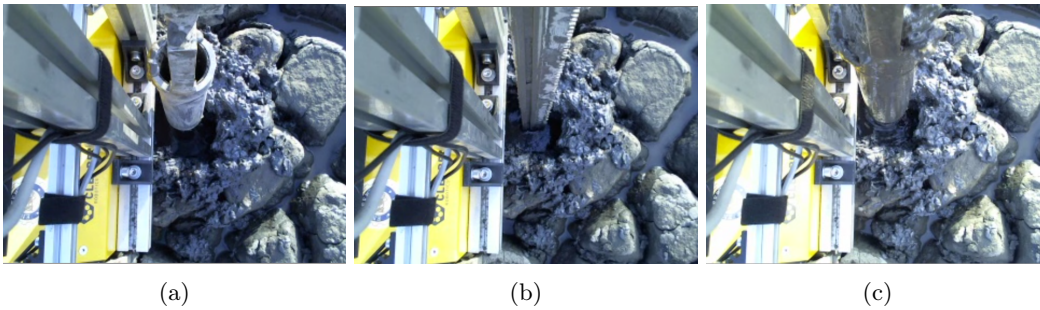


Figure 2.18: (a) Sampling tool repositioned over the drilled hole. (b) Sampling tool lowered through the crust to retrieve a sample. (c) Sampling tool retracted with sample.

2.6 Surface & Subsurface Characterization Results

2.6.1 Sample analysis

The samples collected in the experimental and production cells were sent for analysis. For tailing characterization, typical analyses include bitumen content, particle size analysis, Methylene Blue Index (MBI), and solids content. These analyses were contracted to a laboratory that regularly studies tailings samples for the oil sands tailings operators. The results for the Dean & Stark analysis and MBI analysis are presented in Table 2.2. It is noted that due to an unsecured seal, some moisture of the production cell sample evaporated before the analysis was conducted, and therefore the reported water content of the sample is less than a percentage by weight. The results of the Laser Diffraction Particle Size analysis are presented in Table 2.3. Both samples have similar particle size distributions (Figure 2.19).

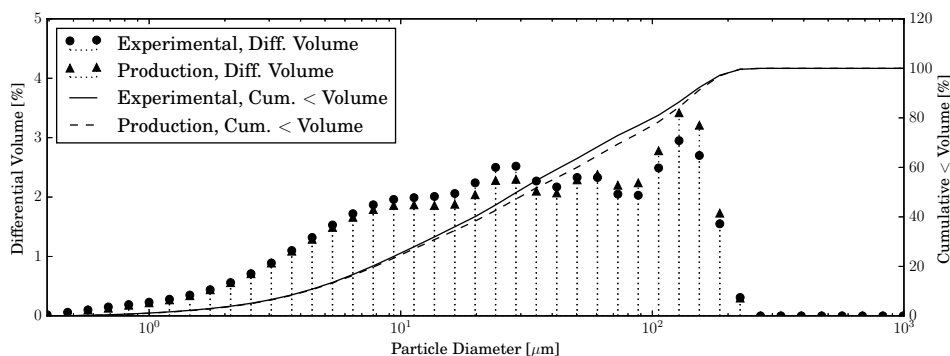


Figure 2.19: Particle size distributions of the samples collected.

Table 2.2: Dean Stark Analysis and Methylene Blue Index (MBI) Report

Sample	Weight [g]	Bitumen [g]	Mineral [g]	Water [g]	Bitumen %	Mineral %	Water %	MBI [meq/100g]
Experimental Cell	134.81	10.47	78.68	45.66	7.77	58.36	33.87	5.81
Production Cell	90.43	7.61	82.22	0.60	8.42	90.92	0.66	6.02

Table 2.3: Laser Diffraction Particle Size Analysis

Sample	Particle Diameter Size [μ m]									
	Mean	Median	Mode	d5	d10	d25	d50	d75	d90	d95
Experimental Cell	50.00	27.58	127.7	2.40	4.00	9.39	27.58	76.73	136.60	161.10
Production Cell	53.83	30.78	140.1	2.44	4.06	9.72	30.78	88.50	142.10	164.50

2.6.2 Terrain parameters estimation

The cohesive stress and internal friction angle of tailings sand can be estimated from the wheel-soil interaction observations during the surface characterization experiments. These parameters can aid in understanding the trafficability of the terrain as described in Section 2.3.2.

This section discusses the parameter estimation results obtained from the field trials.

Tailings sand parameter estimation results

The cohesion stress and internal friction angle of the terrain were estimated recursively from the on-board measurements collected during the field trials. As described in Section 2.5.2, measurements of z , ω , v , and T were obtained during the surface characterization experiments. A least-squares regression was used with Equation 2.8 to obtain \hat{c} and $\hat{\beta}$, the estimates of c and $\tan(\phi)$ respectively. Only measurements of steady-state operation were included in the parameter estimation analysis.

The regression results for \hat{c} and $\hat{\beta}$ are presented in Table 2.4. The P-value of the two-sided test for \hat{c} is higher than 0.05, therefore the analysis fails to reject the null hypothesis: $H_0 : c = 0$ [Pa], for a 95% confidence level. This result is expected for cohesionless soils such as dry sand. The estimates obtained recursively show that after approximately 140 observations, the estimates do not vary significantly (Fig. 2.20a and 2.20b).

The results of the regression analysis assuming cohesionless soil are presented in Table 2.5. The coefficient of determination for this analysis was calculated to be: $R^2 = 0.974$. The 95% confidence intervals of $\hat{\beta}$ correspond to an estimate of the internal friction angle, $\hat{\phi} = 33.64 \pm 0.63$, which is similar to the values obtained from shear failure experiments of washed dry sand reported in literature, $c = 0.65 \pm 0.24$ kPa and $\phi = 32.1 \pm 2.82$ deg [15]. It is expected that different types of sand will have moderate variations in their soil parameters because these are affected by many factors including moisture content, particle size distribution, and particle angularity.

Estimation errors are expected due to the linearization assumptions and further simplifications of the linearized terramechanics model. Additionally, sensor noise and error in the assumed value of the shear displacement under the wheel contribute to the overall error of the estimation. The experiments were conducted on an uncontrolled terrain around the tailings deposit, therefore, it is possible that deviations existed on the homogeneous and isotropic characteristics assumed for the terrain.

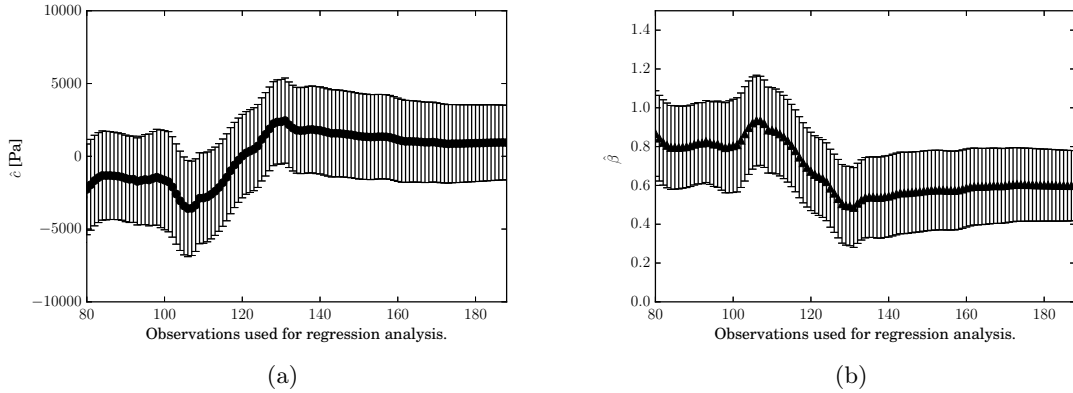


Figure 2.20: (a) Recursive estimation results for \hat{c} (a) and $\hat{\beta}$ (b). Error bars show standard error of the estimates.

Table 2.4: Regression Results

	Est.	Std. Error	95.0% Conf. Int.	t	P> t
\hat{c} [Pa]	940.426	2555.953	-4101.782, 5982.634	0.368	0.713
$\hat{\beta}$	0.599	0.180	0.244, 0.954	3.327	0.001

Table 2.5: Regression Results For Cohesionless Soil

	Est.	Std. Error	95.0% Conf. Int.	t	P> t
$\hat{\beta}$	0.665	0.008	0.650, 0.681	83.758	0.000

2.7 Lessons Learned and Future Work

The results of the field trials indicate that surface and subsurface characterization of oil sands tailings is technically feasible. Sampling and surface characterization have been demonstrated with RTC-I but still several improvement areas have been identified.

A limitation of the current system is that the instrumentation required to collect measurements for the terrain parameter estimation algorithms is coupled to the propulsion mechanism of the robot. While wheels are all right for terrain with good bearing strength, that circumstance may not always be the case with soft tailings deposits. A wheeled platform is generally not suitable to traverse water-saturated terrains, especially in low-bearing strength deposits. Balloon tires can be used, but tracked vehicles and amphibious vehicles are preferred for these applications. In the current design, the terrain parameter estimations can only be conducted when wheels are being used, limiting the terrain surfaces that can be characterized. A separate payload for wheel-soil

interaction force estimation is required. This payload would consist of an actuated wheel that is pressed onto the terrain with variable normal forces, while collecting measurements similarly as the instrumented wheel used in RTC-I. The payload can be integrated into other ground vehicles as part of a collection of instruments to characterize very soft deposits. Spatial verification of the estimated soil parameters can be obtained by integrating standard geotechnical tools for cone-penetrometer and a vane shear testing.

Two limitations were found on the sampling subsystem of RTC-I. First, the sampling mechanism is currently limited to a single sample per trip, which is not desirable when working on large deposits where a large number of samples is required. The subsurface characterization of a deposit can be conducted faster if a sample magazine were added to the rover to collect and store more samples. A design has been created for a magazine that can collect and carry twelve samples. On very large deposits higher sample capacities and multiple unmanned systems may be required. Second, an improvement in the sample collection mechanism is required to minimize the risk of hard material obstructing the sample container as it is lowered through the deposit. The one-way valves of the sample container can be replaced with an actuated mechanism to open and close the container. The closed container can be moved through hard material and be opened to capture material only at the desired sampling depth, reducing the uncertainty of the depth where the material was captured and minimize cross-contamination between material from different depths.

Additional instrumentation and payloads can be mounted on the rover for in-situ analysis. In future field trials, a hyper-spectral imaging camera and data acquisition system mounted on the rover will be used to detect different clay types, quantify material composition, assess hydrocarbon abundance, and to create moisture content maps.

Near-term developments will focus on implementing the improvements discussed, as well as adding different levels of autonomy to the system. Initially, the drilling and sampling subsystems can be automated to operate with minimal human supervision. Further developments can lead to full autonomy of the system, with on-board task planning and mission managing. Possible long-term work will focus on adding cooperation between several unmanned systems, including aerial vehicles that could conduct surveys to identify regions of interest for ground vehicles to explore, and any zones that would not be navigable.

The technologies developed through this work can be used for environmental monitoring of other types of mine tailings, and can be further extended to other applications, such as robotic systems working on agricultural land, on glaciers, and on permafrost.

2.8 Conclusions

The development and field experimentation trials of RTC-I, a rover for tailings characterization, have been described. The design of RTC-I focused on meeting the functional specifications for characterizing soft oil sands tailings. The rover was uniquely configured to estimate terrain parameters while traversing deformable terrain, and capture a subsurface sample from the tailings deposit. The different subsystems of the field-ready prototype have been described. Building and field testing RTC-I has demonstrated that robotic systems can aid in environmental monitoring of potentially hazardous industrial sites, such as a treated tailings impoundment. Field demonstrations have established the concept of collecting samples from tailings deposits, as well as the capability to estimate cohesive stress and internal friction angle of tailings sand. The favourable results of the field trials show that the technologies proposed are suitable for tailings characterization. Limitations of the demonstrated system have led to a set of possible improvements; and future work has been outlined with the intent to develop and implement robotic systems with geotechnical tools to aid in the environmental monitoring of industrial sites and other challenging soil types.

Acknowledgments

Financial support is gratefully acknowledged from the Natural Sciences and Engineering Research Council of Canada (NSERC) and the University of Alberta. The authors wish to thank the Mechanical Engineering Machine Shop staff for their technical support and specially Rick Bubenko, Andrew Campbell, Rick Conrad, Roger Marchand, and Dave Waeye for their collaborations in system concept and integration. Logistical support from the oil sands company operations staff is also much appreciated.

2.9 References

- [1] Alberta-Energy. Oil sands. <http://www.energy.alberta.ca/OurBusiness/oilsands.asp>, 2014.
- [2] Alberta-Energy. Oilsands 101: Reclamation. <http://www.energy.alberta.ca/OilSands/1722.asp>, 2014.
- [3] Alberta-Energy. Oilsands 101: Resource. <http://www.energy.alberta.ca/OilSands/1715.asp>, 2014.
- [4] Alberta-Energy-Regulator. Directive 074: Tailings performance criteria and requirements for oil sands mining schemes. <http://www.aer.ca/rules-and-regulations/directives/directive-074>, 2009.

- [5] Alberta-Energy-Regulator. Ercb conditionally approves tailings plans for shell muskeg river project. <http://www.aer.ca/about-aer/media-centre/news-releases/news-release-2010-09-20-nr2010-13>, 09 2010.
- [6] Erik W. Allen. Process water treatment in canada’s oil sands industry: I. target pollutants and treatment objectives. *Journal of Environmental Engineering and Science*, 7(2):123–138, 2008.
- [7] R.C. Anderson, L. Jandura, A.B. Okon, D. Sunshine, C. Roumeliotis, L.W. Beegle, J. Hurowitz, B. Kennedy, D. Limonadi, S. McCloskey, M. Robinson, C. Seybold, and K. Brown. Collecting samples in gale crater, mars; an overview of the mars science laboratory sample acquisition, sample processing and handling system. *Space Science Reviews*, 170(1-4):57–75, 2012.
- [8] Paul Bartlett, David Wettergreen, and William (Red) L. Whittaker. Design of the scarab rover for mobility and drilling in the lunar cold traps. In *International Symposium on Artificial Intelligence, Robotics and Automation in Space*, February 2008.
- [9] Nicholas Beier, Ward Wilson, Adedeji Dunmola, and David Segó. Impact of flocculation-based dewatering on the shear strength of oil sands fine tailings. *Canadian Geotechnical Journal*, 50(9):1001–1007, 2013.
- [10] M. G. Bekker. *Introduction to Terrain-Vehicle Systems*. University of Michigan Press, Michigan, 1969.
- [11] Maurice B. Dusseault and J. Don Scott. Tailings pond behavior and characterization of oil sand tailings sludge. *Particulate Science and Technology*, 1(3):295–309, 1983.
- [12] Gustavo Freitas, Fernando Lizarralde, Liu Hsu, Vitor Paranhos, Ney R. Salvi dos Reis, and Marcel Bergerman. Design, modeling, and control of a wheel-legged locomotion system for the environmental hybrid robot. In *Proceedings of the IASTED International Conference*, number CMU-RI-TR-, November 2011.
- [13] Daniel Helmick, Scott McCloskey, Avi Okon, Joseph Carsten, Won Kim, and Chris Leger. Mars science laboratory algorithms and flight software for autonomously drilling rocks. *Journal of Field Robotics*, 30(6):847–874, 2013.
- [14] K Iagnemma, H Shibly, and S Dubowsky. On-line terrain parameter estimation for planetary rovers. *Robotics and Automation, 2002. Proceedings. ICRA ’02. IEEE International Conference on*, 3:3142 – 3147, 2002.
- [15] Karl Iagnemma and Steven Dubowsky. *Mobile Robots in Rough Terrain Estimation, Motion Planning, and Control with Application to Planetary Rovers*, volume 12 of *Springer Tracts in Advanced Robotics*. Springer Berlin / Heidelberg, 2004.

- [16] M.G. Lipsett and S.C. Dwyer. A robotic system to characterize soft tailings deposits. In *Proceedings of Mine and Tailings Waste Conference 2009, Banff Alberta*, November 2009.
- [17] M.G. Lipsett, J.D. Yuen, N.A. Olmedo, and S.C. Dwyer. Condition monitoring of remote industrial installations using robotic systems. In Jay Lee, Jun Ni, Jagnathan Sarangapani, and Joseph Mathew, editors, *Engineering Asset Management 2011*, Lecture Notes in Mechanical Engineering, pages 231–241. Springer London, 2014.
- [18] J.G. Matthews, W.H. Shaw, M.D. MacKinnon, and R.G. Cuddy. Development of composite tailings technology at syncrude. *International Journal of Surface Mining, Reclamation and Environment*, 16(1):24–39, 2002.
- [19] Nicolas Olmedo and M.G. Lipsett. Oilsands tailings characterization using a robotic system. In Kris Zacny, editor, *Earth and Space 2012*, pages 1167–1176. American Society of Civil Engineers, 2012.
- [20] Morgan Quigley, Ken Conley, Brian P. Gerkey, Josh Faust, Tully Foote, Jeremy Leibs, Rob Wheeler, and Andrew Y. Ng. Ros: an open-source robot operating system. In *ICRA Workshop on Open Source Software*, 2009.
- [21] David Wettergreen, Scott Jared Moreland, Krzysztof Skonieczny, Dominic Jonak, David Kohanbash, and James Teza. Design and field experimentation of a prototype lunar prospector. *International Journal of Robotics Research*, 29(12):1550 – 1564, October 2010.
- [22] Kazuya Yoshida. Terramechanics-based analysis and traction control of a lunar/planetary rover. *Field and Service Robotics*, 24:225–234, 2006.
- [23] Feng Zhou, Raymond E. Arvidson, Keith Bennett, Brian Trease, Randel Lindemann, Paolo Bellutta, Karl Iagnemma, and Carmine Senatore. Simulations of mars rover traverses. *Journal of Field Robotics*, 31(1):141–160, 2014.

Chapter 3

An Automated Vane Shear Test Tool for Environmental Monitoring with Unmanned Ground Vehicles

Abstract

The present work describes the development of a novel robotic vane shear test tool for characterization of soil parameters with high precision and accuracy. The tool automates industrial standards for testing procedures. The proposed system is capable of performing high resolution torque measurements, which are then used to estimate the shear strength of the soil. The design of the instrument and its advantages over traditional manual instruments are discussed, after which error sources, calibration, and test procedures are described. The developed tool was successfully validated against high-end commercial equipment. Our built unit was employed for characterizing mine waste in a laboratory setting and also deployed in the field on board an Unmanned Ground Vehicle for remote soil characterization.

3.1 Introduction

Automated tools and unmanned robotic systems have become increasingly important for monitoring challenging terrain and hazardous environments. Natural areas affected by industrial operations must be remediated to a state that is equivalent to the original environment once industrial activities are completed [38]. The terrestrial, aquatic, and atmospheric conditions must be actively monitored throughout the operations and until closure certificates are issued. In many cases, unmanned

monitoring solutions can ease access to hazardous environments and reduce the costs and difficulty of working in difficult terrains, as well as reduce the risk to human workers [33].

Tailings storage facilities built for mining activities around the world are an example of industrial sites which require ongoing environmental and geotechnical monitoring. Processes such as mineral extraction and other resource separation processes generate fluid tailings, which cannot be released back into the natural environment without treatment [24]. Fluid tailings are typically stored in dedicated disposal areas to manage and contain liquids and suspended solids until subsequent reclamation activities restore the land to a state suitable for mine closure. The characteristics, environmental impacts and remediation of tailings impoundments are ongoing research topics [24]. The need for monitoring programs has been highlighted throughout the extractive industries [25]. Mine waste can be a very significant ongoing liability to mining companies [14].

In the Athabasca Oil Sands of Alberta, Canada, open-pit mining and water-based bitumen extraction processes produce large volumes of soft tailings composed of sands, silts, clays, process-affected water, and residual bitumen [28]. Oil sands tailings are placed in impoundments to allow preliminary settling of fine solids and recycling of process-affected water [13]. The partially densified material, known as Mature Fine Tailings (MFT) containing approximately 30-35 wt.% solids [1] cannot be reclaimed without further dewatering and consolidation. A number of technologies and treatment methods have been used to accelerate these processes, including flocculation, coagulation, centrifugation, conventional thickening, and dewatering [30]. The resulting materials are then deposited into storage facilities, where they must be constantly monitored for further treatment processes [27], environmental monitoring [34], legislation compliance [38], as well as to identify areas which require additional remediation work [19] as illustrated in the photograph in Figure 3.1.



Figure 3.1: Centrifuged MFT dedicated disposal area, Athabasca Oil Sands, Alberta

Geotechnical investigations of mine waste storage facilities are typically performed using manual geotechnical sampling and measurement campaigns [7]. These activities are costly and are limited

to areas which are accessible to human workers. Floating docks often need to be constructed to provide access to certain areas of tailings treatment cells. In some cases, manned barges are used to carry equipment and workers, disturbing the terrain up to a depth of several metres. Due to the unknown soil conditions and variability in the consistency of tailings, these large amphibious barges risk getting stuck. Because of these factors and associated risks to workers, manual surveys often do not provide a complete or timely characterization and mapping of tailings deposits.

Unmanned Ground Vehicles (UGVs) can be deployed as part of geotechnical campaigns in challenging environments. Robotic systems can reduce risks to workers, investigate locations not accessible in conventional studies, provide timely soil characterization, collect samples from hazardous locations, assess trafficability of terrain, locate and identify hazards, reduce the risk and cost of geotechnical surveys, and produce reports on soil shear strength and fines capture rates for regulatory compliance [26]. The benefits of unmanned site investigations are strong drivers for the development of novel robotic systems to characterize soil properties and collect soil samples [33].

UGVs can be instrumented with tools used in conventional geotechnical investigations of mine waste storage facilities. These terrains are characterized by their shear strength and other geotechnical parameters, such as grain size distribution, solids content, and Atterberg limits [16]. Typical geotechnical analysis includes a combination of in-situ measurements as well as laboratory testing of samples. The results of the analyses are used to calculate load-bearing limits of the terrain at different locations and to track the consolidation progress of the deposits, taken as inputs to tailings management and remediation plans.

The present work focuses on the development of a vane shear test (VST) device for in-situ studies, based on ASTM D2573 [3], as well as for laboratory testing of samples based on ASTM D4648 [4]. The VST method is commonly used to estimate the undrained shear strength of very soft or weak cohesive soils [31] such as tailings. VST is both economical and widely used in field and laboratory studies [12]. The test consists of slowly rotating a vane in the soil to generate shear. The relationship between the torque applied to the vane and the strength of the soil is a function of the vane geometry. Other methods for in-situ testing such as the cone penetrometer [5], the bevameter and other vane-cone devices have been used to investigate terrain trafficability [39], and could also be integrated into UGVs in future studies.

The contribution of this paper is to present the design of a novel automated field vane shear test tool which can be deployed from a UGV in the field. Innovations of the design include a dual encoder structure for measuring the true angular deflection of the spring, a highly precise identification of the torsional spring constant, and a novel friction torque compensation scheme. The built unit is successfully validated against a high-end commercial laboratory instrument for estimating shear strength of various soil samples. Finally, the feasibility of deploying the design onboard a UGV is

demonstrated through experimental results from a field trial.

The remainder of this paper is structured as follows. Related work, industrial measurement standards and limitations of current instruments are discussed in Section 2. Section 3 gives a detailed description of the proposed automated vane shear test tool. Section 4 presents laboratory validation experiments and comparisons with commercially available instruments. Section 5 discusses integration of the developed unit onboard a robotic UGV platform. Finally, conclusions and recommendations for future work are provided in Section 6.

3.2 Background

3.2.1 Robots for Environmental Monitoring of Difficult Environments

UGVs have been used for environmental monitoring in challenging environments. Freitas *et al.* developed an Environmental Hybrid Robot to study the aquatic environments of the Amazon rain forest [15]. It was used to collect water and insect larvae samples, and to detect combustible gases [15], demonstrating the value of using robot systems in areas inaccessible and/or dangerous to human workers.

Recently, UGVs have been used to navigate underground mines and assist workers [20]. Some work has focused on the development of autonomous robots that can map environments that are too dangerous for humans [11, 17], such as abandoned mines [32], or assist in search and rescue operations in underground mines [37].

Our previous work [33] demonstrated the use of a customized UGV, RTC-I, capable of collecting subsurface samples from an oil sands tailings deposit covered by a crust, which was instrumented for characterization of soil terramechanics parameters of oil sands tailings. The robot was designed to operate on low bearing-strength deposits. A Clearpath Robotics Husky A200 platform was outfitted with tracks, a drilling system, and a subsurface sampling end-effector. RTC-I was successfully tested at an industrial site. Subsurface samples were collected from an experimental tailings treatment cell and a production treatment cell (Figure 3.2). These samples were analyzed for solids concentration, bitumen content, and mineral abundance in the tailings. Surface parameter estimation (via least-squares) was run on the tailings sand dyke surrounding the fluid tailings to estimate the cohesion stress and internal friction angle parameters to calculate the shear strength of the soil at the surface. However, the UGV was not equipped with any geotechnical instrumentation which could independently confirm these estimates. The RTC-I demonstrated the benefits of introducing a UGV into tailings operations, and motivated further development of unmanned platforms and instrumentation for monitoring mine waste impoundments.

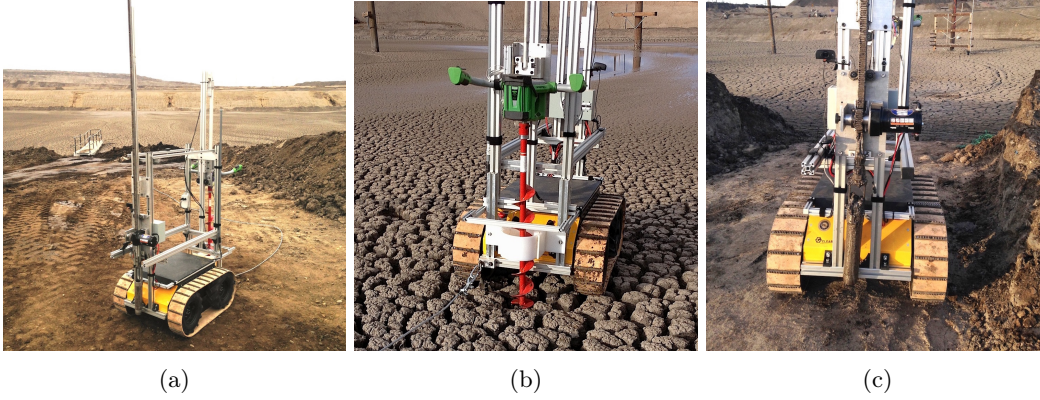


Figure 3.2: (a) Robotic system for tailings characterization. (b) RTC-I drilling through a soft crust. (c) RTC-I with sample collected from 1.7 m depth. Images from [33]

3.2.2 Vane Shear Testing and Tools

The vane shear test method has been extensively used for estimating the undrained shear strength of materials for various applications, including geotechnical investigations [31]. The industry standards for laboratory and field vane testing methods, ASTM D4648 [4] and ASTM D2573 [3], respectively, are widely used. Various addenda have been published to address the needs and constraints of specific applications, for instance vane shear testing in oil sands tailings [22].

The vane shear test tool comprises a section that is inserted into the medium, and a section that measures the torque during interaction between the instrument and the medium. A set of thin blades of height h and width $d/2$ meet at a central axis of rotation, as shown in Figure 3.3. Typically four blades are fixed at an angle of 90 degrees to each other. The vane is inserted into the test material and is then smoothly rotated to generate shear around the vane, using a prescribed turning speed whose value depends on whether the test is conducted in the laboratory or in the field [4, 3].

The vane geometry determines the relationship between the undrained shear stress on the soil C_u and the torque applied to the vane T_v as [9]

$$T_v = C_u \pi \left(\frac{hd^2}{2} + \frac{d^3}{6} \right) \quad (3.1)$$

The VST method can be used to estimate the peak, residual, and remolded shear strength of the soil [4]. The key assumptions of the test are: homogeneous and isotropic soil, negligible disturbance caused by vane insertion, no drainage during the test, no consolidation when inserting the vane or during the test, cylindrical, uniform, and fully mobilized shear surface at failure, and no progressive

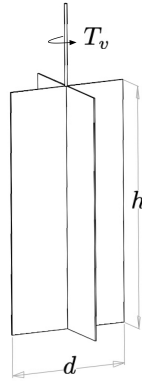


Figure 3.3: Vane diagram.

failure [9, 8, 36].

The relationships between the undrained shear stress at soil failure and vane geometries, as well as soil parameters such as moisture content and bulk density, have been studied in the context of agricultural tillage systems [18]. VST results have been compared with cone penetrometer devices, showing similar performance [6].

The VST has been used to investigate strain rate effects in soils. Motorized rheometers based on the vane shear have been developed for determining soil visco-plastic parameters [23]. The motorized vane tool was used to study the values of yield stress and viscosity of different soils with varying moisture content and soil compaction levels. The authors stated that the vane apparatus is the most widely used tool for in situ measurements of undrained shear strength due to its ease of use and convenience.

VST devices used in the field are typically manually operated and provide low-resolution measurements. A commercially available vane inspection kit (Figure 3.4a) can have a measurement range between 0 to 260 kPa using its four provided vane blade sizes. Vane rod sections approximately 0.5 m long are used to reach subsurface soils. The manufacturer of this vane kit estimates that the accuracy of the readings should be within 10% of the true value [21].

Manual field tests are prone to operator errors, such as applying a twisting motion while inserting the vane, or reading values incorrectly from the graduated ring. Systematic errors can be introduced by an incorrect speed of rotation. Typically, it is very difficult for a human operator to rotate the vane at a constant angular rate and at the prescribed (slow) speed of 6 degrees per minute, or to achieve good repeatability between tests. Vane operators in the field were observed to rotate the vanes between 10 to 100 times the prescribed rate. Generally, measurement of shear strength in the field is considered to be difficult, time-consuming, and costly [2].

Commercially available laboratory VST devices (Figure 3.4) can be manually operated (Figure 3.4b) or motorized (Figure 3.4c). Torque is applied to the vane through interchangeable torsional springs, and the resulting angular displacement is read off a graduated scale. The shear stress C_u is obtained from the vane geometry, spring constant value, and the indicated angular rotation. Depending on the nature of material being tested, vanes with different sizes and springs with different stiffness constants may need to be used.

To run an experiment with a manual device, the operator connects a vane to the end of the spring and places the blades into the tested material. The operator then rotates the handle to transmit a shearing load to the material through the spring and vane. This load is increased until the tested material fails and starts exhibiting slip. The maximum angular displacement shown on the device's dial is used to calculate the peak undrained shear stress before failure of the material. The accuracy of such instruments is estimated to range between 5 to 10 % [21]. The manual equipment is also subject to errors caused by the variable rotation speed used by the human operator. The measurement resolution of the equipment depends on both the vanes and springs selected, and is fundamentally limited by the resolution of the graduated angular displacement scale, typically marked with 1 degree increments.

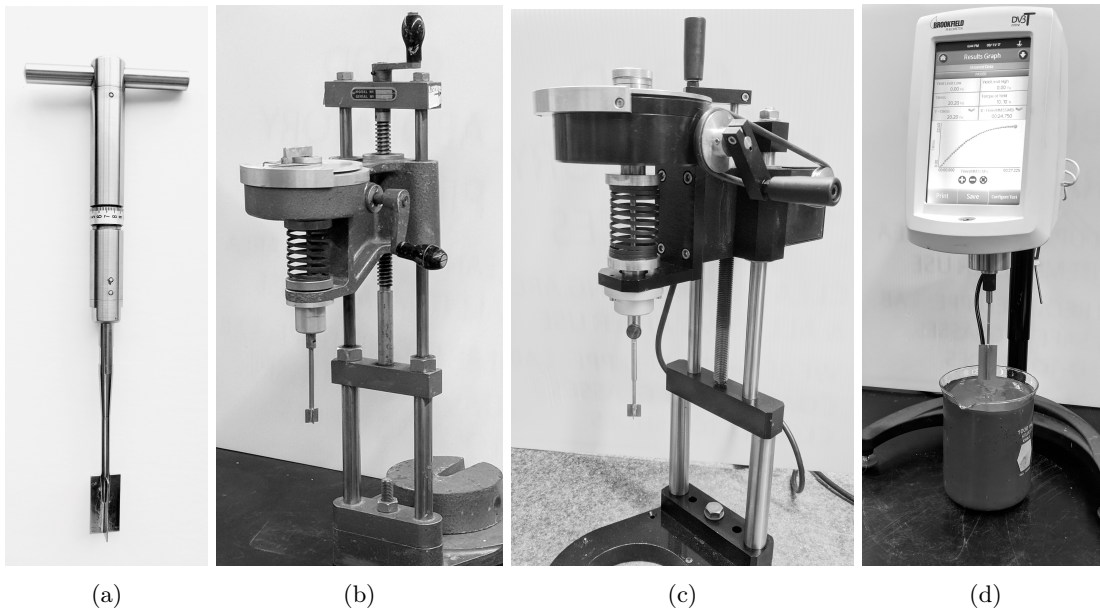


Figure 3.4: (a) Manually operated field VST device. (b) Manually operated laboratory VST device. (c) Motorized laboratory VST device. (d) Laboratory rheometer.

Digital rheometers, such as the Brookfield DV3THB shown in Figure 3.4d, have both higher ac-

curacy and better repeatability than manual devices. They employ stepper motors to control the rotation of the vane, and have a digital display indicating the shear stress being applied to the material. Unfortunately, such tools are expensive, not suitable for in-situ measurements, run on closed-source software, and only measure a subset of parameters at once. For instance, when testing for peak shear stress, the unit does not allow for residual and remolded strength tests to be conducted.

The limitations of commercially available manual VST devices and digital rheometers, as well as the need for unmanned monitoring in difficult environments, motivated our development of a custom automated vane shear test tool.

3.3 Design of an Automated Vane Shear Tool

The development of an Automated Vane Shear Tool (AVST) involves: i) the design of a torque transducer with resolution, precision and accuracy comparable to commercially available digital laboratory rheometers, ii) the design of the electro-mechanical, data acquisition, and software subsystems, and iii) system integration, prototyping and validation.

3.3.1 Design Criteria and Considerations

The resolution and accuracy of the torque transducer used in the VST determines the performance of the tool. Manual devices have a torque measurement resolution of 0.03 Nm and accuracy of 10% [21]. High-end laboratory rheometers, such as the Brookfield DV3THB, have resolutions of 0.006 Nm and accuracy of 1% of the full-scale range [10].

The present work aims to produce a VST device which matches the performance of high-end laboratory tools. During preliminary design, a torque load-cell approach was considered based on mounting strain gauges onto the shaft in a fully-balanced Wheatstone bridge shear configuration, which compensates for temperature changes and the Poisson effect. While this approach is considered appropriate for high load applications, for measurements with small vane shears on soft clays, the reaction torque will be very small. Also, the sensitivity of the transducer depends on the gauge factor of the strain gauges, the material properties of the shaft, and its geometry. Reducing the diameter, cross-sectional area, and the modulus of elasticity of the shaft material would result in higher sensitivity; however, measuring torque with a resolution of 10^{-4} Nm would require the use of highly deformable components, leading to a device which is very fragile, susceptible to creep and plastic deformation over repeated use and accidental impacts, and with a very limited operating

range. Typically, it is recommended to design these transducers so that the operating range is within ten percent of the yield stress in order to obtain an adequate signal to noise ratio.

For all the reasons mentioned above, typical laboratory rheometers use calibrated springs, rather than load cells, to measure torque. The performance of spring torque transducers is limited by the accuracy of the spring constant and the measurement of the effective angular displacement of the spring. The main design differences between high-end digital rheometers and manual laboratory equipment are electronic readings of angular displacement and the use of well-calibrated springs.

3.3.2 Description of Apparatus

An AVST prototype was built as shown in Figure 3.5. The system consists of a geared DC motor, gearbox, optical encoders, torsional spring, and output shaft. The components are mounted onto an aluminum frame. A DC motor was chosen to enable continuous rotation of the vane, and to allow precise control of the rotational speed. Alternative actuators, such as geared stepper motors, could also have been used. The gearbox allows reconfiguring the system to accommodate different motors and loading requirements. The output shaft is connected to standard vanes using shaft couplers. The output shaft is supported with a double ball-bearing assembly and is stepped in order to transmit any vertical loads to the bearings.

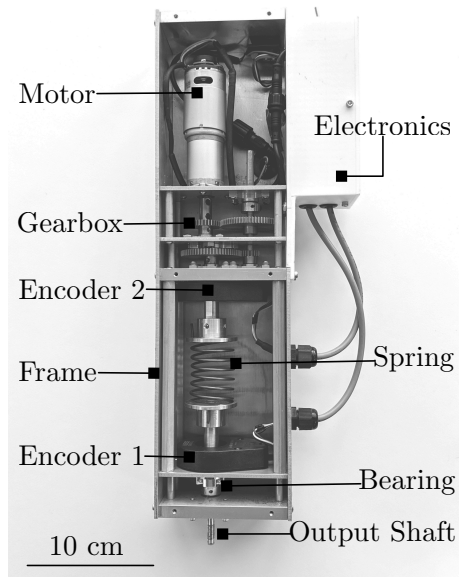


Figure 3.5: Main components of proposed AVST design.

The spring is made from 316 stainless steel round wire with a diameter of 2.3mm. The length and diameter of the spring are 60 mm and 38 mm respectively. The coils are separated to avoid contact and friction as the spring is rotated. The spring provides a restoring torque linearly proportional to the angular displacement between the top and bottom of the spring. It has an identified spring constant of 0.3904 Nm/rad (Section 3.3.3). The recommended maximum angular displacement between the top and bottom of the spring is one-quarter of a revolution.

Two optical quadrature encoders are used to measure the angular displacement of the top and bottom of the spring. The encoders have 40,000 counts per revolution, corresponding to an angular resolution of 0.009 deg. This translates to a torque measurement resolution of 6×10^{-5} Nm.

A system diagram of the AVST is shown in Figure 3.6. A Micro-controller Unit (MCU) is used to interface with a motor driver and the encoders. The MCU sends voltage commands to the motor driver to control the speed of the motor. The MCU counts the pulses generated by the optical encoders to determine the angular positions of the top and bottom of the springs. The pulses can also be used to estimate the speed of rotation obtained from numerical differentiation and moving average filter, despite the low sample rate (10Hz), the results are satisfactory because of the slow movements. In typical laboratory equipment, only the speed of rotation of the top of the spring is measured and controlled. In our proposed design, the rotational speed of the vane (fixed to the output shaft) can be controlled. All measurements from the system are sampled at 10 Hz.

A computer running a custom GUI is used to send commands, program tests, and log measurements. The computer communicates with the AVST's MCU wirelessly over a 900 MHz wireless connection; alternatively, the MCU can be connected to the computer through a USB cable.

The components of the system have an approximate total cost of USD 1500, excluding the computer, with the majority of costs being due to machining parts.

3.3.3 Equipment Calibration

The torsion spring constant k_s was estimated by linear regression between torque applied to the output shaft $T_s(t)$ and the resulting net angular displacement of the spring $\theta(t)$:

$$T_s(t) = k_s \theta(t) \tag{3.2}$$

The net angular displacement of the spring $\theta(t)$ was determined from the encoder measurements $\theta_2(t)$ and $\theta_1(t)$ as

$$\theta(t) = \theta_2(t) - \theta_1(t) \tag{3.3}$$

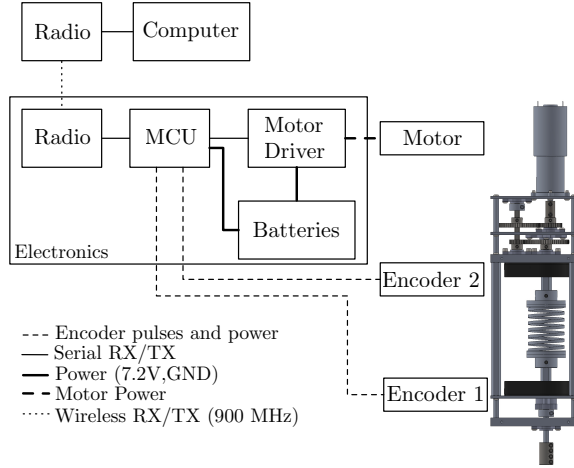


Figure 3.6: AVST system diagram

A known torque was applied to the output shaft by hanging a mass of 0.49957 kg from a symmetrical bar as shown in Figure 3.7. The equipment was placed on its side with the spring unloaded; the bar was attached vertically; and then the mass was hung from one of end of the bar. The calibration dataset was generated by applying a small voltage to the motor, yielding a new equilibrium of the system at a non-zero output shaft angle $\theta_1(t)$.

The resulting torque applied to the spring $T_s(t)$ was calculated from the mass value m , the half-length of the bar l , gravity g , and the angle of the bar to the vertical $\theta_1(t)$:

$$T_s(t) = mlg \sin \theta_1(t) \quad (3.4)$$

Ten calibration datasets were obtained. A sample dataset is shown in Figure 3.8. The points were fitted to the linear model $y_i = \alpha x_i + \beta + \varepsilon_i$ assuming that errors ε_i were statistically independent and identically distributed. The R^2 value of the regression was calculated to be 0.9999. The resulting model parameters and fit errors are presented in Table 3.1, demonstrating that (3.2) with $k_s = 0.39401$ Nm/rad is a valid model. Assuming the maximum net angular displacement of the spring is one-quarter turn, the maximum transmitted torque will be 0.619 Nm.

Table 3.1: Torsion spring calibration results

	α	β	95%CI
k_s [Nm/rad]	0.39401	$3. \times 10^{-5}$	(0.39396, 0.394063)

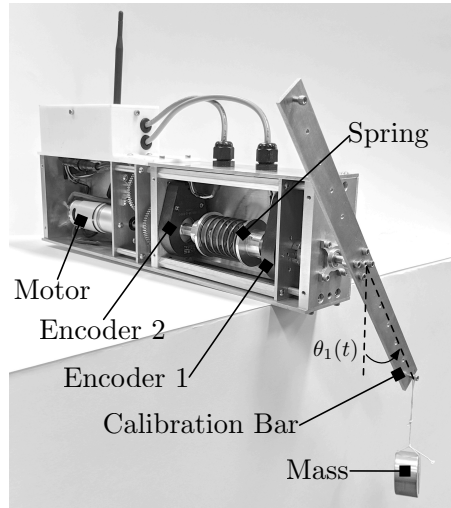


Figure 3.7: AVST calibration setup.

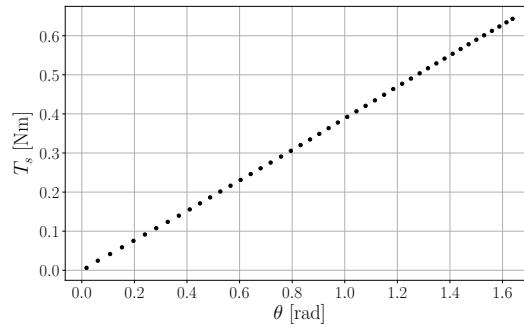


Figure 3.8: Torsion spring calibration. Only one of every seventy-five points used for the calibration are shown.

3.3.4 Equipment Error Analysis

Bearing rolling resistance, misalignment between shafts connected to the top and bottom of the spring, and eccentricity of the spring all contribute to errors in torque measurements. A constant friction torque is expected to be observed due to low speed rolling resistance at the bearings. An oscillating friction torque is also expected to be observed, generated by shaft misalignment and spring eccentricity, which produce loading varying with the angle of the spring.

Even very small-magnitude friction torques can be measured thanks to the high-resolution optical encoders used in our AVST design. To collect these measurements, the output shaft was rotated

at two constant speeds: 60 deg/min and 600 deg/min without any load, then 60 deg/min with a lateral force of 5 N on the output shaft and a load torque of 0.4 N m, both generated by hanging a mass on a pulley attached to the output shaft. Figure 3.9 presents the measured friction torque as a function of the angular position of the output shaft for the three test conditions. This demonstrates that the friction torque does not significantly depend on speed or loading of the output shaft. The peak-to-peak amplitude is approximately 0.003 Nm in all three cases, which corresponds to less than 0.5% of the full-scale reading of the instrument. For the third case, an increase in torque was observed after approximately 800 degrees of rotation. This was caused by the winding around the pulley of the string attached to the hanging mass, increasing the moment arm.

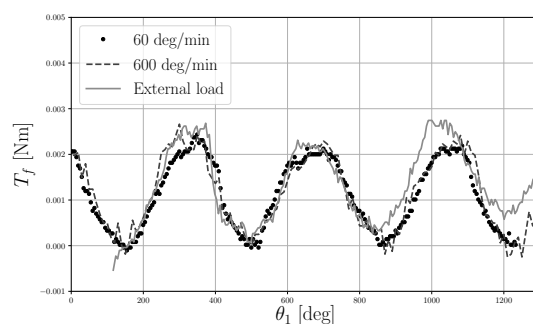


Figure 3.9: Observed friction torque under different test conditions.

In traditional VST devices, the torque applied to the vane, T_v , is assumed exactly equal to the torque measured through the spring, T_s . As seen in Figure 3.9, the system is subject to non-negligible friction torque, which invalidates this assumption. From equation (3.1),

$$C_u = T_v/K_v = (T_s - T_f)/K_v \quad (3.5)$$

where C_u is the undrained shear stress acting on the tested material, T_f is the friction torque and K_v is the vane constant

$$K_v = \frac{\pi d^2 (3h + d)}{6} \quad (3.6)$$

The error in C_u due to T_f can be expressed as

$$C_{ue} = T_f/K_v = \frac{6T_f}{\pi d^2 (3h + d)} \quad (3.7)$$

While the magnitude of T_f can be relatively small — for instance 0.003 Nm peak-to-peak amplitude in the preceding test — note the error C_{ue} is also proportional to $1/K_v$, which can have a very

large magnitude for smaller-sized vanes. The increased errors obtained when using small vanes is highlighted in Figure 3.10, showing the expected error for different vane sizes under a constant friction torque T_f of 0.003 Nm.

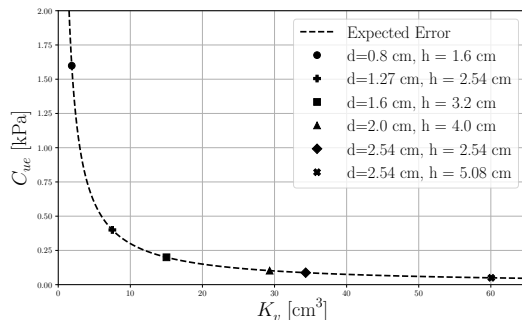


Figure 3.10: Parameter error C_{ue} versus vane constant K_v under a friction torque $T_f = 0.003$ Nm

For large vane sizes, such as those used for field investigations, the errors are negligible (less than 50 Pa). For smaller vane sizes, as used on laboratory equipment, the errors can be significant and reach up to 1 kPa for the smallest vane sizes. Our proposed AVST design is well suited for characterizing substances held in relatively small containers, which limits the vane size which can be used [29]. In these cases, the errors created by friction torques become significant, which motivates the development of a friction compensation strategy.

It is important to note that other sources of error can affect vane shear measurements, for instance the bending of the vane connection rod and contact friction between the rod and the medium. Strategies to mitigate these effects are discussed in [3]. For instance using enclosed and stiff rods has been recommended in order to reduce these errors.

3.3.5 Friction Compensation

In order to increase the accuracy of parameter estimation, we developed a process to estimate the error in the calculated shear stress C_u caused by friction torque within the AVST, then to compensate for it. This error is modeled as a trigonometric function of the output shaft angle θ_1 , whose parameters are estimated from measurements collected by running an unloaded vane. Additionally, we can improve the repeatability of our apparatus by starting each test with the output shaft at approximately the same rotation angle. The details of our process are given below:

1. Collect a set of measured shear stresses $\{C_{ui}\}$ as the unloaded vane is rotated over at least two full revolutions at a constant speed of 60 deg/min.

2. Use the resulting dataset to estimate the parameters of a trigonometric function modeling the relationship between the position of the output shaft θ_1 and C_{ui} , using a non-linear least squares curve fitting method such as Levenberg—Marquardt.
3. Identify the angular position of the output shaft θ_1 with the lowest C_{ui} . This position is to be used as the starting configuration in further experiments.
4. Prior to testing a sample, place the output shaft at the designated starting angular position and zero the encoder counts.
5. Employ the identified error model to correct the measured shear stresses C_u .

A sample friction compensation dataset is shown in Figure 3.11. The fitted curve was produced by finding the parameters β_1 , β_2 and β_3 in the candidate function

$$C_{ui} = \beta_1 \sin(\theta_{1i} + \beta_2) + \beta_3 \quad (3.8)$$

where C_{ui} is the measured shear stress and θ_{1i} is the angular position of the output shaft. The parameters β_1 , β_2 , β_3 can be interpreted as the amplitude, phase, and mean of the trigonometric function (3.8).

The corrected shear stress C_{ci} , can be obtained by subtracting the fitted function from the measured shear stress C_{ui} :

$$C_{ci} = C_{ui} - (\beta_1 \sin(\theta_{1i} + \beta_2) + \beta_3) \quad (3.9)$$

A plot of the distribution of residuals is presented in Figure 3.12. Over 95% of the residuals have a magnitude of less than 0.015 Nm, which is over six times smaller than the amplitude of the fitted function.

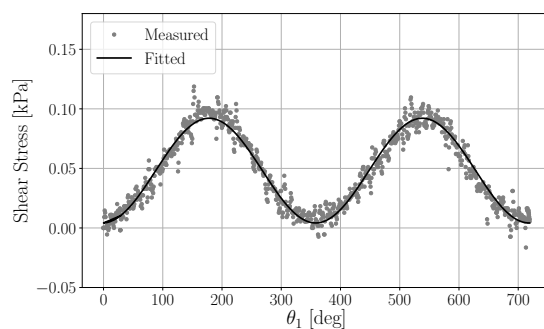


Figure 3.11: Example of a friction compensation dataset and fitted cyclic function.

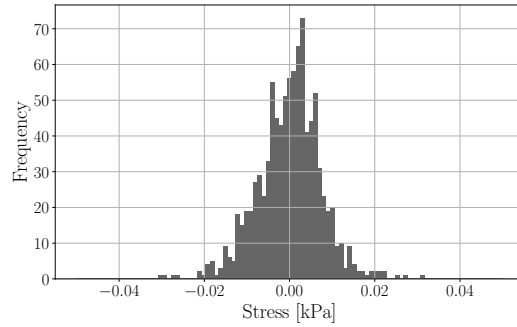


Figure 3.12: Example of distribution of residuals.

A comparison between the measured and compensated shear stress is shown in Figure 3.13. This data set was collected using a vane with a diameter of 1.6 cm and a height of 3.2 cm on a sample of centrifuged oil sands tailings.

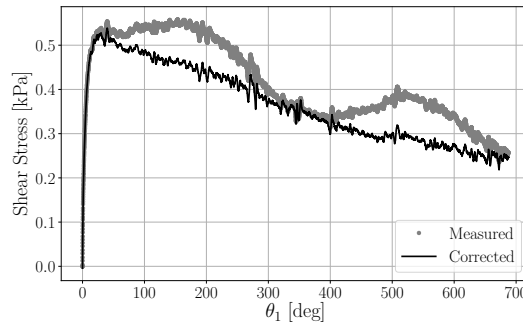


Figure 3.13: Comparison between measured and corrected shear stresses during a test.

3.4 Laboratory Equipment Validation

Our AVST apparatus was validated against a Brookfield DV3THB rheometer. The tests were conducted with materials encountered in geotechnical investigations of oil sands tailings. Specifically, the tailings materials resulting from five different treatment options were used as test samples: MFT, flocculated MFT with concentrations of 650ppm and 850ppm, centrifuged tailings, and aged MFT.

The peak shear stress C_p , representing the shear strength of the material, is reported for both

instruments over five trials on each material in Table 3.2, where μ_{C_p} is the mean shear strength and σ_{C_p} is the standard error. The results are also presented in Figure 3.14. Each test was conducted according to the ASTM D2573 standard [3], using a vane rotation speed of 60 degrees / min, and using the same vane for both units. The materials were tested in containers which had been left to settle for several months. The vane was inserted at least two vane heights deep and at least one diameter from the edges of the container.

The mean of the shear strengths measured with our AVST design are within one standard error of the measurements obtained with the Brookfield rheometer. An illustration of the repeatability of the measurements is presented in Figure 3.15. The favourable results of precision and accuracy demonstrate that our design can be used in place of standard laboratory rheometers without sacrificing the quality of results.

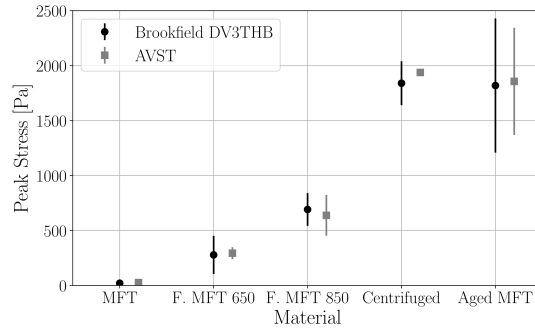


Figure 3.14: Peak stress comparison between AVST and Brookfield DV3THB rheometer. The bars represent the 95% confidence intervals of the tests.

Table 3.2: Instrument evaluations: Comparison of AVST and Brookfield DV3THB rheometer on five treated tailings.

	Brookfield DV3THB			AVST		
	μ_{C_p} [Pa]	σ_{C_p} [Pa]	95%CI [Pa]	μ_{C_p} [Pa]	σ_{C_p} [Pa]	95%CI [Pa]
MFT	20.7	2.6	(15.5,26.0)	26.4	0.3	(25.9,27.0)
F. MFT 650	278.2	86.8	(104.7,451.8)	294.1	27.1	(239.8,348.4)
F. MFT 850	691.4	74.5	(542.4,840.4)	638.3	92.9	(452.6,824.0)
Centrifuged	1840.0	99.9	(1640.6,2039.8)	1937.8	2.4	(1933.0,1942.5)
Aged MFT	1819.0	305.1	(1208.9,2429.1)	1856.7	243.7	(1369.3,2344.1)

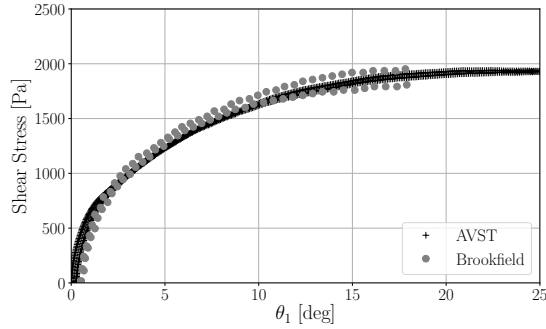


Figure 3.15: Example of shear stress determination for centrifuged tailings using our AVST and a Brookfield DV3THB rheometer. The Brookfield rheometer automatically stops the test once it determines the peak shear stress has been reached.

3.5 Example Laboratory Applications

A key constraint imposed by the ASTM standard for field vane shear testing is the speed of rotation of the vane: a speed of 6 deg/min is recommended. For some materials, such as centrifuged tailings, this leads to a single vane shear test taking between 1 to 5 hours to complete, depending on whether the peak, residual, and remolded strengths are required. For laboratory vane shear testing, the speed of rotation is recommended to be 60 deg/min, ten times faster than in field testing. In this case the tests can take minutes rather than hours. In order to maximize the number of measurements that a robot carrying an AVST can conduct without needing to recharge, we will evaluate the effect of rotation speed on the precision and accuracy of the measurements.

The peak shear stress C_p of centrifuged tailings samples was tested using three rotation rates: 6, 60, and 600 deg/min, corresponding to ASTM D2573, ASTM D4648, and the rate for manual tests. The equipment was lowered manually using a linear guide into a large container that had been left to settle for several months. The vane was inserted at least two vane heights deep and at least one vane diameter from the container edges, as shown in Figure 3.16. The tests were each run four times at 6, 60, and 600 deg/min, as shown in Figure 3.17. The differences observed between 6 and 60 deg/min are significantly lower than the differences between these speeds and 600 deg/min, as shown quantitatively in Table 3.3. The results suggest that a 60 degrees/min vane speed can be used to reduce the time required to conduct a field test without losing accuracy. The tests at 6 and 60 deg/min agree within two standard errors (95% confidence interval). Meanwhile the 600 deg/min results do not agree with the results at the lower speeds. This shows that an operator who conducts a vane test with a handheld instrument quickly, on the order of 600 deg/min, can overestimate the strength of the material being tested, which may lead to reduced safety factors for

the design of impoundments and reclamation activities.

Table 3.3: Comparison of peak shear stress obtained with varying vane speeds.

Speed [deg/min]	μ_{C_p} [Pa]	σ_{C_p} [Pa]	95%CI [Pa]
6	517.5	17.2	(483.2,551.9)
60	542.1	31.9	(478.3,605.9)
600	955.3	50.8	(853.7,1056.8)

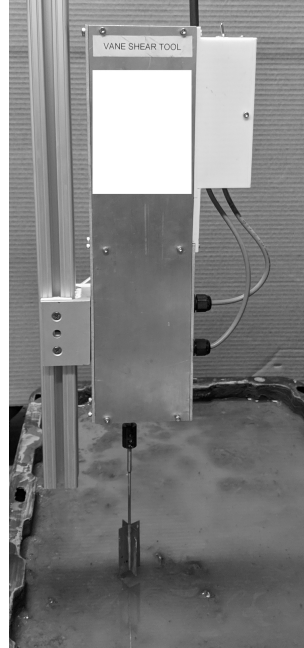


Figure 3.16: AVST laboratory experiments on treated oil sands tailings. The equipment was manually lowered into a container filled with tailings. A linear guide was used to support and lock the equipment in place.

Our AVST apparatus is currently being used in tailings consolidation experiments. It has also been used in the formal comparison of shear strengths of different foods and soft oil sands tailings [29].

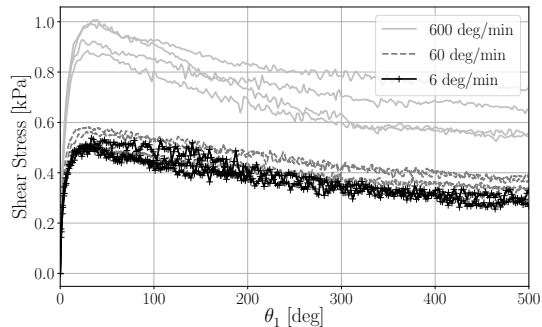


Figure 3.17: Comparison of shear stress measured at varying vane speeds.

3.6 Integration of AVST onto Unmanned Ground Vehicles

Our prototype AVST has been integrated onto field robotic systems as a self-contained payload. A Husky A200 platform was customized with a mechanism to deploy the AVST, as shown in Figure 3.18. A rigid aluminum frame was built to support payloads above the UGV. The AVST was attached to a linear guide on linear bearings and was moved vertically by a linear actuator with a stroke length of 30 cm, allowing the UGV to conduct shear strength tests close to the surface of the terrain. The UGV’s on-board computer running the Linux-based Robot Operating System [35] was used to interface with the tool and to log measurements.

A measurement campaign using an instrumented UGV will generally follow the following steps and guidelines:

1. An operator determines the area that needs to be surveyed, and defines GPS fencing. Additionally, the operator sets the grid spacing for the vane shear measurements to be conducted, as well as general test specifications, such as depth of vane insertions. In the future, an intelligent UGV may be able to determine the boundaries of the areas autonomously and adjust the grid spacing to optimize surveying time.
2. The UGV navigates to the test locations via way-point navigation, while avoiding obstacles.
3. Once the UGV has arrived at a specified test location, it runs payload-specific system checks and preparations before the test. For the AVST, the friction compensation data set can be collected at this point.
4. The UGV deploys the tool. The AVST can be deployed using a rotating actuator driving a rack and pinion mechanism as seen in [33] to deploy tools below the surface; or the payload can be lowered with linear actuators guided by rails.

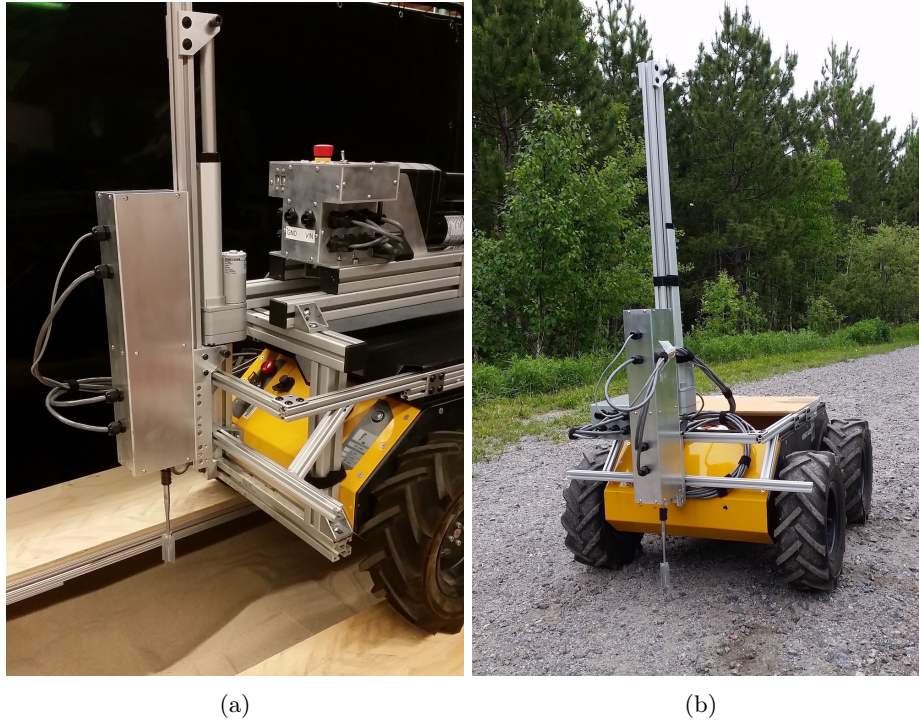


Figure 3.18: (a) AVST mounted on a Husky A200. (b) Instrumented UGV on outdoor trials.

5. The UGV runs automated tests using its instruments. For the AVST, an automated test is programmed to follow ASTM D2573, and can be modified depending on the application, such as increasing the vane speed to 60 deg/min. The peak, residual, and remoulded strengths are measured and recorded, along with other relevant information such as location, date, and time.
6. The UGV transmits the results of the test to a ground station, making the information immediately available to the robot operators and other personnel on site.
7. Once the test is completed and the results transmitted and logged, the UGV moves to the next test location and repeats the procedure.
8. Throughout the operation, the UGV is monitoring system status and health. The UGV may be required to return to the base station to recharge or swap in new batteries.

Proof-of-concept experiments were conducted on clayey soil. Examples of the data collected are presented in Figure 3.19. The robot operated on terrain with sufficient bearing capacity to support its weight. Future work is planned for integrating the tool onboard robots which are capable of

moving on very soft terrains and water-capped materials. Additionally, the current setup requires an operator to switch vanes; a mechanism to switch vanes automatically, depending of the soil strength, has been conceptualized but not yet prototyped.

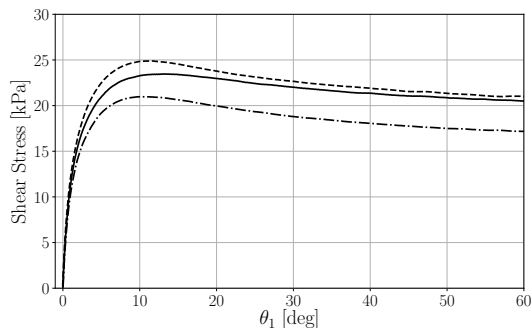


Figure 3.19: Field measurements example. The data was obtained in clayey soil at three different locations.

3.7 Conclusion

Unmanned systems can deploy tools in terrains which are not accessible to human workers. Automated tools can reduce human error and variability. An automated vane shear test (AVST) tool was developed for laboratory and field material characterization applications. The AVST's design criteria, considerations, and build details were described. The requirements of an accurate and precise torque transducer were highlighted, which were met by using a calibrated torsion spring and optical encoders. Sources of error were discussed, and a procedure to correct for friction torques caused by resistance of the bearings and component misalignment was presented.

The equipment was validated against a commercially available high-end instrument, with very favourable results. The AVST was first tested in a laboratory setting to determine the effect of the vane speed. It was determined that on centrifuged oil sands tailings there is no significant difference between rotation speeds of 6 and 60 deg/min, whereas there is a large difference with speeds of 600 deg/min.

The proposed vane tool was also mounted and integrated onto a UGV and tested in outdoor field conditions. Currently the UGV is limited to move on terrain with bearing capacity of 20 kPa or higher. Future work will focus on mounting the AVST on novel platforms which can traverse very soft terrain, as well as making the instrument more rugged and self-contained by packaging it for field use.

Acknowledgements

The authors would like to thank the Natural Sciences and Engineering Research Council of Canada (NSERC), Canada's Oil Sands Innovation Alliance (COSIA) and Alberta Innovates — Clean Energy for their financial support.

3.8 References

- [1] Erik W Allen. Process water treatment in Canada's oil sands industry: I. Target pollutants and treatment objectives. *Journal of Environmental Engineering and Science*, 7(2):123–138, March 2008.
- [2] Elham Amiri Khaboushan, Hojat Emami, Mohammad Reza Mosaddeghi, and Ali Rrza As-taraei. Estimation of unsaturated shear strength parameters using easily-available soil properties. *Soil and Tillage Research*, 184:118–127, December 2018.
- [3] ASTM International. ASTM D2573/D2573M-15 Standard Test Method for Field Vane Shear Test in Saturated Fine-Grained Soils. ASTM International, September 2015.
- [4] ASTM International. D4648/D4648M - 16 Standard Test Method for Laboratory Miniature Vane Shear Test for Saturated Fine-Grained Soils. ASTM International, 2016.
- [5] ASTM International. ASTM D5778-12: Standard Test Method for Electronic Friction Cone and Piezocone Penetration Testing of Soils. ASTM International, 2019.
- [6] J Bachmann, K Contreras, K H Hartge, and R MacDonald. Comparison of soil strength data obtained in situ with penetrometer and with vane shear test. *Soil and Tillage Research*, 87(1):112–118, May 2006.
- [7] Nicholas Beier, Ward Wilson, Adedeji Dunmola, and David Segó. Impact of flocculation-based dewatering on the shear strength of oil sands fine tailings. *Canadian Geotechnical Journal*, 50(9):1001–1007, 2013.
- [8] Geoffrey Blight. *Geotechnical Engineering for Mine Waste Storage Facilities*. CRC Press, November 2009.
- [9] Jean-Louis Briaud. *Geotechnical Engineering. Unsaturated and Saturated Soils*. John Wiley & Sons, October 2013.
- [10] Brookfield Engineering Labs., Inc. *More Solutions to Sticky Problems*, May 2014.

- [11] S Coetzee, H Swart, P Bosscha, and D Oosthuizen. *Design of an industrial all-terrain robot platform lessons learned in the design of a robotic mine safety platform for South African gold mines*. IEEE, 2012.
- [12] D E Daniel. *Geotechnical Practice for Waste Disposal*. Springer US, 1 edition, 1993.
- [13] Maurice B Dusseault and J Don Scott. Tailings Pond Behavior and Characterization of Oil Sand Tailings Sludge. *Particulate Science and Technology*, 1(3):295–309, 1983.
- [14] Daniel M Franks, David V Boger, Claire M Côte, and David R Mulligan. Sustainable development principles for the disposal of mining and mineral processing wastes. *Resources Policy*, 36(2):114–122, June 2011.
- [15] Gustavo Freitas, Fernando Lizarralde, Liu Hsu, Vitor Paranhos, Ney R. Salvi dos Reis, and Marcel Bergerman. Design, modeling, and control of a wheel-legged locomotion system for the environmental hybrid robot. In *Proceedings of the IASTED International Conference*, number CMU-RI-TR-, November 2011.
- [16] Fine Tailings Fundamentals Consortium FTFC. Advances in oil sands tailings research. In *Alberta Department of Energy*, pages 6–7–79–80, Edmonton, 1995.
- [17] Jeremy Green. Underground mining robot: A CSIR project. *SSRR*, pages 1–6, 2012.
- [18] Changbin He, Yong You, Decheng Wang, and Hongjian Wu. Estimating soil failure due to torsion via vane shear test by varying vane diameter and soil properties. *Soil and Tillage Research*, 177:68–78, April 2018.
- [19] Larry A Holm. Strategies for remediation. In *Geotechnical Practice for Waste Disposal*, pages 289–310. Springer US, Boston, MA, 1993.
- [20] S Huh, U Lee, H Shim, J B Park, and J H Noh. Development of an unmanned coal mining robot and a tele-operation system. pages 31–35, 2011.
- [21] Humboldt. Field vane shear set. <https://www.humboldtmg.com/vane-inspection-set.html>, 03 2019.
- [22] Heather Kaminsky. Measuring Strength in Oil Sands Tailings Deposit. In *International Oil Sands Tailings Conference*, pages 185–194, Lake Louise Alberta, December 2014.
- [23] S Karmakar and R L Kushwaha. Development and laboratory evaluation of a rheometer for soil visco-plastic parameters. *Journal of Terramechanics*, 44(2):197–204, April 2007.
- [24] D Kossoff, W E Dubbin, M Alfredsson, S J Edwards, M G Macklin, and K A Hudson-Edwards. Mine tailings dams: Characteristics, failure, environmental impacts, and remediation. *Applied Geochemistry*, 51:229–245, December 2014.

- [25] Erika Levei, Tiberiu Frentiu, Michaela Ponta, Claudiu Tanaselia, and Gheorghe Borodi. Characterization and assessment of potential environmental risk of tailings stored in seven impoundments in the Aries river basin, Western Romania. *Chemistry Central journal*, 7(1):5, 2013.
- [26] M.G. Lipsett and S.C. Dwyer. A robotic system to characterize soft tailings deposits. In *Proceedings of Mine and Tailings Waste Conference 2009, Banff Alberta*, November 2009.
- [27] Michael G Lipsett, Nicolas Olmedo, Benoit Rivard, and Ward Wilson. Robotic Systems for Measuring Properties of Tailings Deposits and Collecting Samples. In *Proceedings of the Fourth International Oil Sands Tailings Conference*, Lake Louise, AB, December 2014.
- [28] Jacob Masliyah, Zhiang Joe Zhou, Zhenghe Xu, Jan Czarnecki, and Hassan Hamza. Understanding Water-Based Bitumen Extraction from Athabasca Oil Sands. *The Canadian Journal of Chemical Engineering*, 82(4):628–654, August 2004.
- [29] G. McKenna, V. Mann, B. Fisseha, N. Beier, and N. Olmedo. This tailings has the consistency of chocolate pudding: A formal comparison of the geotechnical vane shear strength of food and soft tailings. *Geotechnical News*, 35(1):28–34, 2017.
- [30] N R Morgenstern and J D Scott. Geotechnics of fine tailings management. *Geoenvironment*, pages 1663–1673, 1995.
- [31] Tatsuro Muro and Jonathan OBrien. *Terramechanics Land Locomotion Mechanics*. A.A. Balkema Publishers, Lisse, 2004.
- [32] A Nuchter, H Surmann, and K Lingemann. 6D SLAM with an application in autonomous mine mapping. . . . *ICRA '04 2004 IEEE . . .*, pages 1998–2003 Vol.2, 2004.
- [33] Nicolas A Olmedo and Michael G Lipsett. Design and field experimentation of a robotic system for tailings characterization. *Journal of Unmanned Vehicle Systems*, pages juvs–2015–0034, March 2016.
- [34] Geoffrey S Plumlee, Kathleen S Smith, and Walter H Ficklin. *Geoenvironmental Models of Mineral Deposits, and Geology-based Mineral-environmental Assessments of Public Lands*. Number Open-File Report 94-203. U.S. Geological Survey, 1994.
- [35] Morgan Quigley, Ken Conley, Brian P. Gerkey, Josh Faust, Tully Foote, Jeremy Leibs, Rob Wheeler, and Andrew Y. Ng. Ros: an open-source robot operating system. In *ICRA Workshop on Open Source Software*, 2009.
- [36] Adrian F Richards. *Vane Shear Strength Testing in Soils*. Field and Laboratory Studies. ASTM International, 1988.

- [37] W Wang, W Dong, Y Su, D Wu, and Z Du. Development of Search-and-rescue Robots for Underground Coal Mine Applications. *Journal of Field Robotics*, 31(3):386–407, 2014.
- [38] Barry A Wills and James A Finch. Tailings Disposal. In *Wills' Mineral Processing Technology*, pages 439–448. Elsevier, 2016.
- [39] J Y Wong. Chapter 3 - Measurement of Terrain Properties. In J Y Wong, editor, *Terramechanics and Off-Road Vehicle Engineering (Second Edition)*, pages 65–74. Butterworth-Heinemann, Oxford, 2010.

Chapter 4

Experimental Determination of the Inertial Properties Of Small Robotic Systems Using a Torsion Platform

Abstract

The present work describes the development and operation of a novel instrumented torsion platform used to estimate the inertia tensor of small objects with complex geometries, such as mobile robots. Our proposed methodology is capable of estimating the moments and products of inertia plus the center of mass location of the rigid body being measured. The design of the platform is described, along with the equipment calibration procedure and results. Uncertainties are enumerated and quantified. The method is successfully validated in both simulation and experiment. Two case studies illustrate the utility of the system: determining the inertia tensor of a CNC-machined aluminum block and validating against its CAD model, and estimating the inertia properties of a small off-the-shelf quadrotor unmanned aerial vehicle.

4.1 Introduction

Accurate estimates of the inertial properties of components in mechanical systems (mass, centre of mass, mass moments of inertia, and products of inertia) are required to determine whether a mechanical component meets specifications, and to understand the performance of mechanical systems, in design, operation, and control.

For objects with complex geometries such as small ground, aerial, underwater, and space robots, the analytical calculation of the inertial properties is very challenging. While Computer Aided Design (CAD) models provide estimates by direct calculation from the geometry and material density of pieces and assemblies, it is not always practically feasible to model in CAD all of the components in a system that has already been built [35], especially if there are small variations due to manufacturing tolerances and material variability. In some systems, small variations may result in significant changes in dynamic characteristics [18]. Typically, CAD model properties are experimentally verified [4]. In most cases, experimental determination of inertial properties is the best approach to obtain reliable estimates.

The objective of our work is to present the design of a reproducible apparatus and experimental method for its use in the determination of the inertial properties of mechanical systems with complex geometries, such as small mobile robots. The measurement of the inertia tensor and centre of mass is required for the design and analysis of robotic components [10]. These parameters are also needed in model-based control, specifically in nonlinear control strategies, as well as to accurately simulate the resulting designs. An example from aerospace is the requirement for an accurate estimate of the inertia tensor of a small cubic satellite (cubesat) to ensure that it conforms to design specifications prior to launch.

In classical test engineering applications, such as the evaluation of large road vehicle dynamics, handling, stability, and safety, inertia parameter errors and tolerances have been reported as relatively large, with a 3% error and tolerance of $\pm 15 \text{ kg m}^2$ in some components [18]. Some investigations report smaller relative errors, 0.7% - 1.2% that still correspond to large absolute errors, 3.5-19.9 kg m^2 [34]. Specialized test beds for vehicle inertia identification [35] are very expensive and unsuitable for studying smaller objects, such as cubesats, UAVs or small wheeled robots. Such systems have inertial properties with magnitudes on the order of 0.1 kg m^2 with some components with inertias in the order of magnitude of $1 \times 10^{-3} \text{ kg m}^2$. For these reasons, new approaches are required to estimate the inertial properties of such systems with sufficient precision and accuracy.

The proposed test method consists of a series of experimental procedures to determine the inertia tensor of an object and the position of its centre of mass. It is well known that the period of oscillation of a rigid body is a function of its inertia matrix. Our apparatus consists of a torsional platform used to measure the oscillatory motion of the tested object. The object is oscillated in different fixed positions and orientations on the mounting platform, with a total of nine experiments required to estimate the six unique components of the inertia tensor and the three components of the position of the centre of mass.

The precision of the results is estimated from the measurements and equipment calibration errors. The proposed apparatus and experimental method are shown to obtain estimates of inertial prop-

erties with tolerances of at least 1×10^{-4} kg m². Additional advantages of the approach are the simplicity of the test method and the low cost of the equipment required.

The remainder of this paper is organized into seven main sections. Related work and limitations of current approaches are discussed in Section 2. Section 3 presents the general method formulation, experimental methodology, and method verification. Section 4 gives a detailed description of the torsion platform, including design details, device calibration, uncertainty estimation, and initial experimental validation of single-axis inertia estimation. Section 5 presents validation experiments of estimating the inertial properties of a calibration piece. Estimating the inertial properties of a commercially available Unmanned Aerial Vehicle (UAV) is discussed in Section 6. Finally, recommendations are provided and future work is identified in Section 7.

4.2 Background

While the mass and centre of mass location of a rigid body can be determined by static tests, the mass moment of inertia tensor (inertia) can only be measured through dynamic testing [9]. The general approach is to study the dynamic response of the system to initial conditions and/or forcing input to determine its inertial properties.

An arbitrary rigid body rotating about a rotation axis passing through O has inertia properties that can be described by the tensor \mathbf{I}_O expressed in a body-fixed reference frame with its origin at O (Figure 4.1). \mathbf{I}_O is described by:

$$\mathbf{I}_O = \begin{pmatrix} I_{Oxx} & I_{Oxy} & I_{Oxz} \\ I_{Oxy} & I_{Oyy} & I_{Oyz} \\ I_{Oxz} & I_{Oyz} & I_{Ozz} \end{pmatrix} \quad (4.1)$$

The dynamics of the angular velocity vector $\boldsymbol{\omega}(t) = (\omega_x(t), \omega_y(t), \omega_z(t))^T$ of the rigid body expressed in coordinates of its body-fixed frame are governed by the Newton-Euler equation

$$\boldsymbol{\tau} = \mathbf{I}_O \cdot \dot{\boldsymbol{\omega}}(t) + \boldsymbol{\omega}(t) \times (\mathbf{I}_O \cdot \boldsymbol{\omega}(t)) \quad (4.2)$$

where $\boldsymbol{\tau}$ is the net torque vector acting on the body about O , expressed in coordinates of its body-fixed frame.

When the rotation is constrained to the vertical axis \mathbf{z}_O , Figure 4.1, such that the angular velocity vector is expressed as

$$\boldsymbol{\omega}(t) = (0, 0, \dot{\theta}(t))^T \quad (4.3)$$

the equations of motion reduce to:

$$\begin{pmatrix} \tau_x \\ \tau_y \\ \tau_z \end{pmatrix} = \begin{pmatrix} I_{Oxz}\ddot{\theta}(t) - I_{Oyz}\dot{\theta}(t)^2 \\ I_{Oxz}\dot{\theta}(t)^2 + I_{Oyz}\ddot{\theta}(t) \\ I_{Ozz}\ddot{\theta}(t) \end{pmatrix} \quad (4.4)$$

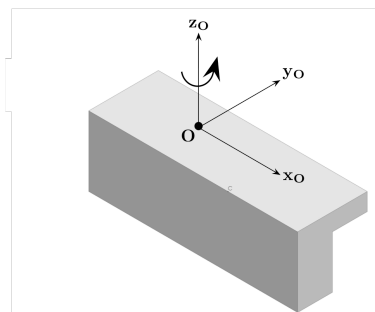


Figure 4.1: Arbitrary rigid body rotating about axis passing through O .

Equation (4.4) has been traditionally used to experimentally determine I_{Ozz} , I_{Oxz} , and I_{Oyz} . Genta *et al* [9] classified the experimental methods for estimating the moment of inertia, I_{Ozz} , into two main categories: angular acceleration methods and oscillation methods.

In acceleration methods, an object is subjected to an external torque or initial condition and the dynamic response is observed. The inertia is estimated from the time required for the object to reach a specific angular configuration. Genta *et al*, [9], discussed three approaches: rolling, falling weight, and running down. The first approach estimates the inertia from the time required for an object to roll down a ramp or rotate about a point due to gravity. The second approach estimates the inertia from the acceleration and deceleration time interval durations that an object experiences after being spun up by a falling weight with a string wound around the axis of rotation. The third approach estimates the inertia from the drag decelerating an object. In all cases, friction, drag, and nonlinearities affect the inertia estimates significantly, and the methods only estimate the moment of inertia about a single axis, I_{Ozz} , and not the products of inertia, I_{Oxz} and I_{Oyz} .

In some investigations, the products of inertia were neglected, due to the difficulty of direct measurement and their relatively small magnitude [15]. These approaches have also been discussed in more recent reviews of inertia parameter identification methods such as Shedlinks *et al* [22].

Acceleration methods have been used for determining the inertia of large objects such as spacecraft [17, 33] and spacecraft payloads with a robotic arm [20]. The inertia of vehicles with masses up to 3500 kg have been determined from measurements of motions of a suspended rigid frame carrying the vehicle [7] with measurement errors reported to be less than 3%, which is acceptable for large-

scale vehicle applications. More recently, another test bed has been commissioned and validated and holds a third-party quality certificate with a reported uncertainty of 1% [11]. Other large-scale instrumented test beds have also been used to measure forces and displacements needed to estimate the inertia of large vehicles [6]. Brancati *et al* identified the difficulty of estimating the products of inertia, which can be very small compared to the products of inertia [6].

In oscillation methods, an external periodic torque is applied to the system and the inertia is estimated from the resulting period of oscillation [18]. Oscillation methods have the advantage that observations can be collected after the system has reached a slowly decaying periodic motion and initial transients have died out. [9] Some examples of oscillation methods include: hanging torsional pendulum, linear spring, compound pendulum, curved rails, multifilar pendulum, and variable centre of mass [9]. The oscillation methods are less affected by damping than acceleration methods; but, for some setups, the dynamics require linearization, which introduces errors into the inertia estimates. Oscillation methods have been used in large-scale test beds to study off-road vehicle inertia properties [30].

Harris *et al* described the three most common oscillation methods: torsional, multifilar, and compound pendulums [13]. The torsional pendulum can be constructed by suspending the body by a single torsional spring, with known spring constant k_s (Figure 4.2a). The object is oscillated about a vertical axis aligned with the spring and the centre of mass of the body. The moment of inertia about the axis of rotation can be determined by measuring the oscillation period T [13] using the relationship

$$I_{TP} = \frac{k_s T^2}{4\pi^2} \quad (4.5)$$

The multifilar pendulum comprises a rigid body suspended by a set of flexible wires that oscillates around an axis passing through its centre of mass (Figure 4.2b). A trifilar pendulum uses three equally spaced wires of length L . The inertia about the rotation axis can be determined from

$$I_{MP} = \frac{mgr^2 T^2}{4\pi^2 L} \quad (4.6)$$

where the r is the distance between the wires and the rotation axis [13]. The derivation of this expression assumes that $L \gg r$ to linearize the equations of motion. An error analysis for the multifilar pendulum is presented in [9]. Some investigations have used the multifilar pendulum method to estimate the moment of inertia components of UAVs [29], but no estimation errors have been reported. Wang *et al*, used a four-cable pendulum to determine the moment of inertia of an electric powered wheelchair with a reported error of 10% [31]. Gobbi *et al* used a multifilar pendulum to test vehicles and highlight the correlations between the mass properties and simple vehicle parameters [12].

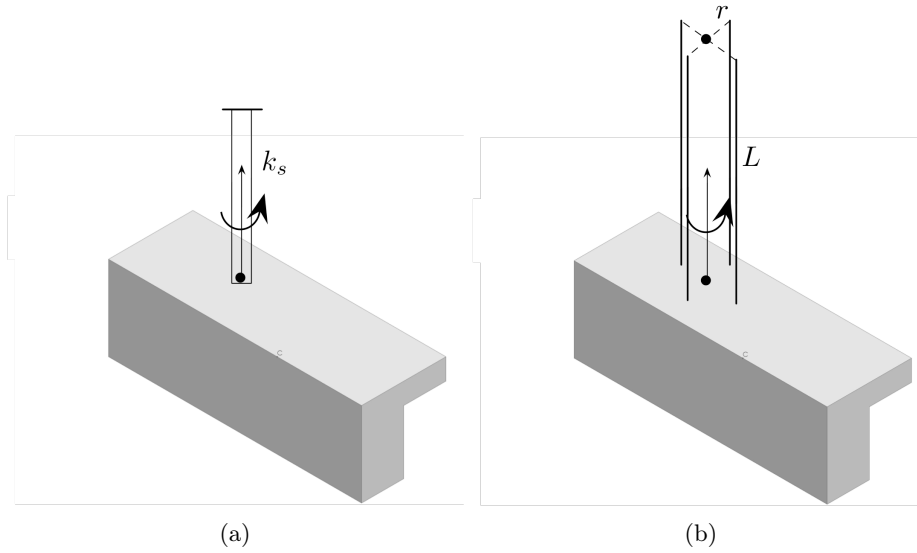


Figure 4.2: (a) A torsional pendulum oscillates an arbitrary object using a spring element with spring constant k_s . The spring can be connected to a light platform to support the object. (b) A multifilar pendulum oscillates an arbitrary object using four wires of length L , spaced at a distance r from the rotation axis. Alternatively, the wires can be connected to a light platform to support the object.

A limitation of the methods using a torsional or multifilar pendulum is that the axis of rotation must be aligned with the centre of mass of the object. Generally, the location of the centre of mass is unknown; but, even assuming that another test is conducted to determine the centre of mass location, it can still be impractical to assume that the body can be positioned with sufficient precision so as not to introduce significant error in the inertia estimate by misalignment [31]. As well, the multifilar pendulum method may suffer from decreased accuracy due to the linearization required to obtain Equation (4.6). The multifilar pendulum can also experience side swaying that reduces estimation accuracy [31].

The compound pendulum can be used when it is difficult to align the centre of mass with the axis of rotation. The object is hung by wires rotating on two overhead points (Figure 4.3a). The moment of inertia about an axis parallel to the two overhead points and through the centre of mass can be calculated by

$$I_{CP} = ml_c^2 \left(\frac{gT^2}{4\pi^2 l_c} - 1 \right) \quad (4.7)$$

where T is the oscillation period, g is gravity, m is the mass of the object, and l_c is the distance between the axis of rotation and the line between the two points of support [13].

The discussed oscillation methods are only useful to determine the moment of inertia about a single

axis. To determine the remaining diagonal components of the inertia tensor, the orientation of the object needs to be changed, which may be cumbersome or require specialized hardware [18]. Furthermore, these methods require very accurate determination of the geometrical parameters of the test setups as well as very precise and accurate measurements of the oscillation period. Typically, for the compound pendulum, the distance to the centre of mass from the rotation axis cannot be easily determined, especially when the centre of mass point is inaccessible and so a direct measurement is not practical [13].

Equations (4.5), (4.6), and (4.7), are very sensitive to the measurements of T and other parameters (l , L , r , and k_s). For high accuracy inertia estimates, T needs to be measured with uncertainties on the order of less than a millisecond.

A method to estimate the products of inertia is by spinning the object at a constant angular speed about an axis through its centre of mass [13], as shown in Figure 4.3b. From equation (4.4), if the object is spinning with constant angular speed $\omega_C = \dot{\theta}(t)$ such that $\dot{\omega}_C(t) = 0$, the products of inertia can be determined from the reaction torques, τ_x and τ_y , and ω_C as

$$I_{O_{yz}} = -\frac{\tau_x}{\omega_C^2} \quad (4.8)$$

$$I_{O_{xz}} = \frac{\tau_y}{\omega_C^2} \quad (4.9)$$

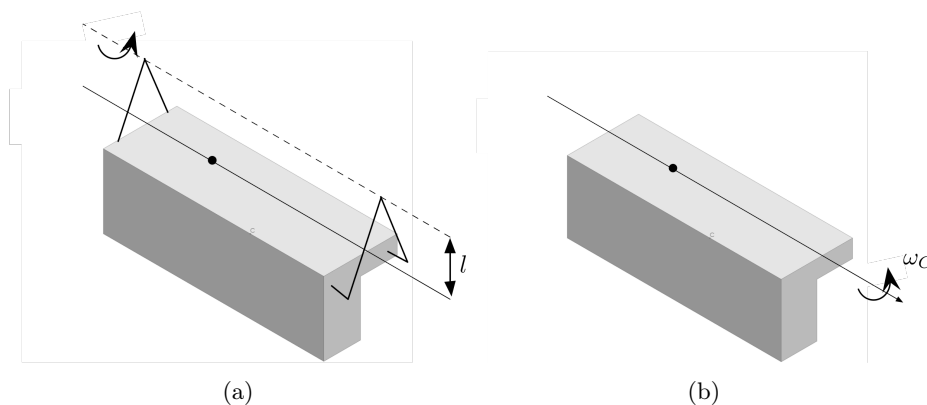


Figure 4.3: (a) A compound pendulum oscillates an arbitrary object hung by wires rotating on overhead pins. (b) An arbitrary object spins at a constant angular speed ω_C about an axis through its centre of mass.

For small products of inertia, high angular speeds may be necessary to measure reaction torques accurately. Practically, there may be constraints on the maximum speed that the object can

withstand; and measurements of reaction forces at the bearings supporting the object requires additional instrumentation such as force transducers mounted perpendicularly to each other.

Schedlinski *et al* used modal parameter methods [22] for mechanical systems supported by weak springs which requires special caution in the test setup, the limits of the excitation forces, and geometry transformations. Low accuracy results were attained, $\pm 10\%$ to 20% for all parameters [22] Schedlinski *et al* concluded indicating that the modal parameter method is less accurate than the acceleration methods while requiring higher hardware requirements than the torsional pendulum method. The torsional pendulum method was the recommended solution [22]. Further developments of methods using frequency response approaches have been discussed in [1, 2], with reported errors of approximately 5% to 14% . A comparison between the time-domain multifilar pendulum and frequency-domain frequency response approaches concluded that the multifilar method was much more accurate [19].

Recently, other approaches have been proposed using very specialized test setups, such as parallel manipulators. Tixian *et al* demonstrated a hydraulic Stewart platform for identifying the diagonal terms of the inertia tensor, with errors of approximately 10% to 15% for inertias of approximately 30 to 55 kg m^2 [28]. Barreto *et al* reduced the uncertainty of the estimated inertia tensor by using a custom set of trajectories on a parallel manipulator [4] to maintain the center of mass fixed while the object is rotated. The errors reported on the moments of inertia were between 0.1% to 2.2% , corresponding to 0.3 to $4.5 \times 10^{-3} \text{ kg m}^2$ [4]. In these methods, the inertia tensor components were determined by the least-squares method of parameter estimation from the governing equations of motion, using measurements of the applied torques.

Currently, there exist several commercial products to estimate the inertia tensor of measured objects. SMARTMechanical offers two products, InTenso and InTensino [23, 24], for testing large vehicles and their components, respectively. The systems are based on the work by Gobbi *et al* [12]. Inertia Dynamics sells a torsion platform which estimates the MOI of an object about the vertical rotation axis [3]. Resonic offers the Resonic K system, a torsional platform together with a carrier adapter to support the test object in one of twenty-four possible orientations. The object is sequentially placed into a configuration specified by the unit's software, followed by a measurement of the free oscillation response. Once all the data are collected, the system calculates the inertia tensor and CM location of the test object [16, 21]. Space Electronics offers a variety of high-precision torsional platforms. Their KSR series offer the highest accuracy and sensitivity. These systems use spherical air bearings to minimize rotational friction and force feedback for balancing and eliminating leveling errors [25]. Other systems include the XR and XKR [27], and the GB series [26].

All these commercially available systems are summarized in Table 4.1. The cost and measurement

precision of our proposed system will be presented in sections 4.4 and 4.5 respectively.

Table 4.1: Commercial Systems Presently Available, with Moment of Inertia Uncertainty (MOIu), Product of Inertia Accuracy (POIa), Centre of Mass Uncertainty (CoMu) and Approximate Cost. Unreported values are noted as N/A.

Brand Model	Mass (kg)	MOIu	POIa	CoMu	Price (USD)
SMARTMechanical InTenso	500-3500	1%	0.5%	1.5 mm	\$400k
SMARTMechanical InTensino	7-400	1%	0.5%	1.5 mm	N/A
Inertia Dynamics	11.4 max	0.5%	0.5%	0.5%	~\$17k
Resonic K	N/A	1%	N/A	0.5%	N/A
Space Electronics KSR330-6	N/A	0.1%	N/A	0.025 mm	~\$345k
Space Electronics XR	114 max	0.25%	N/A	N/A	~\$55k
Space Electronics XKR	2.3 max	0.1%	N/A	N/A	~\$70k
Space Electronics GB	heavy	N/A	N/A	N/A	~\$115k
Space Electronics MP1100	500 max	0.25%	N/A	2.54 mm	~\$220k

Most of the above-mentioned products estimate only the MOI of the test object. In order to obtain the POI and CM location, Resonic requires employing twenty-four object orientations during testing [16], while Space Electronics suggests a method to calculate POI from MOI estimates [32] requiring the rotation axis to pass through the CM of the object and the series of rotation axes to be exactly perpendicular to each other. Our proposed method does not require *a priori* knowledge of the CM location, nor does it constrain the directions of the rotation axes, and is able to estimate all nine inertial parameters of the body (MOI, POI, and position of CM) using only nine configurations of the test object. This simplifies experimental setup and provides faster testing times.

4.3 Estimating the Inertia Tensor Components and the Position of the Centre of Mass of an Object

This section describes our proposed method to estimate all six inertia tensor components and the position of the centre of mass of a rigid-body object. The method can be used with the measurements collected using the torsion platform described in Section 4.4, or another equivalent platform. The method requires a set of estimates of the mass moment of inertia of the object about a vertical axis (I_{Rzz} , defined in this section). In the case of a torsion platform, these are obtained by measuring the period of oscillation of the base platform with the object mounted in a series of specified configurations.

The proposed method considers an object (Figure 4.4) with its CM located at \mathbf{r}_C with respect to

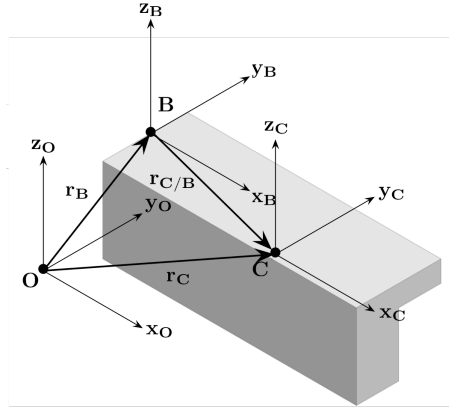


Figure 4.4: Arbitrary object with a center of mass located at C .

frame O . Frame O has the axis z_O aligned with the axis of rotation of the system (Figure 4.8). Frame B is a body fixed frame located at an arbitrary location r_B with respect to frame O and is initially parallel to it. Frame C is a body fixed frame with origin at the CM and parallel to frame B .

The object has an unknown inertia tensor I with respect to frame C :

$$I = \begin{pmatrix} I_{xx} & I_{xy} & I_{xz} \\ I_{xy} & I_{yy} & I_{yz} \\ I_{xz} & I_{yz} & I_{zz} \end{pmatrix} \quad (4.10)$$

Vector r_B can be measured directly:

$$r_B = (x_B, y_B, z_B)^T \quad (4.11)$$

while the vectors $r_{C/B}$ and r_C are unknown:

$$r_{C/B} = (x_{C/B}, y_{C/B}, z_{C/B})^T \quad (4.12)$$

$$r_C = r_B + r_{C/B} = (x_C, y_C, z_C)^T \quad (4.13)$$

The inertia of the object prior to any rotations can be determined relative to frame O from the parallel axis theorem:

$$I_O = I + m(r_C^T r_C I_3 - r_C r_C^T) \quad (4.14)$$

where I_3 is a 3 by 3 identity matrix, and m is the mass of the object.

The vector \mathbf{r}_B , which determines the position of a point on the object with respect to frame \mathbf{O} , can be chosen to simplify measurements. If the body is rotated about the origin of frame \mathbf{O} , such that $\|\mathbf{r}_C\|$ is kept constant, the resulting inertia matrix \mathbf{I}_R is given by:

$$\mathbf{I}_R = \mathbf{R}(\mathbf{I} + m(\mathbf{r}_C^T \mathbf{r}_C \mathbf{I}_3 - \mathbf{r}_C \mathbf{r}_C^T)) \mathbf{R}^T \quad (4.15)$$

where \mathbf{R} is a rotation matrix of the body-fixed frame \mathbf{C} relative to frame \mathbf{O} . Note vector \mathbf{r}_C is measured with respect to frame \mathbf{O} , and \mathbf{I}_R is the body's inertia tensor with respect to frame \mathbf{O} in the final rotated configuration.

4.3.1 General Method Description and Formulation

The objective of our method is to estimate all of the unique components of \mathbf{I} and $\mathbf{r}_{C/B}$. The strategy relies on being able to translate the object by \mathbf{r}_B and then rotate it by \mathbf{R} with respect to frame \mathbf{O} which is defined by the apparatus.

The term \mathbf{I}_R in Equation (4.15) can be expanded to:

$$\mathbf{I}_R = \mathbf{R} \begin{pmatrix} I_{xx} + m(y_C^2 + z_C^2) & I_{xy} - mx_C y_C & I_{xz} - mx_C z_C \\ I_{xy} - mx_C y_C & I_{yy} + m(x_C^2 + z_C^2) & I_{yz} - my_C z_C \\ I_{xz} - mx_C z_C & I_{yz} - my_C z_C & I_{zz} + m(x_C^2 + y_C^2) \end{pmatrix} \mathbf{R}^T \quad (4.16)$$

The selection of \mathbf{R} is very important. It was found that the rotations presented in Figures 4.5 and 4.6 are of mathematical and experimental convenience. For experimental testing, the object is first rotated about \mathbf{y}_O by angle β , then about \mathbf{x}_1 by angle α , as shown in Figures 4.5 and 4.6, where the bases $\mathbf{x}_1, \mathbf{y}_1, \mathbf{z}_1$ and $\mathbf{x}_2, \mathbf{y}_2, \mathbf{z}_2$ are the result of the first and second rotations respectively.

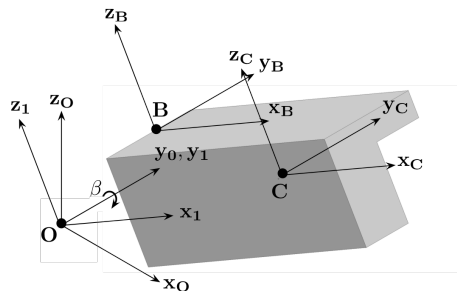


Figure 4.5: Rotation with $\beta = -\pi/6$.

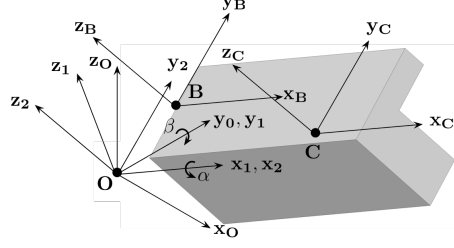


Figure 4.6: Rotation by $\beta = -\pi/6$, followed by a rotation by $\alpha = \pi/6$.

The resulting rotation matrix is written as:

$$\mathbf{R} = R_{y,\beta}R_{x,\alpha} = \begin{pmatrix} \cos(\beta) & \sin(\alpha)\sin(\beta) & \cos(\alpha)\sin(\beta) \\ 0 & \cos(\alpha) & -\sin(\alpha) \\ -\sin(\beta) & \cos(\beta)\sin(\alpha) & \cos(\alpha)\cos(\beta) \end{pmatrix} \quad (4.17)$$

We focus on the bottom-right component of \mathbf{I}_R (4.16), denoted as I_{Rzz} , whose value can be measured directly (c.f. Section 4.4):

$$\begin{aligned} I_{Rzz} &= I_{xx} \sin^2(\beta) - 2I_{xy} \sin(\alpha) \sin(\beta) \cos(\beta) \\ &\quad + 2 \cos(\alpha) \cos(\beta) (\sin(\beta) (m x_C z_C - I_{xz}) + \sin(\alpha) \cos(\beta) (I_{yz} - m y_C z_C)) \\ &\quad + \sin^2(\alpha) \cos^2(\beta) (I_{yy} + m (x_C^2 + z_C^2)) \\ &\quad + \cos^2(\alpha) \cos^2(\beta) (I_{zz} + m (x_C^2 + y_C^2)) \\ &\quad + m x_C y_C \sin(\alpha) \sin(2\beta) + m y_C^2 \sin^2(\beta) + m z_C^2 \sin^2(\beta) \end{aligned} \quad (4.18)$$

where from (4.13),

$$x_C = x_B + x_{C/B} \quad (4.19)$$

$$y_C = y_B + y_{C/B} \quad (4.20)$$

$$z_C = z_B + z_{C/B} \quad (4.21)$$

The choice of rotation and translation configuration parameters β , α , x_B , y_B , and z_B can simplify the experimental determination of the desired inertia tensor \mathbf{I} and CM location vector $\mathbf{r}_{C/B}$.

This method requires a minimum of nine experimental configurations to estimate nine unknowns: I_{xx} , I_{yy} , I_{zz} , I_{xy} , I_{xz} , I_{yz} , $x_{C/B}$, $y_{C/B}$, $z_{C/B}$. It is assumed that the mass of the object, m , is known or can be measured.

In experiments, motion measurements allow estimation of I_{Ozz} , the total mass moment of inertia

about the oscillation axis, which is the summation of the inertia of the rotating assembly (plate, attachment blocks, etc) I_P and the inertia of the measured object I_{Rzz} . For a given experiment with index i , the inertia corresponding to the measured object can be found from:

$$I_{Rzz,i} = (I_{Ozz,i} - I_{P,i}) := I_{e,i} \quad (4.22)$$

The terms $I_{P,i}$ can be estimated through direct experiments, which will be done in Section 4.4.7.

It is worth noting that $I_{Ozz,i}$ is assumed to be constant during a given experiment, which means the parameters β , α , x_B , y_B , and z_B are configured before the tests, and remain constant.

4.3.2 Experimental Determination of the Position of the Centre of Mass and Diagonal Components of the Inertia Tensor

Estimating I_{zz} , $x_{C/B}$, $y_{C/B}$

With $\beta = 0$, $\alpha = 0$, Equation (4.18) reduces to:

$$I_{zz} = I_{e,i} - m((x_{C/B} + x_{B,i})^2 + (y_{C/B} + y_{B,i})^2) \quad (4.23)$$

where $I_{e,i}$ was defined in equation (4.22) and is directly measurable, and i is the index of the experiment. A minimum of three tests are required to estimate I_{zz} , $x_{C/B}$, $y_{C/B}$. Using the configurations in Table 4.2 leads to three equations with three unknowns:

Table 4.2: Experiments 1-3

i	β	α	x_B	y_B	z_B
1	0	0	0	0	0
2	0	0	0	$y_{B,2}$	0
3	0	0	$x_{B,3}$	0	0

$$I_{zz} = I_{e,1} - m(x_{C/B}^2 + y_{C/B}^2) \quad (4.24)$$

$$I_{zz} = I_{e,2} - m(x_{C/B}^2 + (y_{B,2} + y_{C/B})^2) \quad (4.25)$$

$$I_{zz} = I_{e,3} - m((x_{B,3} + x_{C/B})^2 + y_{C/B}^2) \quad (4.26)$$

which can be solved to give:

$$y_{C/B} = -\frac{I_{e,1} - I_{e,2} + my_{B,2}^2}{2my_{B,2}} \quad (4.27)$$

$$x_{C/B} = -\frac{I_{e,1} - I_{e,3} + mx_{B,3}^2}{2mx_{B,3}} \quad (4.28)$$

$$I_{zz} = \frac{(I_{e,1} - I_{e,2} + my_{B,2}^2)^2}{4my_{B,2}^2} - \frac{(I_{e,1} - I_{e,3} + mx_{B,3}^2)^2}{4mx_{B,3}^2} + I_{e,1} \quad (4.29)$$

Alternatively, a linear regression can be set up to use more than two translations $(x_{B,i}, y_{B,i})$ to reduce the error of the $x_{C/B}$, $y_{C/B}$ estimates:

$$I_{e,1} + m(2x_{C/B}x_{B,i} + x_{B,i}^2 + 2y_{C/B}y_{B,i} + y_{B,i}^2) = I_{e,i} \quad (4.30)$$

Estimating I_{yy} , $z_{C/B}$

With $\beta = 0$, $\alpha = \pi/2$, Equation (4.18) reduces to:

$$I_{yy} = I_{e,i} - m((x_{C/B} + x_{B,i})^2 + (z_{C/B} + z_{B,i})^2) \quad (4.31)$$

A minimum of two configurations are required to estimate I_{yy} and $z_{C/B}$, assuming $x_{C/B}$ has been determined as described in the previous section. Using the configurations of Table 4.3 leads to two equations with two unknowns:

Table 4.3: Experiments 4-5

i	β	α	x_B	y_B	z_B
4	0	$\pi/2$	0	0	0
5	0	$\pi/2$	0	0	$z_{B,5}$

$$I_{yy} = I_{e,4} - m(x_{C/B}^2 + z_{C/B}^2) \quad (4.32)$$

$$I_{yy} = I_{e,5} - m(x_{C/B}^2 + (z_{B,5} + z_{C/B})^2) \quad (4.33)$$

which solve to:

$$z_{C/B} = -\frac{I_{e,4} - I_{e,5} + mz_{B,5}^2}{2mz_{B,5}} \quad (4.34)$$

$$I_{yy} = I_{e,4} - m\left(\frac{(I_{e,4} - I_{e,5} + mz_{B,5}^2)^2}{4m^2z_{B,5}^2} + x_{C/B}^2\right) \quad (4.35)$$

A linear regression can be formulated to reduce the estimation error:

$$I_{e,4} + m(2x_{C/B}x_{B,i} + x_{B,i}^2 + 2z_{C/B}z_{B,i} + z_{B,i}^2) = I_{e,i} \quad (4.36)$$

Estimating I_{xx}

With $\beta = -\pi/2$, $\alpha = 0$, Equation (4.18) reduces to:

$$I_{xx} = I_{e,i} - m \left((y_{C/B} + y_{B,i})^2 + (z_{C/B} + z_{B,i})^2 \right) \quad (4.37)$$

One configuration is required to estimate I_{xx} , assuming that $y_{C/B}$ and $z_{C/B}$ have been determined as described in the previous sections. For simplicity, consider the no-translation case in Table 4.4

Table 4.4: Experiment 6

i	β	α	x_B	y_B	z_B
6	$-\pi/2$	0	0	0	0

$$I_{xx} = -\frac{(I_{e,1} - I_{e,2} + my_{B,2})^2}{4my_{B,2}^2} + \frac{(I_{e,4} - I_{e,5} + mz_{B,5})^2}{4mz_{B,5}^2} + I_{e,6} \quad (4.38)$$

A linear regression can be formulated to reduce the error of the estimates:

$$I_{e,6} + m(2y_{C/B}y_{B,i} + y_{B,i}^2 + 2z_{C/B}z_{B,i} + z_{B,i}^2) = I_{e,i} \quad (4.39)$$

4.3.3 Experimental Determination of Off-Diagonal Components of the Inertia Tensor

At this point, values of I_{xx} , I_{yy} , I_{zz} , $x_{C/B}$, $y_{C/B}$, $z_{C/B}$ have been experimentally determined. Three more configurations are required to determine I_{xy} , I_{xz} , and I_{yz} . The proposed configuration parameters are presented in Table 4.5, where β_7 , α_8 , β_9 , α_9 are non-zero angles that are not multiples of $\pi/2$.

For configurations 7, 8 and 9, I_{xz} , I_{yz} and I_{xy} can be found from Equation (4.18) as, respectively:

$$I_{xz} = \frac{1}{2} \tan(\beta) \left(-I_{e,7} \csc^2(\beta) + \cot^2(\beta) (I_{zz} + m(x_C^2 + y_C^2)) \right) + 2mx_C z_C \cot(\beta) + I_{xx} + my_C^2 + mz_C^2 \quad (4.40)$$

$$\begin{aligned}
I_{yz} = & -\frac{1}{2} \tan(\alpha) (-I_{e,8} \csc^2(\alpha) + \cot^2(\alpha) (I_{zz} + m(x_C^2 + y_C^2))) \\
& - 2m y_C z_C \cot(\alpha) + I_{yy} + m x_C^2 + m z_C^2
\end{aligned} \tag{4.41}$$

$$\begin{aligned}
I_{xy} = & \frac{1}{2} (-I_{e,9} \csc(\alpha) \csc(\beta) \sec(\beta) + I_{xx} \csc(\alpha) \tan(\beta) \\
& + \cot(\alpha) (\cos(\alpha) \cot(\beta) (I_{zz} + m(x_C^2 + y_C^2)) - 2I_{xz} + 2m x_C z_C) \\
& + I_{yy} \sin(\alpha) \cot(\beta) + 2 \cos(\alpha) \cot(\beta) (I_{yz} - m y_C z_C) \\
& + m x_C^2 \sin(\alpha) \cot(\beta) + m y_C^2 \csc(\alpha) \tan(\beta) + m z_C^2 \sin(\alpha) \cot(\beta) \\
& + m z_C^2 \csc(\alpha) \tan(\beta) + 2m x_C y_C)
\end{aligned} \tag{4.42}$$

where x_C , y_C , and z_C are defined in Equations (4.19), (4.20), and (4.21), respectively, and depend on known parameters.

Table 4.5: Experiments 7 - 9

Config	β	α	x_B	y_B	z_B
7	β_7	0	0	0	0
8	0	α_8	0	0	0
9	β_9	α_9	0	0	0

In addition to the above approaches, it is also possible to use a nonlinear least-squares estimation method (such as Newton's method, Levenberg-Marquardt, or Conjugate Gradient) to simultaneously determine all nine unknown parameters in Equation (4.18) from a large (≥ 9) set of experiments. This will be demonstrated in Section 4.5.2.

4.3.4 Method Verification

The proposed method was first verified in simulation in order to validate the provided equations. A computer-generated solid model of the 6061-T6 aluminum block shown in Figure 4.7 was created, with a resulting mass of 5.5700 kg. SolidWorks was used to calculate the inertia tensor relative to frame \mathbf{O} for the nine configurations shown in Table 4.6. The body-fixed frame \mathbf{B} was placed at the dimensional centre of the block (150mm lengthwise and 50mm from the top and sides); note the dimensional centre and the centre of mass are at different locations due to the geometry of the block.

The procedure given in the previous sections was used to calculate the inertia parameters and the

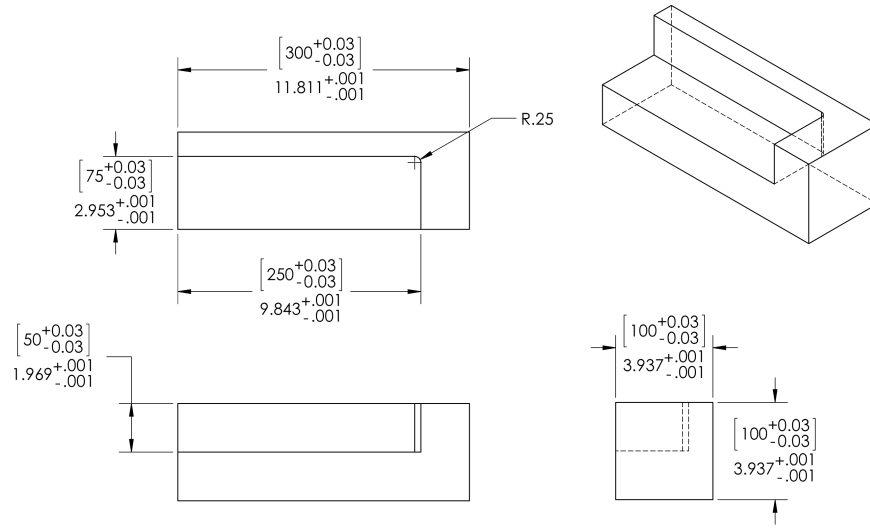


Figure 4.7: General dimensions of validation block. The cutout section has a fillet with 0.8mm radius.

Table 4.6: Method Verification Experiments

Config	β rad	α rad	x_B mm	y_B mm	z_B mm
1	0	0	0	0	0
2	0	0	0	10	0
3	0	0	10	0	0
4	0	$\pi/2$	0	0	0
5	0	$\pi/2$	0	0	10
6	$-\pi/2$	0	0	0	0
7	$-\pi/4$	0	0	0	0
8	0	$\pi/4$	0	0	0
9	$-\pi/4$	$-\pi/2$	0	0	0

location of the centre of mass. The errors between the results from SolidWorks and our equations differ by a maximum error with order of magnitude of 1×10^{-8} , which is expected because the inertias from the computer-generated model are reported to eight decimal points.

The inertia tensor and center of mass were calculated to be:

$$\mathbf{I}_{obj} = \begin{pmatrix} 0.008911945 & 0.001148855 & 0.002304845 \\ 0.001148855 & 0.049198284 & 0.001151337 \\ 0.002304845 & 0.001151337 & 0.050263570 \end{pmatrix} \text{ kg m}^2 \quad (4.43)$$

$$\mathbf{r}_{C/B} = \begin{pmatrix} -0.0113818 & -0.0056859 & -0.0113557 \end{pmatrix}^T \text{ m} \quad (4.44)$$

The differences between the SolidWorks-reported inertia tensor and CM position vector and our calculated values are:

$$\mathbf{I}_{Obj_{err}} = \begin{pmatrix} 5 \times 10^{-9} & 5 \times 10^{-9} & -1 \times 10^{-8} \\ 5 \times 10^{-9} & -4 \times 10^{-9} & 3 \times 10^{-9} \\ -1 \times 10^{-8} & 3 \times 10^{-9} & 1 \times 10^{-8} \end{pmatrix} \text{ kg m}^2 \quad (4.45)$$

$$\mathbf{r}_{C/B_{err}} = \begin{pmatrix} 7 \times 10^{-8} & 8 \times 10^{-8} & -3 \times 10^{-8} \end{pmatrix}^T \text{ m} \quad (4.46)$$

4.4 Design of an Instrumented Torsional Platform

An instrumented torsion platform was developed and built to experimentally validate the proposed method in Section 4.3 (Figure 4.8). In this section, we describe the design, equations of motion, calibration and uncertainty analysis of this apparatus.

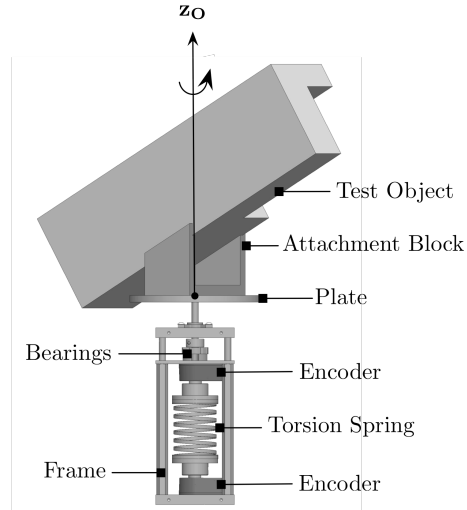


Figure 4.8: Instrumented torsion platform.

4.4.1 Apparatus: Main System Components

An instrumented torsion platform prototype was built and is shown in Figure 4.9. The system is designed to oscillate a small object about a vertical axis. The rotation shaft is supported by a small double bearing block that is attached to an aluminum fixed frame, as shown in Figure 4.8. The top end of the shaft is rigidly attached to a rotation plate with a clamping hub. The shaft is stepped and rests on the edge of the bearing to carry the weight of the plate. The bottom end of the shaft is connected to the top end of a linear torsion spring. The bottom end of the spring is connected to the fixed frame with a rigid coupler. The spring is made from 316 stainless steel round wire with a diameter of 2.29 mm. The diameter and length of the spring are 38 mm and 60 mm, respectively. The coils are separated to avoid interference. The spring stores energy during angular displacement and provides the restoring torque to oscillate the plate assembly. The spring was selected such that the period of oscillation of the plate assembly is at least 1 s.

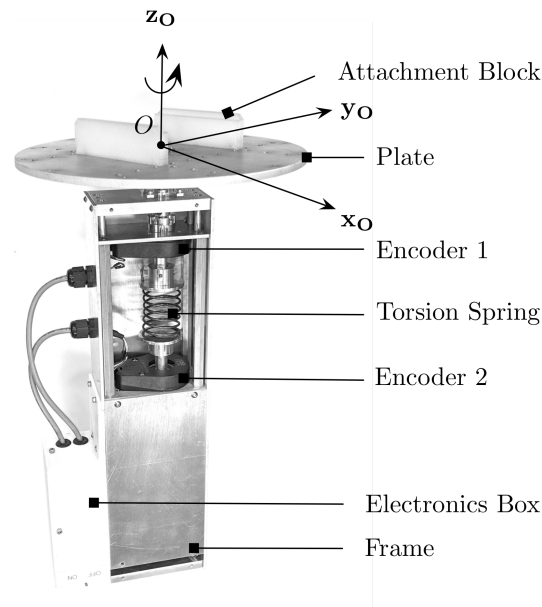


Figure 4.9: Torsion pendulum apparatus.

The test object is supported on the rotating plate by customized attachment blocks. The rotation plate was fabricated from 6061-T6 aluminum by water-jet cutting, with a dimensional tolerance of 0.05 mm, and has the dimensions specified in Figure 4.10. The components of the rotating assembly are shown in Figure 4.11. The rotation plate has a pattern of machined holes that allow blocks to attach in different positions and orientations with respect to the rotation axis. The attachment blocks can be 3D printed to reduce costs of manufacturing, or can be machined and positioned

with high tolerance positioning pins to reduce the uncertainty of the position and orientation of the object. A two-degree-of-freedom joint mechanism can also be used instead of several attachment blocks. In that case, the joints may need to be instrumented or have mechanical stops to set the orientation of the object, or the orientation can be measured directly.

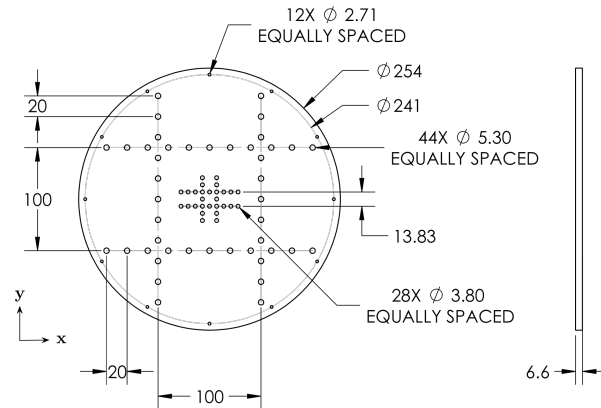


Figure 4.10: Dimensions of the rotation plate. All dimensions in mm.

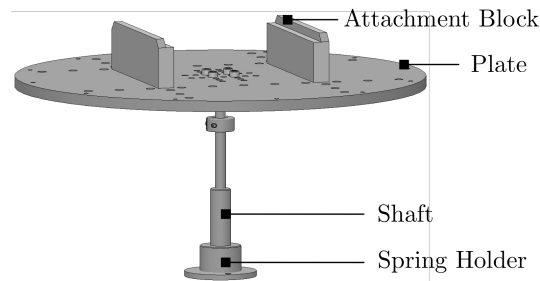


Figure 4.11: Plate and other rotating components

A high-resolution, quadrature optical encoder measures the angular position of the shaft at the top of the spring. A second encoder is placed at the bottom of the spring and is used for its calibration as described in Section 4.4.4. The encoder has 40000 counts per revolution, corresponding to an angular resolution of 0.009 deg. The output signals of the encoders are sampled by a micro-controller or other data acquisition system to measure the angular displacement of the spring. Half-periods of oscillation are calculated from the angular displacement measurements during the negative angle portions of the motion. It was found that the spring constants differ by approximately 4% between the positive and negative rotation angles, 0.3904 Nm/rad and 0.4070 Nm/rad respectively. Thus only the negative angle portion of the motions is considered and half-periods are used instead of the full periods in order to use a single spring constant in the calculations. The position measurements $\theta(t)$ are logged to an attached computer.

The current system can carry objects of up to approximately 10 kg. There are no hard limits on the test object's geometry as long as it can be held rigidly during oscillations. Since the longest period of oscillation for reasonable experiment times is approximately 10 s, the largest measurable MOI is approximately 1 kg m^2 for the existing spring by (4.5). The present design could be modified through a redesign of the frame, shaft, bearings and plate to carry larger or smaller loads, and the torsional spring sized to produce oscillations of adequate amplitude and period to obtain a good signal-to-noise ratio. The components of our described system have an approximate cost of USD 1200, with the majority being labour costs for machining components, one or two orders of magnitude less than the commercial torsion platforms discussed in Section 4.2.

4.4.2 Equations of Motion of the Torsion Pendulum and Inertia Estimation Method

The dynamics of an object rotating about a vertical axis z_O were given in equation (4.4). For the torsion platform, τ_x and τ_y correspond to reaction moments, and τ_z is the torque driving the oscillatory motions. The block bearings of the torsion platform support the rotating shaft and generate the reaction torques τ_x and τ_y . Torque τ_z is the result of the restoring torque of the spring $\tau_s(t)$, and torques resulting from friction forces on the rotating elements $\tau_f(t)$ such that

$$\tau_z = -\tau_s(t) - \tau_f(t) \quad (4.47)$$

The torque of the spring is assumed to be linearly proportional to the angular displacement by a spring constant k_s :

$$\tau_s(t) = k_s \theta(t) \quad (4.48)$$

If friction torque $\tau_f(t)$ is negligible, the equation of motion along the z component of (4.4) reduces to:

$$I_{Ozz} \ddot{\theta}(t) + k_s \theta(t) = 0 \quad (4.49)$$

which is a second order linear ODE. For an initial displacement, θ_0 , and initial velocity, ω_0 , its solution is

$$\theta(t) = \theta_0 \cos\left(\sqrt{\frac{k_s}{I_{Ozz}}} t\right) + \omega_0 \sqrt{\frac{I_{Ozz}}{k_s}} \sin\left(\sqrt{\frac{k_s}{I_{Ozz}}} t\right) \quad (4.50)$$

The system has a natural frequency ω_n and a period of oscillation T :

$$\omega_n = \sqrt{\frac{k_s}{I_{Ozz}}} \quad (4.51)$$

$$T = 2\pi\sqrt{\frac{I_{Ozz}}{k_s}} \quad (4.52)$$

and the moment of inertia term I_{Ozz} can be estimated from the measured period of oscillation as:

$$I_{Ozz} = \frac{k_s T^2}{4\pi^2} \quad (4.53)$$

4.4.3 Effects of Friction on the Inertia Estimates

Equation (4.53) is only valid for mechanical systems in which $\tau_f(t)$ is negligible. For typical engineering applications, $\tau_f(t)$ can be modeled as

$$\tau_f(t) = c(t) + d\dot{\theta}(t) \quad (4.54)$$

where the first and second terms of the RHS correspond to Coulomb and viscous friction components respectively. The types of friction encountered are functions of the type of bearings, weight of the object supported by the bearing blocks, and the lubrication of the bearings. The assumed friction model (4.54) is tested in Section 4.4.7. More complex expressions for $\tau_f(t)$ could include the effects of additional loading resulting from the reaction torques τ_x and τ_y , which depend on inertial properties and angular velocities and accelerations, for instance an offset between the centre of mass and the axis of rotation leading to centripetal acceleration during the oscillations. In the present work, only the effects of viscous and Coulomb friction are investigated.

Effect of Viscous Friction

Assuming $\tau_f(t) = d\dot{\theta}(t)$, the equation of motion of the torsional platform is

$$I_{Ozz}\ddot{\theta}(t) + d\dot{\theta}(t) + k_s\theta(t) = 0 \quad (4.55)$$

where d is a constant damping coefficient. Defining the damping ratio

$$\zeta = \frac{d}{2I_{Ozz}\omega_n} \quad (4.56)$$

and assuming $0 < \zeta < 1$, the solution of (4.55) with initial displacement θ_0 and velocity $\dot{\theta}_0$ is

$$\theta(t) = \frac{e^{-t\zeta\omega_n}}{\omega_d} \left(\omega_d\theta_0 \cos(\omega_d t) + \left(\dot{\theta}_0 + \zeta\theta_0\omega_n \right) \sin(\omega_d t) \right) \quad (4.57)$$

where

$$\omega_d = \omega_n \sqrt{1 - \zeta^2} \quad (4.58)$$

is the frequency of oscillation of the damped system, with corresponding period

$$T_d = \frac{2\pi}{\omega_n \sqrt{1 - \zeta^2}} \quad (4.59)$$

The inertia of the damped system can be calculated from:

$$I_{Ozz} = \frac{k_s T_d^2 (1 - \zeta^2)}{4\pi^2} \quad (4.60)$$

The error of the inertia estimate due to ignoring viscous damping e_d can be quantified by:

$$e_d = \frac{I_{Ozz \text{ damped}} - I_{Ozz \text{ undamped}}}{I_{Ozz \text{ undamped}}} = \zeta^2 \quad (4.61)$$

where $I_{Ozz \text{ undamped}}$ is given by (4.53) and $I_{Ozz \text{ damped}}$ by (4.60). This results indicates that e_d is constant and can be found by estimating ζ empirically. The parameter ζ can be obtained from the ratio of the amplitudes of successive cycles using the well-known log decrement method [14].

The log decrement is defined as:

$$\delta = \ln \left(\frac{\theta_i}{\theta_{i+1}} \right) \quad (4.62)$$

where θ_i and θ_{i+1} are the amplitudes at the start of successive cycles. Their ratio A_R is constant,

$$A_R = \frac{\theta_i}{\theta_{i+1}} = e^{2\pi\zeta/\sqrt{1-\zeta^2}} = e^{\zeta\omega_n T_d} \quad (4.63)$$

and can be used to calculate ζ as

$$\zeta = \frac{\ln(A_R)}{\sqrt{4\pi^2 + (\ln(A_R))^2}} = \frac{\delta}{\sqrt{4\pi^2 + \delta^2}} \quad (4.64)$$

For low-friction torsional platforms e_d can be very small, as shown experimentally in Section 4.4.7.

Effect Of Coulomb Friction

Coulomb friction can be modeled as a constant opposing moment τ_c , independent of velocity magnitude, but dependent on its direction:

$$c(t) = \tau_c \operatorname{sgn}(\dot{\theta}(t)) \quad (4.65)$$

where the $\operatorname{sgn}(\cdot)$ function is defined as:

$$\operatorname{sgn}(\dot{\theta}(t)) = \begin{cases} 1 & \dot{\theta}(t) > 0 \\ 0 & \dot{\theta}(t) = 0 \\ -1 & \dot{\theta}(t) < 0 \end{cases} \quad (4.66)$$

The equation of motion with Coulomb friction is:

$$I_{Ozz}\ddot{\theta}(t) + k_s\theta(t) + \tau_c \operatorname{sgn}(\dot{\theta}(t)) = 0 \quad (4.67)$$

The piecewise solution can be found by separating the motion into half-period intervals corresponding to segments of motion in the same direction, separated by zero velocity points. For an initial displacement θ_0 , and starting from rest, the solution for the first half period, $0 < t < T/2$, is:

$$\theta_{hp1}(t) = (\theta_0 - \tau_c/k_s) \cos(\omega_n t) + \tau_c/k_s \quad (4.68)$$

and for the second half period, $T/2 < t < T$:

$$\theta_{hp2}(t) = (-\theta_0 + 3\tau_c/k_s) \cos(\omega_n(t - T/2)) - \tau_c/k_s \quad (4.69)$$

The period of oscillation, T , can be used to calculate the inertia of the system by Equation (4.53). The oscillations may stop at a point where the restoring torque of the spring is not enough to overcome Coulomb friction; the period T must be measured *before* this occurs. Generally the amplitude for the start of cycle n is:

$$\theta_n = \theta_0 - n \frac{4\tau_c}{k_s} \quad (4.70)$$

indicating that successive amplitudes at the start of each cycle decrease by a constant angle $\Delta\theta$, linearly proportional to τ_c :

$$\Delta\theta = \frac{4\tau_c}{k_s} \quad (4.71)$$

While a constant A_R characterizes the effect of viscous friction and can be used to estimate ζ (Equation (4.63)), a constant $\Delta\theta$ characterizes dry friction and can be used to estimate τ_c .

Effect of Combined Viscous and Coulomb Friction

In the case where viscous and Coulomb friction are present, the equation of motion is:

$$I_{Ozz}\ddot{\theta}(t) + d\dot{\theta}(t) + k_s\theta(t) + \tau_c \operatorname{sgn}(\dot{\theta}(t)) = 0 \quad (4.72)$$

The solutions for the first and second half periods are:

$$\theta_{hp1}(t) = e^{-t\zeta\omega_n} \left(\theta_0 - \frac{\tau_c}{k_s} \right) \left(\cos(\omega_d t) + \frac{\omega_n}{\omega_d} \zeta \sin(\omega_d t) \right) + \frac{\tau_c}{k_s} \quad (4.73)$$

$$\theta_{hp2}(t) = e^{-(t-\frac{T}{2})\zeta\omega_n} \left(\theta_0 + \frac{\tau_c}{k_s} \right) \left(\cos(\omega_d(t - \frac{T}{2})) + \frac{\omega_n}{\omega_d} \zeta \sin(\omega_d(t - \frac{T}{2})) \right) - \frac{\tau_c}{k_s} \quad (4.74)$$

The period of oscillation is the same as for the damped system (Equation (4.58)), but in this case it is not possible to estimate ζ and τ_c simultaneously from the ratios or differences of successive amplitudes. In practice, preliminary experiments can be conducted to identify whether a viscous or dry friction model best fits the system, and then use one or the other.

4.4.4 Torsion Platform Calibration Procedure and Results

The torsion spring constant k_s introduced in Equation (4.48) was identified through a linear regression between applied torques and observed angular displacements. To find k_s the torsion platform was fixed sideways and a weight was hanged from a symmetrical bar attached to the shaft to apply a known torque around the axis of rotation (Figure 4.12). The spring was unloaded by loosening the shaft attached to the bottom of the spring and letting it unwind. The encoders were zeroed in the unloaded position, with the weight hanging directly below the axis of rotation. The calibration dataset was generated by applying a torque to the shaft attached to the bottom of the spring and measuring the resulting rotation θ . The angular displacements measured by both encoders were recorded. The spring's net angular displacement, $\theta(t)$, is calculated from the measurements of the top and bottom encoders, $\theta_1(t)$ and $\theta_2(t)$ as

$$\theta(t) = \theta_2(t) - \theta_1(t) \quad (4.75)$$

The torque applied to the shaft, $\tau_s(t)$, is calculated by

$$\tau_s(t) = m_c l g \sin \theta_1(t) \quad (4.76)$$

where m_c is the mass used for calibration (0.49957 kg), g is gravity, and l is the lever arm of the bar (15.24 cm). An example calibration dataset is presented in Figure 4.13.

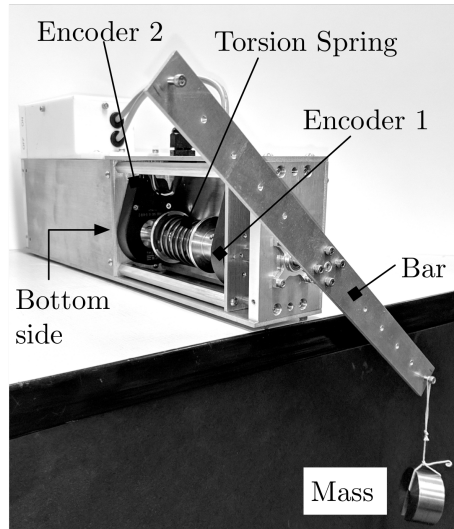


Figure 4.12: Calibration setup.

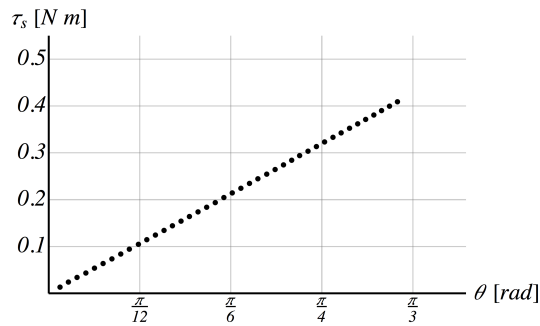


Figure 4.13: Torsion spring calibration. Only one of every twenty-five points used for the calibration are shown.

The calibration range was adjusted to the maximum expected amplitude of oscillations $\pi/3$. Only positive angular displacements were used for the calibration. There was a small difference between the calibration constants calculated from positive or negative angular displacements due to the nature of the twisting of the spring, as described in the beginning of this section. In this investigation, the half-period of oscillation was measured during positive displacements. This approach does not require the reformulation the equations of motion with two spring constants that depend on the sign of displacement.

The calibration experiment was repeated five times. $\theta(t)$ and $\tau_s(t)$ were fitted to a linear model assuming the errors were independent and identically distributed (i.i.d). The model parameters and

parameter fitting errors are presented in Table 4.7. The R^2 value of the regression was calculated to be 0.9998.

Table 4.7: Torsion spring calibration results

	$\hat{\beta}_k$	$\hat{\sigma}_k$	95%CI
k_s [Nm/rad]	0.40699	5×10^{-5}	(0.40688, 0.40710)

4.4.5 Uncertainty of Inertia Estimation with a Torsion Platform

The experimental determination of I_{Ozz} is subject to errors from the uncertainty of k_s and T (Equation (4.53)) for the case of negligible friction or Coulomb friction (which does not affect the oscillation period), or the uncertainty of ζ if the oscillation is affected by viscous friction (Equation (4.60)). Generally, the uncertainty of I_{Ozz} , u_I , can be approximated from the uncertainties of (k_s, T, ζ) , (u_k, u_T, u_ζ) respectively, using the root of sum of squares method, assuming u_k , u_T , and u_ζ , are small, possess the same confidence interval, and are statistically independent [8, 5]:

$$\begin{aligned}
 u_I &= \sqrt{\left(\frac{\partial I_{Ozz}}{\partial k_s} u_k\right)^2 + \left(\frac{\partial I_{Ozz}}{\partial T} u_T\right)^2 + \left(\frac{\partial I_{Ozz}}{\partial \zeta} u_\zeta\right)^2} \\
 &= \sqrt{\left(\frac{(1-\zeta^2)T^2}{4\pi^2} u_k\right)^2 + \left(\frac{(1-\zeta^2)Tk_s}{2\pi^2} u_T\right)^2 + \left(\frac{\zeta T^2 k_s}{2\pi^2} u_\zeta\right)^2}
 \end{aligned} \tag{4.77}$$

Noting that u_I depends on T and k_s , the torsion pendulum can be designed to meet a specified uncertainty range for the inertias being tested. Different springs can be used to tailor k_s to the desired experimental parameters. For the equipment presented here, u_k was determined by doubling the standard deviation of the calibration, $\hat{\sigma}_k$, to obtain a 95% confidence interval, which was calculated to be 1×10^{-4} N m/rad. Uncertainty u_T was determined for each experiment by doubling the standard deviation of the measurements collected to obtain a 95% confidence; this is expected to have an order of magnitude of 1×10^{-4} s. For a system with negligible friction and an oscillation period on the order of 1 s, the uncertainty of u_I is calculated to be on the order of 1×10^{-5} kg m² (Section 4.4.7).

4.4.6 Experimental Procedure

The experimental procedure to determine I_{Ozz} using our apparatus is outlined below.

1. Calibrate the torsion spring for positive angular displacements (Section 4.4.4).

2. Configure the electronics to record the half-period of oscillation during the positive displacement part of the motion.
3. Rigidly attach the rotation plate, attachment blocks, and test specimens in the desired position and orientation, to the torsion platform (Figure 4.8).
4. Collect dataset:
 - (a) Start the motion of the platform by providing an initial angular displacement θ_0 and releasing it from rest. A θ_0 of approximately $\pi/3$ is recommended.
 - (b) Record the amplitudes and half-periods of successive oscillations for the positive displacement part of the motion until the amplitudes have reduced by approximately 50%.
 - (c) Calculate T_k , the period of oscillation, assuming that it is twice the half-period recorded.
 - (d) Report any external factors that could have affected the dataset obtained.
5. Select a subset of the dataset that is free of outliers.
6. Calculate the mean \bar{T} and uncertainty u_T of the set of periods $\{T_k\}$ from the selected subset.
7. Investigate the decay of oscillations and deduce the friction model. In the case of viscous friction, calculate ζ (Equation (4.64)).
8. Use \bar{T} , u_T , k_s , u_k , ζ , and u_ζ to determine I_{Ozz} (Equation (4.60)) and its uncertainty u_I (Equation (4.77)).

Step 5 is required to reduce the experimental uncertainty. A desirable subset of the data can be determined by investigating any trends in the oscillation period. It is desired to find a region where the random experimental errors have a normal distribution, and the data is free from outliers. The measurements should also be tested to see whether their errors meet the i.i.d. assumption used by linear regression.

4.4.7 Apparatus Validation

A set of experiments was conducted to validate the torsional platform apparatus described in Section 4.4.1. These tests consisted of estimating I_{Ozz} of the rotating assembly in six attachment configurations and comparing the estimates to the inertias obtained from a SolidWorks model of this assembly in the same configurations (Figure 4.11).

The SolidWorks model is in close agreement with the physical assembly; for instance the mass of the rotation plate was reported to be 0.87041 kg and it was measured to be 0.870 kg on a calibrated

balance. The components can be expected to have constant densities, therefore, the inertia tensors are expected to be in close agreement.

Apparatus Validation Experiments

Six different configurations were selected and ten datasets were collected for each configuration following the procedure in Section 4.4.6. The system was configured by connecting the shaft to the rotating plate in six different locations. The plate was displaced laterally in the directions of x_O and y_O in Figure 4.9, and attached using the hole patterns near its center. The displacements used for each configuration are presented in Table 4.8. The SolidWorks model was set to match the experimental configurations of Table 4.8. The attachment blocks were removed for these validation tests.

Table 4.8: Position of the center of the rotating plate

Config.	x_O [mm]	y_O [mm]	z_O [mm]
1	0	0	0
2	6.92	0	0
3	13.83	0	0
4	20.74	0	0
5	0	6.92	0
6	0	13.83	0

The oscillation period and decaying amplitude measurements for 10 datasets in configuration 1 are presented in Figures 4.14 and 4.15 respectively. The bounded region on the plots represents the subset of measurements selected for further analysis.

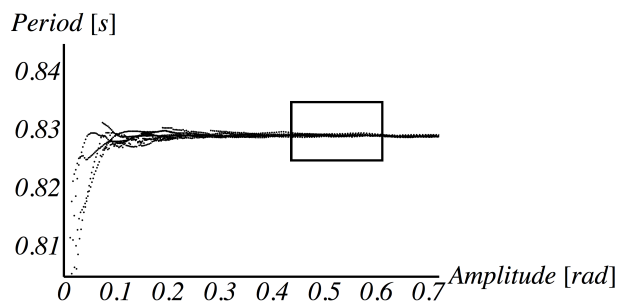


Figure 4.14: Example measurements of the oscillation period for ten datasets for configuration 1. The bounded region shows the subset of data used for further analysis.

The mean oscillation periods \bar{T} and corresponding 95% confidence intervals for ten datasets for the

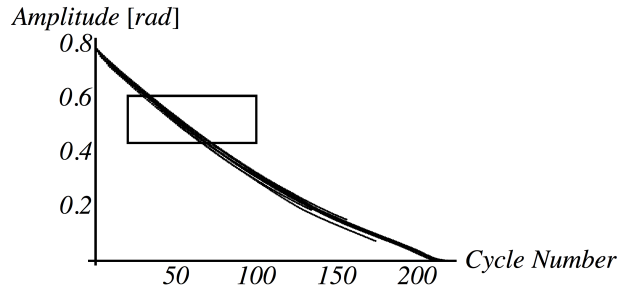


Figure 4.15: Example measurements of the oscillation amplitude for ten datasets for configuration 1. The bounded region shows the subset of data used for further analysis.

first four configurations are shown in Figure 4.16. Configurations 5 and 6 are not shown since they overlap with configurations 2 and 3 due to the symmetry of the rotation plate. The means and uncertainties of all the datasets are reported in Tables 4.9 and 4.10. For each dataset, at least 30 measurements were used to calculate the mean and standard error.

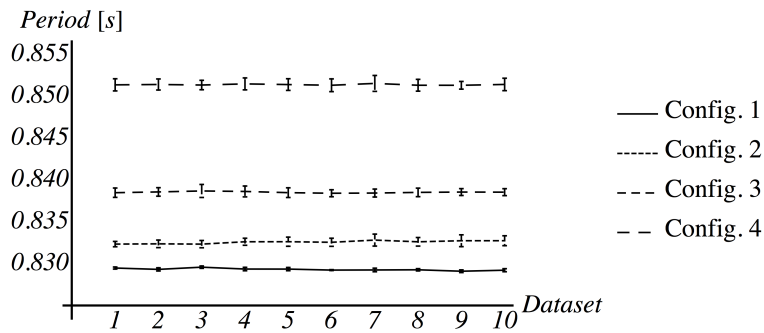


Figure 4.16: Mean oscillation period measurements for all datasets for configurations 1–4. The error bars represent the 95% confidence intervals of the average oscillation periods.

The consistent means between datasets of the same configuration demonstrate repeatability of the apparatus within the selected experimental data regions. The small uncertainties of each data set demonstrate that the equipment has high precision. Because of the high resolution and sampling rate of the angular encoder, the apparatus is able to detect very small changes in oscillation period, and therefore is sensitive to even very small changes of inertia between configurations.

Apparatus Friction

As discussed in Section 4.4.3, friction can be characterized by investigating successive amplitudes of oscillation. An example of the decreasing amplitudes for ten datasets in configuration 1 is presented

Table 4.9: Mean oscillation period, \bar{T} , for all datasets. Units in s.

	Configuration					
	1	2	3	4	5	6
1	0.82949	0.83235	0.83849	0.85137	0.83250	0.84004
2	0.82933	0.83238	0.83858	0.85141	0.83240	0.84010
3	0.82960	0.83235	0.83870	0.85135	0.83241	0.83995
4	0.82937	0.83263	0.83864	0.85148	0.83248	0.83998
5	0.82937	0.83264	0.83849	0.85140	0.83251	0.83997
6	0.82925	0.83257	0.83842	0.85132	0.83252	0.83994
7	0.82926	0.83283	0.83845	0.85154	0.83248	0.83989
8	0.82928	0.83263	0.83853	0.85132	0.83242	0.83992
9	0.82911	0.83275	0.83857	0.85132	0.83230	0.83985
10	0.82923	0.83276	0.83855	0.85142	0.83256	0.83993
Avg	0.82933	0.83259	0.83854	0.85139	0.83246	0.83996

Table 4.10: Uncertainty u_T for each dataset for 95% confidence. Units in s.

	Configuration					
	1	2	3	4	5	6
1	1×10^{-4}	3×10^{-4}	6×10^{-4}	7×10^{-4}	3×10^{-4}	3×10^{-4}
2	2×10^{-4}	5×10^{-4}	5×10^{-4}	7×10^{-4}	4×10^{-4}	6×10^{-4}
3	1×10^{-4}	4×10^{-4}	8×10^{-4}	6×10^{-4}	5×10^{-4}	4×10^{-4}
4	2×10^{-4}	4×10^{-4}	6×10^{-4}	7×10^{-4}	3×10^{-4}	3×10^{-4}
5	2×10^{-4}	5×10^{-4}	6×10^{-4}	7×10^{-4}	4×10^{-4}	3×10^{-4}
6	5×10^{-5}	5×10^{-4}	4×10^{-4}	8×10^{-4}	5×10^{-4}	3×10^{-4}
7	2×10^{-4}	7×10^{-4}	5×10^{-4}	9×10^{-4}	4×10^{-4}	3×10^{-4}
8	1×10^{-4}	5×10^{-4}	5×10^{-4}	7×10^{-4}	4×10^{-4}	4×10^{-4}
9	2×10^{-4}	7×10^{-4}	4×10^{-4}	5×10^{-4}	3×10^{-4}	4×10^{-4}
10	2×10^{-4}	6×10^{-4}	4×10^{-4}	7×10^{-4}	2×10^{-4}	4×10^{-4}
All	3×10^{-4}	6×10^{-4}	6×10^{-4}	7×10^{-4}	4×10^{-4}	4×10^{-4}

in Figure 4.15. The corresponding amplitude changes, $\Delta\theta$, and ratios, AR , of successive cycles, are presented in Figures 4.17 and 4.18. The calculated Coulomb friction torque τ_c and viscous friction damping ratio ζ , calculated from Equations (4.71) and (4.64), respectively, are presented in Figures 4.19 and 4.20. In the region of interest τ_c and ζ were calculated to be in orders of magnitude of 1×10^{-4} and 1×10^{-3} respectively. As previously shown in Section 4.4.3, Coulomb friction does not have an effect on the period of oscillation, but viscous friction does. The expected error in the estimate of the inertia due to ignoring viscous friction (Equation (4.61)) is in the order of 1×10^{-6} kg m², demonstrating that neglecting friction in our apparatus leads to a negligible contribution to error.

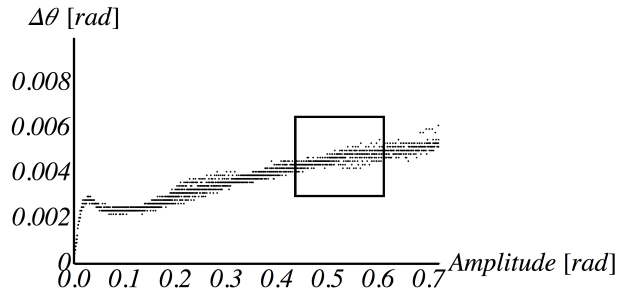


Figure 4.17: Amplitude differences $\Delta\theta$ for successive cycles of an apparatus friction experiment. The bounded region shows the range of data used for the analysis.

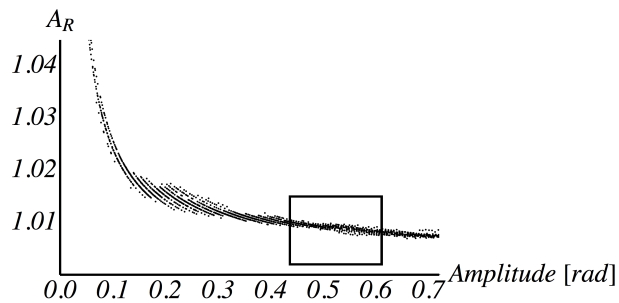


Figure 4.18: Amplitude ratios A_R for successive cycles of an apparatus friction experiment. The bounded region shows the range of data used for the analysis.

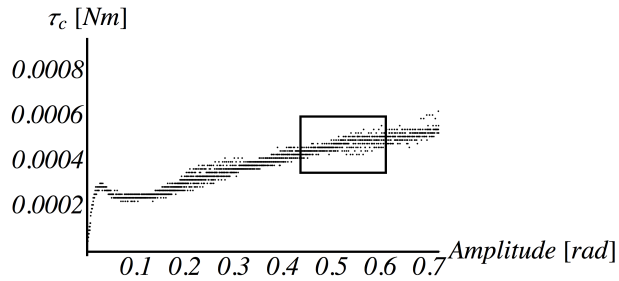


Figure 4.19: Friction torque τ_c for successive cycles of an apparatus friction experiment. The bounded region shows the range of data used for the analysis.

4.4.8 Equipment Validation Results

The mean of the periods and the uncertainties for each configuration were used to calculate I_{Ozz} and u_I , using Equations (4.53) and (4.77) respectively. The results for each configuration are presented in Table 4.11. The inertias obtained from SolidWorks are also tabulated, along with their difference with respect to the experimental results. The results indicate that the inertias were estimated with

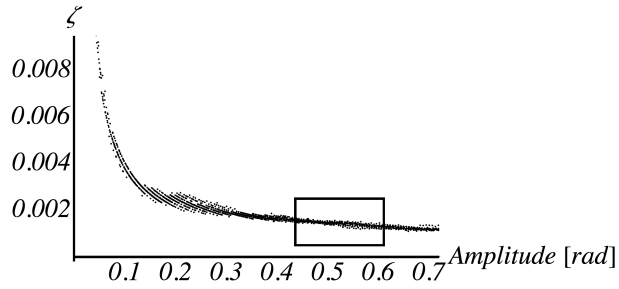


Figure 4.20: Damping ratio ζ for successive cycles of an apparatus friction experiment. The bounded region shows the range of data used for the analysis.

an uncertainty having a maximum order of magnitude of $1 \times 10^{-5} \text{ kg m}^2$, with a 95% confidence, and the difference to the CAD model was calculated to be on the order of $1 \times 10^{-5} \text{ kg m}^2$, which corresponds to less than 1% error. These results demonstrate that the torsion platform can be used to experimentally determine I_{Ozz} with high accuracy and precision, both on the order of $1 \times 10^{-5} \text{ kg m}^2$ in our apparatus.

Table 4.11: Equipment validation results

	\bar{T} s	\bar{u}_T s	I_{Ozz} kg m ²	u_I kg m ²	I_{OSM} kg m ²	$(I_{Ozz} - I_{OSM})$ kg m ²	%
1	0.8293	3×10^{-4}	7.091×10^{-3}	6×10^{-6}	7.088×10^{-3}	2×10^{-6}	0.03
2	0.8326	6×10^{-4}	7.147×10^{-3}	1×10^{-5}	7.130×10^{-3}	2×10^{-5}	0.2
3	0.8385	6×10^{-4}	7.249×10^{-3}	1×10^{-5}	7.255×10^{-3}	-6×10^{-6}	-0.08
4	0.8514	7×10^{-4}	7.473×10^{-3}	1×10^{-5}	7.463×10^{-3}	1×10^{-5}	0.1
5	0.8325	4×10^{-4}	7.144×10^{-3}	7×10^{-6}	7.130×10^{-3}	1×10^{-5}	0.2
6	0.8400	4×10^{-4}	7.274×10^{-3}	7×10^{-6}	7.255×10^{-3}	2×10^{-5}	0.3

4.5 Validation Experiments: Estimating the Inertia Properties of a Calibration Object

The proposed method and equipment were validated by estimating the inertia properties of a calibration object (Figure 4.21). The object consisted of a block of 6061-T6 Aluminum machined to the dimensions specified in Figure 4.7, which was previously used for the method verification calculations in Section 4.3.4. The mass of the machined block was directly measured to be 5.5740 kg, a difference of 0.07% with the earlier SolidWorks model.

This section presents two sets of experiments. First, nine configurations are used to estimate the inertial properties (minimum number of configurations). Then, as a comparison, 22 configurations

are used to solve for the inertial properties using a nonlinear least-squares estimation method, as described at the end of Section 4.3.3.

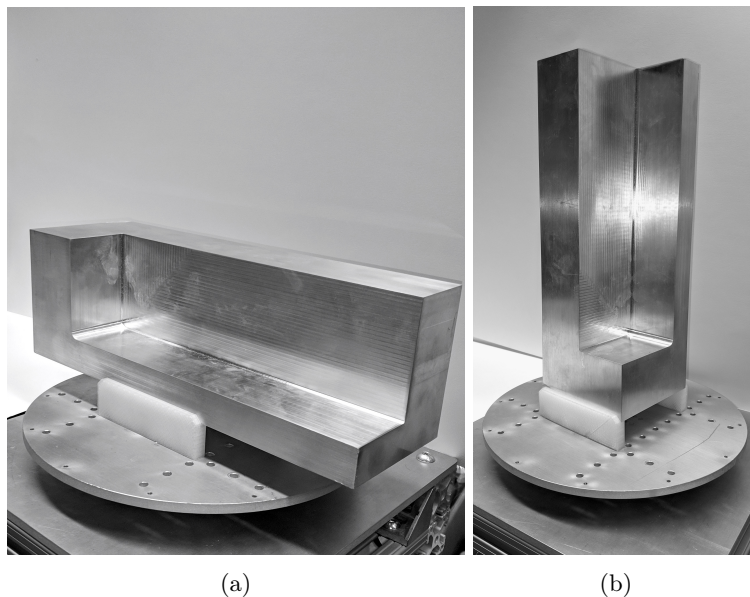


Figure 4.21: The aluminum block supported by attachment blocks on the torsion platform. Two configurations (a) and (b) are shown.

4.5.1 Estimating Inertial Properties With the Minimum Number of Configurations

Nine different configurations were selected, and ten data sets were collected for each. Similarly to Section 4.3.4, the body fixed frame \mathbf{B} was defined at the dimensional centre of the block, and mounted relative to the torsional platform's frame \mathbf{O} according to the configurations listed in Table 4.12. The attachment blocks were 3D printed. The hole patterns on the rotation plate were used to offset the block by x_B and y_B . The oscillation periods and corresponding uncertainties were used to calculate the inertia I_{Ozz} and uncertainty u_I for each configuration (Table 4.13). The calculated inertias were compared to the values reported by SolidWorks for each configuration. The results indicate that the uncertainties of the estimates have a maximum order of magnitude of 1×10^{-4} kg m², with 95% confidence, and the difference with the CAD model was calculated to be on the order of magnitude of 1×10^{-4} kg m², which corresponds to less than 1% error, except for the case of configuration 6. In that case the error is still on the order of magnitude of 1×10^{-4} kg m², but since the inertia value of that configuration is lower, a higher error percentage results.

Table 4.12: Validation Block Experiments

Config	β rad	α rad	x_B mm	y_B mm	z_B mm
1	0	0	0	0	0
2	0	0	0	6.9	0
3	0	0	10	0	0
4	0	$\pi/2$	0	0	0
5	0	$\pi/2$	0	0	6.9
6	$-\pi/2$	0	0	0	0
7	$-\pi/12$	0	15	0	15
8	0	$\pi/4$	0	5	5
9	$-\pi/12$	$\pi/4$	11.2	25	25

Table 4.13: Validation Experiments For 9 Configurations

	\bar{T} s	\bar{u}_T s	I_{Ozz} kg m ²	u_I kg m ²	I_{OSM} kg m ²	$(I_{Ozz} - I_{OSM})$ kg m ²	%
1	2.375	2×10^{-3}	5.094×10^{-2}	9×10^{-5}	5.117×10^{-2}	-2×10^{-4}	-0.4
2	2.370	3×10^{-3}	5.061×10^{-2}	1×10^{-4}	5.099×10^{-2}	-4×10^{-4}	-0.8
3	2.362	2×10^{-3}	5.027×10^{-2}	9×10^{-5}	5.045×10^{-2}	-2×10^{-4}	-0.4
4	2.368	5×10^{-3}	5.058×10^{-2}	2×10^{-4}	5.064×10^{-2}	-5×10^{-5}	-0.1
5	2.359	2×10^{-3}	5.014×10^{-2}	9×10^{-5}	5.003×10^{-2}	1×10^{-4}	0.2
6	1.300	2×10^{-3}	1.020×10^{-2}	4×10^{-5}	9.810×10^{-3}	4×10^{-4}	4.0
7	2.337	2×10^{-3}	4.901×10^{-2}	8×10^{-5}	4.886×10^{-2}	2×10^{-4}	0.3
8	2.401	2×10^{-3}	5.186×10^{-2}	1×10^{-4}	5.169×10^{-2}	2×10^{-4}	0.3
9	2.357	2×10^{-3}	4.965×10^{-2}	9×10^{-5}	4.959×10^{-2}	6×10^{-5}	0.1

The results of the nine experiments were used to estimate the inertial properties of the object as described in Section 4.3. The inertia tensor \mathbf{I} relative to the centre of mass frame \mathbf{C} , and the position vector $\mathbf{r}_{C/B}$ of the centre of mass with respect to the body fixed frame \mathbf{B} were calculated to be:

$$\mathbf{I}_{-9} = \begin{pmatrix} 0.00937 & 0.00020 & 0.00286 \\ 0.00020 & 0.04943 & 0.00150 \\ 0.00286 & 0.00150 & 0.04992 \end{pmatrix} \text{kg m}^2 \quad (4.78)$$

$$\mathbf{r}_{C/B}_{-9} = \begin{pmatrix} -0.0110 & -0.0078 & -0.0093 \end{pmatrix}^T \text{m} \quad (4.79)$$

The differences between the SolidWorks-reported inertia tensor and CM position vector and the above values are:

$$\mathbf{I}_{-9_{err}} = \begin{pmatrix} 4 \times 10^{-4} & -9 \times 10^{-4} & 5 \times 10^{-4} \\ -9 \times 10^{-4} & -2 \times 10^{-4} & 3 \times 10^{-4} \\ 5 \times 10^{-4} & 3 \times 10^{-4} & -3 \times 10^{-4} \end{pmatrix} \text{kg m}^2 \quad (4.80)$$

$$\mathbf{r}_{C/B_9_err} = \begin{pmatrix} -4 \times 10^{-4} & -2.1 \times 10^{-3} & -2.1 \times 10^{-3} \end{pmatrix}^T \text{ m} \quad (4.81)$$

The small errors indicate that the inertial properties can be estimated with high accuracy. The two millimeter accuracy of the estimate of the position of the centre of mass corresponds to less than 1% of the maximum linear dimension of the block. The errors of the inertia tensor are approximately 1% of the largest component, except for the case of $I_{xy,\{1,2\}}$ which has an error of approximately 2% of the largest component. A larger error of $I_{xy,\{1,2\}}$ is expected because the estimates of the other components of the inertia tensor and position of the centre of mass are used for its calculation, leading to an accumulation of error in Equation (4.42).

In addition to the sources of uncertainty discussed before, the experiments have other sources of error. The most significant is the positioning of the object. Errors introduced by the configuration parameters x_B , y_B , z_B , β , and α need to be minimized. The attachment blocks to support the object may need to be machined with high tolerances to reduce the errors, and additional direct measurements of the rotation angles and positioning may be required. The rotation angles can be precisely measured with an Inertial Measurement Unit (IMU), typically used in robotic systems, and the positioning can be measured with digital calipers or laser range finders.

4.5.2 Estimating Inertial Properties With Nonlinear Least Squares

Twenty-two experimental configurations were used (Table 4.14), with measurement results listed in Table 4.15. In this experiment, the Conjugate Gradient nonlinear estimation method was used on Equation 4.18, as previously mentioned at the end of Section 4.3.3. This yields the inertia tensor \mathbf{I} and centre of mass position vector $\mathbf{r}_{C/B}$ as

$$\mathbf{I}_{_22} = \begin{pmatrix} 0.00904 & 0.00019 & 0.00274 \\ 0.00019 & 0.04917 & 0.00141 \\ 0.00274 & 0.00141 & 0.05020 \end{pmatrix} \text{ kg m}^2 \quad (4.82)$$

$$\mathbf{r}_{C/B_22} = \begin{pmatrix} -0.01158 & -0.0054 & -0.0118 \end{pmatrix}^T \text{ m} \quad (4.83)$$

The differences between the SolidWorks model values and the estimated values were:

$$\mathbf{I}_{obj_22_err} = \begin{pmatrix} 1 \times 10^{-4} & -9 \times 10^{-4} & 4 \times 10^{-4} \\ -9 \times 10^{-4} & -3 \times 10^{-5} & 3 \times 10^{-4} \\ 4 \times 10^{-4} & 3 \times 10^{-4} & -6 \times 10^{-5} \end{pmatrix} \text{ kg m}^2 \quad (4.84)$$

$$\mathbf{r}_{C/B_22_err} = \begin{pmatrix} -5 \times 10^{-4} & -2 \times 10^{-4} & -2 \times 10^{-4} \end{pmatrix}^T \text{ m} \quad (4.85)$$

Table 4.14: 22 Configurations For Validation Block Experiments

Config	β rad	α rad	x_B mm	y_B mm	z_B mm
1	0	0	0	0	0
2	0	0	5.0	0	0
3	0	0	10.	0	0
4	0	0	20.	0	0
5	0	0	0	6.9	0
6	0	0	0	-6.9	0
7	0	0	0	14.	0
8	0	$\pi/2$	0	0	0
9	0	$\pi/2$	5.0	0	0
10	0	$\pi/2$	10.	0	0
11	$-\pi/2$	0	0	0	0
12	$-\pi/2$	0	0	0	5.0
13	$-\pi/2$	0	0	0	10.
14	$-\pi/2$	0	0	6.9	0
15	$-\pi/2$	0	0	6.9	10.
16	$-\pi/2$	0	0	14.	10.
17	0	$\pi/2$	0	0	6.9
18	0	$\pi/2$	0	0	14.
19	0	$\pi/4$	0	5.0	5.0
20	0	$\pi/4$	10.	5.0	5.0
21	$-\pi/12$	0	15.	0	15.
22	$-\pi/12$	$\pi/4$	11.2	25.	25.

In the present case the position of the centre of mass was estimated with sub-millimeter accuracy, and the error of the diagonal components of the inertia matrix were reduced by a factor of approximately four. The estimates of the off-diagonal components were not significantly improved because no configurations had different angles α and β .

Table 4.15: Validation Experiments For 22 Configurations

	\bar{T}	\bar{u}_T	I_{Ozz}	u_I	I_{OSM}	$(I_{Ozz} - I_{OSM})$	
	s	s	kg m ²	kg m ²	kg m ²	kg m ²	%
1	2.375	$2. \times 10^{-3}$	5.094×10^{-2}	9×10^{-5}	5.117×10^{-2}	-2×10^{-4}	-0.4
2	2.363	$2. \times 10^{-3}$	5.033×10^{-2}	1×10^{-4}	5.067×10^{-2}	-3×10^{-4}	-0.7
3	2.362	$2. \times 10^{-3}$	5.027×10^{-2}	9×10^{-5}	5.045×10^{-2}	-2×10^{-4}	-0.4
4	2.374	$2. \times 10^{-3}$	5.090×10^{-2}	8×10^{-5}	5.086×10^{-2}	4×10^{-5}	0.1
5	2.370	$3. \times 10^{-3}$	5.061×10^{-2}	1×10^{-4}	5.099×10^{-2}	-4×10^{-4}	-0.8
6	2.402	$3. \times 10^{-3}$	5.221×10^{-2}	1×10^{-4}	5.187×10^{-2}	3×10^{-4}	0.7
7	2.396	$3. \times 10^{-3}$	5.172×10^{-2}	1×10^{-4}	5.135×10^{-2}	4×10^{-4}	0.7
8	2.368	$5. \times 10^{-3}$	5.058×10^{-2}	2×10^{-4}	5.064×10^{-2}	-5×10^{-5}	-0.1
9	2.361	$3. \times 10^{-3}$	5.023×10^{-2}	1×10^{-4}	5.014×10^{-2}	9×10^{-5}	0.2
10	2.352	$3. \times 10^{-3}$	4.981×10^{-2}	1×10^{-4}	4.993×10^{-2}	-1×10^{-4}	-0.2
11	1.300	$2. \times 10^{-3}$	1.020×10^{-2}	4×10^{-5}	9.810×10^{-3}	4×10^{-4}	4.0
12	1.271	$2. \times 10^{-3}$	9.430×10^{-3}	4×10^{-5}	9.317×10^{-3}	1×10^{-4}	1.0
13	1.257	$2. \times 10^{-3}$	9.065×10^{-3}	4×10^{-5}	9.102×10^{-3}	-4×10^{-5}	-0.4
14	1.290	$2. \times 10^{-3}$	9.869×10^{-3}	6×10^{-5}	9.639×10^{-3}	2×10^{-4}	2.0
15	1.255	$1. \times 10^{-3}$	8.954×10^{-3}	3×10^{-5}	8.931×10^{-3}	2×10^{-5}	0.3
16	1.281	$1. \times 10^{-3}$	9.492×10^{-3}	4×10^{-5}	9.292×10^{-3}	2×10^{-4}	2.0
17	2.359	$2. \times 10^{-3}$	5.014×10^{-2}	9×10^{-5}	5.003×10^{-2}	1×10^{-4}	0.2
18	2.361	$2. \times 10^{-3}$	5.007×10^{-2}	9×10^{-5}	4.995×10^{-2}	1×10^{-4}	0.2
19	2.401	$2. \times 10^{-3}$	5.186×10^{-2}	1×10^{-4}	5.169×10^{-2}	2×10^{-4}	0.3
20	2.390	$2. \times 10^{-3}$	5.133×10^{-2}	1×10^{-4}	5.098×10^{-2}	3×10^{-4}	0.7
21	2.337	$2. \times 10^{-3}$	4.901×10^{-2}	8×10^{-5}	4.886×10^{-2}	2×10^{-4}	0.3
22	2.357	$2. \times 10^{-3}$	4.965×10^{-2}	9×10^{-5}	4.959×10^{-2}	6×10^{-5}	0.1

4.6 Case Study: Estimating the Inertia Tensor of a UAV

The proposed method and equipment were used to estimate the inertia tensor of a small robotic system. A commercially available Parrot Bebop 2 UAV was used for these experiments (Figure 4.22). The UAV has a mass of 504 g. As shown, the UAV was attached to the torsion platform using a lightweight support structure. The orientation and position of the UAV were set using a two degree of freedom gimbal and hole patterns in the support structure. The orientation angles of the UAV were measured using an IMU.

The oscillations of the UAV were tested in nine configurations (Table 4.16). Five datasets were collected for each configuration. The base frame O was defined at the intersection of the pivot point of the gimbal and the rotation axis of the torsion platform. This placement is necessary to directly control the rotation angles α and β with the gimbal's degrees of freedom. A misalignment would introduce systematic errors into the estimates.

Employing the procedure outlined in Section 4.4.6, the estimated inertia and position of the centre

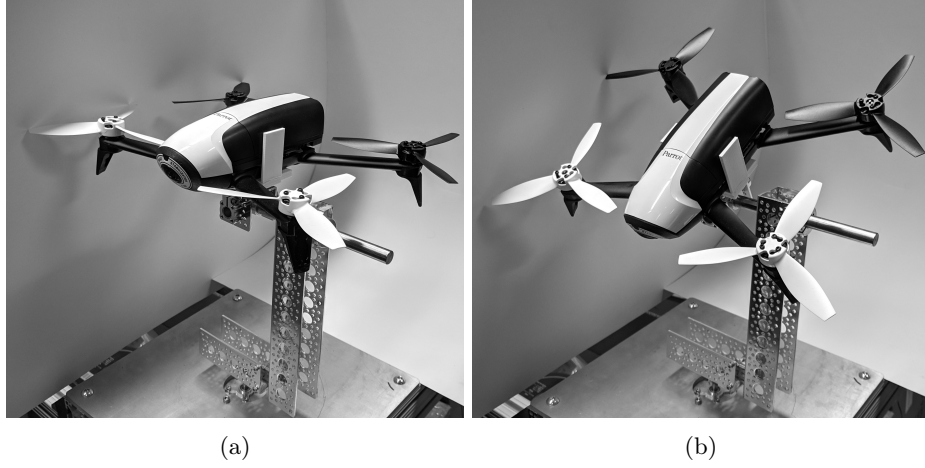


Figure 4.22: The UAV supported by a lightweight metal structure and gimbal mounted on torsional platform. Two configurations (a) and (b) are shown.

Table 4.16: Configurations For UAV Experiments

Config	β rad	α rad	x_B mm	y_B mm	z_B mm	I_{Ozz} kg m ²	u_I kg m ²
1	0	0	0	0	0	3.380×10^{-3}	1.2×10^{-5}
2	0	0	0	6.9	0	3.404×10^{-3}	1.2×10^{-5}
3	0	0	6.9	0	0	3.359×10^{-3}	1.1×10^{-5}
4	0	$\frac{\pi}{2}$	0	0	0	4.513×10^{-3}	1.3×10^{-5}
5	0	$-\frac{\pi}{2}$	0	0	19.1	5.999×10^{-3}	9×10^{-6}
6	$-\frac{\pi}{2}$	0	0	0	0	4.422×10^{-3}	1.6×10^{-5}
7	$-\frac{\pi}{4}$	0	0	0	0	4.301×10^{-3}	9×10^{-6}
8	0	$\frac{\pi}{4}$	0	0	0	4.138×10^{-3}	7×10^{-6}
9	$-\frac{\pi}{4}$	$\frac{\pi}{4}$	0	0	0	4.726×10^{-3}	1.7×10^{-5}

of mass were estimated to be:

$$\mathbf{I}_{\text{UAV}} = \begin{pmatrix} 0.00210 & 0.00023 & 0.00018 \\ 0.00023 & 0.00217 & 0.00019 \\ 0.00018 & 0.00019 & 0.00336 \end{pmatrix} \text{kg m}^2 \quad (4.86)$$

$$\mathbf{r}_{C/B_UAV} = \begin{pmatrix} -0.0065 & 0.0000 & 0.0678 \end{pmatrix}^T \text{m} \quad (4.87)$$

As shown in Figure 4.23, we define a reference point on the UAV located at the geometric centre of the four propellers and on the surface of the battery attachment plane. By direct measurement, the position vector of the point relative to the gimbal-centered frame O is $\mathbf{r}_p = (-6, 0, 67.9)^T$ mm.

Combined with the \mathbf{r}_{C/B_UAV} estimate, the position of the centre of mass of the UAV with respect to the geometric reference point is thus

$$\mathbf{r}_{CM_UAV} = \begin{pmatrix} -0.5 & 0.0 & -0.1 \end{pmatrix}^T \text{ mm} \quad (4.88)$$

The small values in \mathbf{r}_{CM_UAV} are as expected, since UAV designers place the centre of mass as close as possible to the centre of pressure in order to simplify flight control.

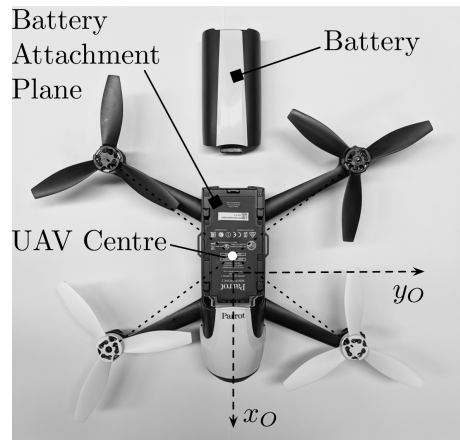


Figure 4.23: Location of UAV centre reference point. Frame O origin is located under and forward.

4.7 Conclusions and Future Work

This paper described the development and construction of a torsional platform and novel calculation method used to determine the inertia tensor and center of mass location of small rigid bodies with high precision. The design and test method were described in detail to be reproducible. The experimental procedure requires measuring the oscillation period of the system in at least nine different configurations. A larger number of configurations can be used with a nonlinear least squares method to obtain more precise estimates. The proposed calculation method is not specific to the proposed torsion platform design, and could be used with other measurement systems.

The theoretical method was first verified in simulation, then the torsion platform was calibrated and validated in experiments. A quantitative uncertainty analysis was performed, demonstrating the high precision of the resulting estimates and showing that friction effects could be neglected. The inertia tensor of a precisely machined aluminum block was estimated and compared against SolidWorks, yielding errors of approximately 1% and orders of magnitude 1×10^{-4} , while the position

vector of the centre of mass was estimated with an error of less than 1% of the maximum linear dimension. Finally, the inertia tensor of a commercially available quadrotor UAV was measured using the proposed apparatus, demonstrating its interest for broader applications such as model-based control and simulation.

The overall system offers an alternative to commercial high-precision platforms at a fraction of their cost. While the achieved 1% error cannot match the 0.1% accuracy offered by the highest-end commercial instruments, it can still be considered as highly accurate for applications such model-based control.

Future work will focus on using the apparatus to build a catalogue of estimated inertia parameters for a variety of commercially available small robotic systems. A scaled-up version of the apparatus will also be built in order to estimate inertias of larger-scale robots.

4.8 Acknowledgment

This work was partially supported by the National Science and Engineering Research Council of Canada (NSERC).

4.9 References

- [1] R A B Almeida, A P V Urgueira, and N M M Maia. Evaluation of the Performance of Three Different Methods Used in the Identification of Rigid Body Properties. *Shock and Vibration*, 15(3-4):467–479, 2008.
- [2] Raquel A B Almeida, António P V Urgueira, and Nuno M M Maia. Further developments on the estimation of rigid body properties from experimental data. *Mechanical Systems and Signal Processing*, 24(5):1391–1408, July 2010.
- [3] Altra-Industrial-Motion. Moment of inertia measurement instrument products inertia dynamics. www.idicb.com/products/moment-of-inertia-measurement-instruments/moment-of-inertia-measurement-instruments, 03 2019.
- [4] J P Barreto and L E Muñoz. Low uncertainty method for inertia tensor identification. *Mechanical Systems and Signal Processing*, 68:207–216, February 2016.
- [5] T. G. Beckwith, Roy D. Marangoni, and John H. Lienhard. *Mechanical measurements*. Upper Saddle River, NJ: Pearson Prentice Hall, sixth edition edition, 2007.

- [6] Renato Brancati, Riccardo Russo, and Sergio Savino. Method and equipment for inertia parameter identification. *Mechanical Systems and Signal Processing*, 24(1):29–40, January 2010.
- [7] C Doniselli, M Gobbi, and G Mastinu. Measuring the inertia tensor of vehicles. *Vehicle System Dynamics*, 37(sup1):301–313, January 2002.
- [8] R. S. Figliola and Donald E. Beasley. *Theory and design for mechanical measurements*. Hoboken: John Wiley and Sons, sixth edition edition, 2015.
- [9] G Genta and C Delprete. Some considerations on the experimental determination of moments of inertia. *Meccanica*, 29(2):125–141, 1994.
- [10] A Gentile, L Mangialardi, G Mantriota, and A Trentadue. Measurement of the inertia tensor: An experimental proposal. *Measurement*, 14(3-4):241–254, 1995.
- [11] M Gobbi, G Mastinu, and G Previati. A method for measuring the inertia properties of rigid bodies. *Mechanical Systems and Signal Processing*, 25(1):305–318, January 2011.
- [12] Massimiliano Gobbi, Giampiero Mastinu, Mario Pennati, and Giorgio Previati. InTenso+ System: Measured Centre of Gravity Locations and Inertia Tensors of Road Vehicles. In *ASME 2014 International Design Engineering Technical Conferences and Computers and Information in Engineering Conference*, page V003T01A037. ASME, August 2014.
- [13] Cyril M Harris and Allan G Piersol. *Harris’ Shock and Vibration Handbook*. McGraw-Hill Companies, November 2001.
- [14] Daniel J. Inman. *Engineering Vibration*. Pearson, 4th edition, 2013.
- [15] Sepehr P Khaligh, Farbod Fahimi, and Charles Robert Koch. A system identification strategy for nonlinear model of small-scale unmanned helicopters. *Journal of the American Helicopter Society*, 61(4):1–13, October 2016.
- [16] R Klopper and H P Groebelbauer. A Multi-Sided Kinematic Coupling Combined with an Air Bearing Pendulum for Fast and Accurate Mass Property Measurements. In *13th European Conference on Spacecraft Structures, Materials Environmental Testing*, page 18, June 2014.
- [17] Ou Ma, Hung Dang, and Khanh Pham. On-orbit identification of inertia properties of spacecraft using robotics technology. In *AIAA Guidance, Navigation and Control Conference and Exhibit*, page 139, Reston, Virginia, 2007. American Institute of Aeronautics and Astronautics.
- [18] G Mastinu, M Gobbi, and C M Miano. The Influence of the Body Inertia Tensor on the Active Safety and Ride Comfort of Road Vehicles. *International Body Engineering Conference & Exhibition and Automotive & Transportation Technology Congress*, 1:2002–01–2058, July 2002.

- [19] E Mucchi, S Fiorati, R Di Gregorio, and G Dalpiaz. Determining the Rigid-Body Inertia Properties of Cumbersome Systems: Comparison of Techniques in Time and Frequency Domain. *Experimental Techniques*, 35(3):36–43, May 2011.
- [20] Seyed Yaser Nabavi Chashmi and Seyed Mohammad-Bagher Malaek. Fast estimation of space-robots inertia parameters: A modular mathematical formulation. *Acta Astronautica*, 127:283–295, October 2016.
- [21] Resonic. Resonic k. <http://www.resonic.de/resonic-k.php>, 03 2019.
- [22] Carsten Schedlinski and Michael Link. A Survey of Current Inertia Parameter Identification Methods. *Mechanical Systems and Signal Processing*, 15(1):189–211, 2001.
- [23] SMARTMechanical-Company. Intensino full mass properties measurement. <http://www.smartmechanical-company.it/en/products/intensino#information>, 03 2019.
- [24] SMARTMechanical-Company. Intenso full mass properties measurement. <http://www.smartmechanical-company.it/en/products/intenso#information>, 03 2019.
- [25] SpaceElectronics. Ksr cg moi series. <https://www.space-electronics.com/Products/ksr-cg-moi-series>, 03 2019.
- [26] SpaceElectronics. Mp weight cg moi series. <https://www.space-electronics.com/Products/mpweight-cg-moi-series>, 03 2019.
- [27] SpaceElectronics. Xr production series. <https://www.space-electronics.com/Products/xr-production-series>, 03 2019.
- [28] Tixian Tian, Hongzhou Jiang, Zhizhong Tong, Jingfeng He, and Qitao Huang. An inertial parameter identification method of eliminating system damping effect for a six-degree-of-freedom parallel manipulator. *Chinese Journal of Aeronautics*, 28(2):582–592, April 2015.
- [29] Gerardo Ortiz Torres, Ricardo Schacht Rodriguez, Juan Reyes Reyes, Carlos Daniel Garcia Beltran, Maria Eusebia Guerrero Sanchez, and Carlos Manuel Astorga Zaragoza. Development of experimental platform for control system of a planar vertical take-off and landing unmanned aerial vehicle. *IEEE Latin America Transactions*, 16(2):342–349, 2018.
- [30] P E Uys, P S Els, M J Thoresson, K G Voigt, and W C Combrinck. Experimental determination of moments of inertia for an off-road vehicle in a regular engineering laboratory. *International Journal of Mechanical Engineering Education*, 34(4):291–314, 2006.
- [31] Hongwu Wang, Garrett G Grindle, Samuel Connor, and Rory A Cooper. An experimental method for measuring the moment of inertia of an electric power wheelchair. *Conference proceedings : ... Annual International Conference of the IEEE Engineering in Medicine*

- and Biology Society. IEEE Engineering in Medicine and Biology Society. Annual Conference*, 2007:4798–4801, 2007.
- [32] Kurt Wiener and Richard Boynton. Using the Moment of Inertia Method to Determine Product of Inertia. In *51st Annual Conference of the Society of Allied Weight Engineers*, pages 1–29, Hartford, Connecticut, 1992.
- [33] Kun Zhai, Tianshu Wang, and Dongbo Meng. Optimal excitation design for identifying inertia parameters of spacecraft. *Acta Astronautica*, 140:370–379, November 2017.
- [34] Tianjun Zhu and Fei Li. Experimental investigation and performance analysis of inertia properties measurement for heavy truck cab. *Advances in Mechanical Engineering*, 7(11):168781401561862, November 2015.
- [35] Tianjun Zhu, Fudong Zhang, Jianying Li, Fei Li, and Changfu Zong. Development Identification Method of Inertia Properties for Heavy Truck Engine Based on MIMS Test Rig. *MATEC Web of Conferences*, 153(6):04009, February 2018.

Chapter 5

A UGV-based modular robotic manipulator for soil sampling and terramechanics investigations on mine waste

Abstract

Unmanned systems have been used to collect samples and investigate soil properties in difficult to access environments. Mine waste monitoring can benefit from advanced robotic systems that are able to collect soft soil samples and geotechnical measurements used to improve waste treatment processes, monitor the environment, and determine whether a deposit is ready for reclamation. The design of a robotic arm and two payloads are presented for evaluating soil properties near the surface. The robotic arm was developed to be modular and sufficiently rugged for field deployment. It is used to carry our custom payloads: a surface sampler to collect undisturbed surface samples from soft terrain, or an instrumented wheel for terramechanics-based soil parameter estimation. The developed system is successfully tested in field experiments.

5.1 Introduction

Mobile robots have been used for environmental monitoring and in-situ investigations in hazardous and challenging terrains, on Earth as well as on other planets [42, 40]. On Earth, environmental

monitoring is done for both scientific and industrial analyses of soil characteristics, aquatic zones, ecological systems, and their interactions. Measuring parameters of interest and collecting samples for study and analysis is predicated on the ability to deploy instruments and samplers to locations of interest. In the case of mine waste or areas affected by mining activities, monitoring programs can greatly benefit from recent developments of autonomous mobile robots which can collect samples and measure environmental parameters of interest [34]. Mine waste storage areas are required by regulation to be monitored until the affected regions are reclaimed and restored to a state equivalent to the undisturbed condition, at which point closure certificates are issued [43]. Until then, these partially reclaimed areas are significant liabilities to the mining companies [12].

Inadequate mine waste disposal practices can lead to poor soil performance and in some cases even catastrophic failures [39]. Fluid mine waste (tailings) require environmental monitoring and characterization throughout the stages of being safely contained, treated, and remediated. Their environmental impacts, treatment effects, and remediation processes are continuously monitored [21].

Unmanned ground vehicles (UGVs) instrumented with specialized tools and sensors can reduce the costs and difficulty of working in hazardous terrains, provide access to conventionally inaccessible locations, and reduce the risks to human workers [34].

An example of a tailings disposal process is mining of the Athabasca Oil Sands in Alberta, Canada, shown in Figure 5.1. The fluid waste from bitumen extraction processes, known as oil sands tailings, is composed of sands, silts, clays, process-affected water, and residual bitumen [28]. Fluid Fine Tailings (FFT) are deposited in ponds surrounded by sand dykes for initial settling of solids and recycling of process-affected water [9]. The suspended solids slowly settle as a soft mud at the bottom of the pond. This material is called Mature Fine Tailings (MFT), defined as FFT with a sand-to-fines ratio that is less than 0.3, and a solids content greater than 30 % w.t. [1]. MFT does not readily consolidate and cannot be reclaimed without further treatment [29]. Many treatment options have been researched, and several technologies have been deployed to increase water recovery, densify the MFT, and consolidate the tailings into a soil. Examples of processes implemented at commercial scale include conventional thickening, centrifugation, coagulation, atmospheric drying, and flocculation, often with sand added to increase the strength of the final deposit. It is becoming common to combine several of these processes. Standard industrial practices for treating fine tailings have been reviewed in [41].

Figure 5.2 depicts a Dedicated Disposal Area (DDA). These storage facilities are required to be monitored for legislative compliance [43], environmental performance [35], and operational decisions regarding repairs to DDAs or additional treatments [19]. Monitoring treatment processes in a timely manner is key to determining which setpoints are effective for processing [26].



Figure 5.1: Example of tailings processing and storage.

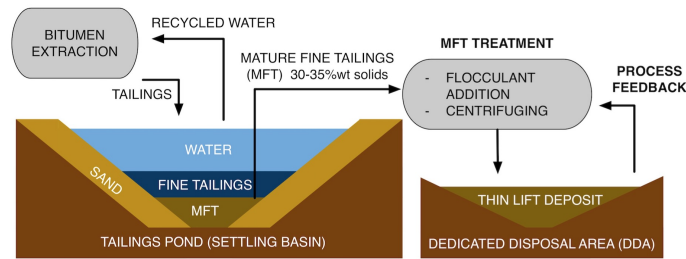


Figure 5.2: Oil sands tailings dedicated disposal area, Athabasca, Alberta.

Conditions within the dedicated disposal area, such as soil shear strength and tailings fines capture rates, need to be regularly measured to comply with environmental regulations [3]. This is traditionally carried out by manual terrain sampling and measurement campaigns by human workers. In the case of tailings ponds, the terrain may be water-capped or have low strength, and the materials themselves may be toxic to people. In these cases, human monitoring activities are limited in scope, expensive to perform, and potentially hazardous to the workers. The difficulty of gathering data increases monitoring uncertainty and may delay reclamation activities [24].

Deploying UGVs outfitted with autonomous or remotely controlled sampling and measurement instruments is an attractive option, which greatly increases worker safety as well as the speed and

coverage of the sampling. UGVs are lighter than vehicles that carry humans and thus cause less disturbances to the deposits, and can also precisely georeference the collected data for later analysis. Clearly such unmanned site investigations can deliver monitoring data quickly and safely, which motivates the development of novel robotic tools for measurement and sampling. In previous work, a UGV was developed for mine waste monitoring and experimentally validated in field experiments [34]. This paper extends that work by developing new tools for undisturbed terrain sampling and parameter estimation.

Soil samples are used to determine geotechnical properties such as solids content, particle size distribution, and Atterberg limits [14]. Depending on the application, samples can also be analyzed for mineral content, and properties such as cation exchange activity (methylene blue index) [15]. Identifying the parameters of soil models can also yield useful information. For instance, undrained shear strength is important to determine static stability of tailings impoundments [39], assess load-bearing limits, and track consolidation progress. Shear strength can also help to determine whether the storage facility meets design criteria, and if it is ready for reclamation or requires additional work. Shear strength is also important for terrain trafficability studies [44].

This paper details the development of a robotic manipulator and end-effectors for soil characterization and sampling. The end-effectors were designed for two main tasks: i) excavating and collecting soil samples; and ii) estimating soil properties using an instrumented terramechanics wheel. Limitations of current sampling and measurement equipment are presented. Advantages of the proposed solutions are noted, including dexterity, payload modularity, and capability for deployment onboard a UGV platform. The equipment was tested in laboratory conditions and field trials to validate these claims.

The remainder of this paper is structured into five sections. Section 2 reviews the literature on robotic systems for environmental monitoring and sampling, and instruments for terramechanics model parameter estimation. Section 3 provides a detailed description of the proposed robotic manipulator and its end-effectors. Section 4 presents tests of the equipment and field trials. Conclusions and recommendations for future work are given in Section 5.

5.2 Background and Literature Review

This section reviews the state of the art in UGVs capable of environmental monitoring, recent advances in robotics relevant to mine waste surface sampling, and parameter estimation from wheel-soil interactions.

5.2.1 UGVs for Environmental Monitoring

Unmanned systems have demonstrated the capability to access difficult terrain, make measurements, and collect samples. The development of new systems and their implementation in real world applications are active areas of research. Early deployments of remotely operated vehicles with tracks allowed rudimentary surveys and certain simple tasks to be carried out in hazardous industrial environments, such as nuclear power plants [38], as well as risky natural environments such as the calderas of volcanoes. Examples of such systems are hybrid robots to study the Amazon rain forest [13] and autonomous surface vessels to monitor water resources [18]. Aerial and ground robots are also seeing more use [8], showcasing the benefits of using unmanned solutions to work in areas too dangerous for human workers [24].

Robotic systems can be used to detect anomalies and identify faults and their locations [23]. Collaborations between different robots, such as unmanned aerial vehicles (UAVs) and UGVs, can achieve better results in timeliness and accuracy of measurements [23]. Work has been completed towards solving the limitations of aerial vehicles that are able to travel quickly, but have limited payload capacities, mission durations, and ability to interact with the environment by direct contact [25]. Also, UAVs have legal restrictions on where they can be flown, and have exclusion zones near airports, built-up areas, and restricted air space. On the other hand, UGVs are less mobile but are well suited to carry large payloads, such as specialized sensors, geotechnical and sampling tools, and extra batteries or other power sources for longer endurance.

UGVs have been used in the mapping of underground mines [6, 16, 31] that are too dangerous for humans to access. Application of robotics in mining is reviewed in [27], and includes activities such as dozing, excavation, haulage, mapping, surveying, drilling, and explosives handling.

5.2.2 Robotic Surface and Subsurface Sampling

Sampling payloads for UGVs have been developed for space exploration, such as regolith sampling tools for sample-return missions [40]. Robots designed for Lunar regolith core drilling have been proposed [42]. Drilling and on-board sample analysis payloads are being used in Mars rovers [2] and have conducted the first extraterrestrial drilling of rocks [17]. Advanced drilling tools have been developed to identify regolith mechanical properties [49], and miniature flexible samplers have been designed for lunar explorations to reduce weight, volume, and power requirements [22].

Previous work by part of our group produced a UGV for collecting subsurface samples from oil sands tailings DDAs [34]. This robot, RTC-I shown in Figure 5.3, drilled through the crust of the deposit and deployed an industry-standard mud sampler to collect saturated tailings samples at

depths of up to 2m. The samples were then analyzed to measure water, mineral, and bitumen content and solids concentration [34].

New methods for remote tailings testing require different types of samples. Tailings characterization has been conducted using non-contact techniques such as hyperspectral observations. Broad-band infrared reflectance spectra have been used for bitumen content estimation [37]. Prediction of water content and normalized evaporation of oil sands tailings has been demonstrated in a laboratory setting with potential for field applications [10]. Validation of the techniques requires calibration samples, which need to be collected from the surface of the deposit and must be kept with the surface intact.

To address this requirement, a scoop-type design for collecting undisturbed surface samples was initially conceptualized for UAV-based deployment [32]. The soil deformation while sampling was minimized by the design's geometry, in which the axis of curvature of the scoop was placed at the axis of rotation of the mechanism, keeping reaction forces low and reducing power consumption during sampling [30]. The mass of the sample was limited to the payload capacity of the UAV, and the system has not been tested in outdoor conditions.



Figure 5.3: RTC-I collecting subsurface samples from an oil sands tailings DDA.

Novel geotechnical tools have been developed, such as an automatic vane shear test tool for undrained shear strength estimation of cohesive soils which can be deployed from a UGV [33].

These tools can be used to independently validate soil parameters estimated with methods discussed in this paper and other papers.

5.2.3 Estimating Soil Parameters Using Terramechanics Wheels

Wheel-soil interaction models have been used to study loads on a wheel of a vehicle with respect to its motion and soil parameters such as cohesion stress and internal friction angle [4, 46, 45]. These methods have been applied to determine mobility in rough terrain, investigate trafficability of an environment, and estimate soil properties [47]. They have also been used in high fidelity simulations of planetary rovers [50] and real-time simulations [11, 20].

Our past work demonstrated terramechanics-based soil parameter estimation from onboard a wheeled platform on a mine site [34]. One of the wheels of the robot was instrumented to collect measurements as it moved over dry sand on a tailings dyke (Figure 5.4). These measurements were used to estimate the cohesion and internal friction angle of the terrain, which required the terrain to have sufficient load bearing capacity to support the robot.



Figure 5.4: RTC-I conducting terramechanics experiments on dry tailings sand.

The work reported here presents the development of a novel instrumented terramechanics wheel deployed on a robotic arm manipulator. This active sensor is required for two main reasons:

- Some terrains might not have sufficient bearing capacity to support wheeled vehicles, particularly semi-aquatic environments where tracked or amphibious vehicles are required. The

proposed design can still be deployed in these types of environments.

- The normal load and slip ratio of the terramechanics measurement wheel can be controlled independently of the vehicle's motions. This allows setting a broad range of operating points for the collected data employed in the soil parameter estimation algorithms.

The proposed instrument enables real-time estimation of soil properties and terrain characterization. The terramechanics wheel can be used to increase the density of measurements collected during a survey, which is important since under-sampling areas can limit the accuracy of site characterization [5].

5.3 Development of a Robotic Manipulator and End-Effectors

5.3.1 Design Requirements

The robotic manipulator was designed to carry payloads capable of collecting undisturbed surface samples, conducting simple excavator-soil interaction experiments, and employing an instrumented wheel for terramechanics investigations. The design requirements include:

- mountable on a mobile platform,
- sufficient payload capacity to carry tools of up to 50 kg at least 30 cm in front and 30 cm below the first joint,
- sufficient dexterity to wield a surface sampling tool, an excavator, and a terramechanics wheel,
- end-effector velocity of at least 1 cm/s throughout the reachable workspace,
- joint angle sensors and end-effector load cells for position and force feedback during tasks,
- low mass and high structural stiffness,
- low power consumption,
- ruggedness for field deployment.

The following subsections present the development of the robotic manipulator and end effectors.

5.3.2 Robotic Manipulator

A serial 3-degree-of-freedom manipulator was developed as shown in Figure 5.5. The mechanism comprises three revolute joints driven by linear actuators (linear-drive nut-screw mechanisms). This new design was motivated by a lack of readily available commercial manipulators which could meet the design requirements described above.



Figure 5.5: Robot manipulator mounted on a UGV.

Small and medium sized (less than 35 kg) commercial manipulators which could be attached to our mobile platform were found to have limited payload carrying capacity (approximately 10kg) and not sufficiently rugged for field applications. Most commercial manipulators are designed to operate in clean environments and manipulate small end-effectors and payloads. Conversely, robot arms with high lifting capacities, such as those for industrial assembly lines, are not suitable for deployment from a mobile robot due to their large size, mass, and power requirements.

The main components of the proposed design are shown in Figure 5.6. Linear actuators consisting of DC motors and lead screws were chosen over direct rotary drives for each joint. Many small and medium-sized commercial manipulators use rotary drives with DC, stepper, or brushless DC motors in combination with planetary or harmonic gearboxes to increase the torque available at the joints. These configurations offer high joint speeds, especially for lightweight robots, and minimum backlash. Typically the joints are back-driveable, meaning they can be moved when the motors are not powered.

The main disadvantage of direct rotary drives in our application is that power would be required to

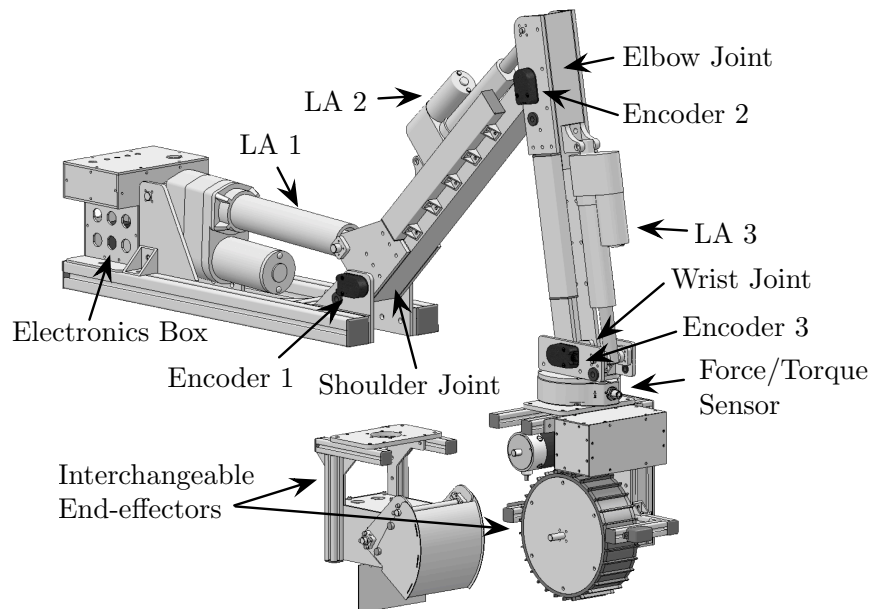


Figure 5.6: Robotic manipulator components.

hold a joint position. The mass of the end effectors and links of the arm are significant and create large moments at each joint. This would greatly increase the overall energy requirements of the system, since during most instrument deployment operations the arm remains in one pose for most of the time, for instance when the mobile platform is driving. For this reason, a self-locking joint design is preferred for our application.

The linear actuators used to rotate each joint comprise small DC motors, gearboxes, and a lead screw-nut transmission to convert rotary motion to linear displacement. This transmission system is not back-driveable and does not move unless the DC motors are energized. Each linear actuator is instrumented with a linear potentiometer to measure the linear displacement of the lead screw nut. The measurements of each linear actuator along with the link geometry of the robot are sufficient to determine the angle of each joint and thus the forward kinematics.

A proof-of-concept manipulator prototype was built as shown in Figure 5.7 to test the linear actuators and control systems. Costs were reduced by fabricating a lightweight shell using water-jet cutting of aluminum sheet-metal, and joining the links with standard connection brackets. The linear actuators were tested through simple load-carrying operations in the workspace. This configuration was found to deliver sufficient force to lift the front of the mobile robot off the ground.

The linear potentiometers were unable to provide adequate feedback of joint angles for two main

reasons. First, the analog output signals of the sensors were corrupted by electrical noise generated in the DC motors. Software and hardware filters attenuated these errors, at the cost of introducing a small time delay to the measurements. Second, the linear position sensors could not measure the backlash of the joints. Small joint angle measurement errors due to backlash can result in a significant difference between the calculated and true pose of the end-effector, leading to inaccurate motion planning and the risk of collision between the manipulator and mobile robot body. For contact tasks, a small end-effector position error could result in excessively large forces on the end-effector tool.

To address both these issues, optical quadrature encoders were added at each joint output shaft to directly measure the rotation angles. Because these sensors are digital, their readings are immune to electrical noise. The units selected were US Digital E5-4096-313 rotary encoders.



Figure 5.7: Robotic manipulator prototype for laboratory testing.

The final, field-deployed version of the manipulator is shown in Figure 5.5. Aluminum structural u-channels were used for each link to increase rigidity while keeping weight down. Oil-embedded flanged sleeve bearings, suitable for high-load and low-speed applications, were used to house the stainless steel axles of each joint. Optical encoders on the joints measured rotation angles with a resolution of 0.09 degrees.

The geometry of the arm was designed in parallel with actuator selection. Three design constraints were imposed: i) the arm needs to be easily mounted on top of a mobile robot such as the Clearpath Husky A200, ii) the arm needs to be able to apply a vertical force of at least 500 N and a horizontal

force of at least 100 N in any configuration, and iii) the arm must be capable of moving the end effector at a speed of at least 1 cm/s horizontally and vertically in any configuration. The linear actuators were selected to have an environmental protection rating of IP65, which is adequate for field operations in dusty conditions with the potential for water splashes. The mechanical components were designed with a factor of safety of at least 10 to prevent damage in the event of impacts during field operations. The arm was mounted on two aluminum extrusions for easy attachment to a mobile robot platform, as seen in Figure 5.5.

A computer program was developed to aid in the design and analysis process. It consisted of Python code used to calculate parameters of interest (listed next) for a given set of link geometries and actuator attachment points. The performance of the manipulator arm was investigated in terms of the forces and velocities achievable at the end-effector connection point. The forward and inverse kinematics of the manipulator were used to compute these as functions of the torques and angular speeds applied at each joint, and the geometry of the system as defined in Figure 5.8. The design parameters were the lengths of the links and the attachment points for each linear actuator. Several design iterations were required to find a configuration which satisfied all the design constraints. The specifications of the selected linear actuators are presented in Table 5.1.

Table 5.1: Chosen ServoCity Linear Actuators

Joint	Part No.	Gear Ratio	Max Load N	Stroke mm
1	SDA4-30	40:1	7000	102
2	HDA4-30	40:1	1000	100
3	HDA4-30	40:1	1000	100

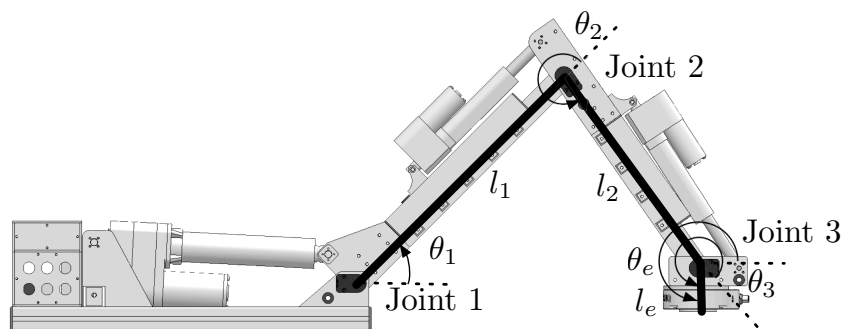


Figure 5.8: Robot manipulator angle and link geometry definitions.

Given the joint angles θ_1 , θ_2 and θ_3 , and the link lengths l_1 , l_2 and l_e , the end-effector position x_e ,

y_e and orientation θ_e can be found from the forward kinematics of the manipulator as:

$$x_e = l_1 \cos(\theta_1) + l_2 \cos(\theta_1 + \theta_2) + l_e \cos(\theta_1 + \theta_2 + \theta_3) \quad (5.1)$$

$$y_e = l_1 \sin(\theta_1) + l_2 \sin(\theta_1 + \theta_2) + l_e \sin(\theta_1 + \theta_2 + \theta_3) \quad (5.2)$$

$$\theta_e = \theta_1 + \theta_2 + \theta_3 \quad (5.3)$$

The inverse kinematics of the arm are found to be:

$$\theta_1 = \text{atan2}(y_e - l_e \sin \theta_e, x_e - l_e \cos \theta_e) - \text{atan2}(l_2 \sin \theta_2, l_1 + l_2 \cos \theta_2) \quad (5.4)$$

$$\theta_2 = \text{atan2}(-\sqrt{1 - D^2}, D) \quad (5.5)$$

$$\theta_3 = \theta_e - (\theta_1 + \theta_2) \quad (5.6)$$

$$D = [(x_e - l_e \cos \theta_e)^2 + (y_e - l_e \sin \theta_e)^2 - l_1^2 - l_2^2] / (2l_1 l_2) \quad (5.7)$$

The velocity vector of the end-effector $\mathbf{v}_{\text{ef}} = (\dot{\mathbf{x}}_e, \dot{\mathbf{y}}_e, \dot{\theta}_e)^{\mathbf{T}}$ can be calculated from the joint rates vector $\dot{\mathbf{q}} = (\dot{\theta}_1, \dot{\theta}_2, \dot{\theta}_3)^{\mathbf{T}}$ using the Jacobian matrix \mathbf{J} as

$$\mathbf{v}_{\text{ef}} = \mathbf{J} \dot{\mathbf{q}} \quad (5.8)$$

where

$$\mathbf{J} = \begin{pmatrix} J_{11} & J_{12} & J_{13} \\ J_{21} & J_{22} & J_{23} \\ 1 & 1 & 1 \end{pmatrix} \quad (5.9)$$

$$J_{11} = -l_1 \sin(\theta_1) - l_2 \sin(\theta_1 + \theta_2) - l_e \sin(\theta_1 + \theta_2 + \theta_3) \quad (5.10)$$

$$J_{12} = -l_2 \sin(\theta_1 + \theta_2) - l_e \sin(\theta_1 + \theta_2 + \theta_3) \quad (5.11)$$

$$J_{13} = -l_e \sin(\theta_1 + \theta_2 + \theta_3) \quad (5.12)$$

$$J_{21} = l_1 \cos(\theta_1) + l_2 \cos(\theta_1 + \theta_2) + l_e \cos(\theta_1 + \theta_2 + \theta_3) \quad (5.13)$$

$$J_{22} = l_2 \cos(\theta_1 + \theta_2) + l_e \cos(\theta_1 + \theta_2 + \theta_3) \quad (5.14)$$

$$J_{23} = l_e \cos(\theta_1 + \theta_2 + \theta_3) \quad (5.15)$$

$$(5.16)$$

Similarly, the instantaneous forces and moment on the end effector $\mathbf{W}_{\text{ef}} := (F_{x_e}, F_{y_e}, M_e)^{\mathbf{T}}$ resulting from the joint torques $\mathbf{T}_{\mathbf{j}} := (T_1, T_2, T_3)^{\mathbf{T}}$ are given by

$$\mathbf{W}_{\text{ef}} = (\mathbf{J}^{\mathbf{T}})^{-1} \mathbf{T}_{\mathbf{j}} \quad (5.17)$$

The manipulator was designed to position payloads in front and below Joint 1 in Figure 5.8. This is because the manipulator is mounted on top of a mobile platform and reaches to interact with the terrain ahead. Figure 5.9 visualizes the workspace of the manipulator. The boundaries delineate areas in which the end-effector can be positioned for a given angular orientation. The key constraints are the range of angles for each joint, which are in turn determined by the strokes and attachment points of the linear actuators as well as the link geometries.

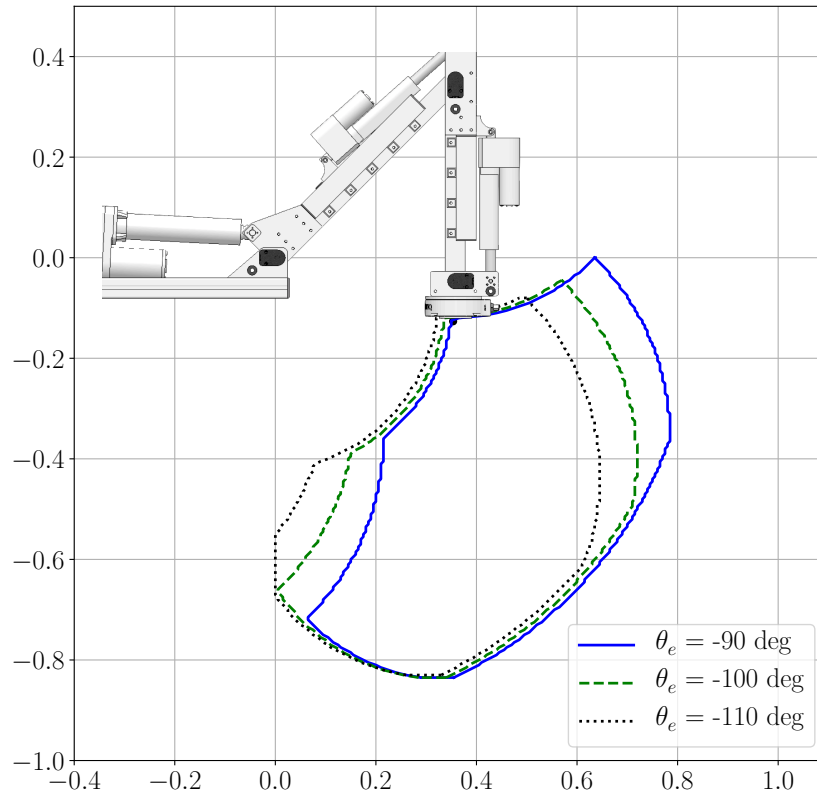


Figure 5.9: Robot manipulator reachable workspace. The boundaries delineate areas in which the robot manipulator can position the end effector for a given angle.

A system diagram of our design is presented in Figure 5.10. An Atmel SAM3X8E ARM Cortex-M3 microcontroller unit (MCU) within the manipulator electronics box interfaces with three Parallax HB25 motor controllers which modulate power to the motors at 9.2 kHz. The MCU samples the three linear potentiometers and three quadrature encoders to determine the joint angles. The linear potentiometers are used to determine the initial position of the robot arm at power-on, at which time the manipulator is in a known configuration such that backlash can be measured and then

removed. Alternatively, the position of the arm can be saved to flash memory, and used to restart the arm in its last measured configuration. In this case, the encoders are zeroed during operation using mechanical hardstops within the workspace of the robot. During regular operation, only encoder feedback is used. A sensor fault detection scheme (part of a self-diagnostic routine) could be implemented by comparing the feedback from the potentiometers and encoders along with inputs to the motors.

The manipulator arm is equipped with an Inertial Measurement Unit (IMU) fixed to the base of the arm. The IMU uses feedback from a triaxial accelerometer, gyroscope and magnetometer to determine the attitude of the base of the arm with respect to the horizontal plane. This is used to determine whether the mobile robot carrying the arm is on sloped ground. While most mobile robots carry on-board IMUs, having an IMU integrated into the manipulator arm design makes it independent of the mobile platform used. An emergency stop button is available to disconnect power to the actuators. A dedicated 12V lead-acid battery is used to power the manipulator.

The manipulator arm is designed to be modular. An end-effector attachment plate with multiple bolt patterns allows attaching different end-effector payloads. A serial communication line is available to interface the payloads with the onboard computer, as well as to supply power. A Robotiq FT 150 force-torque sensor is mounted between the distal manipulator link and the end-effector attachment plate. This sensor measures the forces and moments along three axes, allowing to measure and control the tool-environment interaction forces and moments. Additionally, feedback from this sensor is used to prevent overloading the manipulator and end-effectors.

Independent joint angle PID controllers are used to drive the linear actuators. In this scheme, nonlinearities in the conversion of linear motion of the actuator to rotary motion of the joint are automatically handled by the controller. This setup was found to successfully track joint angle trajectories with negligible errors and was thus determined to be suitable for our application. Note the end-effector moves at relatively slow speeds thus the joint reference trajectories are slowly varying.

High level task planning, trajectory generation, and the user interface were developed within the Robot Operating System (ROS) [36]. A linear-segment, parabolic-blending approach is used to prescribe limits for acceleration and velocity of the end-effector during operation. Different software modules were implemented as ROS nodes which communicate with each other in a publisher-subscriber architecture. Both the manipulator arm and each of the end-effectors publish their state information and subscribe to command inputs from the path planning and user interface modules. Built-in ROS modules are used to visualize sensor feedback and build a graphical user interface (GUI) to control the robot arm. A screenshot of the running interface is shown in Figure 5.11.

The next Sections detail the development of two end effectors: a scoop-based surface sampler and

excavation tool, and an instrumented terramechanics wheel.

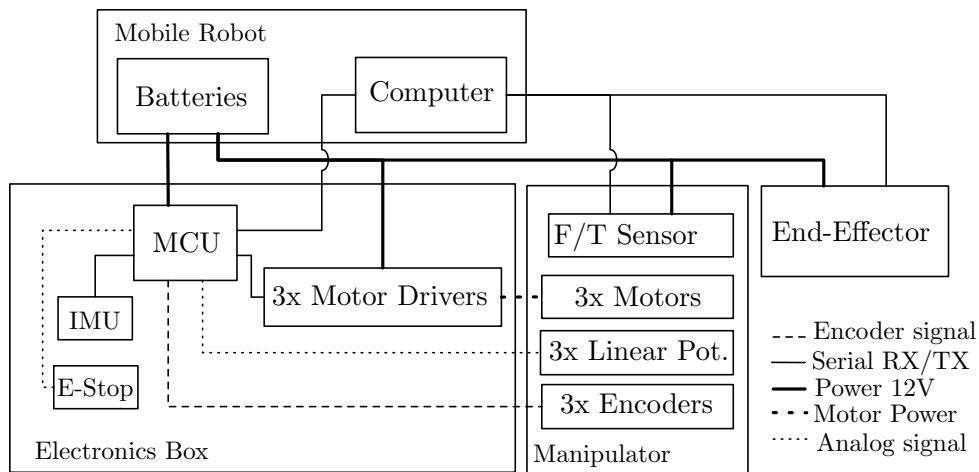


Figure 5.10: System diagram for the overall design.

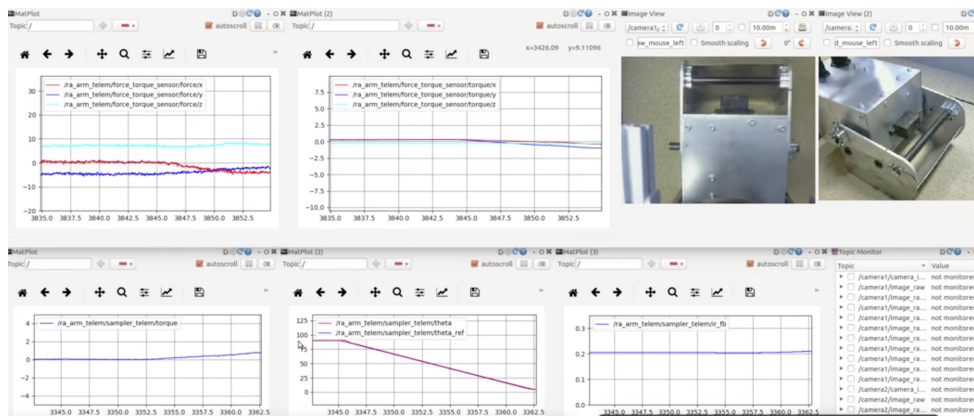


Figure 5.11: User interface screenshot. Two cameras are used to supervise the payload from different angles, and plots present the loads and relevant state variables.

5.3.3 Surface Sampler And Excavation Tool

Scoop-type samplers can be used to collect undisturbed soil samples from the surface of a region of soft terrain such as a tailings deposit, and the measurements of the reaction forces can be used to characterize the terrain (c.f. Section 5.2.2).

This section presents the development of an instrumented surface sampler for terrain investigations. The mechanism comprises a detachable curved scoop actuated by a geared DC motor, as illustrated

in Figure 5.12. The scoop was designed to be detachable from the rest of the sampler for transferring the soil sample to a container with minimal deformation. The overall subsystem attaches to the endplate of the manipulator arm, which is instrumented to measure the forces and moments acting on the end-effector.

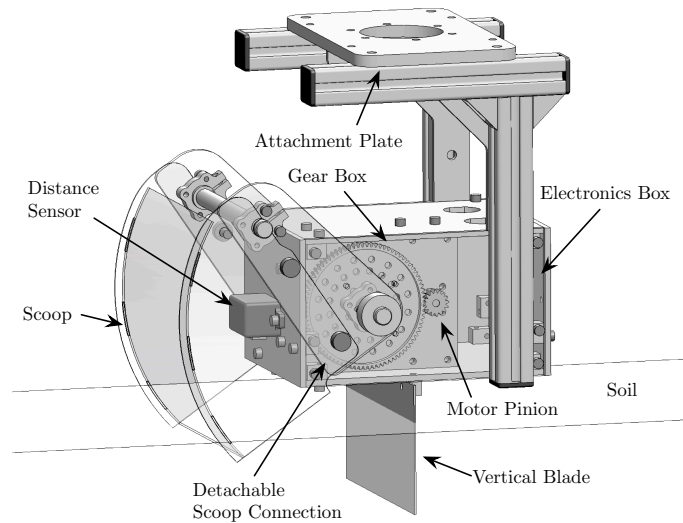


Figure 5.12: Surface sampler main components. The side plates are shown as transparent to make the internal components visible.

The sampler was designed to move approximately 90 degrees to its final closed configuration. This design is different from the 180 degree movement of the scoop sampler proposed by Mori *et al* [30]. Preliminary tests showed that during sampling, the surface of the medium remains close to unchanged during the first 90 degrees of the scoop's motion. As shown by the Particle Image Velocimetry (PIV) results reported in [30], the sample is significantly disturbed during the second half of the scooping motion. In our proposed design, the sample material is contained between the curved blade, the side walls of the sampler, and an additional vertical blade fixed to the bottom of the sampler body. A side view of the sampler with physical dimensions is presented in Figure 5.13.

The vertical blade serves several purposes. First, it provides a bracing support against the terrain during sampling, reducing undesirable motions due to reaction forces. Second, the blade reduces the disturbance to the surface of the sampled soil, by limiting the allowable deformation of the terrain. Lastly, the vertical blade can be used as a simple excavation blade, and thus the end-effector can be used to perform on-line estimation of soil parameters based on cutting force measurements, as previously demonstrated by part of our group [48].

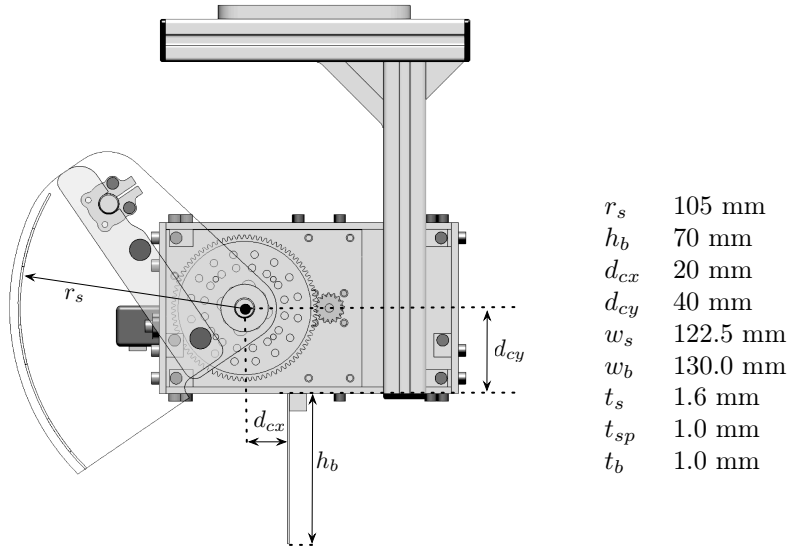


Figure 5.13: Surface sampler dimensions. The widths of the sampler and vertical blade are w_s and w_b , respectively, and the thickness of the scoop curved blade, side plates, and vertical blade are t_s , t_{sp} , and t_b , respectively.

A DC motor is used to actuate the scoop (Actobotics 638296 52RPM Planetary Gear Motor), with a quadrature encoder to determine the angular position of the sampler. An optical limit switch is used to initialize the encoder count from a known angle. The torque on the scoop is measured using strain gauges attached to the scoop axle in a Wheatstone bridge circuit. This measurement of torque can be used for terrain characterization and also to prevent overloading the system.

Additional sensors include an IMU (Adafruit 10-DOF IMU 1604) to determine the orientation of the sampler and to confirm the end-effector pose estimated by the robotic manipulator, and a distance sensor (SHARP GP2Y0A51SK0F) to measure the distance between the sampler and the ground to aid in positioning the scoop prior to sampling. The latter sensor is necessary because the distance to the ground can vary depending on the geometry of the terrain, orientation of the mobile platform, as well as sinkage of the vehicle (which can be on the order of several centimeters on soft ground). In these conditions, measuring the pose of the end-effector is not sufficient to determine its distance to the soil surface. The relative distance sensor allows precise and safe positioning of the scoop mechanism above the soil to sample or excavate. Meanwhile for parameter identification, the governing equations relating the reaction forces and terrain properties depend on the precise positioning of the tool with respect to the ground. The sensor was selected to have high sensitivity, approximately 350mV/cm, when the tool is approaching the ground and is closer than 6cm.

The sampler is primarily manufactured from aluminum to be sufficiently strong for field deployment while being lightweight. The material and surface roughness of the sampler scoop and vertical blade parts can be chosen to minimize friction and adhesion effects. Materials such as nylon and teflon can be used to reduce friction, while other coatings can optimize the surface-medium interaction (for instance hydrophobic or hydrophilic coatings, depending on the desired effect). In our case, the surface of the tool was not treated other than being smoothed with fine-grit sandpaper.

5.3.4 Terramechanics Wheel End-Effector

An instrumented terramechanics wheel end-effector was developed to address the limitations outlined in Section 5.2.3. This system mounts on the manipulator arm and comprises an actuated wheel plus a set of sensors measuring its state and the loads acting on it. The design of this instrument is illustrated in Figure 5.14. The orientation of the payload with respect to the horizontal plane is estimated by an IMU mounted inside the electronics box.

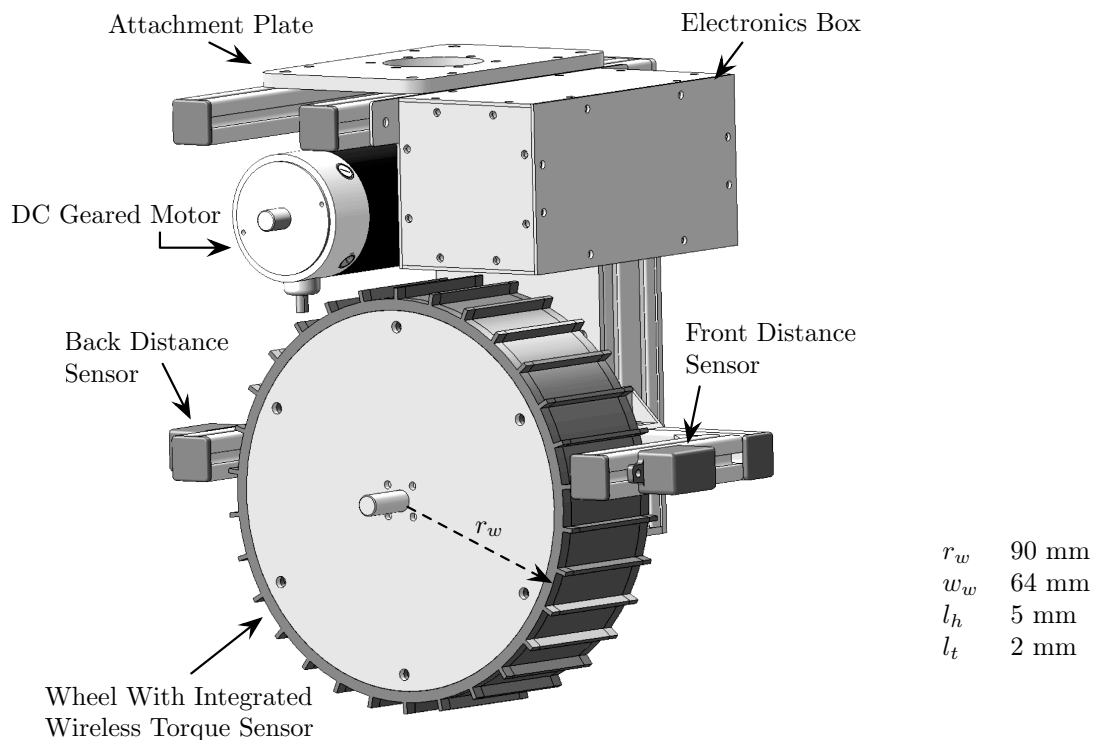


Figure 5.14: Terramechanics wheel design. The radius and width of the wheel are r_w and w_w , respectively, and the lug height and thickness are l_h and l_t , respectively.

The wheel consists of a rim with lugs 3D-printed from ABS plastic mounted on two circular aluminum plates. This choice of materials was used to reduce costs of prototyping and iterating of various geometries; the final design could be machined from metal if desired. The wheel dimensions were chosen to be similar to those used in planetary rovers to allow for comparative testing with existing wheel-based parameter estimation methods [7]. The wheel is driven by a geared DC motor (Midwest Motion S22-346F-12V GP52-022) connected to a timing belt and pulley transmission.

The wheel is instrumented with optical encoders, whose readings are numerically differentiated to estimate its angular velocity. In this way, the wheel speed can be precisely set using a closed-loop control law. Using a combination of prescribed linear velocity of the vehicle platform and angular velocity of the wheel enables the latter to achieve a desired slip ratio. In order to reduce power consumption and the risk of getting stuck, the mobile platform's linear velocity is first set to a safe and constant value, then the slip ratio of the terramechanics wheel is varied by commanding its angular velocity.

An integrated wireless torque sensor is used to measure the torque applied to the wheel. The torque is calculated from the amplified output of a Wheatstone bridge employing strain gauges arranged in a shear strain configuration. The amplified signal is sampled by a low-power microcontroller unit (NXP MK20DX256ZVMD7) mounted inside the wheel. The MCU communicates wirelessly to the robot vehicle's computer using 2.4GHz transceivers (Digi XB24CZ7WITB003). The wheel MCU receives commands from this computer to start data transmission, stop and go to low-power sleep mode, and modify signal conditioning gains and measurement transmission rates. The measured data can also be logged by the MCU inside the terramechanics wheel to achieve higher data logging rates and serve as a backup.

Two distance sensors are mounted on the frame of the wheel. The sensors selected were the SHARP GP2Y0A41SK0F, which have a range up to 30cm with a sensitivity of 100 mV/cm at distances between 8 cm and 16 cm. These sensors are used to estimate the sinkage of the wheel in the terrain by measuring the distances to the ground in front and behind the wheel. This is used to determine the contact angle between the wheel and the terrain and calculate the normal and shear stresses acting on the wheel. To estimate sinkage from the measurements obtained from the distance sensors, the terrain is assumed to be flat and level.

The set of measurements of the wheel's interaction forces and its translational velocity (obtained from the mobile platform's onboard state estimation system) can be used to estimate soil properties by estimating the parameters of a wheel-soil interaction model.

The next Section discusses equipment testing field trials.

5.4 Equipment Testing Experiments

The manipulator arm and its end-effectors discussed in the previous Section were tested during the NSERC Canadian Field Robotics Network (NCFRN) field trials in Kelowna, B.C., Canada. The trials were conducted on a sandy beach, which allowed testing of the instruments on uncompacted dry sand as well as on regions of transition into saturated sand.

The robotic manipulator was mounted on a Clearpath Husky A200 UGV. We refer to this combined system as the second-generation rover for terrain characterization or RTC-II. The RTC-II's onboard computer runs ROS and our developed software discussed in Section 5.3.2. The UGV is outfitted with a GPS receiver, and a simple waypoint navigation controller was used to drive the robot autonomously through a series of assigned waypoints to reach a tool deployment location. Two types of experiments were conducted: a sample return mission, and a terramechanics wheel investigation.

5.4.1 Terrain Sampling Equipment Test Field Experiments

In this test, locations with different terrain characteristics were manually selected by the robot operator. Figure 5.15 shows the robot working on (a) a location covered in dry sand, and (b) a location close to the edge of a body of water.



Figure 5.15: (a) RTC-II traversing dry uncompacted sand. (b) RTC-II deploying the surface sampler on wet sand.

A sequence of images of the sampler payload operating on dry sand is presented in Figure 5.16, and pictures of the overall vehicle sampling wet sand are shown in Figure 5.17. In both cases, the surface of the collected samples remained undisturbed. Wet sand had sufficient cohesion to maintain the shape of the collected sample, while in dry sand the hole created by the sample removal collapsed

as the scoop was lifted. The input torque to the scoop and the reaction forces were measured and logged throughout the sampling procedures. Measurements collected while sampling dry sand are shown in Figure 5.18.



Figure 5.16: Sampler payload collecting a sample on dry sand.



Figure 5.17: RTC-II collecting a sample on saturated sand. (a) The manipulator arm positions the sampler on the terrain and the scoop is closed slowly to collect material. (b) The manipulator lifts the instrument carrying a sample of saturated sand. The soil had sufficient cohesion to maintain the shape of the material collected after the sampler was removed from the ground.

5.4.2 Terramechanics Wheel Field Test Experiments

The instrumented terramechanics wheel payload was deployed using the manipulator arm onboard the RTC-II. As pictured in Figure 5.19, data collection was performed on (a) dry homogeneous

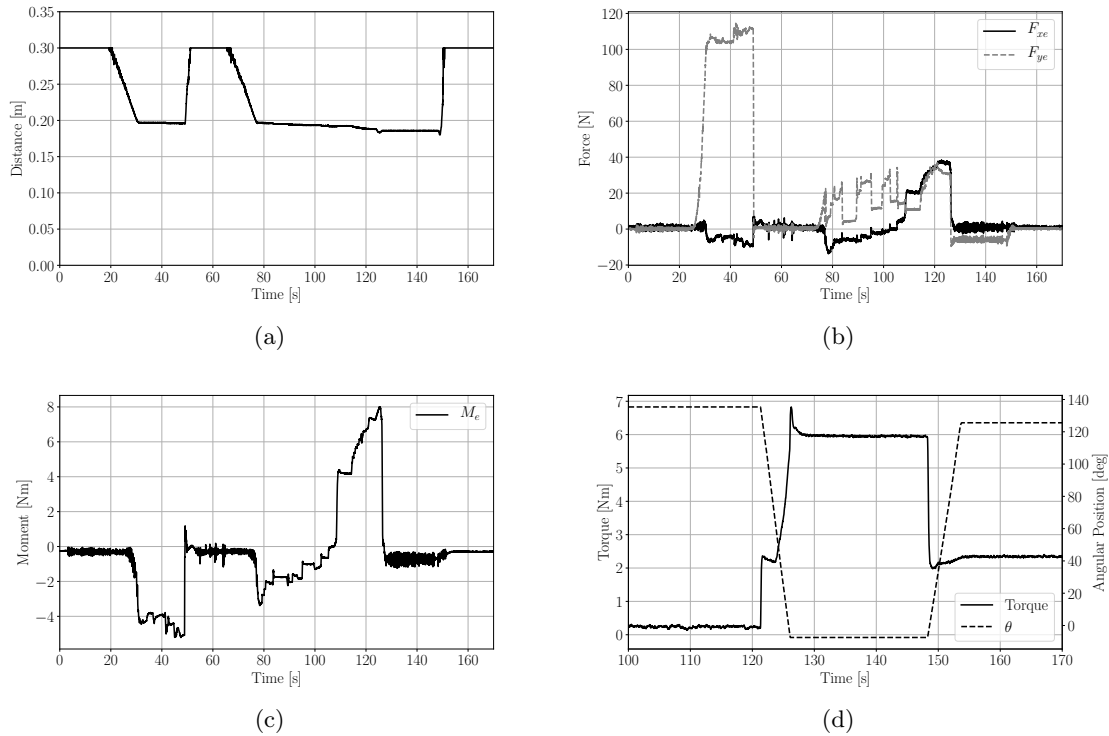


Figure 5.18: Measurements collected while sampling on dry sand. (a) The distance to the ground from the end-effector connection plate. Two approaches were conducted, resulting in large and small soil deformations. (b) The forces along two axes. There is a large normal force shown during the first approach to collect a sample resulting in large deformations. The second approach, after time 60 s, is smoother and results in smaller reaction forces. (c) The moment measured at the connection plate. It is the combination of the reaction moments with the ground and the interaction forces of the sampler while closing. (d) The torque and angular position of the sampler scoop. The sampler is closed at 0 degrees, as it contacts the vertical blade and pushes against it. The plot shows the sampler closing to collect a sample and opening to drop it. The torque measured is the combination of the tool-terrain interactions and the moment generated by the weight of the rotating scoop.

sand, (b) a transition area between dry sand and water. The UGV was controlled over a WiFi network connection with a ground station computer. The human operator used a ROS graphical user interface to command the pose of the manipulator’s end-effector, the forward velocity of the UGV, and the angular speed of the instrumented wheel.

The normal load on the wheel was varied by changing the pose of the robotic manipulator and using the compliance of the terrain to obtain different loads. The alternative of using a force controller to track a desired load was not used for two reasons. First, because of the uneven terrain, tracking a

given load would require extremely fast actuation of the manipulator arm. This is not feasible in the current design, which uses lead-screw actuation to provide high payload capacity and self-locking at the cost of speed. Second, unlike direct-drive motors, lead-screw actuators do not provide direct measurements of torque applied to the joint, meaning Equation (5.17) relating joint torques to end-effector forces cannot be used directly.



Figure 5.19: RTC-II deploying the instrumented terramechanics wheel on (a) dry sand, (b) transition between dry and wet sand.

During each experiment, the torque on the wheel, angular velocity, and reaction forces on the wheel were logged. A plot of this data from a test on dry sand is shown in Figure 5.20.

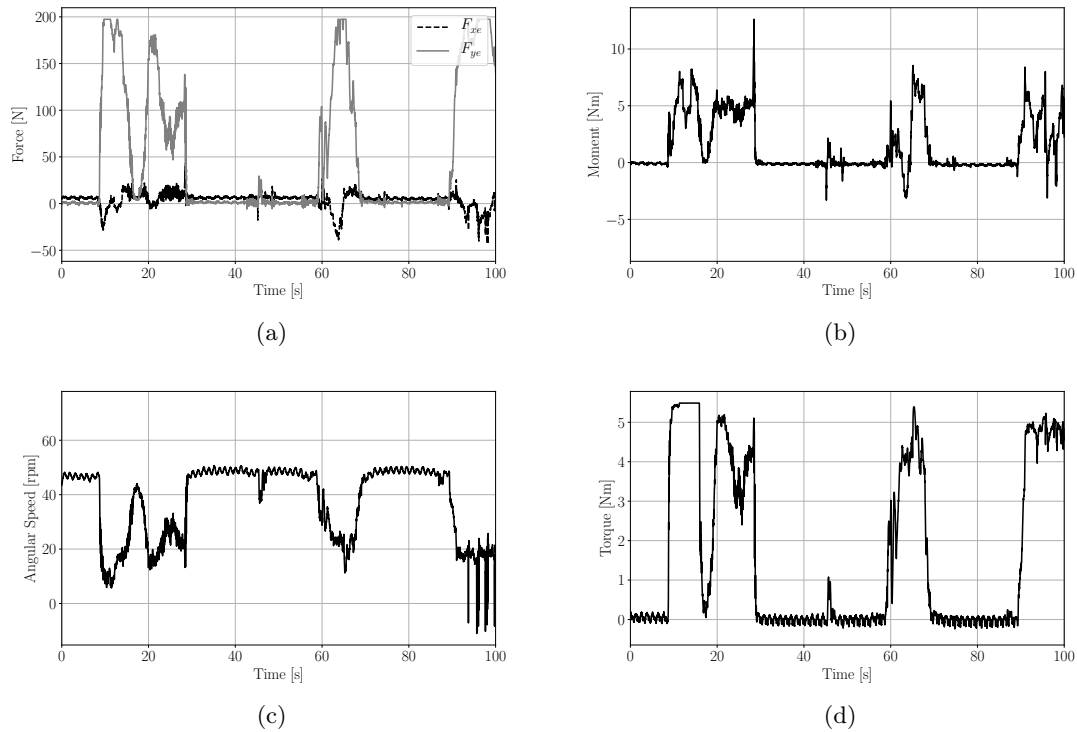


Figure 5.20: Measurements collected while sampling on dry sand. (a) The reaction forces on the wheel. The wheel was contacted against the dry sand several times and the normal load and draw bar pull recorded. (b) The reaction moment at the end-effector plate. It is a combination of reaction forces on the wheel, including the traction forces and vertical reactions. (c) The angular speed of the wheel. This was controlled in open loop and is seen to slow down as higher rolling resistance is applied when it contacts the ground. Oscillations are observed due to unbalanced masses of the components mounted inside the wheel, such as the wireless torque transducer battery. (d) The torque measured at the wheel. Increased torque was observed when the wheel was pushed into the ground. Oscillations due to unbalanced masses are observed. Limits on the strain gauge signal amplifiers resulted in the measurements being truncated at approximately 5.6 Nm.

5.5 Conclusion and Future Work

This paper detailed the design and development of a robotic manipulator arm and two payloads used for soil sampling and parameter identification from a mobile UGV platform. The sampling payload is a scoop mechanism designed to collect undisturbed surface samples, while the characterization payload is an instrumented wheel used to estimate terramechanics model parameters from dynamic testing. The various design challenges and their solutions were presented, and the final designs were experimentally validated in field trial experiments.

Future work will focus on i) developing novel models to predict cutting forces of the scoop surface sampler and ii) developing soil parameter estimation algorithms which take advantage of the wide range of operating points enabled by the terramechanics wheel sensor. These will be verified in soils with known characteristics.

Long-term plans are to deploy the robotic manipulator and its measurement payloads onboard novel robotic mobile platforms which can traverse terrains with little or no bearing capacity. This would allow the instruments to be used on tailing deposits which are inaccessible to wheeled and tracked vehicles.

5.6 Acknowledgments

The authors would like to thank the Natural Sciences and Engineering Research Council of Canada (NSERC), Canada's Oil Sands Innovation Alliance (COSIA) and Alberta Innovates — Clean Energy for their financial support.

5.7 References

- [1] Erik W Allen. Process water treatment in Canada's oil sands industry: I. Target pollutants and treatment objectives. *Journal of Environmental Engineering and Science*, 7(2):123–138, March 2008.
- [2] R.C. Anderson, L. Jandura, A.B. Okon, D. Sunshine, C. Roumeliotis, L.W. Beegle, J. Hurowitz, B. Kennedy, D. Limonadi, S. McCloskey, M. Robinson, C. Seybold, and K. Brown. Collecting samples in gale crater, mars; an overview of the mars science laboratory sample acquisition, sample processing and handling system. *Space Science Reviews*, 170(1-4):57–75, 2012.
- [3] Nicholas Beier, Ward Wilson, Adedeji Dunmola, and David Segoo. Impact of flocculation-based dewatering on the shear strength of oil sands fine tailings. *Canadian Geotechnical Journal*, 50(9):1001–1007, 2013.
- [4] M. G. Bekker. *Introduction to Terrain-Vehicle Systems*. University of Michigan Press, Michigan, 1969.
- [5] Richard C Benson. Geophysical techniques for subsurface site characterization. In *Geotechnical Practice for Waste Disposal*, pages 311–357. Springer US, Boston, MA, 1993.

- [6] S Coetzee, H Swart, P Bosscha, and D Oosthuizen. *Design of an industrial all-terrain robot platform lessons learned in the design of a robotic mine safety platform for South African gold mines*. IEEE, 2012.
- [7] L Ding, Z Deng, H Gao, J Guo, D Zhang, and K D Iagnemma. Experimental study and analysis of the wheels' steering mechanics for planetary exploration wheeled mobile robots moving on deformable terrain. *The International Journal of Robotics Research*, 32(6):712–743, June 2013.
- [8] Matthew Dunbabin and Lino Marques. Robots for Environmental Monitoring: Significant Advancements and Applications. *IEEE Robotics & Automation Magazine*, 19(1):24–39, March 2012.
- [9] Maurice B Dusseault and J Don Scott. Tailings Pond Behavior and Characterization of Oil Sand Tailings Sludge. *Particulate Science and Technology*, 1(3):295–309, 1983.
- [10] Iman Entezari, Benoit Rivard, Michael G Lipsett, and G Ward Wilson. Prediction of water content and normalized evaporation from oil sands soft tailings surface using hyperspectral observations. *Canadian Geotechnical Journal*, 53(10):1742–1750, October 2016.
- [11] C W Fervers. Improved FEM simulation model for tire–soil interaction. *Journal of Terramechanics*, 41(2-3):87–100, April 2004.
- [12] Daniel M Franks, David V Boger, Claire M Côte, and David R Mulligan. Sustainable development principles for the disposal of mining and mineral processing wastes. *Resources Policy*, 36(2):114–122, June 2011.
- [13] Gustavo Freitas, Fernando Lizarralde, Liu Hsu, Vitor Paranhos, Ney R. Salvi dos Reis, and Marcel Bergerman. Design, modeling, and control of a wheel-legged locomotion system for the environmental hybrid robot. In *Proceedings of the IASTED International Conference*, number CMU-RI-TR-, November 2011.
- [14] Fine Tailings Fundamentals Consortium FTFC. Advances in oil sands tailings research. In *Alberta Department of Energy*, pages 6–7–79–80, Edmonton, 1995.
- [15] James E. Funk and Dennis R. Dinger. *Methylene Blue Index*, pages 669–689. Springer US, 1994.
- [16] Jeremy Green. Underground mining robot: A CSIR project. *SSRR*, pages 1–6, 2012.
- [17] Daniel Helmick, Scott McCloskey, Avi Okon, Joseph Carsten, Won Kim, and Chris Leger. Mars science laboratory algorithms and flight software for autonomously drilling rocks. *Journal of Field Robotics*, 30(6):847–874, 2013.

- [18] Gregory Hitz, Francois Pomerleau, Marie-Eve Garneau, Cedric Pradalier, Thomas Posch, Jakob Pernthaler, and Ronald Siegwart. Autonomous Inland Water Monitoring: Design and Application of a Surface Vessel. *IEEE Robotics & Automation Magazine*, 19(1):62–72, March 2012.
- [19] Larry A Holm. Strategies for remediation. In *Geotechnical Practice for Waste Disposal*, pages 289–310. Springer US, Boston, MA, 1993.
- [20] M A Knuth, J B Johnson, M A Hopkins, R J Sullivan, and J M Moore. Discrete element modeling of a Mars Exploration Rover wheel in granular material. *Journal of Terramechanics*, 49(1):27–36, February 2012.
- [21] D Kossoff, W E Dubbin, M Alfredsson, S J Edwards, M G Macklin, and K A Hudson-Edwards. Mine tailings dams: Characteristics, failure, environmental impacts, and remediation. *Applied Geochemistry*, 51:229–245, December 2014.
- [22] Yun Ling, Wei Lu, Pengwen Xiong, and Aiguo Song. A miniature flexible sampler for subsurface lunar exploration. *Acta Astronautica*, 123:8–15, June 2016.
- [23] M G Lipsett, J D Yuen, N A Olmedo, and S C Dwyer. Condition Monitoring of Remote Industrial Installations Using Robotic Systems. In *Engineering Asset Management 2011*, pages 231–241. Springer London, London, July 2013.
- [24] M.G. Lipsett and S.C. Dwyer. A robotic system to characterize soft tailings deposits. In *Proceedings of Mine and Tailings Waste Conference 2009, Banff Alberta*, November 2009.
- [25] Michael Lipsett, Rijesh Augustine, and Mark Sherstan. Aerial manipulation for remote robotic machinery diagnostics. In *Proceedings of the Machinery Failure and Prevention Technology Conference*, May 2019.
- [26] Michael G Lipsett, Nicolas Olmedo, Benoit Rivard, and Ward Wilson. Robotic Systems for Measuring Properties of Tailings Deposits and Collecting Samples. In *Proceedings of the Fourth International Oil Sands Tailings Conference*, Lake Louise, AB, December 2014.
- [27] Joshua A Marshall, Adrian Bonchis, Eduardo Nebot, and Steven Scheduling. Robotics in Mining. In Bruno Siciliano and Oussama Khatib, editors, *Springer Handbook of Robotics*, pages 1549–1576. Springer International Publishing, Cham, 2016.
- [28] Jacob Masliyah, Zhiang Joe Zhou, Zhenghe Xu, Jan Czarnecki, and Hassan Hamza. Understanding Water-Based Bitumen Extraction from Athabasca Oil Sands. *The Canadian Journal of Chemical Engineering*, 82(4):628–654, August 2004.
- [29] N R Morgenstern and J D Scott. Geotechnics of fine tailings management. *Geoenvironment*, pages 1663–1673, 1995.

- [30] Daiki Mori and Genya Ishigami. Excavation model of soil sampling device based on particle image velocimetry. *Journal of Terramechanics*, 62:19–29, December 2015.
- [31] A Nuchter, H Surmann, and K Lingemann. 6D SLAM with an application in autonomous mine mapping. . . . *ICRA '04 2004 IEEE . . .*, pages 1998–2003 Vol.2, 2004.
- [32] Nicolas Olmedo, Stephen Dwyer, Michael Lipsett, and James Yuen. Soft soil sampling device and system US9513193B2, December 2016.
- [33] Nicolas A. Olmedo, Bereket Fisseha, Ward Wilson, Martin Barczyk, Hong Zhang, and Michael G. Lipsett. An automated vane shear test tool for environmental monitoring with unmanned ground vehicles. Submitted, 2020.
- [34] Nicolas A Olmedo and Michael G Lipsett. Design and field experimentation of a robotic system for tailings characterization. *Journal of Unmanned Vehicle Systems*, pages juvs–2015–0034, March 2016.
- [35] Geoffrey S Plumlee, Kathleen S Smith, and Walter H Ficklin. *Geoenvironmental Models of Mineral Deposits, and Geology-based Mineral-environmental Assessments of Public Lands*. Number Open-File Report 94-203. U.S. Geological Survey, 1994.
- [36] Morgan Quigley, Ken Conley, Brian P. Gerkey, Josh Faust, Tully Foote, Jeremy Leibs, Rob Wheeler, and Andrew Y. Ng. Ros: an open-source robot operating system. In *ICRA Workshop on Open Source Software*, 2009.
- [37] B Rivard, D Lyder, J Feng, A Gallie, E Cloutis, P Dougan, S Gonzalez, D Cox, and M G Lipsett. Bitumen content estimation of Athabasca oil sand from broad band infrared reflectance spectra. *The Canadian Journal of Chemical Engineering*, 88(5), June 2010.
- [38] Ioannis Tsitsimpelis, C. James Taylor, Barry Lennox, and Malcolm J. Joyce. A review of ground-based robotic systems for the characterization of nuclear environments. *Progress in Nuclear Energy*, 111:109 – 124, 2019.
- [39] Dirk Van Zyl. Mine waste disposal. In *Geotechnical Practice for Waste Disposal*, pages 269–286. Springer US, Boston, MA, 1993.
- [40] R Volpe, E Baumgartner, P Scheaker, and S Hayati. Technology development and testing for enhanced Mars Rover Sample Return operations. 7:247–257 vol.7, 2000.
- [41] Chen Wang, David Harbottle, Qingxia Liu, and Zhenghe Xu. Current state of fine mineral tailings treatment: A critical review on theory and practice. *Minerals Engineering*, 58:113–131, April 2014.

- [42] David Wettergreen, Scott Jared Moreland, Krzysztof Skonieczny, Dominic Jonak, David Kohanbash, and James Teza. Design and field experimentation of a prototype lunar prospector. *International Journal of Robotics Research*, 29(12):1550 – 1564, October 2010.
- [43] Barry A Wills and James A Finch. Tailings Disposal. In *Wills' Mineral Processing Technology*, pages 439–448. Elsevier, 2016.
- [44] J Y Wong. Chapter 3 - Measurement of Terrain Properties. In J Y Wong, editor, *Terramechanics and Off-Road Vehicle Engineering (Second Edition)*, pages 65–74. Butterworth-Heinemann, Oxford, 2010.
- [45] J Y Wong and A R Reece. Prediction of rigid wheel performance based on the analysis of soil-wheel stresses part I. Performance of driven rigid wheels. *Journal of Terramechanics*, 4(1):81–98, 1967.
- [46] J Y Wong and A R Reece. Prediction of rigid wheel performance based on the analysis of soil-wheel stresses: Part II. Performance of towed rigid wheels. *Journal of Terramechanics*, 4(2):4, 1967.
- [47] J.Y. Wong. *Terramechanics and Off-Road Vehicle Engineering*. Butterworth-Heinemann, Oxford, 2 edition, 2010.
- [48] R Yousefi Moghaddam, A Kotchon, and M G Lipsett. Method and apparatus for on-line estimation of soil parameters during excavation. *Journal of Terramechanics*, 49(3-4):173–181, June 2012.
- [49] Weiwei Zhang, Shengyuan Jiang, Jie Ji, and Dewei Tang. A drilling tool design and in situ identification of planetary regolith mechanical parameters. *Advances in Space Research*, 61(9):2444–2456, May 2018.
- [50] Feng Zhou, Raymond E Arvidson, Keith Bennett, Brian Trease, Randel Lindemann, Paolo Bellutta, Karl Iagnemma, and Carmine Senatore. Simulations of Mars Rover Traverses. *Journal of Field Robotics*, 31(1):141–160, September 2013.

Chapter 6

An improved terramechanics model for a robotic soil surface sampler

Abstract

Robotic systems have been developed and deployed for sample collection and geotechnical measurements of soil characteristics. A custom scoop-type robotic soil sampler has been designed and built for sampling operations. We propose a novel terramechanics model which captures the interaction of this sampler with soil better than existing models, then validate this model and demonstrate its improved performance using simulation and experimental data.

6.1 Introduction

Robotic systems have been used to investigate and increase the scientific understanding of challenging and hazardous environments such as extraterrestrial bodies [42]. In extraterrestrial landing missions, collecting and analyzing soil samples is a critical task. Custom regolith sampling tools for coring and drilling have been developed for sample-return missions [42, 41], as well as for sampling asteroids [5, 47]. Terrain properties have been studied by measuring interaction forces during the operation of these tools, as well as using on-board sample analysis instruments [50, 2]. Design of sampling tools with reduced weight and power requirements such as miniaturized flexible samplers are active areas of research [21].

On Earth, ground, aerial, and aquatic robotic systems have been used to monitor challenging and dangerous environments such as mine-waste deposits [33]. Hybrid robots have been used to

investigate Amazon rainforest rivers [13]; surface vessels were used to study bodies of water [15]; and teams of unmanned aerial vehicles (UAVs) and unmanned ground vehicles (UGVs) have been used to conduct tasks too risky and costly for humans, such as mine waste pond sampling [10, 23]. Specialized UGVs have been used for mapping underground mines that human workers can't access [7, 14, 29], and for other mining applications such as explosives handling, haulage, surveying, dozing, excavation, and drilling [26].

Our group has been focusing on developing robotic systems for mine-waste monitoring, as shown in the photos of Figure 6.1 [33, 32, 31]. These systems have been designed to collect subsurface and surface samples, deploy geotechnical instruments such as vane shear test tools, and measure terrain properties in oil sands tailings ponds. Site investigations of these areas are required for legislative compliance [43], environmental monitoring [34], identifying risks and readiness for reclamation [16], and to improve mine waste treatment processes [24]. Until they are fully restored, these sites are significant financial liabilities for the operating mining companies [12].

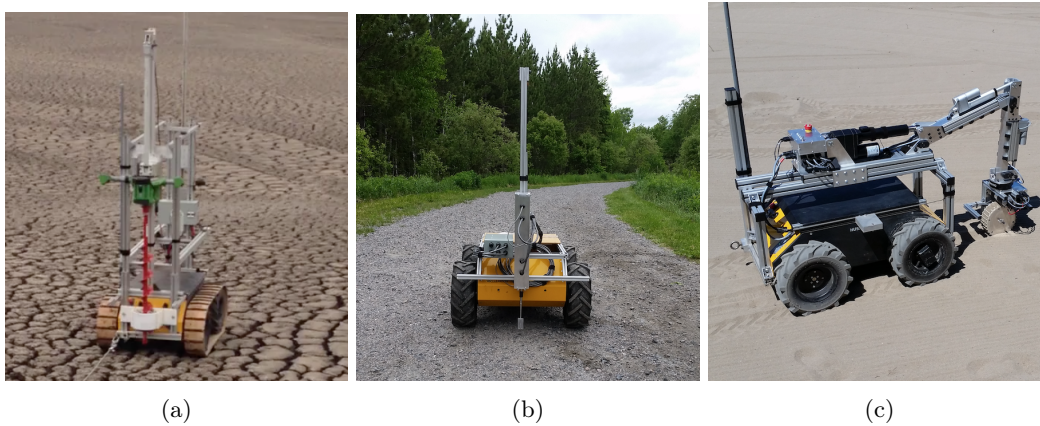


Figure 6.1: (a) RTC-I, a UGV for tailings characterization was deployed on an oil sands mine waste dedicated disposal area to collect subsurface samples by drilling through a crust and deploying a soft tailings sampler [33]. (b) A custom vane shear test tool was developed for mine waste monitoring and integrated onboard a UGV for remote site investigations [32]. (c) RTC-II, a UGV outfitted with a custom robotic manipulator to deploy soil sampling and terrain characterization tools, such as an instrumented wheel for terramechanics experiments and a surface soil sampler [31].

This paper describes the development and experimental validation of a novel terramechanics model for a scoop-type robotic sampler. This robotic sampler, whose electro-mechanical design is detailed in [31], was designed for two simultaneous tasks: i) collecting undisturbed surface soil samples, and ii) measuring interaction forces for soil characterization. The proposed terramechanics model extends previously proposed models [28] by accounting for cohesion and adhesion of the soil. The proposed model is successfully validated in both simulation and experimental testing, and demon-

Nomenclature

β	excavator rake angle (rad)	h_0	height of sampler axis (m)
δ	external friction angle (rad)	j	shear displacement (m)
λ	shear plane failure angle (rad)	k	shear deformation modulus (m)
ϕ	internal friction angle (rad)	K_0	coefficient of static earth pressure
ρ	soil density (kg/m^3)	k_ϕ	friction moduli of deformation (kPa/m^n)
σ	normal stress (kPa)	k_c	cohesive moduli of deformation ($\text{kPa}/\text{m}^{n-1}$)
τ	shear stress (kPa)	n	pressure sinkage exponent
θ_s	sampler rotation angle (rad)	q	surcharge (kPa)
θ_{sb}	sampler back contact angle (rad)	r_s	sampler radius (m)
c	cohesion stress (kPa)	t_s	sampler edge thickness (m)
c_a	soil-tool adhesion (kPa)	v_e	excavator cutting speed (m/s)
c_t	thickness ratio (%)	w_s	sampler width (m)
d	excavator cutting depth (m)		
g	gravity (m/s^2)		

strates improved force prediction performance over the earlier model.

The remainder of this paper is structured as follows. Section 6.2 reviews the literature on scoop-type samplers and the state-of-the-art in tool-soil interaction models. Section 6.3 details the proposed terramechanics model. Section 6.4 presents model analyses and comparisons with existing models. Section 6.5 presents experimental model validation results using characterized soils. Conclusions and recommendations for future work are given in Section 6.

6.2 Background and Literature Review

Surface sampling yields important measurements regarding terrain, and is regularly used in applications such as planetary exploration and environmental monitoring of industrial activities. The Mars Exploration Rovers and Phoenix Mars Lander used robotic arms for in-situ sampling and excavation [40]. The Icy Soil Acquisition Device payload of the Phoenix Lander's robotic manipu-

lator was used to collect samples on Mars [6]. It consisted of a scoop-type sampler with blades for excavating and rasping. End-effectors with detachable scoops have been proposed to prevent cross-contamination of samples [48]. Meanwhile, continuous excavation tools, such as bucket wheels for collecting large (on the order of cubic meters) volumes of material, have been discussed for in-situ resource utilization applications [37].

Scoop-type samplers have been deployed to collect undisturbed surface samples for mine waste monitoring. Samples with intact surfaces are required to calibrate non-contact testing techniques such as hyperspectral measurements. Bitumen content estimation and prediction of water content as well as normalized evaporation of oil sands tailings have been demonstrated using broad-band infrared reflectance spectra measurements [36, 11]. Scoop-type samplers were used for these tests to minimize soil deformation of the samples. A lightweight scoop design for sampling from a hovering UAV was demonstrated in [30]. When designing scoop samplers, reaction forces, power requirements, soil bulldozing, and large deformations can all be reduced by placing the axis of rotation and the axis of curvature at the same location [28].

Xue *et al* investigated the interaction forces between miniaturized scoop-type excavators and regolith or gravels based on the excavation torque required to collect samples [46]. The effects of bulk density of the sampled material and the geometrical parameters of the sampling mechanism were discussed. Trajectory design for surface sampling tools has also been investigated [19]. Flexible-rigid scoop-style sampling tools have been developed to reduce mass, volume, and power consumption [22]. The dynamics and control of a flexible-rigid scoop-style sampling tool have been presented in [20].

Our RTC-II robot, shown in Figure 6.2, is used for tailings characterization and can deploy an instrumented scoop-type sampler using its robotic manipulator. Details of this design are given in [31]. The sampler includes a vertical blade to brace against reaction forces during sampling, which can also be used to excavate the surface of the terrain.

In the next section, we will review the leading models in tool-soil interaction for scoop samplers, then in simple excavation tools.

6.2.1 Tool-Soil Interaction Model for Scoop Samplers

Mori *et al* developed a tool-soil force interaction model for a hemispherical scoop sampler, illustrated in Figure 6.3, based on experimental measurements of reaction forces and torques and soil deformations measured via particle image velocimetry (PIV) [28]. Their objective was to obtain a reliable model to design energy-efficient sampling tools and techniques, as well as their associated robotic manipulators, actuators, and control strategies. They argued that soil terramechanics models are a more suitable approach to calculate the soil-tool interaction forces than finite-element



Figure 6.2: RTC-II with scoop sampler attached to the robotic manipulator. The robot is used to collect surface samples for environmental monitoring in mine waste.

methods, which would lead to unmanageably large calculations [28].

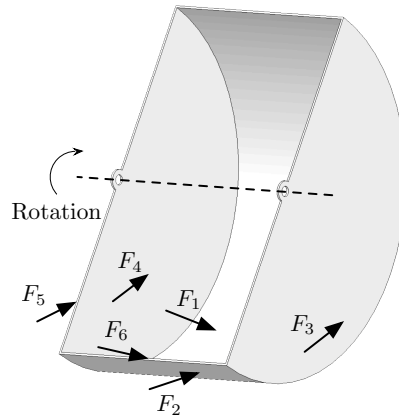


Figure 6.3: Hemispherical tool for soil sampling.

The Mori tool-soil interaction model estimates the six forces shown in Figure 6.3: F_1 and F_2 act

on the inner and outer surfaces of the circular wall, respectively; F_3 and F_4 act on the outer and inner surfaces of the flat side walls, respectively; F_5 and F_6 act on the edges of the side walls and circular wall, respectively. Forces F_1 , F_4 , and F_6 are assumed to be included in the passive earth pressure force P_p calculated from Coulomb's passive earth theory [9]:

$$P_p = \frac{\sin(\phi + \lambda)}{\sin(\pi - \theta_p - \delta - \phi - \lambda)} W \quad (6.1)$$

The angle terms in (6.1) are illustrated in Figure 6.4: ϕ is the soil's internal friction angle, λ is the failure surface angle, δ is the friction angle between the soil and the tool, θ_s is the sampler rotation angle, and θ_p is defined for $\theta_s > 0$ as:

$$\theta_p = \frac{\theta_s + \theta_{sb}}{2} \quad (6.2)$$

where θ_{sb} is the back contact angle of the sampler. The weight of the soil is $W = S_{\text{soil}} w_s \rho g$ where S_{soil} is the surface area within points {A,B,C,D} (coloured in grey in Figure 6.4), w_s is the sampler width, ρ is the soil density, and g is gravity acceleration.

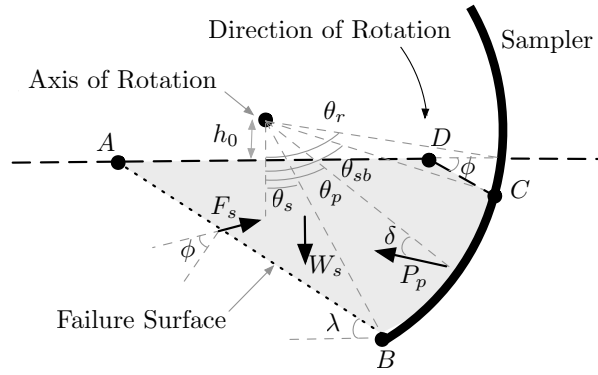


Figure 6.4: Angles and forces between the soil and sampler.

Mori *et al* found that F_2 was negligible in their model due to negative dilatancy effects in the loose soil used in their experiments [28]. The components of F_3 are calculated by integrating the stresses generated at the outer surfaces of the side walls, as illustrated in Figure 6.5:

$$F_{3x} = 2 \int_{h_0}^{r_s} \int_{\theta_r}^{\theta_s} \tau(r, \alpha) \cos \alpha \, d\alpha \, dr \quad (6.3)$$

$$F_{3y} = 2 \int_{h_0}^{r_s} \int_{\theta_r}^{\theta_s} \tau(r, \alpha) \sin \alpha \, d\alpha \, dr \quad (6.4)$$

where r_s is the sampler radius and h_0 is the height of the rotation axis above the soil¹. Angle θ_r is

$$\theta_r = \arccos(h_0/r_s) \quad (6.5)$$

The term $\tau(r, \alpha)$ is the shear stress given by

$$\tau(r, \alpha) = \tau_{max}(1 - \exp^{-j/k}) \quad (6.6)$$

where $j = r(\alpha - \theta_s)$ is the shearing displacement at the element located at angle α and distance r from the rotation axis (Figure 6.5), k is the shear deformation modulus, and τ_{max} is the maximum shear stress obtained from the Mohr-Coulomb equation:

$$\tau_{max} = c + \sigma \tan \phi \quad (6.7)$$

where c is the cohesion of the soil and σ is the horizontal normal stress

$$\sigma_h(r, \alpha) = K_0(r \cos \alpha - h_0)\rho g \quad (6.8)$$

where K_0 is the coefficient of static earth pressure. For coarse-grained soils, K_0 can be approximated as [18]

$$K_0 = 1 - \sin \phi \quad (6.9)$$

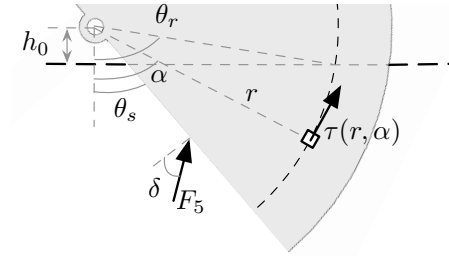


Figure 6.5: Side surface shear stress and edge pressure.

Force F_5 acting on the scoop side wall edges is calculated from the integration of the Bekker plate sinkage equation [3]:

$$\sigma(h) = (k_c/t_s + k_\phi) h^n \quad (6.10)$$

$$F_5 = 2 \int_{h_0}^{r_s \cos \theta_s} \sigma(h) c_t t_s \frac{1}{\cos \theta_s} dh \quad (6.11)$$

¹Note the limits of integration and the integrands in (6.3), (6.4) were originally published with an error, which will be discussed in Section 6.4.

where k_c , k_ϕ and n are soil parameters, t_s is the thickness of the edge, and $0 < c_t < 1$ is an edge thickness factor. The direction of F_5 is determined by the rotation of the sampler and the friction angle between the soil and tool, as shown in Figure 6.4.

Mori *et al* found that F_5 is the dominant force during the initial rotation of the sampler ($0 \leq \theta \leq \pi/2$), and P_p is dominant in the subsequent part. Their PIV measurements showed increased soil deformations when $\theta_s \leq 0$. Their experiments found negligible velocity-dependent forces at slow rotation speeds, in the range of 3 to 7 deg/s [28]. The rotation speed of the robot sampler in Figure 6.2 can be controlled to meet this range.

The model proposed in [28] was only validated in loose soils used in the study. In many field applications, such as mine waste, fine-grained cohesive soils are present. In this case, it is expected that the cohesion stress which affects F_3 will play a dominant role. In addition, we expect cohesion to affect F_2 , such that this term can no longer be neglected. Finally, the formulation of P_p (6.1) is only valid for cohesionless soils with no adhesion to the tool, and will need to be modified. Our proposed soil-tool interaction model will remove these assumptions to make it applicable to cohesive terrains, and their associated adhesion between tool and soil and resulting surcharge during sampling operations.

6.2.2 Estimating Soil Parameters Using Robotic Excavation Tools

A review of resistive force models for earthmoving processes is given in [4]. Simplified blade-shovel models have been used to study cutting forces and estimate soil parameters. Althoefer *et al* used a robotic manipulator with a blade end-effector to estimate the soil-tool and soil internal friction angles δ and ϕ , cohesion c , and density of the medium ρ using a hybrid of the Mohr-Coulomb model and the Chen and Liu upper-bound soil model [1]. Yousefi-Moghaddam *et al* demonstrated a bench-scale shovel assembly used for on-line estimation of soil parameters from cutting forces [49]. The authors used the Newton-Raphson method to iteratively estimate parameters δ , ϕ and c in the Mohr-Coulomb model (Figure 6.6). These investigations focused on the application of the developed methods to large-scale mining and construction equipment.

Recently, models which predict tillage and excavation forces have been proposed, including the effects of surcharge accumulation [38]. A review of the current analytical models used for lunar excavation is available in [45] with experimental verification in idealized conditions. The McKyes soil-cutting model [27] and the Swick and Perumpral model [39] were recommended, as they include the effects of adhesion, weight, surcharge, cohesion and inertia of the displaced soil [45].

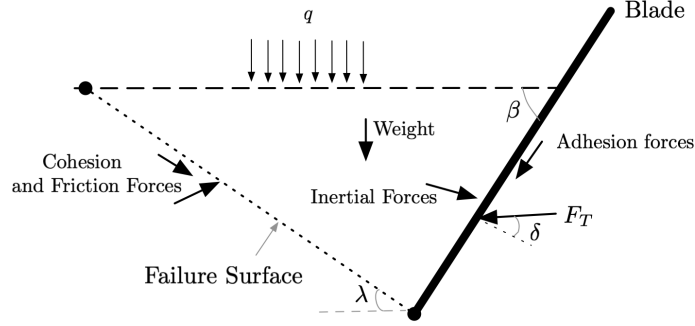


Figure 6.6: Simplified shovel assembly interaction forces based on Mohr-Coulomb model.

The McKyes model [27] predicts the total excavation force, F_T , to be

$$\begin{aligned}
 F_T = & \left[\frac{g\rho d}{2}(\cot \beta + \cot \lambda) + q(\cot \beta + \cot \lambda) + c(1 + \cot \lambda \cot(\lambda + \phi)) \right. \\
 & \left. + c_a(1 - \cot \beta \cot(\lambda + \phi)) + \frac{\rho v_e^2(\tan \lambda + \cot(\lambda + \phi))}{1 + \tan \lambda \cot \beta} \right] \\
 & \times \left(\frac{wd}{\cos(\beta + \delta) + \sin(\beta + \delta) \cot(\lambda + \phi)} \right)
 \end{aligned} \tag{6.12}$$

The Swick and Perumpral model[39] predicts this force to be:

$$\begin{aligned}
 F_T = & \left[\frac{g\rho d}{2}(\cot \beta + \cot \lambda) \sin(\phi + \lambda) + q(\cot \beta + \cot \lambda) \sin(\phi + \lambda) \right. \\
 & \left. + \frac{c \cos \phi}{\sin \lambda} + \frac{-c_a \cos(\beta + \phi + \lambda)}{\sin \beta} + \frac{\rho v_e^2 \sin \beta \cos \phi}{\sin(\beta + \lambda)} \right] \\
 & \times \left(\frac{wd}{\sin(\beta + \phi + \lambda + \delta)} \right)
 \end{aligned} \tag{6.13}$$

where d is the cutting depth, β is the rake angle, v_e is the cutting speed, c_a is the soil-tool adhesion, ρ is the soil density, λ is the shear plane failure angle, q is the surcharge pressure, c is the cohesion, w is the tool width, and g is the acceleration of gravity.

6.3 Robotic Sampler Model

In this section we propose an analytical model of the forces acting on a scoop-type surface sampler whose geometry is schematically illustrated in Figure 6.7. The UGV robot previously seen in Figure 6.2 carries a scoop sampler with this geometry. Further mechanical design details are provided in [31].

The forces acting on the scoop sampler are listed in Table 6.1. All the forces listed have a comparable element in Mori *et al*'s Sampler Model (MSM) [28] detailed in Section 6.2.1 and visualized in Figure 6.3.

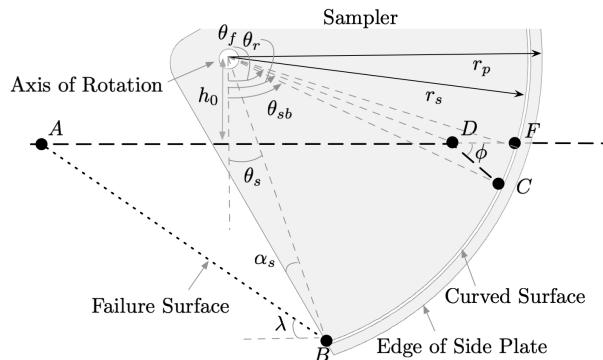


Figure 6.7: Scoop sampler geometry.

Table 6.1: Sampler-soil interaction forces.

Force	Description	Analogue in MSM
P	Earth pressure force	P_p
F_{oc}	Force on outer surface of the curved wall	F_2
F_o	Force on outer surface of the side wall	F_3
F_i	Force on inner surface of the side wall	F_4
F_e	Force on edge of the side wall	F_5
F_{ec}	Force on edge of the curved wall	F_6

The force acting on the edge of the curved wall F_{ec} is assumed to be included in the earth pressure force P , just like F_6 was assumed to be included in P_p in MSM. The PIV results in [28] demonstrated that the force on the outer surface of the curved wall F_{oc} (F_2 in MSM) is negligible for loose soils with negative dilatancy.

The key differences between MSM and our proposed Robotic Sampler Model (RSM) are:

- P is formulated to include the effects of cohesion, adhesion, and surcharge; F_i is kept separate from P to model possible adhesion effects. In MSM F_4 is assumed to be included in P_p .
- F_o and F_i result from friction and adhesion forces, rather than cohesion forces like in MSM.
- F_e is formulated to model the side-edge interactions with the soil as a pressure-sinkage relationship, similarly to F_5 in MSM but using a higher-fidelity model.
- F_{oc} is included in the model as an adhesion force, unlike MSM which assumes F_2 to be negligible.

Mori *et al* only considered a sampler with α_s , the front edge angle seen in Figure 6.7, equal to zero. Adding this parameter increases the design flexibility of the scoop sampler. Additionally, the sides of the sampler can be extended past the radius of the curved surface, up to a radius r_p .

The effect of wedges formed on the sides of the failure wedge in front of the tool was assumed to be negligible because the sampler is not plowing through terrain as a tillage tool. Reviews of other excavation models have assumed the same when soil deformations on the sides of the tool are not significant [45]. An empirical model for narrow tillage tools with side effects was proposed by Swick *et al* in [39]. The significance of the side effects in their application was demonstrated by the large soil deformations on the sides of the tool. Larger effects can exist in applications with tools moving at high speeds [39].

6.3.1 Forces Acting on the Idealized Failure Wedge

Consider the scoop sampler illustrated in Figure 6.8, with an idealized failure wedge with an approximately flat failure surface and geometry parameters defined in Figure 6.7. The forces acting on the soil wedge during a soil sampling operation are shown in Figure 6.8. The model could be extended to consider other geometries such as a logarithmic failure plane.

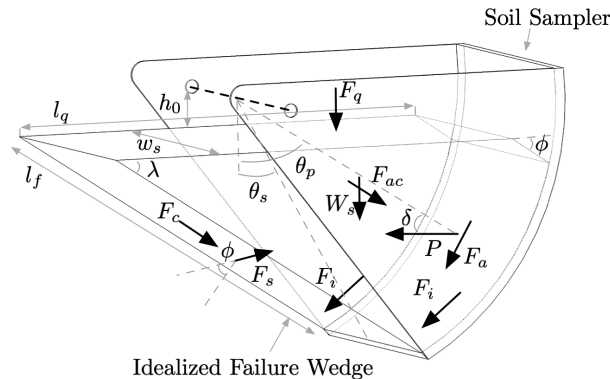


Figure 6.8: Forces acting on the idealized failure wedge.

In Figure 6.8, F_{ac} represents the force resisting acceleration. F_{ac} is assumed to be parallel to the failure surface, similarly to [39]. F_{ac} is assumed to be negligible, because the sampling action is very slow and does not displace a significant amount of material, as would be the case for tillage or plowing tools. This force is used to investigate the effects of horizontal speed in applications involving fast-moving tools.

F_q is the force resulting from surcharge pressure q acting on the upper surface of the wedge with length l_q and width w_s . F_q is calculated by

$$F_q = qw_sl_q \quad (6.14)$$

where l_q is obtained from the geometry of Figure 6.8:

$$l_q = r(\sin \theta_{sb} - \sin \theta_s) + (r \cos \theta_s - h_0) \cot \lambda + (h_0 - r \cos \theta_{sb}) \cot \phi \quad (6.15)$$

F_s is the friction force at the failure surface. It can be decomposed into F_{sp} and F_{sn} , the frictional force components parallel and normal to the failure surface, respectively:

$$F_{sp} = F_s \sin \phi \quad (6.16)$$

$$F_{sn} = F_s \cos \phi \quad (6.17)$$

F_c is the cohesion force on the failure surface:

$$F_c = cw_sl_f \quad (6.18)$$

where l_f , the length of the failure surface, is obtained as

$$l_f = (r_s \cos \theta_s - h_0) / \sin \lambda \quad (6.19)$$

F_a is the force at the soil touching the curved surface of the sampler due to soil-tool adhesion c_a . The net horizontal and vertical components F_{ax} and F_{ay} acting on the soil are

$$F_{ax} = c_a w_s \int_{\theta_s}^{\theta_{sb}} r_s \cos \alpha d\alpha = c_a w_s r_s (\sin \theta_{sb} - \sin \theta_s) \quad (6.20)$$

$$F_{ay} = c_a w_s \int_{\theta_s}^{\theta_{sb}} r_s \sin \alpha d\alpha = c_a w_s r_s (\cos \theta_s - \cos \theta_{sb}) \quad (6.21)$$

W_s is the weight of the soil wedge:

$$W_s = w_s \rho g S_{soil} \quad (6.22)$$

where S_{soil} is the cross-sectional area of the wedge given by

$$\begin{aligned}
S_{soil} = & \frac{1}{2} \csc(\lambda) \sec(\theta_s) \cos(\lambda + \theta_s) (h_0 - r_s \cos(\theta_s))^2 \\
& + \frac{1}{2} (h_0^2 (\tan(\theta_s) - \tan(\theta_{sb})) + r_s^2 (\theta_{sb} - \theta_s)) \\
& - \frac{1}{2} \csc(\phi) \sec(\theta_{sb}) \cos(\phi + \theta_{sb}) (h_0 - r_s \cos(\theta_{sb}))^2
\end{aligned} \tag{6.23}$$

F_i is the frictional and adhesional force resisting movement on the internal surface of the side walls of the sampler. Its net horizontal and vertical components, F_{ix} and F_{iy} , are given by

$$\begin{aligned}
F_{ix} = & 2 \int_{r_{i1}}^{r_{i2}} \int_{\theta_{i1}}^{\theta_{i2}} \tau_a(r, \alpha) r \cos \alpha \, d\alpha \, dr \\
& - 2 \int_{r_{i3}}^{r_{i4}} \int_{\theta_{i3}}^{\theta_{i4}} \tau_a(r, \alpha) r \cos \alpha \, d\alpha \, dr
\end{aligned} \tag{6.24}$$

$$\begin{aligned}
F_{iy} = & 2 \int_{r_{i1}}^{r_{i2}} \int_{\theta_{i1}}^{\theta_{i2}} \tau_a(r, \alpha) r \sin \alpha \, d\alpha \, dr \\
& - 2 \int_{r_{i3}}^{r_{i4}} \int_{\theta_{i3}}^{\theta_{i4}} \tau_a(r, \alpha) r \sin \alpha \, d\alpha \, dr
\end{aligned} \tag{6.25}$$

where τ_a is the shear stress generated by frictional and adhesional forces on the internal surfaces,

$$\tau_a(r, \alpha) = \tau_{a,max} (1 - \exp^{-j/k_a}) \tag{6.26}$$

where j is the shear displacement at radius r and angle α (c.f. Figure 6.5), k_a is the shear deformation modulus of the soil-tool interaction, and $\tau_{a,max}$ is given by

$$\tau_{a,max} = c_a + \sigma \tan \delta \tag{6.27}$$

where σ is the horizontal normal stress given by (6.8). The first terms in F_{ix} (6.24) and F_{iy} (6.25) integrate the stress over the area of the side plate up to height h_0 , and the second terms subtract the contribution of the side plate area at the back of the wedge, delineated by points DCF in Figure 6.7. The integration limits in (6.24), (6.25) are given by:

$$\theta_{i1} = \alpha_s + \theta_s - \arcsin(\sin \alpha_s (r_s/r)) \tag{6.28}$$

$$\theta_{i2} = \arccos(h_0/r) \tag{6.29}$$

$$\theta_{i3} = \arccos(\cos(\phi + \theta_{sb})(r_s/r)) - \phi \tag{6.30}$$

$$\theta_{i4} = \arccos(h_0/r) \quad (6.31)$$

$$r_{i1} = \sqrt{r_s^2 + \left(\frac{(r_s \cos \theta_s - h_0)}{\cos(\alpha_s + \theta_s)} \right)^2 - 2r_s \cos \alpha_s \frac{(r_s \cos \theta_s - h_0)}{\cos(\alpha_s + \theta_s)}} \quad (6.32)$$

$$r_{i2} = r_s \quad (6.33)$$

$$r_{i3} = \sqrt{r_s^2 + \left(\frac{(r_s \cos \theta_{sb} - h_0)}{\sin(\phi)} \right)^2 - 2r_s \sin(\phi + \theta_{sb}) \frac{(r_s \cos \theta_{sb} - h_0)}{\sin(\phi)}} \quad (6.34)$$

$$r_{i4} = r_s \quad (6.35)$$

The pressure force P can be determined from the balance of forces acting on the idealized failure wedge. Summing forces in the horizontal and vertical directions yields the following expressions:

$$P \sin(\theta_p + \delta) = -(F_{ax} + F_{ix}) + F_{sn} \sin \lambda + (F_{sp} + F_c + F_{ac}) \cos \lambda \quad (6.36)$$

$$P \cos(\theta_p + \delta) = W_s + F_q + (F_{ay} + F_{iy}) - F_{sn} \cos \lambda + (F_{sp} + F_c + F_{ac}) \sin \lambda \quad (6.37)$$

Combining Equations (6.36) and (6.37) yields

$$P = \left((W_s + F_q + F_{ay} + F_{iy}) \sin(\phi + \lambda) - (F_{ax} + F_{ix}) \cos(\phi + \lambda) + (F_c + F_{ac}) \cos \phi \right) / \sin(\theta_p + \delta + \phi + \lambda) \quad (6.38)$$

Angle θ_p is obtained from Equation (6.2) if $\theta_s > 0$; if $\theta_s < 0$, the expression for θ_p can be found in [28].

In Equation (6.38), the failure angle λ is unknown, and so it must be found by minimizing the pressure force P with respect to λ . Passive failure occurs when resistance of the soil wedge is minimum [39].

6.3.2 Forces and Moments Acting on Sampler

The scoop sampler experiences reaction forces from the soil wedge (P , F_a , and F_i in Figure 6.8) and soil-tool interaction forces on the edges and outer surfaces of the side plates, F_e and F_o respectively.

The components of pressure force P in the horizontal and vertical directions, P_x and P_y , and the moment generated by P about the sampler's rotation axis, M_P , are given by

$$P_x = P \cos(\pi/2 - \theta_p - \delta) \quad (6.39)$$

$$P_y = -P \sin(\pi/2 - \theta_p - \delta) \quad (6.40)$$

$$M_P = r_s P \sin(\delta) \quad (6.41)$$

The components of F_a and F_i in the x and y directions were given in Equations (6.20), (6.21), 6.24 and (6.25), respectively. The moments M_{F_a} and M_{F_i} , respectively generated by F_a and F_i about the sampler rotation axis, are given by

$$M_{F_a} = c_a w_s \int_{\theta_s}^{\theta_{sb}} r_s^2 d\alpha = c_a w_s r_s^2 (\theta_{sb} - \theta_s) \quad (6.42)$$

$$\begin{aligned} M_{F_i} = & 2 \int_{r_{i1}}^{r_{i2}} \int_{\theta_{i1}}^{\theta_{i2}} r^2 \tau_a(r, \alpha) d\alpha dr \\ & - 2 \int_{r_{i3}}^{r_{i4}} \int_{\theta_{i3}}^{\theta_{i4}} r^2 \tau_a(r, \alpha) d\alpha dr \end{aligned} \quad (6.43)$$

The side wall outer surface force F_o is calculated by integrating the shear stress τ_a on the outer sides of the sampler. This stress is obtained from Equations (6.26) and (6.27). The components of F_o along the horizontal and vertical directions, F_{ox} and F_{oy} , and the moment generated by F_o about the sampler axis of rotation, M_{F_o} , are:

$$F_{ox} = 2 \int_{r_{o1}}^{r_{o2}} \int_{\theta_{o1}}^{\theta_{o2}} \tau_a(r, \alpha) r \cos \alpha d\alpha dr \quad (6.44)$$

$$F_{oy} = 2 \int_{r_{o1}}^{r_{o2}} \int_{\theta_{o1}}^{\theta_{o2}} \tau_a(r, \alpha) r \sin \alpha d\alpha dr \quad (6.45)$$

$$M_{F_o} = 2 \int_{r_{o1}}^{r_{o2}} \int_{\theta_{o1}}^{\theta_{o2}} r^2 \tau_a(r, \alpha) d\alpha dr \quad (6.46)$$

The limits of the above integrals are:

$$\theta_{o1} = \alpha_s + \theta_s - \arcsin(\sin(\alpha_s)(r_p/r)) \quad (6.47)$$

$$\theta_{o2} = \arccos(h_0/r) \quad (6.48)$$

$$r_{o1} = \sqrt{r_p^2 + \left(\frac{(r_p \cos \theta_s - h_0)}{\cos(\alpha_s + \theta_s)} \right)^2} - 2r_p \cos \alpha_s \frac{(r_p \cos \theta_s - h_0)}{\cos(\alpha_s + \theta_s)} \quad (6.49)$$

$$r_{o2} = r_p \quad (6.50)$$

Remark the above limits become identical to the earlier (6.24), (6.25) F_i integral limits (6.28)–(6.35) when $r_p = r_s$.

The outside force F_{oc} , used to model tool-soil interaction at the outer surface of the curved scoop blade, is calculated from the shear and normal stresses acting on this surface. Its components along the horizontal and vertical directions and the associated moment about the scoop axis are given by

$$F_{ocx} = w_s(r_s + t_s) \left(\int_{\theta_s}^{\theta_{oc}} \tau_{oc}(\alpha) \cos \alpha d\alpha - \int_{\theta_s}^{\theta_{oc}} \sigma_{oc}(\alpha) \sin \alpha d\alpha \right) \quad (6.51)$$

$$F_{ocy} = w_s(r_s + t_s) \left(\int_{\theta_s}^{\theta_{oc}} \tau_{oc}(\alpha) \sin \alpha d\alpha + \int_{\theta_s}^{\theta_{oc}} \sigma_{oc}(\alpha) \cos \alpha d\alpha \right) \quad (6.52)$$

$$M_{F_{oc}} = w_s(r_s + t_s)^2 \int_{\theta_s}^{\theta_{oc}} \tau_{oc}(\alpha) d\alpha \quad (6.53)$$

The value of the upper integration limit θ_{oc} , representing the contact angle of the surface, can be lower than θ_f if there is significant shearing and remoulding of the surface of the soil as the sampler is introduced into it. In this case θ_{oc} needs to be determined experimentally. The shear and normal stresses τ_{oc} and σ_{oc} are given by:

$$\tau_{oc}(\alpha) = (c_a + \sigma_{oc}(\alpha) \tan \phi)(1 - \exp^{-j/k_a}) \quad (6.54)$$

$$\sigma_{oc}(\alpha) = \begin{cases} K_0 \rho g ((r_s + t_s) \cos \alpha - h_0) & \alpha > \theta_p \\ K_0 \rho g (r_s + t_s) \cos(\theta_s - (\alpha - \theta_s)(\theta_{oc} - \theta_{ocm})/(\theta_{ocm} - \theta_s)) & \alpha \leq \theta_{ocm} \end{cases} \quad (6.55)$$

where θ_{ocm} is the midway angle between the contact angles θ_s and θ_{oc} :

$$\theta_{ocm} = \theta_s + (\theta_{oc} - \theta_s)/2 \quad (6.56)$$

Alternative formulations for F_o (force at side walls) and F_{oc} (force at curved blade) can be employed if the cohesion forces of the material are much smaller than the adhesion forces of the soil-tool interaction. In this case, the shear stress expressions (6.6) and (6.54) would need to replace the adhesion soil parameters with those in the integrals of F_{ox} , F_{oy} , and M_{F_o} , F_{ocx} , F_{ocy} , and $M_{F_{oc}}$, since soil failure would occur prior to soil slip on the surface of the tool.

The edge force F_e is calculated by integration of the earlier sinkage-dependent stress expression $\sigma(h)$ (6.10) along the edges of the sides of the sampler. The horizontal and vertical components, F_{ex} and F_{ey} , and the moment about the axis of rotation generated by F_e , M_{F_e} , are then given by

$$F_{ex} = \int_{r_{e1}}^{r_{e2}} t_s \left(\frac{k_c}{t_s} + k_\phi \right) (r \cos(\theta_s + \alpha_s) - h_0)^n \cos(\delta + \theta_s + \alpha_s) dr \quad (6.57)$$

$$F_{ey} = \int_{r_{e1}}^{r_{e2}} t_s \left(\frac{k_c}{t_s} + k_\phi \right) (r \cos(\theta_s + \alpha_s) - h_0)^n \sin(\delta + \theta_s + \alpha_s) dr \quad (6.58)$$

$$M_{F_e} = \int_{r_{e1}}^{r_{e2}} t_s \left(\frac{k_c}{t_s} + k_\phi \right) r (r \cos(\theta_s + \alpha_s) - h_0)^n \cos(\delta) dr \quad (6.59)$$

where the limits of the integrals are

$$r_{e1} = h_0 / \cos(\theta_s + \alpha_s) \quad (6.60)$$

$$r_{e2} = r_p \quad (6.61)$$

Remark than unlike F_5 in Equation (6.11), the present F_e does not depend on the fitting parameter c_t .

The net horizontal force F_x , vertical force F_y and moment M acting on the sampler are given by

$$F_x = F_{ax} + F_{ix} + F_{ox} + F_{ex} + F_{ocx} + P_x \quad (6.62)$$

$$F_y = F_{ay} + F_{iy} + F_{oy} + F_{ey} + F_{ocy} + P_y \quad (6.63)$$

$$M = M_p + M_{F_a} + M_{F_i} + M_{F_o} + M_{F_{ocx}} + M_{F_e} \quad (6.64)$$

6.4 Analysis and Comparison of Models

A sampling operation was simulated using the MSM and our proposed RSM. The purpose is to gain insights into the effects of the individual components of the RSM and its key differences with the MSM. The models were simulated using the open source Python library, SciPy, assuming quasi-static conditions, $F_a c = 0$.

A sampling operation was simulated in three terrains: Dry Sand (DS), Sandy Loam (SL), and Clayey Soil (CS). These were chosen to compare the models across a range of terrains with different characteristics. For example, the effects of cohesion and adhesion are expected to be significant in clay but very small in dry sand. The simulated material properties are listed in Table 6.2 and were obtained from [17]. δ was assumed to be 2/3 of ϕ [25], and K_0 was calculated by Equation (6.9). The adhesion of each material was assumed to be half of its cohesion. This was done for simplicity and to avoid artificially inflating the effect of adhesion. Additionally, all the materials were assumed to be loose, such that the effects of F_{oc} would be negligible. The robotic sampler geometrical parameters used for the simulation are listed in Table 6.3.

For fairness of comparison, the scoop geometry (Figure 6.7) parameter r_p was assumed to be equal to

Table 6.2: Properties of simulated materials

Property	Dry Sand	Sandy Loam	Clayey soil
ρ (kg/m ³)	1442	1280	1600
ϕ (deg)	30.0	29.0	13.0
δ (deg)	20.0	19.3	8.70
K_0	0.50	0.52	0.78
c (Pa)	0	1700	4140
k (m)	0.025	0.025	0.01
n	1.10	0.70	0.50
k_c (kPa/m ^{$n-1$})	0.90	5.30	13.2
k_ϕ (kPa/m ^{n})	1523.4	1515.0	692.2

Table 6.3: Geometric parameters of simulated sampler

Parameter	Value
r_s (m)	0.105
w_s (m)	0.123
t_s (m)	0.001

r_s , while α_s was assumed to be zero, since MSM does not include these parameters. The distance to the ground from the axis of rotation h_0 was chosen to be 63 mm to mirror experimental conditions. The edge thickness parameter c_t in MSM was determined to be 20%, 30%, and 45% for dry sand, sandy loam, and clayey soil respectively, as discussed at the end of Section 6.4.2.

A correction was required to the published MSM equations [28, Eqs. (9),(10)]. The updated expressions for the components of F_3 in the horizontal and vertical directions, F_{3x} and F_{3y} , and the moment about the axis of rotation generated by F_3 , M_{F_3} , are given by:

$$F_{3x} = \int_{h_0/\cos\theta_s}^{r_s} \int_{\theta_s}^{\theta_r} \tau(r, \alpha) r \cos \alpha \, d\alpha \, dr \quad (6.65)$$

$$F_{3y} = \int_{h_0/\cos\theta_s}^{r_s} \int_{\theta_s}^{\theta_r} \tau(r, \alpha) r \sin \alpha \, d\alpha \, dr \quad (6.66)$$

$$M_{F_3} = \int_{h_0/\cos\theta_s}^{r_s} \int_{\theta_s}^{\theta_r} r^2 \tau(r, \alpha) \, d\alpha \, dr \quad (6.67)$$

The simulations were conducted by numerically integrating the equations of MSM and RSM across the range of motion of the scoop during a sampling operation, taken as $55^\circ \geq \theta_s \geq 0$. SciPy uses the Clenshaw-Curtis quadrature method and was set to have an absolute error tolerance of 1×10^{-10} .

The following subsections discuss the differences in the computed total forces and moments acting

on the sampler, analyze the sensitivity of the results to the individual components of the models, and discuss the effects which are modeled only by RSM such as surcharge while sampling.

6.4.1 Comparison of Total Forces and Moments Acting on the Sampler

The total forces F_x and F_y and the moment M acting on the sampler are plotted in Figure 6.9. There are differences between the results obtained with MSM and RSM. These differences are small for dry sand, but are significant for sandy loam and clayey soil.

The small differences between models for dry sand and large differences for sandy loam and clayey soil are due to the properties of the different materials. The effects of cohesion at the failure surface and adhesion between the soil and the sampler are captured by RSM but not MSM. Since cohesion and adhesion of dry sand are negligible, their effect on the RSM results is also negligible, and indeed the forces and moments estimated by RSM and MSM are nearly the same as seen in Figures 6.9a and 6.9b. The angle of the failure surface λ predicted by MSM is very close to that predicted by RSM. For cohesionless soils, P is primarily determined by the weight of the soil. The small differences between the models on dry sand is primarily due to the effect of F_i on P and the formulation of F_5 and F_e . This will be further discussed in Section 6.4.2.

The magnitudes of the cohesion forces at the failure surfaces and the adhesion forces on the sampler are presented in Figure 6.10a for the three simulated materials. Both forces are significant for sandy loam and clayey soil and are zero for dry sand. The effects of F_a and F_c are reflected in the magnitude of P in Figure 6.10b. In the MSM P_p is very similar for all three materials, while the RSM predicts them to be approximately two (sandy loam) and three (clayey soil) times larger than for dry sand. The increased P is a major reason for the differences between the forces and moments on sandy loam and clayey soil seen in Figures 6.9c, 6.9d, 6.9e, 6.9f.

6.4.2 Sensitivity analysis of model components

An analysis of the contribution of the individual components of F_x , F_y and M for MSM and RSM is compiled in Tables 6.4 and 6.5 for dry sand and clayey soil, respectively. Plots of the individual components of F_x for MSM and RSM on clayey soil are shown in Figure 6.11.

The contributions of F_3 , F_i , F_o are relatively small in dry sand. This is as expected since cohesion and adhesion are negligible in this material and the sampler does not sink enough into the soil for normal stresses on the sides of the sampler to become significant. As shown in Table 6.4, the relative contributions of F_3 on F_x , F_y and M are 2.9%, 1.7%, and 4.6%, respectively. On clayey soil,

Table 6.4: Components of F_x , F_y , and M on Dry Sand

θ_s deg	F_x MSM DS			F_x RSM DS				
	P_{px} %	F_{5x} %	F_{3x} %	P_x %	F_{ex} %	F_{ax} %	F_{ix} %	F_{ox} %
0	58.2	38.8	2.9	58.8	36.3	0.0	2.4	2.4
15	58.0	40.4	1.4	61.0	36.3	0.0	1.2	1.2
30	55.5	43.8	0.5	65.3	33.5	0.0	0.5	0.5
45	42.9	56.9	0.0	72.7	27.0	0.0	0.0	0.0

θ_s deg	F_y MSM DS			F_y RSM DS				
	P_{py} %	F_{5y} %	F_{3y} %	P_y %	F_{ey} %	F_{ay} %	F_{iy} %	F_{oy} %
0	78.1	20.1	1.7	78.4	18.7	0.0	1.4	1.4
15	58.8	39.8	1.2	62.0	35.8	0.0	1.0	1.0
30	36.1	63.2	0.5	46.2	52.5	0.0	0.5	0.5
45	11.7	88.1	0.0	32.2	67.4	0.0	0.1	0.1

θ_s deg	M MSM DS			M RSM DS				
	M_{P_p} %	M_{F_5} %	M_{F_3} %	M_P %	M_{F_e} %	M_{F_a} %	M_{F_i} %	M_{F_o} %
0	44.1	51.2	4.6	43.1	49.3	0.0	3.7	3.7
15	38.0	59.4	2.4	39.5	56.1	0.0	2.1	2.1
30	27.9	71.1	0.8	35.8	62.3	0.0	0.9	0.9
45	11.8	88.0	0.0	31.7	67.9	0.0	0.1	0.1

these contributions increase to 9.1%, 21.1%, and 10.8%, respectively. The relative contributions of F_i and F_o on F_x , F_y and M are less than approximately 5% on dry sand and clayey soil. On clayey soil the relative contribution of F_a to F_x , F_y and M is between 7% to 15%.

MSM and RSM predict a large contribution of P_p and P respectively. On dry sand, the maximum contribution of P_p to F_x , F_y and M is 58.2%, 78.1%, and 44.1%, respectively. The relative contribution of P on dry sand to F_x , F_y and M matches the corresponding contributions of P_p within 1%. On clayey soil, the relative contributions of P and P_p decrease while the relative contributions of F_5 and F_e increase. In clayey soil MSM predicts that F_x , F_y and M are almost completely determined by F_5 over the majority of the range of motion.

Although F_5 and F_e employ the same pressure-sinkage equation and soil parameters, they still predict very different results. Experiments on dry sand, to be presented in Section 6.5.3, had to be used to determine that the fitting parameter c_t of F_5 was approximately 20%, while estimates of F_e approximated the experimental data closely without the need for a fitting parameter. The values of c_t for sandy loam and clayey soil were selected to be 30%, and 45% respectively so that the magnitude of F_5 matched F_e closely, as shown in Figure 6.12. In this way, the comparison between the models, such as the contributions of the components to the total loads, were not skewed due to

Table 6.5: Components of F_x , F_y , and M on Clayey Soil

θ_s deg	F_x MSM CS			F_x RSM CS				
	P_{px} %	F_{5x} %	F_{3x} %	P_x %	F_{ex} %	F_{ax} %	F_{ix} %	F_{ox} %
0	1.5	89.3	9.1	8.5	74.2	9.9	3.6	3.6
15	1.3	92.6	5.9	12.1	75.0	8.0	2.3	2.3
30	1.0	95.6	3.2	17.2	72.5	7.3	1.3	1.3
45	0.5	98.6	0.8	28.5	62.5	8.0	0.4	0.4

θ_s deg	F_y MSM CS			F_y RSM CS				
	P_{py} %	F_{5y} %	F_{3y} %	P_y %	F_{ey} %	F_{ay} %	F_{iy} %	F_{oy} %
0	10.6	68.1	21.1	37.9	35.7	15.7	5.2	5.2
15	3.2	88.3	8.3	23.9	60.3	10.0	2.8	2.8
30	1.1	95.3	3.5	17.6	71.3	8.0	1.4	1.4
45	0.2	99.0	0.6	15.8	74.9	8.2	0.4	0.4

θ_s deg	M MSM CS			M RSM CS				
	M_{P_p} %	M_{F_5} %	M_{F_3} %	M_P %	M_{F_e} %	M_{F_a} %	M_{F_i} %	M_{F_o} %
0	0.4	88.6	10.8	2.6	74.9	13.8	4.2	4.2
15	0.3	92.5	7.1	3.1	79.5	11.5	2.9	2.9
30	0.1	96.0	3.7	3.4	82.8	10.1	1.7	1.7
45	0.0	99.1	0.7	4.3	83.8	10.6	0.5	0.5

MSM overestimating F_5 .

6.4.3 Effect of surcharge

The predicted effect by RSM of a surcharge q is shown in Figure 6.13. A surcharge of 1 kPa was set in the models for dry sand and clayey soil. As expected, the total forces on the sampler increased in magnitude. The relative effect is more pronounced on dry sand because the total horizontal and vertical forces are small. The effect is less significant relative to the magnitude of the forces on clayey soil. Surcharge q affected the angle of the failure surface λ more on dry sand than in clayey soil because the relative contribution of F_q on P is larger when F_c and F_a are smaller. As seen from Equation (6.38), P is identically affected by F_q and W_s .

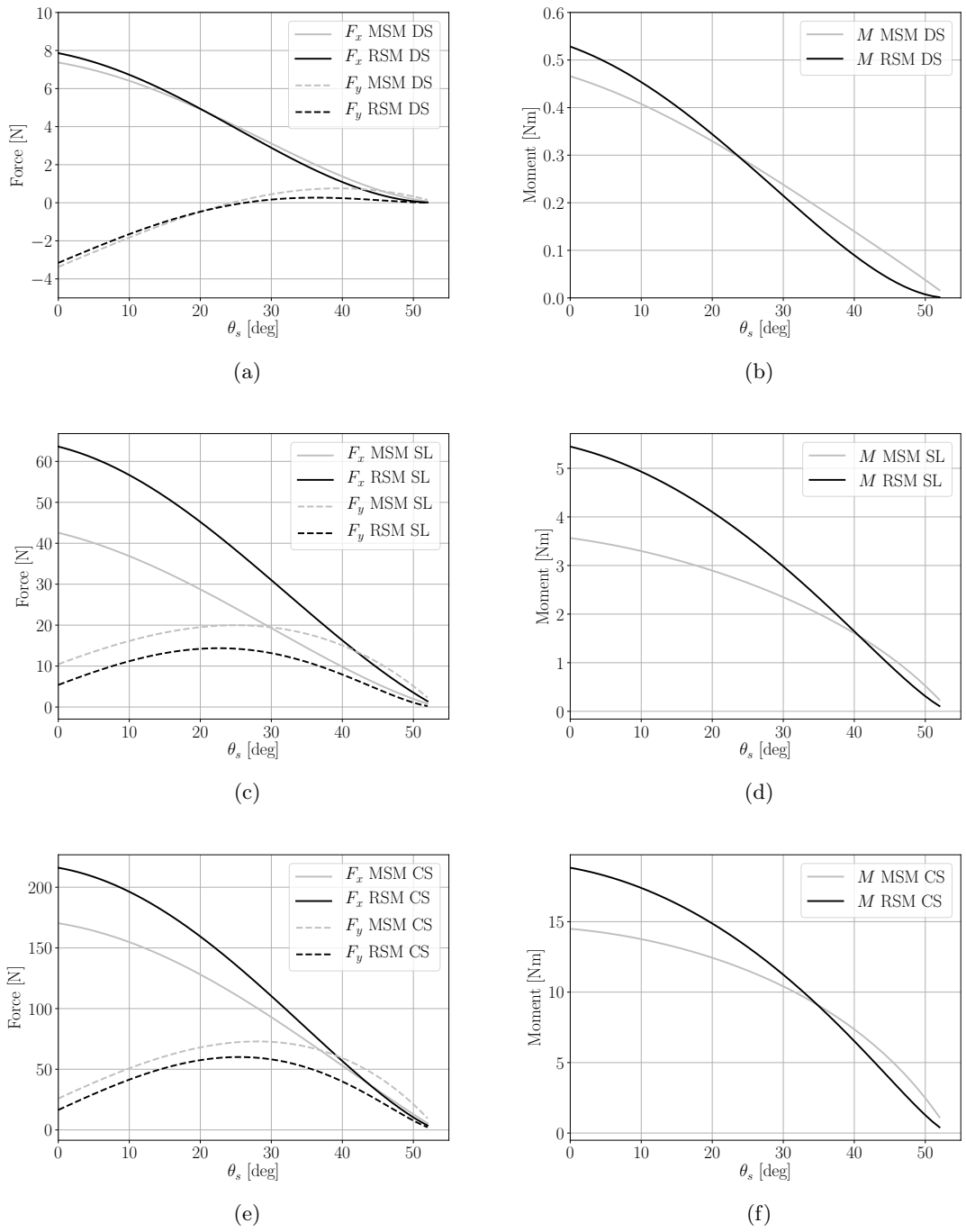


Figure 6.9: Comparisons of F_x , F_y , and M between MSM and RSM on three materials. (a) forces on dry sand, (b) moments on dry sand, (c) forces on sandy loam, (d) moments on sandy loam, (e) forces on clayey soil, and (f) moments on clayey soil.

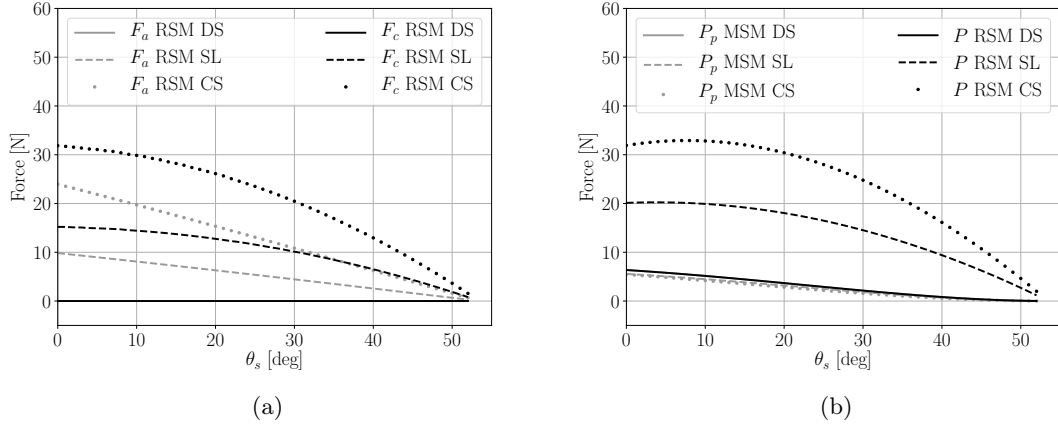


Figure 6.10: (a) Adhesion and cohesion forces estimated with MSM and RSM on three materials. (b) P_p and P estimated with MSM and RSM on three materials.

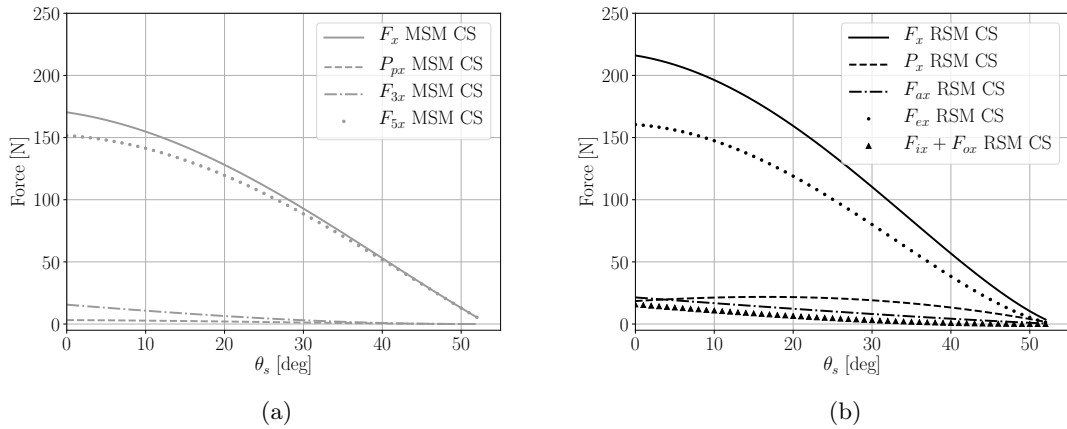


Figure 6.11: (a) Components of F_x predicted by MSM on clayey soil. (b) Components of F_x predicted by RSM on clayey soil.

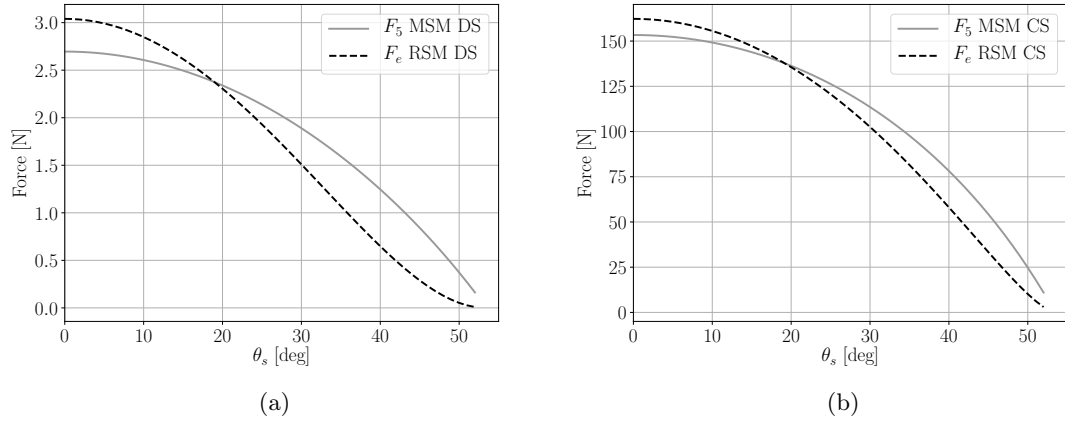


Figure 6.12: (a) F_5 and F_e on dry sand with c_t equal to 15%. (b) F_5 and F_e on clayey soil with c_t equal to 45%.

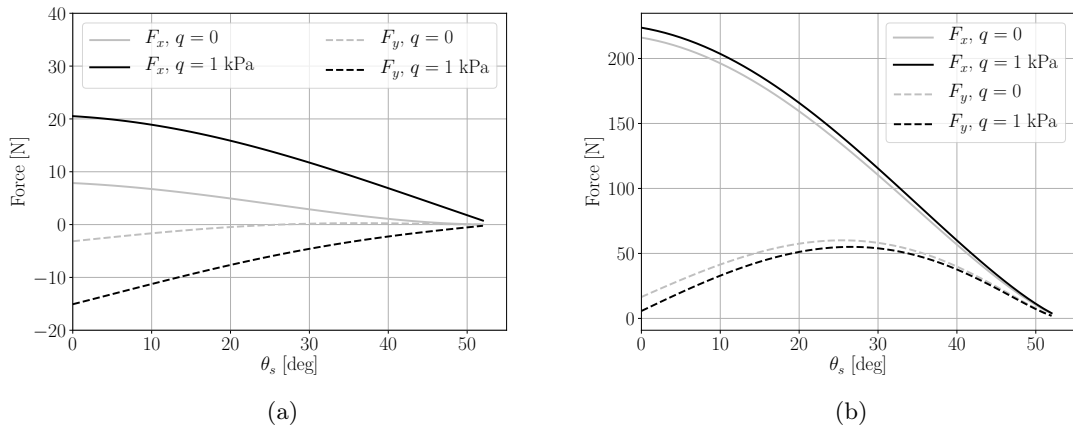


Figure 6.13: (a) Effect of a surcharge q on F_x and F_y on dry sand. (b) Effect of a surcharge q on F_x and F_y on clayey soil.

6.5 Laboratory Experiments

The field robot RTC-II was used to collect surface samples in field conditions, as pictured in Figure 6.2. Samples were collected in various terrains for environmental monitoring [31] and for characterizing mine waste. Examples of these operations are pictured in Figure 6.14. The objective of this section is to present reproducible laboratory experiments, first on dry sand, then on Centrifuged Tailings (CT). These two materials were selected due to their large difference in soil properties. The next two subsections describe the test materials and the robotic equipment used. The experimental results for dry sand and CT are presented in Sections 6.5.3 and 6.5.4, respectively. Modeling assumptions and results are discussed in Section 6.5.5.



Figure 6.14: Surface samples are collected using a robotic manipulator on (a) sandy terrain and, (b) centrifuged tailings.

6.5.1 Materials

Dry Sand

Recreation Sand from Sil Industrial Minerals was used for dry sand experiments (Figure 6.15a). This material has a bulk density approximately of 1497 kg/m^3 (ASTM C-29) and is composed of sub-angular crystalline silica grains (SiO_2 92.3% w.t). The results of particle size analysis from the product datasheet are presented in Table 6.6.

The sand friction parameters were obtained using a direct-shear test [8] in dry conditions. The internal friction angle and cohesion stress parameters were estimated to be $\phi_{ds} = 33.8^\circ$ and $c_{ds} = 0.0$

kPa, respectively. The shear deformation modulus k_{ds} was estimated to be 0.33 mm by fitting the shear-displacement measurements show in Figure 6.15b to Equation (6.6). These tests were conducted at a strain rate of 0.735 mm/min, the maximum rate available on the apparatus.

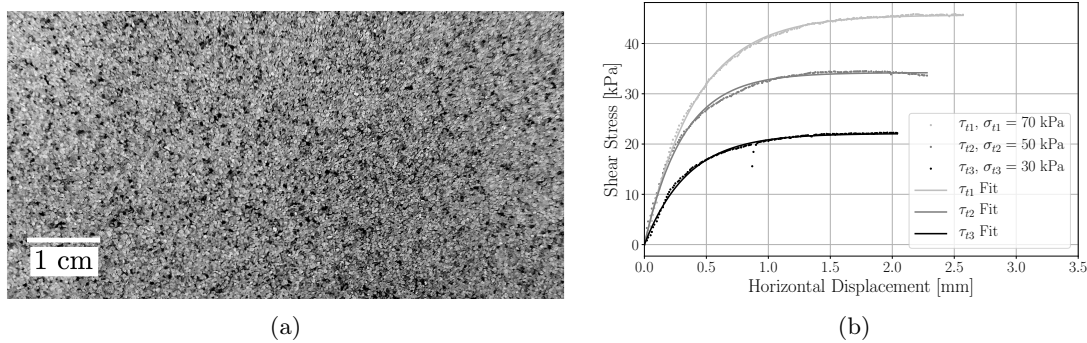


Figure 6.15: (a) Picture of sand. (b) Shear response obtained from direct-shear testing of dry sand at three different normal loads ($\sigma_{t1}, \sigma_{t2}, \sigma_{t3}$). The curves of the shear stress response were produced by fitting the measured responses to Equation (6.6).

Table 6.6: Particle Size Analysis

Mesh (ASTM E-11-17)	Typical mean % retained on individual sieve
16	0.0
20	0.3
30	5.0
40	51.1
50	38.9
60	3.6
80	0.8
PAN	0.3

Centrifuged Tailings

A sample of centrifuged tailings, representative of oil sands mine waste, was used for the experiments. The geotechnical and physicochemical properties of this material have been published in [35]. The clay fraction (≤ 0.002 mm) of the material is 52% with kaolinite and illite comprising 36% and 15% of the mass, respectively. The solids and bitumen content of the sample were reported to be 53% and 5.7%, respectively. The specific gravity is 2.24. The shear strength properties of the samples has been discussed in [35] and [32]. The soil strength was measured with robotic vane

shear test tools to be in the range of 0.5-1 kPa, with a shear deformation modulus of approximately 1 mm.

CT have very different characteristics from dry sand. In dry sand, shear forces are primarily due to friction, while cohesion and adhesion have little effect; but in CT, cohesion and adhesion are the dominant forces. In the present work, CT are modeled to have no friction forces. The coefficients of the pressure-sinkage relationship were taken as zero to reflect the fact that CT have essentially no bearing capacity, and the internal friction angle is approximately zero. This results in cohesion and adhesion dominating the tool-soil interaction.

6.5.2 Equipment

The robotic system used for the experiments was pictured in Figures 6.2 and 6.14. The main system components are illustrated in Figure 6.16. The robotic sampler is deployed using a robotic manipulator that is mounted on a mobile platform. The robotic manipulator has revolute joint sensors to calculate the position of the sampler, and a six-axis Force/Torque (F/T) sensor mounted on the tool connection plate.

The robotic sampler has a detachable scoop actuated by a motor through a gearbox. A torque sensor is installed internally on the rotation shaft of the scoop. A distance sensor is used to measure the position of the sampler relative to the ground. An inertial measurement unit reports the roll and pitch angles. Further design and instrumentation details are presented in [31]. Vertical and horizontal forces on the sampler are measured with the F/T sensor of the robotic manipulator, while the torque on the sampler is measured by the internally mounted torque sensor. Direct torque measurement is superior to estimation from motor current measurements because the torque sensor is not affected by ripples in the motor current or friction in the gearbox. The measured torque was statically calibrated to remove the torque created by the weight of the scoop sampler. All measurements were collected at a frequency of 50 Hz. The errors were tested to be normal and identically distributed. The sampler geometry parameters t_s , r_s , and r_p have values of 0.8 mm, 105.0 mm, 110.0 mm, respectively and $\alpha_s = 11^\circ$.

The experiments were automated to increase repeatability.

6.5.3 Experiments on Dry Sand

The dry sand experiments were conducted in a laboratory sandbox with approximate dimensions of 4 m long by 1 m wide. The sandbox is lined with plastic to accommodate testing of wet materials. Approximately 1.4 m³ of dry sand was used to fill the box to a height of 40 cm. The sandbox is

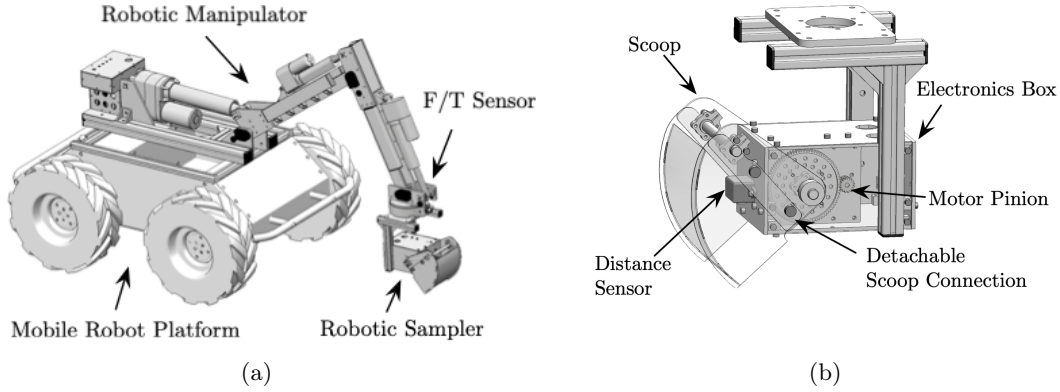


Figure 6.16: Schematics of (a) the robotic system, (b) the robotic sampler.

outfitted with two planks above it, allowing the mobile robot to drive along the length, deploy tools and perform sampling of the test material without affecting the soil and minimizing edge effects. The planks are removable so the mobile robot can also be placed directly on the test material if desired.

Two experiments were conducted on dry sand. First, we validated the predictions by RSM of the forces acting on the side edges and side walls of the sampler. For these experiments, the curved scoop part of the sampler was removed, and measurements of the loads acting on the remaining sampler were recorded. Since the curved surface is removed, the RSM terms P and F_a can be discarded, such that the horizontal force F_{sx} , vertical force F_{sy} , and moment M_s acting on the sampler are given by

$$F_{sx} = F_{ix} + F_{ox} + F_{ex} \quad (6.68)$$

$$F_{sy} = F_{iy} + F_{oy} + F_{ey} \quad (6.69)$$

$$M_s = M_{F_i} + M_{F_o} + M_{F_e} \quad (6.70)$$

In the second experiment, the curved surface is re-installed, such that the complete RSM model from Section 6.3.2 is used.

The pressure-sinkage model parameters for dry sand were taken from the earlier Table 6.2.

Side Edge and Side Wall Forces and Moments on Dry Sand

In these experiments, r_s is equal to r_p since the curved portion of the sampler is removed (c.f. Figure 6.7). The distance to the ground, h_0 , was measured by the distance sensor of the sampler to be

62.5 mm. The side walls were rotated into the dry sand as pictured in Figure 6.17. The forces and moment acting on the sampler were recorded and are plotted in Figure 6.18.

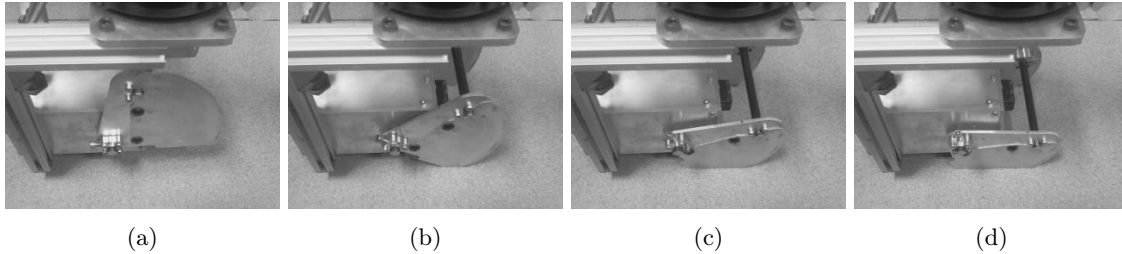


Figure 6.17: Sequence (a)-(d) of sampler with removed curved section indenting into dry sand.

The total forces and moment predicted by RSM show good agreement with the experimental measurements in Figure 6.18. Since F_e is the dominant force on the side plates, this good agreement suggests that the proposed model is able to accurately predict F_e . As shown in Figure 6.18b, outliers occur in F_{sy} and M_s when θ_s is approximately 10 degrees. At this angle, the sampler experienced an abrupt motion in the horizontal direction, which caused the spike in F_{sy} and M_s measurements.

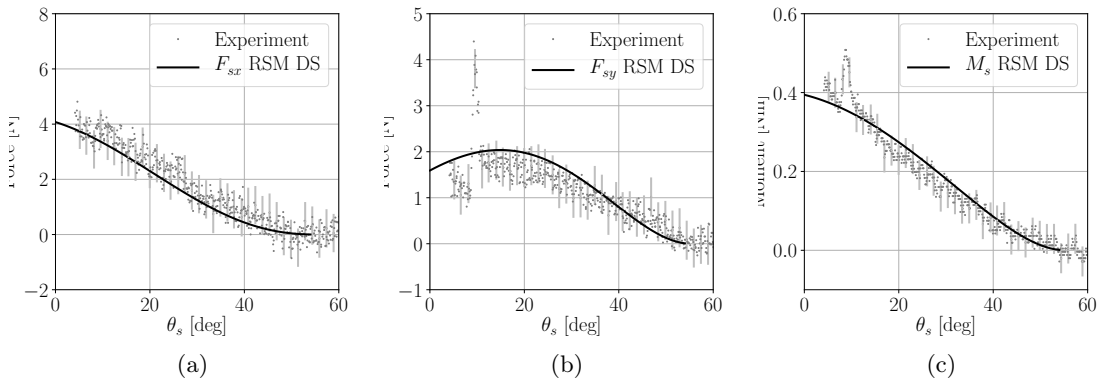


Figure 6.18: Experimentally measured and predicted forces F_{sx} (a), F_{sy} (b) and moment M_s (c) during side wall experiment on dry sand. The error bars are shown every 15 points and represent two times the standard deviation of the measurement errors.

Total Forces and Moment on Dry Sand

The complete sampler was deployed on dry sand as shown in Figure 6.19. For this experiment the sampler was placed at $h_0 = 80$ mm. The forces and moment acting on the sampler were

recorded and are plotted in Figure 6.20. The measurements are in close agreement with the RSM predictions.

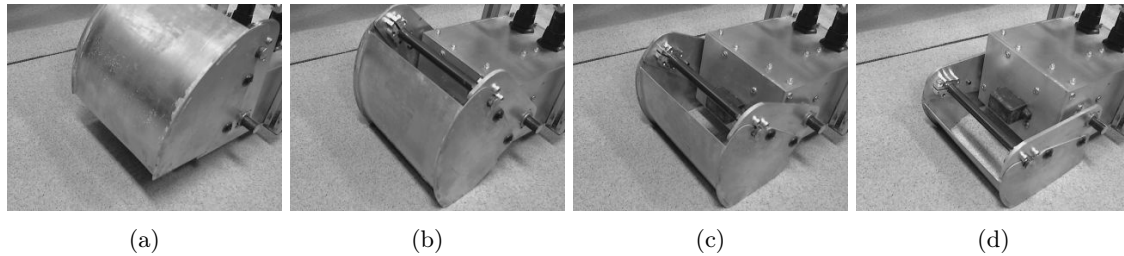


Figure 6.19: Sequence (a)-(d) of complete sampler indenting into dry sand.

Comparing F_{sy} in Figure 6.18b and F_y in 6.20b, it is clear that the curved surface affects the forces on the sampler, and that the proposed RSM accurately predicts this. The difference between plots for angles lower than 20 degrees is primarily due to the term P in the F_y expression. All the experiments were repeated five times.

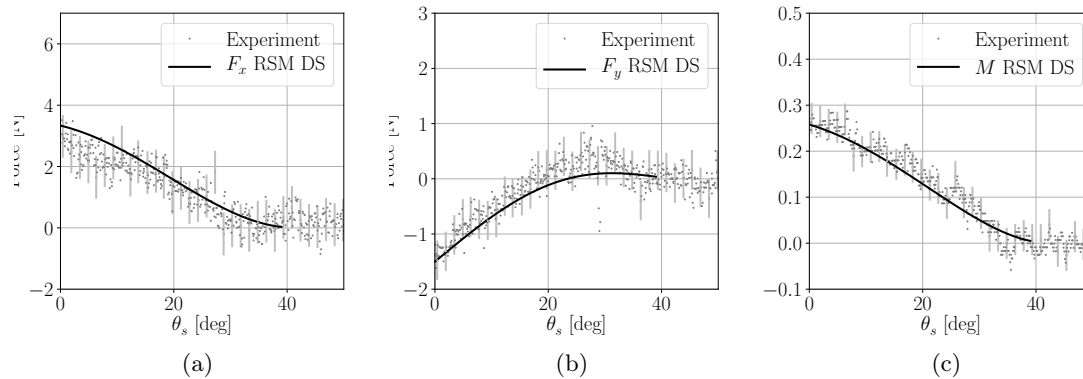


Figure 6.20: Experimentally measured and predicted forces F_{sx} (a), F_{sy} (b) and moment M_s (c) during complete sampler experiment on dry sand. The error bars are shown every 15 points and represent two times the standard deviation of the measurement errors.

6.5.4 Experiments on Centrifuged Tailings

The two experimental procedures described for dry sand were repeated on CT. First, the curved surface was removed to measure the forces on the sides of the sampler during a sampling maneuver. The sampler was positioned at a height of $h_0 = 59$ mm, and the side blades driven into the medium as pictured in Figure 6.21a. The measured reaction forces are plotted in Figure 6.21 (b) and

(c). Unlike the dry sand case, we employed both our proposed RSM and the previously published MSM as force models. While the RSM predictions closely match the measured forces, the forces predicted by MSM are underestimated because that model does not consider the internal wall side forces independently.

The close agreement by RSM also confirms our earlier assumption that friction and pressure-sinkage forces are negligible in CT. This is the opposite of the dry sand case, where term F_e is the dominant contribution. In CT, F_o and F_i are the only significant terms. Because the material was observed to stick to the sampler, we postulated the cohesion forces to be weaker, therefore we employed them as the failure criteria in (6.26). This corresponds to the soil failing internally rather than at the contact surface.

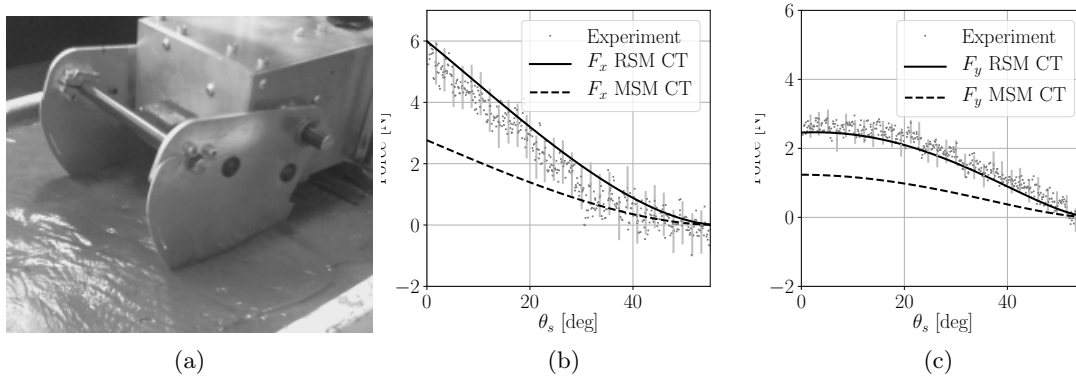


Figure 6.21: (a) Sampler side walls driven into CT. Measured, RSM- and MSM-predicted forces F_x (b) and F_y (c) during a sampling operation. The error bars are shown every 15 points and represent two times the standard deviation of the measurement errors.

The second experiment used the complete sampler instrument to collect a CT sample with the tool positioned at a height of $h = 80$ mm. This is pictured in Figure 6.22a. It can be seen that the material has sufficient cohesion to hold its shape, and does not fall off even when the sampler is half open. Furthermore, the CT in contact with the back face of the curved sampler portion was significantly disturbed, and was pulled out as the robot arm lifted the sampler. This last effect suggests that the term F_{oc} has a significant impact on the force prediction by RSM. Visual estimations of the internal and external contact angles on the curved blade were approximately half-way between θ_f and θ_s (c.f. Figure 6.7). This was used to obtain the values of θ_{oc} and limits of the integrals of F_a .

The measured forces in Figure 6.22 (b) and (c) have a close agreement with the RSM predictions. As expected, the forces were underestimated by MSM. Note the force plots for CT demonstrate a

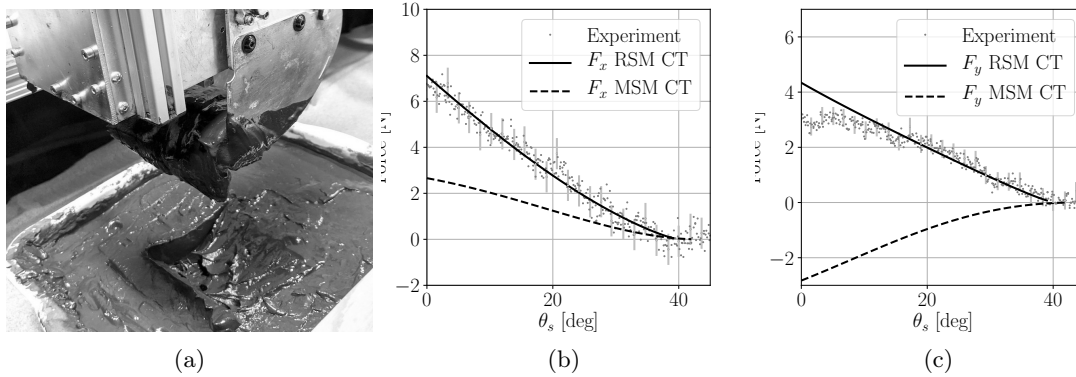


Figure 6.22: (a) Complete sampler collecting a sample of CT. Measured, RSM- and MSM-predicted forces F_x (b) and F_y (c) during the sampling operation. The error bars are shown every 15 points and represent two times the standard deviation of the measurements.

completely different material response than the dry sand case.

As seen in Figure 6.20b, the vertical force became negative (sampler pulled down) when sampling dry sand, which is as expected since force P supports most of the weight of the material collected. In dry sand, the force on the back surface F_{oc} is negligible [28]. The opposite effect occurs in CT. The vertical force is positive, even though the material is denser than loose sand. P is much larger than in dry sand because it balances the adhesion forces on the inside of the scoop and the cohesion forces at the shear surface of the material. The resulting vertical force is positive due to the contributions of F_i , F_o , F_a and especially F_{oc} . The change of direction of F_y — and specifically the large contribution of F_{oc} — was accurately predicted by RSM and confirmed by experimental measurements. Meanwhile for MSM, the unmodeled forces resulted in a completely incorrect (wrong direction) prediction of the vertical force F_y .

6.5.5 Model Assumptions

Sections 6.5.3 and 6.5.4 presented experimental results for two different soil types. In this Section we discuss the four main assumptions of our proposed model.

First, the density of the soil material was assumed to be a constant, which is reasonable provided the tool does not cause significant compaction during sampling. In general, since sampling tools are designed and operated to minimize power requirements and keep the samples intact, this assumption is reasonable.

Second, the effect of the wedge at the back of the soil sample, shown in Figure 6.7 as the area inside

CDF, was assumed to have a negligible effect on the forces and moment on the sampler. It was not possible to measure the wedge angle ϕ reliably and so it was ignored. While PIV techniques can be used in a laboratory setting to measure this angle, they cannot be deployed in field applications. The close agreement between the measured and predicted loads on the sampler suggests this assumption is reasonable for the soils tested. To remove this assumption, depth sensors yielding 3D point clouds could be used to measure the geometry of the soil during sampling in order to directly measure this angle.

Third, the shear curve was assumed to be modeled by an exponential function, as seen in Equation (6.6). This may not be sufficiently accurate for soils which exhibit a peak shear stress which decreases as shear displacement increases. Alternative models for the shear curve are summarized in [44] and could be used instead of (6.6), at the cost of extra complexity due to additional soil parameters.

Fourth, the shape of the failure surface was assumed to be flat. Investigating other shapes and the resulting change in model prediction accuracy are left for future work.

The favourable results obtained with the proposed RSM motivate further validation on other soil types. Potential uses of this model include the design of optimized sampling tools and making these tools more intelligent - for instance estimating soil properties from measured interaction forces in real-time.

6.6 Conclusion and Future Work

A novel terramechanics model for a scoop-type sampler was presented. The key improvements of the proposed model over earlier work is that it accounts for the effects of cohesion, adhesion, and surcharge. The details of the model formulation were given.

The new model was compared to the current state-of-the-art model [28]. The most important soil interaction forces are the earth-pressure force acting on the curved surface of the sampler, and the force acting on the edges of the side plates. The contributions of cohesion, adhesion, and surcharge to the reaction forces on the sampler were investigated in simulation, and found to be significant for the materials being considered. These effects could not be captured by the earlier model.

The proposed model was first validated through laboratory experiments on dry sand. Good agreement was found between the measured and predicted forces and moment acting on the robotic sampler. In a second test with centrifuged tailings, a soil dominated by adhesion and cohesion effects, the proposed model also showed excellent agreement with experimental measurements. Meanwhile

the earlier model was demonstrated to provide incorrect predictions due to not accounting for these effects.

Accurate models are important to improve the design and capabilities of sampling tools. Future work will focus on the development and testing of a field robotic system which can estimate soil properties while performing sampling operations. This capability would be very useful in navigating and characterizing difficult terrains.

Acknowledgments

The authors would like to thank the Natural Sciences and Engineering Research Council of Canada (NSERC) and the University of Alberta for their financial support.

6.7 References

- [1] K Althoefer, C P Tan, Y H Zweiri, and L D Seneviratne. Hybrid Soil Parameter Measurement and Estimation Scheme for Excavation Automation. *IEEE Transactions on Instrumentation and Measurement*, 58(10):3633–3641, August 2009.
- [2] R.C. Anderson, L. Jandura, A.B. Okon, D. Sunshine, C. Roumeliotis, L.W. Beegle, J. Hurowitz, B. Kennedy, D. Limonadi, S. McCloskey, M. Robinson, C. Seybold, and K. Brown. Collecting samples in gale crater, mars; an overview of the mars science laboratory sample acquisition, sample processing and handling system. *Space Science Reviews*, 170(1-4):57–75, 2012.
- [3] M. G. Bekker. *Introduction to Terrain-Vehicle Systems*. University of Michigan Press, Michigan, 1969.
- [4] S. Blouin, A. Hemami, and M. Lipsett. Review of resistive force models for earthmoving processes. *J. Aerosp. Eng.*, 14(3):102–111, 2001.
- [5] Hermann Boehnhardt, Jean-Pierre Bibring, Istvan Apathy, Hans Ulrich Auster, Amalia Ercoli Finzi, Fred Goesmann, Göstar Klingelhöfer, Martin Knapmeyer, Wlodek Kofman, Harald Krüger, Stefano Mottola, Walter Schmidt, Klaus Seidensticker, Tilman Spohn, and Ian Wright. The Philae lander mission and science overview. *Philosophical transactions. Series A, Mathematical, physical, and engineering sciences*, 375(2097), July 2017.
- [6] Robert Bonitz, Lori Shiraishi, Matthew Robinson, Joseph Carsten, Richard Volpe, Ashitey Trebi-Ollennu, Raymond E Arvidson, P C Chu, J J Wilson, and K R Davis. The Phoenix Mars Lander Robotic Arm. In *2009 IEEE Aerospace conference*, pages 1–12. IEEE, 2009.

- [7] S Coetzee, H Swart, P Bosscha, and D Oosthuizen. *Design of an industrial all-terrain robot platform lessons learned in the design of a robotic mine safety platform for South African gold mines*. IEEE, 2012.
- [8] R. F. Craig. *Soil Mechanics (Fifth Edition)*. Chapman and Hall, 1992.
- [9] Braja M. Das. *Fundamentals of Geotechnical Engineering (Second Edition)*. Thomson, 2005.
- [10] Pedro Deusdado, Eduardo Pinto, Magno Guedes, Francisco Marques, Paulo Rodrigues, André Lourenço, Ricardo Mendonça, André Silva, Pedro Santana, José Corisco, Marta Almeida, Luís Portugal, Raquel Caldeira, José Barata, and Luis Flores. An Aerial-Ground Robotic Team for Systematic Soil and Biota Sampling in Estuarine Mudflats. In *Robot 2015: Second Iberian Robotics Conference*, pages 15–26. Springer International Publishing, Cham, November 2015.
- [11] Iman Entezari, Benoit Rivard, Michael G Lipsett, and G Ward Wilson. Prediction of water content and normalized evaporation from oil sands soft tailings surface using hyperspectral observations. *Canadian Geotechnical Journal*, 53(10):1742–1750, October 2016.
- [12] Daniel M Franks, David V Boger, Claire M Côte, and David R Mulligan. Sustainable development principles for the disposal of mining and mineral processing wastes. *Resources Policy*, 36(2):114–122, June 2011.
- [13] Gustavo Freitas, Fernando Lizarralde, Liu Hsu, Vitor Paranhos, Ney R. Salvi dos Reis, and Marcel Bergerman. Design, modeling, and control of a wheel-legged locomotion system for the environmental hybrid robot. In *Proceedings of the IASTED International Conference*, number CMU-RI-TR-, November 2011.
- [14] Jeremy Green. Underground mining robot: A CSIR project. *SSRR*, pages 1–6, 2012.
- [15] Gregory Hitz, Francois Pomerleau, Marie-Eve Garneau, Cedric Pradalier, Thomas Posch, Jakob Pernthaler, and Ronald Siegwart. Autonomous Inland Water Monitoring: Design and Application of a Surface Vessel. *IEEE Robotics & Automation Magazine*, 19(1):62–72, March 2012.
- [16] Larry A Holm. Strategies for remediation. In *Geotechnical Practice for Waste Disposal*, pages 289–310. Springer US, Boston, MA, 1993.
- [17] K Iagnemma, S Kang, H Shibly, and S Dubowsky. Online Terrain Parameter Estimation for Wheeled Mobile Robots With Application to Planetary Rovers. *IEEE Transactions on Robotics*, 20(5):921–927, October 2004.
- [18] J. Jaky. The coefficient of earth pressure at rest. *Journal of the Society of Hungarian Architects and Engineers*, 7:355–358, 1944.

- [19] Qian Li, Lanlan Xie, and Junping Li. Modular Motion-Structure Design Model for Planetary Surface Sampling. *International Journal of Aerospace Engineering*, 2019(3):1–15, April 2019.
- [20] Yun Ling, Wei Lu, Changcheng Wu, Aiguo Song, and Chao Feng. A novel rigid-flexible link combined lunar sampler and its basic dynamics and control. *Aerospace Science and Technology*, 38:41–47, October 2014.
- [21] Yun Ling, Wei Lu, Pengwen Xiong, and Aiguo Song. A miniature flexible sampler for subsurface lunar exploration. *Acta Astronautica*, 123:8–15, June 2016.
- [22] Yun Ling, Aiguo Song, and Wei Lu. A novel rigid-flexible combined sampler for lunar exploration. *Mechanism and Machine Theory*, 77:25–34, July 2014.
- [23] M G Lipsett, J D Yuen, N A Olmedo, and S C Dwyer. Condition Monitoring of Remote Industrial Installations Using Robotic Systems. In *Engineering Asset Management 2011*, pages 231–241. Springer London, London, July 2013.
- [24] Michael G Lipsett, Nicolas Olmedo, Benoit Rivard, and Ward Wilson. Robotic Systems for Measuring Properties of Tailings Deposits and Collecting Samples. In *Proceedings of the Fourth International Oil Sands Tailings Conference*, Lake Louise, AB, December 2014.
- [25] Burt G. Look. *Handbook of geotechnical investigation and design tables*. Taylor and Francis, 2007.
- [26] Joshua A Marshall, Adrian Bonchis, Eduardo Nebot, and Steven Scheduling. Robotics in Mining. In Bruno Siciliano and Oussama Khatib, editors, *Springer Handbook of Robotics*, pages 1549–1576. Springer International Publishing, Cham, 2016.
- [27] E Mckyes. *Soil Cutting and Tillage*. Elsevier Sciences, 1985.
- [28] Daiki Mori and Genya Ishigami. Excavation model of soil sampling device based on particle image velocimetry. *Journal of Terramechanics*, 62:19–29, December 2015.
- [29] A Nuchter, H Surmann, and K Lingemann. 6D SLAM with an application in autonomous mine mapping. . . . *ICRA'04 2004 IEEE . . .*, pages 1998–2003 Vol.2, 2004.
- [30] Nicolas Olmedo, Stephen Dwyer, Michael Lipsett, and James Yuen. Soft soil sampling device and system US9513193B2, December 2016.
- [31] Nicolas A. Olmedo, Martin Barczyk, Hong Zhang, Ward Wilson, and Michael G. Lipsett. A ugv-based modular robotic manipulator for soil sampling and terramechanics investigations on mine waste. Submitted, 2020.

- [32] Nicolas A. Olmedo, Bereket Fisseha, Ward Wilson, Martin Barczyk, Hong Zhang, and Michael G. Lipsett. An automated vane shear test tool for environmental monitoring with unmanned ground vehicles. Submitted, 2020.
- [33] Nicolas A Olmedo and Michael G Lipsett. Design and field experimentation of a robotic system for tailings characterization. *Journal of Unmanned Vehicle Systems*, pages juvs-2015-0034, March 2016.
- [34] Geoffrey S Plumlee, Kathleen S Smith, and Walter H Ficklin. *Geoenvironmental Models of Mineral Deposits, and Geology-based Mineral-environmental Assessments of Public Lands*. Number Open-File Report 94-203. U.S. Geological Survey, 1994.
- [35] Umme Salma Rima and Nicholas Beier. Evaluation of temperature and multiple freeze-thaw effects on the strength properties of centrifuged tailings. In *Geo Edmonton*, 2018.
- [36] B Rivard, D Lyder, J Feng, A Gallie, E Cloutis, P Dougan, S Gonzalez, D Cox, and M G Lipsett. Bitumen content estimation of Athabasca oil sand from broad band infrared reflectance spectra. *The Canadian Journal of Chemical Engineering*, 88(5), June 2010.
- [37] K Skonieczny, D S Wettergreen, and WL Red Whittaker. Advantages of continuous excavation in lightweight planetary robotic operations. *The International Journal of Robotics Research*, 35(9):1121–1139, December 2015.
- [38] Krzysztof Skonieczny. Modeling the effects of surcharge accumulation on terrestrial and planetary wide-blade soil–tillage tool interactions. *Soil and Tillage Research*, 176:104–111, March 2018.
- [39] W.C. Swick and J.V. Perumpral. A model for predicting soil-tool interaction. *Journal of Terramechanics*, 25(1):43 – 56, 1988.
- [40] Ashitey Trebi-Ollenu, Richard Volpe, Robert Bonitz, Matthew Robinson, and Joseph Carsten. In situ robotic arm operations. *IEEE Robotics & Automation Magazine*, 16(4):34–43, December 2009.
- [41] R Volpe, E Baumgartner, P Scheaker, and S Hayati. Technology development and testing for enhanced Mars Rover Sample Return operations. 7:247–257 vol.7, 2000.
- [42] David Wettergreen, Scott Jared Moreland, Krzysztof Skonieczny, Dominic Jonak, David Kohanbash, and James Teza. Design and field experimentation of a prototype lunar prospector. *International Journal of Robotics Research*, 29(12):1550 – 1564, October 2010.
- [43] Barry A Wills and James A Finch. Tailings Disposal. In *Wills’ Mineral Processing Technology*, pages 439–448. Elsevier, 2016.

- [44] J.Y. Wong. *Terramechanics and Off-Road Vehicle Engineering*. Butterworth-Heinemann, Oxford, 2 edition, 2010.
- [45] Banglu Xi, Mingjing Jiang, Liang Cui, Jun Liu, and Huayang Lei. Experimental verification on analytical models of lunar excavation. *Journal of Terramechanics*, 83:1–13, June 2019.
- [46] Long Xue, Baichao Chen, Zhenjia Zhao, Zhaolong Dang, and Meng Zou. Experimental Study of Torque Using a Small Scoop on the Lunar Surface. *International Journal of Aerospace Engineering*, 2016(6):1–8, 2016.
- [47] Toru YADA, Akio FUJIMURA, Masanao ABE, Tomoki NAKAMURA, Takaaki NOGUCHI, Ryuji OKAZAKI, Keisuke NAGAO, Yukihiro ISHIBASHI, Kei SHIRAI, Michael E ZOLENSKY, Scott SANDFORD, Tatsuaki OKADA, Masayuki UESUGI, Yuzuru KAROUJI, Maho OGAWA, Shogo YAKAME, Munetaka UENO, Toshifumi MUKAI, Makoto YOSHIKAWA, and Junichiro KAWAGUCHI. Hayabusa-returned sample curation in the Planetary Material Sample Curation Facility of JAXA. *Meteoritics & Planetary Science*, 49(2):135–153, February 2013.
- [48] P Younse, A Stroupe, T Huntsberger, M Garrett, J L Eigenbrode, L G Benning, M Fogel, and A Steele. Sample acquisition and caching using detachable scoops for mars sample return. In *2009 IEEE Aerospace conference*, pages 1–12. IEEE, 2009.
- [49] R Yousefi Moghaddam, A Kotchon, and M G Lipsett. Method and apparatus for on-line estimation of soil parameters during excavation. *Journal of Terramechanics*, 49(3-4):173–181, June 2012.
- [50] Weiwei Zhang, Shengyuan Jiang, Jie Ji, and Dewei Tang. A drilling tool design and in situ identification of planetary regolith mechanical parameters. *Advances in Space Research*, 61(9):2444–2456, May 2018.

Chapter 7

Conclusions

This chapter summarizes the conclusions and contributions of the papers presented in the previous chapters. Areas of future work are then recommended.

7.1 Contributions

In all of the work reported in this thesis, the author developed the conceptual framework with input from the supervisory committee, developed the apparatus with some input from supervisors, wrote measurement and control software, conducted the experiments, analyzed results, and wrote the first draft of manuscripts.

The results presented in Chapter 2 of the thesis indicate that the surface and subsurface characterization of oil sands tailings (and other types of terrain) is useful and technically feasible for unmanned ground vehicles. This motivated the continued development of robotic systems for monitoring difficult terrains. The favorable results suggested that such systems are suitable for tailings characterization as well as for monitoring other types of environments such as aquatic and terrestrial.

The robotic vane shear test tool presented in Chapter 3 was designed to reduce human error and variability in measurement, and was validated against commercially available high-end instruments with favorable results. To obtain high-accuracy and precision measurements, a technique was developed to measure and compensate for friction within the equipment. The developed robotic vane shear test tool was used to show that the measurements of shear strength on oil sands tailings are affected by the speed of rotation of the vane. Since humans may overestimate the shear strength

of the deposits by rotating the vane too quickly, an automatic instrument offers improved accuracy and reproducibility of results, in addition to the capability for remote data collection. While the current design is limited by how deeply the instrument can be deployed into the ground, future generations of UGVs could be equipped with a modified vane shear test tool which could be driven up to several meters into the terrain.

The novel methodology and equipment presented in Chapter 4 for estimating the inertia tensor and center of mass location of robotic systems was shown to achieve an error of around 1%, provide a viable alternative to commercially available high-precision measurement platforms at a fraction of their cost. The achieved performance is sufficient to implement dynamic simulation and design model-based control algorithms, which will be necessary for future generations of autonomous UGVs operating on difficult terrain.

The robotic manipulator, scoop-type surface sampler, and terramechanics wheel presented in Chapter 5 can be used for soil investigations onboard mobile robots. The robotic manipulator allows varying the tool-soil interaction forces, leading to measurements from a wider operating envelope. The terramechanics wheel can be used to estimate soil model parameters, and combined with UGV motion can achieve a range of slip ratios, leading to more operating points for parameter identification as compared to relying solely on traction behaviour of the vehicle's wheels. The manipulator design exhibited some backlash, which was compensated through the selection of manipulator poses; quantifying this effect as well as re-designing the manipulator would be a more elegant solution to this problem.

Chapter 6 proposed a terramechanics model for the scoop-type sampler which improves on current state-of-the-art models by accounting for the adhesive and cohesive interaction forces with the soil as well as surcharge effects. The advantages of the new formulation were highlighted in simulation and the model was validated in laboratory experiments for two different soil types. The magnitude and direction of the forces predicted by the proposed model was shown to agree with the experimental measurements and provide estimates which clearly outperformed the previous model.

7.2 Recommendations for Future Work

A number of limitations of the current work have been identified. Further work is needed to overcome these limitations, as well as to develop new applications and field demonstrations for the tools and methods developed in this thesis.

The robotic vane shear test tools developed could be used by amphibious robots operating in very soft deposits. The tools need to be further ruggedized and submersible, so that they can be deployed

industrially and provide rheological data for deep soft deposits. Soil parameter estimation techniques can be further developed using the terramechanics model proposed for the surface sampler to allow real-time estimation of terrain parameters while moving, and to enable improved locomotion of rovers by estimating variables related to traction control.

The robots and tools developed can be used to autonomously characterize a tailings deposit and build a map of the terrain conditions. Demonstrating this capability is an opportunity for future work.

The UGVs used in this thesis are wheeled or tracked. Some tailings deposits have little or no bearing capacity. In this case access to deposits is generally difficult and measurements are likely to be taken in a range of soft or liquefied terrains, meaning amphibious robots are a more appropriate platform. The development of amphibious robots for tailings characterization has been started and is currently reaching the commercialization stage. Improvements in terramechanics models for amphibious vehicle locomotion on varied terrains are required to make autonomous operations practical. Model-based control, which involves obtaining the inertia matrix of the vehicle, will be important to achieve fast locomotion with these systems. The design of such amphibious rovers for operations in a range of terrains, overall system reliability of locomotion methods, communications and power management, and matching payload capacity to a particular rover type are all future work areas.

Robotic systems with increased payload capacities are required for sampling operations. The current systems are limited to one sample per trip. Tooling magazines could be used to employ different tools or to make a range of measurements during a single remote mission. Concepts and demonstrations are needed of instruments which can collect multiple samples of different terrains, or to make a set of measurements at the ground deposit at both the surface and at different depths.

The technologies developed for mine waste monitoring can also be adapted for use in agriculture, glaciology, vulcanology, wetland and permafrost operations, as well as other investigations of challenging as well as potentially unsafe terrains such as eroding shorelines and flood zones. Understanding the associated technical and functional requirements will allow adaptations of tooling and instrumentation for operating within such areas. In this way, the potential of carrying measurement payloads on new types of autonomous rovers to perform a range of environmental monitoring and remediation tasks can be realized.

References

- [1] Alberta-Energy. Oil sands. <http://www.energy.alberta.ca/OurBusiness/oilsands.asp>, 2014.
- [2] Alberta-Energy. Oilsands 101: Reclamation. <http://www.energy.alberta.ca/OilSands/1722.asp>, 2014.
- [3] Alberta-Energy. Oilsands 101: Resource. <http://www.energy.alberta.ca/OilSands/1715.asp>, 2014.
- [4] Alberta-Energy-Regulator. Directive 074: Tailings performance criteria and requirements for oil sands mining schemes. <http://www.aer.ca/rules-and-regulations/directives/directive-074>, 2009.
- [5] Alberta-Energy-Regulator. Erceb conditionally approves tailings plans for shell muskeg river project. <http://www.aer.ca/about-aer/media-centre/news-releases/news-release-2010-09-20-nr2010-13>, 09 2010.
- [6] Alberta-Energy-Regulator. Backgrounder, directive 085: Fluid tailings management for oil sands mining projects. <https://www.aer.ca/documents/news-releases/NR2016-04-Backgrounder.pdf>, 2016.
- [7] Alberta-Energy-Regulator. State of fluid tailings management for mineable oil sands, 2018. <https://www.aer.ca/documents/oilsands/2018-State-Fluid-Tailings-Management-Mineable-OilSands.pdf>, 2019.
- [8] Erik W. Allen. Process water treatment in canada’s oil sands industry: I. target pollutants and treatment objectives. *Journal of Environmental Engineering and Science*, 7(2):123–138, 2008.
- [9] Erik W Allen. Process water treatment in Canada’s oil sands industry: I. Target pollutants and treatment objectives. *Journal of Environmental Engineering and Science*, 7(2):123–138, March 2008.

- [10] R A B Almeida, A P V Urgueira, and N M M Maia. Evaluation of the Performance of Three Different Methods Used in the Identification of Rigid Body Properties. *Shock and Vibration*, 15(3-4):467–479, 2008.
- [11] Raquel A B Almeida, António P V Urgueira, and Nuno M M Maia. Further developments on the estimation of rigid body properties from experimental data. *Mechanical Systems and Signal Processing*, 24(5):1391–1408, July 2010.
- [12] K Althoefer, C P Tan, Y H Zweiri, and L D Seneviratne. Hybrid Soil Parameter Measurement and Estimation Scheme for Excavation Automation. *IEEE Transactions on Instrumentation and Measurement*, 58(10):3633–3641, August 2009.
- [13] Altra-Industrial-Motion. Moment of inertia measurement instrument products inertia dynamics. www.idicb.com/products/moment-of-inertia-measurement-instruments/moment-of-inertia-measurement-instruments, 03 2019.
- [14] Elham Amiri Khaboushan, Hojat Emami, Mohammad Reza Mosaddeghi, and Ali Rrza As-taraei. Estimation of unsaturated shear strength parameters using easily-available soil prop-erties. *Soil and Tillage Research*, 184:118–127, December 2018.
- [15] R.C. Anderson, L. Jandura, A.B. Okon, D. Sunshine, C. Roumeliotis, L.W. Beegle, J. Hurowitz, B. Kennedy, D. Limonadi, S. McCloskey, M. Robinson, C. Seybold, and K. Brown. Collecting samples in gale crater, mars; an overview of the mars science labo-ratory sample acquisition, sample processing and handling system. *Space Science Reviews*, 170(1-4):57–75, 2012.
- [16] ASTM International. ASTM D2573/D2573M-15 Standard Test Method for Field Vane Shear Test in Saturated Fine-Grained Soils. ASTM International, September 2015.
- [17] ASTM International. D4648/D4648M - 16 Standard Test Method for Laboratory Miniature Vane Shear Test for Saturated Fine-Grained Soils. ASTM International, 2016.
- [18] ASTM International. ASTM D5778-12: Standard Test Method for Electronic Friction Cone and Piezocone Penetration Testing of Soils. ASTM International, 2019.
- [19] J Bachmann, K Contreras, K H Hartge, and R MacDonald. Comparison of soil strength data obtained in situ with penetrometer and with vane shear test. *Soil and Tillage Research*, 87(1):112–118, May 2006.
- [20] J P Barreto and L E Muñoz. Low uncertainty method for inertia tensor identification. *Me-chanical Systems and Signal Processing*, 68:207–216, February 2016.

- [21] Paul Bartlett, David Wettergreen, and William (Red) L. Whittaker. Design of the scarab rover for mobility and drilling in the lunar cold traps. In *International Symposium on Artificial Intelligence, Robotics and Automation in Space*, February 2008.
- [22] T. G. Beckwith, Roy D. Marangoni, and John H. Lienhard. *Mechanical measurements*. Upper Saddle River, NJ: Pearson Prentice Hall, sixth edition edition, 2007.
- [23] Nicholas Beier, Ward Wilson, Adedeji Dunmola, and David Segó. Impact of flocculation-based dewatering on the shear strength of oil sands fine tailings. *Canadian Geotechnical Journal*, 50(9):1001–1007, 2013.
- [24] M. G. Bekker. *Introduction to Terrain-Vehicle Systems*. University of Michigan Press, Michigan, 1969.
- [25] Richard C Benson. Geophysical techniques for subsurface site characterization. In *Geotechnical Practice for Waste Disposal*, pages 311–357. Springer US, Boston, MA, 1993.
- [26] Geoffrey Blight. *Geotechnical Engineering for Mine Waste Storage Facilities*. CRC Press, November 2009.
- [27] S. Blouin, A. Hemami, and M. Lipsett. Review of resistive force models for earthmoving processes. *J. Aerosp. Eng.*, 14(3):102–111, 2001.
- [28] Hermann Boehnhardt, Jean-Pierre Bibring, Istvan Apathy, Hans Ulrich Auster, Amalia Ercoli Finzi, Fred Goesmann, Göstar Klingelhöfer, Martin Knapmeyer, Wlodek Kofman, Harald Krüger, Stefano Mottola, Walter Schmidt, Klaus Seidensticker, Tilman Spohn, and Ian Wright. The Philae lander mission and science overview. *Philosophical transactions. Series A, Mathematical, physical, and engineering sciences*, 375(2097), July 2017.
- [29] Robert Bonitz, Lori Shiraishi, Matthew Robinson, Joseph Carsten, Richard Volpe, Ashitey Trebi-Ollennu, Raymond E Arvidson, P C Chu, J J Wilson, and K R Davis. The Phoenix Mars Lander Robotic Arm. In *2009 IEEE Aerospace conference*, pages 1–12. IEEE, 2009.
- [30] Renato Brancati, Riccardo Russo, and Sergio Savino. Method and equipment for inertia parameter identification. *Mechanical Systems and Signal Processing*, 24(1):29–40, January 2010.
- [31] Jean-Louis Briaud. *Geotechnical Engineering. Unsaturated and Saturated Soils*. John Wiley & Sons, October 2013.
- [32] Brookfield Engineering Labs., Inc. *More Solutions to Sticky Problems*, May 2014.

- [33] S Coetzee, H Swart, P Bosscha, and D Oosthuizen. *Design of an industrial all-terrain robot platform lessons learned in the design of a robotic mine safety platform for South African gold mines*. IEEE, 2012.
- [34] R. F. Craig. *Soil Mechanics (Fifth Edition)*. Chapman and Hall, 1992.
- [35] D E Daniel. *Geotechnical Practice for Waste Disposal*. Springer US, 1 edition, 1993.
- [36] Braja M. Das. *Fundamentals of Geotechnical Engineering (Second Edition)*. Thomson, 2005.
- [37] Pedro Deusdado, Eduardo Pinto, Magno Guedes, Francisco Marques, Paulo Rodrigues, André Lourenço, Ricardo Mendonça, André Silva, Pedro Santana, José Corisco, Marta Almeida, Luís Portugal, Raquel Caldeira, José Barata, and Luis Flores. An Aerial-Ground Robotic Team for Systematic Soil and Biota Sampling in Estuarine Mudflats. In *Robot 2015: Second Iberian Robotics Conference*, pages 15–26. Springer International Publishing, Cham, November 2015.
- [38] L Ding, Z Deng, H Gao, J Guo, D Zhang, and K D Iagnemma. Experimental study and analysis of the wheels’ steering mechanics for planetary exploration wheeled mobile robots moving on deformable terrain. *The International Journal of Robotics Research*, 32(6):712–743, June 2013.
- [39] C Doniselli, M Gobbi, and G Mastinu. Measuring the inertia tensor of vehicles. *Vehicle System Dynamics*, 37(sup1):301–313, January 2002.
- [40] Matthew Dunbabin and Lino Marques. Robots for Environmental Monitoring: Significant Advancements and Applications. *IEEE Robotics & Automation Magazine*, 19(1):24–39, March 2012.
- [41] Maurice B. Dusseault and J. Don Scott. Tailings pond behavior and characterization of oil sand tailings sludge. *Particulate Science and Technology*, 1(3):295–309, 1983.
- [42] Maurice B Dusseault and J Don Scott. Tailings Pond Behavior and Characterization of Oil Sand Tailings Sludge. *Particulate Science and Technology*, 1(3):295–309, 1983.
- [43] Iman Entezari, Benoit Rivard, Michael G Lipsett, and G Ward Wilson. Prediction of water content and normalized evaporation from oil sands soft tailings surface using hyperspectral observations. *Canadian Geotechnical Journal*, 53(10):1742–1750, October 2016.
- [44] C W Fervers. Improved FEM simulation model for tire–soil interaction. *Journal of Terramechanics*, 41(2-3):87–100, April 2004.
- [45] R. S. Figliola and Donald E. Beasley. *Theory and design for mechanical measurements*. Hoboken: John Wiley and Sons, sixth edition edition, 2015.

- [46] Daniel M Franks, David V Boger, Claire M Côte, and David R Mulligan. Sustainable development principles for the disposal of mining and mineral processing wastes. *Resources Policy*, 36(2):114–122, June 2011.
- [47] Gustavo Freitas, Fernando Lizarralde, Liu Hsu, Vitor Paranhos, Ney R. Salvi dos Reis, and Marcel Bergerman. Design, modeling, and control of a wheel-legged locomotion system for the environmental hybrid robot. In *Proceedings of the IASTED International Conference*, number CMU-RI-TR-, November 2011.
- [48] Fine Tailings Fundamentals Consortium FTFC. Advances in oil sands tailings research. In *Alberta Department of Energy*, pages 6–7–79–80, Edmonton, 1995.
- [49] James E. Funk and Dennis R. Dinger. *Methylene Blue Index*, pages 669–689. Springer US, 1994.
- [50] G Genta and C Delprete. Some considerations on the experimental determination of moments of inertia. *Meccanica*, 29(2):125–141, 1994.
- [51] A Gentile, L Mangialardi, G Mantriota, and A Trentadue. Measurement of the inertia tensor: An experimental proposal. *Measurement*, 14(3-4):241–254, 1995.
- [52] M Gobbi, G Mastinu, and G Previati. A method for measuring the inertia properties of rigid bodies. *Mechanical Systems and Signal Processing*, 25(1):305–318, January 2011.
- [53] Massimiliano Gobbi, Giampiero Mastinu, Mario Pennati, and Giorgio Previati. InTenso+ System: Measured Centre of Gravity Locations and Inertia Tensors of Road Vehicles. In *ASME 2014 International Design Engineering Technical Conferences and Computers and Information in Engineering Conference*, page V003T01A037. ASME, August 2014.
- [54] Jeremy Green. Underground mining robot: A CSIR project. *SSRR*, pages 1–6, 2012.
- [55] Cyril M Harris and Allan G Piersol. *Harris’ Shock and Vibration Handbook*. McGraw-Hill Companies, November 2001.
- [56] Changbin He, Yong You, Decheng Wang, and Hongjian Wu. Estimating soil failure due to torsion via vane shear test by varying vane diameter and soil properties. *Soil and Tillage Research*, 177:68–78, April 2018.
- [57] Daniel Helmick, Scott McCloskey, Avi Okon, Joseph Carsten, Won Kim, and Chris Leger. Mars science laboratory algorithms and flight software for autonomously drilling rocks. *Journal of Field Robotics*, 30(6):847–874, 2013.
- [58] Gregory Hitz, Francois Pomerleau, Marie-Eve Garneau, Cedric Pradalier, Thomas Posch, Jakob Pernthaler, and Ronald Siegwart. Autonomous Inland Water Monitoring: Design and

- Application of a Surface Vessel. *IEEE Robotics & Automation Magazine*, 19(1):62–72, March 2012.
- [59] Larry A Holm. Strategies for remediation. In *Geotechnical Practice for Waste Disposal*, pages 289–310. Springer US, Boston, MA, 1993.
- [60] S Huh, U Lee, H Shim, J B Park, and J H Noh. Development of an unmanned coal mining robot and a tele-operation system. pages 31–35, 2011.
- [61] Humboldt. Field vane shear set. <https://www.humboldtmg.com/vane-inspection-set.html>, 03 2019.
- [62] K Iagnemma, S Kang, H Shibly, and S Dubowsky. Online Terrain Parameter Estimation for Wheeled Mobile Robots With Application to Planetary Rovers. *IEEE Transactions on Robotics*, 20(5):921–927, October 2004.
- [63] K Iagnemma, H Shibly, and S Dubowsky. On-line terrain parameter estimation for planetary rovers. *Robotics and Automation, 2002. Proceedings. ICRA '02. IEEE International Conference on*, 3:3142 – 3147, 2002.
- [64] Karl Iagnemma and Steven Dubowsky. *Mobile Robots in Rough Terrain Estimation, Motion Planning, and Control with Application to Planetary Rovers*, volume 12 of *Springer Tracts in Advanced Robotics*. Springer Berlin / Heidelberg, 2004.
- [65] Daniel J. Inman. *Engineering Vibration*. Pearson, 4th edition, 2013.
- [66] J. Jaky. The coefficient of earth pressure at rest. *Journal of the Society of Hungarian Architects and Engineers*, 7:355–358, 1944.
- [67] Heather Kaminsky. Measuring Strength in Oil Sands Tailings Deposit. In *International Oil Sands Tailings Conference*, pages 185–194, Lake Louise Alberta, December 2014.
- [68] S Karmakar and R L Kushwaha. Development and laboratory evaluation of a rheometer for soil visco-plastic parameters. *Journal of Terramechanics*, 44(2):197–204, April 2007.
- [69] Sepehr P Khaligh, Farbod Fahimi, and Charles Robert Koch. A system identification strategy for nonlinear model of small-scale unmanned helicopters. *Journal of the American Helicopter Society*, 61(4):1–13, October 2016.
- [70] R Klopper and H P Groebelbauer. A Multi-Sided Kinematic Coupling Combined with an Air Bearing Pendulum for Fast and Accurate Mass Property Measurements. In *13th European Conference on Spacecraft Structures, Materials Environmental Testing*, page 18, June 2014.

- [71] M A Knuth, J B Johnson, M A Hopkins, R J Sullivan, and J M Moore. Discrete element modeling of a Mars Exploration Rover wheel in granular material. *Journal of Terramechanics*, 49(1):27–36, February 2012.
- [72] D Kossoff, W E Dubbin, M Alfredsson, S J Edwards, M G Macklin, and K A Hudson-Edwards. Mine tailings dams: Characteristics, failure, environmental impacts, and remediation. *Applied Geochemistry*, 51:229–245, December 2014.
- [73] Erika Levei, Tiberiu Frentiu, Michaela Ponta, Claudiu Tanaselia, and Gheorghe Borodi. Characterization and assessment of potential environmental risk of tailings stored in seven impoundments in the Aries river basin, Western Romania. *Chemistry Central journal*, 7(1):5, 2013.
- [74] Qian Li, Lanlan Xie, and Jumping Li. Modular Motion-Structure Design Model for Planetary Surface Sampling. *International Journal of Aerospace Engineering*, 2019(3):1–15, April 2019.
- [75] Yun Ling, Wei Lu, Changcheng Wu, Aiguo Song, and Chao Feng. A novel rigid-flexible link combined lunar sampler and its basic dynamics and control. *Aerospace Science and Technology*, 38:41–47, October 2014.
- [76] Yun Ling, Wei Lu, Pengwen Xiong, and Aiguo Song. A miniature flexible sampler for sub-surface lunar exploration. *Acta Astronautica*, 123:8–15, June 2016.
- [77] Yun Ling, Aiguo Song, and Wei Lu. A novel rigid-flexible combined sampler for lunar exploration. *Mechanism and Machine Theory*, 77:25–34, July 2014.
- [78] M G Lipsett, J D Yuen, N A Olmedo, and S C Dwyer. Condition Monitoring of Remote Industrial Installations Using Robotic Systems. In *Engineering Asset Management 2011*, pages 231–241. Springer London, London, July 2013.
- [79] M.G. Lipsett and S.C. Dwyer. A robotic system to characterize soft tailings deposits. In *Proceedings of Mine and Tailings Waste Conference 2009, Banff Alberta*, November 2009.
- [80] M.G. Lipsett, J.D. Yuen, N.A. Olmedo, and S.C. Dwyer. Condition monitoring of remote industrial installations using robotic systems. In Jay Lee, Jun Ni, Jagnathan Sarangapani, and Joseph Mathew, editors, *Engineering Asset Management 2011*, Lecture Notes in Mechanical Engineering, pages 231–241. Springer London, 2014.
- [81] Michael Lipsett, Rijesh Augustine, and Mark Sherstan. Aerial manipulation for remote robotic machinery diagnostics. In *Proceedings of the Machinery Failure and Prevention Technology Conference*, May 2019.

- [82] Michael G Lipsett, Nicolas Olmedo, Benoit Rivard, and Ward Wilson. Robotic Systems for Measuring Properties of Tailings Deposits and Collecting Samples. In *Proceedings of the Fourth International Oil Sands Tailings Conference*, Lake Louise, AB, December 2014.
- [83] Burt G. Look. *Handbook of geotechnical investigation and design tables*. Taylor and Francis, 2007.
- [84] Ou Ma, Hung Dang, and Khanh Pham. On-orbit identification of inertia properties of spacecraft using robotics technology. In *AIAA Guidance, Navigation and Control Conference and Exhibit*, page 139, Reston, Virginia, 2007. American Institute of Aeronautics and Astronautics.
- [85] Joshua A Marshall, Adrian Bonchis, Eduardo Nebot, and Steven Scheduling. Robotics in Mining. In Bruno Siciliano and Oussama Khatib, editors, *Springer Handbook of Robotics*, pages 1549–1576. Springer International Publishing, Cham, 2016.
- [86] Jacob Masliyah, Zhiang Joe Zhou, Zhenghe Xu, Jan Czarnecki, and Hassan Hamza. Understanding Water-Based Bitumen Extraction from Athabasca Oil Sands. *The Canadian Journal of Chemical Engineering*, 82(4):628–654, August 2004.
- [87] G Mastinu, M Gobbi, and C M Miano. The Influence of the Body Inertia Tensor on the Active Safety and Ride Comfort of Road Vehicles. *International Body Engineering Conference & Exhibition and Automotive & Transportation Technology Congress*, 1:2002–01–2058, July 2002.
- [88] J.G. Matthews, W.H. Shaw, M.D. MacKinnon, and R.G. Cuddy. Development of composite tailings technology at syncrude. *International Journal of Surface Mining, Reclamation and Environment*, 16(1):24–39, 2002.
- [89] G. McKenna, V. Mann, B. Fisseha, N. Beier, and N. Olmedo. This tailings has the consistency of chocolate pudding: A formal comparison of the geotechnical vane shear strength of food and soft tailings. *Geotechnical News*, 35(1):28–34, 2017.
- [90] E Mckyes. *Soil Cutting and Tillage*. Elsevier Sciences, 1985.
- [91] N R Morgenstern and J D Scott. Geotechnics of fine tailings management. *Geoenvironment*, pages 1663–1673, 1995.
- [92] Daiki Mori and Genya Ishigami. Excavation model of soil sampling device based on particle image velocimetry. *Journal of Terramechanics*, 62:19–29, December 2015.
- [93] E Mucchi, S Fiorati, R Di Gregorio, and G Dalpiaz. Determining the Rigid-Body Inertia Properties of Cumbersome Systems: Comparison of Techniques in Time and Frequency Domain. *Experimental Techniques*, 35(3):36–43, May 2011.

- [94] Tatsuro Muro and Jonathan OBrien. *Terramechanics Land Locomotion Mechanics*. A.A. Balkema Publishers, Lisse, 2004.
- [95] Seyed Yaser Nabavi Chashmi and Seyed Mohammad-Bagher Malaek. Fast estimation of space-robots inertia parameters: A modular mathematical formulation. *Acta Astronautica*, 127:283–295, October 2016.
- [96] A Nuchter, H Surmann, and K Lingemann. 6D SLAM with an application in autonomous mine mapping. . . . *ICRA '04 2004 IEEE . . .*, pages 1998–2003 Vol.2, 2004.
- [97] Nicolas Olmedo, Stephen Dwyer, Michael Lipsett, and James Yuen. Soft soil sampling device and system US9513193B2, December 2016.
- [98] Nicolas Olmedo and M.G. Lipsett. Oilsands tailings characterization using a robotic system. In Kris Zacny, editor, *Earth and Space 2012*, pages 1167–1176. American Society of Civil Engineers, 2012.
- [99] Nicolas A. Olmedo, Martin Barczyk, and Michael Lipsett. Experimental determination of the inertial properties of small robotic systems using a torsion platform. *Mechanical Systems and Signal Processing*, 131:71 – 96, 2019.
- [100] Nicolas A. Olmedo, Martin Barczyk, and Michael G. Lipsett. An improved terramechanics model for a robotic soil surface sampler. Submitted, 2020.
- [101] Nicolas A. Olmedo, Martin Barczyk, Hong Zhang, Ward Wilson, and Michael G. Lipsett. A ugv-based modular robotic manipulator for soil sampling and terramechanics investigations on mine waste. Submitted, 2020.
- [102] Nicolas A. Olmedo, Bereket Fisseha, Ward Wilson, Martin Barczyk, Hong Zhang, and Michael G. Lipsett. An automated vane shear test tool for environmental monitoring with unmanned ground vehicles. Submitted, 2020.
- [103] Nicolas A Olmedo and Michael G Lipsett. Design and field experimentation of a robotic system for tailings characterization. *Journal of Unmanned Vehicle Systems*, pages juvs–2015–0034, March 2016.
- [104] Geoffrey S Plumlee, Kathleen S Smith, and Walter H Ficklin. *Geoenvironmental Models of Mineral Deposits, and Geology-based Mineral-environmental Assessments of Public Lands*. Number Open-File Report 94-203. U.S. Geological Survey, 1994.
- [105] Morgan Quigley, Ken Conley, Brian P. Gerkey, Josh Faust, Tully Foote, Jeremy Leibs, Rob Wheeler, and Andrew Y. Ng. Ros: an open-source robot operating system. In *ICRA Workshop on Open Source Software*, 2009.

- [106] Resonic. Resonic k. <http://www.resonic.de/resonic-k.php>, 03 2019.
- [107] Adrian F Richards. *Vane Shear Strength Testing in Soils*. Field and Laboratory Studies. ASTM International, 1988.
- [108] Umme Salma Rima and Nicholas Beier. Evaluation of temperature and multiple freeze-thaw effects on the strength properties of centrifuged tailings. In *Geo Edmonton*, 2018.
- [109] B Rivard, D Lyder, J Feng, A Gallie, E Cloutis, P Dougan, S Gonzalez, D Cox, and M G Lipsett. Bitumen content estimation of Athabasca oil sand from broad band infrared reflectance spectra. *The Canadian Journal of Chemical Engineering*, 88(5), June 2010.
- [110] Carsten Schedlinski and Michael Link. A Survey of Current Inertia Parameter Identification Methods. *Mechanical Systems and Signal Processing*, 15(1):189–211, 2001.
- [111] K Skonieczny, D S Wettergreen, and WL Red Whittaker. Advantages of continuous excavation in lightweight planetary robotic operations. *The International Journal of Robotics Research*, 35(9):1121–1139, December 2015.
- [112] Krzysztof Skonieczny. Modeling the effects of surcharge accumulation on terrestrial and planetary wide-blade soil–tillage tool interactions. *Soil and Tillage Research*, 176:104–111, March 2018.
- [113] SMARTMechanical-Company. Intensino full mass properties measurement. <http://www.smartmechanical-company.it/en/products/intensino#information>, 03 2019.
- [114] SMARTMechanical-Company. Intenso full mass properties measurement. <http://www.smartmechanical-company.it/en/products/intenso#information>, 03 2019.
- [115] SpaceElectronics. Ksr cg moi series. <https://www.space-electronics.com/Products/ksr-cg-moi-series>, 03 2019.
- [116] SpaceElectronics. Mp weight cg moi series. <https://www.space-electronics.com/Products/mpweight-cg-moi-series>, 03 2019.
- [117] SpaceElectronics. Xr production series. <https://www.space-electronics.com/Products/xr-production-series>, 03 2019.
- [118] W.C. Swick and J.V. Perumpral. A model for predicting soil-tool interaction. *Journal of Terramechanics*, 25(1):43 – 56, 1988.
- [119] Tixian Tian, Hongzhou Jiang, Zhizhong Tong, Jingfeng He, and Qitao Huang. An inertial parameter identification method of eliminating system damping effect for a six-degree-of-freedom parallel manipulator. *Chinese Journal of Aeronautics*, 28(2):582–592, April 2015.

- [120] Gerardo Ortiz Torres, Ricardo Schacht Rodriguez, Juan Reyes Reyes, Carlos Daniel Garcia Beltran, Maria Eusebia Guerrero Sanchez, and Carlos Manuel Astorga Zaragoza. Development of experimental platform for control system of a planar vertical take-off and landing unmanned aerial vehicle. *IEEE Latin America Transactions*, 16(2):342–349, 2018.
- [121] Ashitey Trebi-Ollennu, Richard Volpe, Robert Bonitz, Matthew Robinson, and Joseph Carsten. In situ robotic arm operations. *IEEE Robotics & Automation Magazine*, 16(4):34–43, December 2009.
- [122] Ioannis Tsitsimpelis, C. James Taylor, Barry Lennox, and Malcolm J. Joyce. A review of ground-based robotic systems for the characterization of nuclear environments. *Progress in Nuclear Energy*, 111:109 – 124, 2019.
- [123] P E Uys, P S Els, M J Thoresson, K G Voigt, and W C Combrinck. Experimental determination of moments of inertia for an off-road vehicle in a regular engineering laboratory. *International Journal of Mechanical Engineering Education*, 34(4):291–314, 2006.
- [124] Dirk Van Zyl. Mine waste disposal. In *Geotechnical Practice for Waste Disposal*, pages 269–286. Springer US, Boston, MA, 1993.
- [125] R Volpe, E Baumgartner, P Scheaker, and S Hayati. Technology development and testing for enhanced Mars Rover Sample Return operations. 7:247–257 vol.7, 2000.
- [126] Chen Wang, David Harbottle, Qingxia Liu, and Zhenghe Xu. Current state of fine mineral tailings treatment: A critical review on theory and practice. *Minerals Engineering*, 58:113–131, April 2014.
- [127] Hongwu Wang, Garrett G Grindle, Samuel Connor, and Rory A Cooper. An experimental method for measuring the moment of inertia of an electric power wheelchair. *Conference proceedings : ... Annual International Conference of the IEEE Engineering in Medicine and Biology Society. IEEE Engineering in Medicine and Biology Society. Annual Conference*, 2007:4798–4801, 2007.
- [128] W Wang, W Dong, Y Su, D Wu, and Z Du. Development of Search-and-rescue Robots for Underground Coal Mine Applications. *Journal of Field Robotics*, 31(3):386–407, 2014.
- [129] David Wettergreen, Scott Jared Moreland, Krzysztof Skonieczny, Dominic Jonak, David Kohanbash, and James Teza. Design and field experimentation of a prototype lunar prospector. *International Journal of Robotics Research*, 29(12):1550 – 1564, October 2010.
- [130] Kurt Wiener and Richard Boynton. Using the Moment of Inertia Method to Determine Product of Inertia. In *51st Annual Conference of the Society of Allied Weight Engineers*, pages 1–29, Hartford, Connecticut, 1992.

- [131] Barry A Wills and James A Finch. Tailings Disposal. In *Wills' Mineral Processing Technology*, pages 439–448. Elsevier, 2016.
- [132] J Y Wong. Chapter 3 - Measurement of Terrain Properties. In J Y Wong, editor, *Terramechanics and Off-Road Vehicle Engineering (Second Edition)*, pages 65–74. Butterworth-Heinemann, Oxford, 2010.
- [133] J Y Wong and A R Reece. Prediction of rigid wheel performance based on the analysis of soil-wheel stresses part I. Performance of driven rigid wheels. *Journal of Terramechanics*, 4(1):81–98, 1967.
- [134] J Y Wong and A R Reece. Prediction of rigid wheel performance based on the analysis of soil-wheel stresses: Part II. Performance of towed rigid wheels. *Journal of Terramechanics*, 4(2):4, 1967.
- [135] J.Y. Wong. *Terramechanics and Off-Road Vehicle Engineering*. Butterworth-Heinemann, Oxford, 2 edition, 2010.
- [136] Banglu Xi, Mingjing Jiang, Liang Cui, Jun Liu, and Huayang Lei. Experimental verification on analytical models of lunar excavation. *Journal of Terramechanics*, 83:1–13, June 2019.
- [137] Long Xue, Baichao Chen, Zhenjia Zhao, Zhaolong Dang, and Meng Zou. Experimental Study of Torque Using a Small Scoop on the Lunar Surface. *International Journal of Aerospace Engineering*, 2016(6):1–8, 2016.
- [138] Toru YADA, Akio FUJIMURA, Masanao ABE, Tomoki NAKAMURA, Takaaki NOGUCHI, Ryuji OKAZAKI, Keisuke NAGAO, Yukihiro ISHIBASHI, Kei SHIRAI, Michael E ZOLENSKY, Scott SANDFORD, Tatsuaki OKADA, Masayuki UESUGI, Yuzuru KAROUJI, Maho OGAWA, Shogo YAKAME, Munetaka UENO, Toshifumi MUKAI, Makoto YOSHIKAWA, and Junichiro KAWAGUCHI. Hayabusa-returned sample curation in the Planetary Material Sample Curation Facility of JAXA. *Meteoritics & Planetary Science*, 49(2):135–153, February 2013.
- [139] Kazuya Yoshida. Terramechanics-based analysis and traction control of a lunar/planetary rover. *Field and Service Robotics*, 24:225–234, 2006.
- [140] P Younse, A Stroupe, T Huntsberger, M Garrett, J L Eigenbrode, L G Benning, M Fogel, and A Steele. Sample acquisition and caching using detachable scoops for mars sample return. In *2009 IEEE Aerospace conference*, pages 1–12. IEEE, 2009.
- [141] R Yousefi Moghaddam, A Kotchon, and M G Lipsett. Method and apparatus for on-line estimation of soil parameters during excavation. *Journal of Terramechanics*, 49(3-4):173–181, June 2012.

- [142] Kun Zhai, Tianshu Wang, and Dongbo Meng. Optimal excitation design for identifying inertia parameters of spacecraft. *Acta Astronautica*, 140:370–379, November 2017.
- [143] Weiwei Zhang, Shengyuan Jiang, Jie Ji, and Dewei Tang. A drilling tool design and in situ identification of planetary regolith mechanical parameters. *Advances in Space Research*, 61(9):2444–2456, May 2018.
- [144] Feng Zhou, Raymond E Arvidson, Keith Bennett, Brian Trease, Randel Lindemann, Paolo Bellutta, Karl Iagnemma, and Carmine Senatore. Simulations of Mars Rover Traverses. *Journal of Field Robotics*, 31(1):141–160, September 2013.
- [145] Feng Zhou, Raymond E. Arvidson, Keith Bennett, Brian Trease, Randel Lindemann, Paolo Bellutta, Karl Iagnemma, and Carmine Senatore. Simulations of mars rover traverses. *Journal of Field Robotics*, 31(1):141–160, 2014.
- [146] Tianjun Zhu and Fei Li. Experimental investigation and performance analysis of inertia properties measurement for heavy truck cab. *Advances in Mechanical Engineering*, 7(11):168781401561862, November 2015.
- [147] Tianjun Zhu, Fudong Zhang, Jianying Li, Fei Li, and Changfu Zong. Development Identification Method of Inertia Properties for Heavy Truck Engine Based on MIMS Test Rig. *MATEC Web of Conferences*, 153(6):04009, February 2018.